THE UNIVERSITY *of* EDINBURGH

Analysis of Random Orientation and User Mobility in LiFi Networks

Mohammad Dehghani Soltani

THE UNIVERSITY
of EDINBURGH

Thesis submitted for the degree of
Doctor of Philosophy

The University of Edinburgh
School of Engineering
Institute for Digital Communications

2019

Abstract

Mobile data traffic is anticipated to surpass 49 exabyte per month by 2021. Smartphones, as the main factor of generating this huge data traffic (86%), are expected to require average speed connection of 20 Mbps by 2021. Light-fidelity (LiFi) is a novel bidirectional, high-speed and fully networked optical wireless communication and it is a promising solution to undertake this huge data traffic. However, to support seamless connectivity in LiFi networks, real-time knowledge of channel state information (CSI) from each user is required at the LiFi access point (AP). The CSI availability enables us to achieve optimal resource allocation and throughput maximization but it requires feedback transmitted through the uplink channel. Furthermore, the important aspects of the indoor LiFi channel such as the random orientation of user device, user mobility and link blockage need to be carefully analysed and effective solutions should be developed.

In contrast to radio frequency (RF) channels, the LiFi channel is relatively less random. This feature of LiFi channel enables a potential reduction in the amount of feedback required to achieve high throughputs in a dynamic LiFi network. Based on this feature, two techniques for reducing the amount of feedback in LiFi cellular networks are proposed: 1) limited-content feedback scheme based on reducing the content of feedback information and 2) limited-frequency feedback scheme based on the update interval. It is shown that these limited-feedback schemes can provide almost the same downlink performance as full feedback scheme. Furthermore, an optimum update interval which provides maximum bidirectional user equipment (UE) throughput, has been derived.

Device orientation and its statistics is an important determinant factor that can affect the users throughput remarkably in LiFi networks. However, device orientation has been ignored in many previous performance studies of LiFi networks due to the lack of a proper statistical model. In this thesis, a novel model for the orientation of user device are proposed based on experimental measurements. The statistics of the device orientation for both sitting and walking activities are presented. Moreover, the statistics of the line-of-sight (LOS) channel gain are calculated. The influence of random device orientation on the received signal-to-noise-ratio (SNR) and bit-error ratio (BER) performance of LiFi systems has been also evaluated.

To support the seamless connectivity of future LiFi-enabled devices in the presence of random device orientation, mobility and blockage, efficient handover between APs are required. In this thesis, an orientation-based random waypoint (ORWP) mobility model is proposed to analyze the performance of mobile users considering the effect of random device orientation. Based on this model, an analysis of handover due to random orientation and user mobility is presented. Finally, in order to improve seamless connectivity, a multi-directional receiver (MDR) configuration is proposed. The MDR configuration shows a robust performance in the presence of user mobility, random device orientation and blockage.

Lay summary

In order to address future data traffic growth, plenty of studies and research have been carried out. Recently, a novel technology called light-fidelity (LiFi) has gained attention, as it is considered as a promising solution to fulfil future data requirements. In LiFi systems, data is transmitted by turning a light-emitting diode on and off very quickly, which is not detectable by the human eye. LiFi can be employed as a complementary structure along with radio frequency networks. The possible challenges of realizing the full potential of LiFi systems are user mobility, random device orientation and link blockage, which are studied in this thesis.

Feedback is one solution to leverage the performance in wireless networks. However, this at the cost of low uplink throughput. Hence, limited-feedback mechanisms can help to reduce the amount of feedback while maintaining the downlink performance close to real-time feedback schemes. Two techniques for reducing the amount of feedback in LiFi systems are proposed: 1) limited-content feedback scheme based on reducing the content of feedback information and 2) limited-frequency feedback scheme based on the update interval. Furthermore, an optimum update interval has been derived, which provides maximum bidirectional throughput for mobile users.

Device orientation is another important factor in a LiFi system, which has been modeled based on experimental measurements of forty participants. The experimental measurements have been carried out for both sitting and walking activities. Hence, the model is valid for both mobile and static users. Based on this model, the performance of LiFi systems in a real-life scenario has been evaluated.

To support seamless connectivity for mobile users within a LiFi system with several access points (APs), handover between APs is required. In LiFi networks, the device orientation may also lead to handover between different APs. In order to provide a more realistic framework for user mobility in LiFi networks, the device orientation should be also incorporated with the mobility model.

Finally, we proposed a new configuration for location of photodiodes, in which the photodiodes are located on different sides of a smartphone. This configuration exhibits a robust performance in the presence of random device orientation, user mobility and blockage. This new configuration is a promising solution for future LiFi-enabled smartphones.

Declaration of originality

I hereby declare that the research recorded in this thesis and thesis itself have been composed solely by myself and that it has not been submitted, either in whole or in part, in any previous application for a degree. Except where otherwise acknowledged, the work presented is entirely my own.

Mohammad Dehghani Soltani
Edinburgh, UK
May 2019

Acknowledgements

First of all, I would like to offer my sincerest gratitude to my supervisor, Dr. Majid Safari. This research would not have been accomplished without his constant support and great guidance. Majid has been beyond a supervisor to me and I have learnt a lot from him. I truly appreciate his patience and encouragement throughout my Ph.D study.

I would like to give my special thanks to Prof. Harald Haas as my second supervisor, from whom I have gained so much knowledge in the field of LiFi. My thanks also go to Ms Hannah Brown for proof-reading this thesis.

I would like to thank my friends, who have helped and encouraged me during my academic experience in Edinburgh. The time shared with them is the most precious memory in my life. I am surely blessed to have met you all. Please forgive me if I have forgotten to thank you... The list is too long!

Finally, I would like to appreciate my parents for their love without condition, their help and support without any expectations. I would offer my sincere gratitude to my mother, *Eshrat Hamedi* and my father, *Masoud*, that without them I could not accomplish this thesis.

Contents

List of figures

List of tables

Acronyms and abbreviations

5G	5th generation
ACF	autocorrelation function
ACK	acknowledgment
ACO-OFDM	asymmetrically clipped optical orthogonal frequency division multiplexing
ADC	analog to digital converter
ADR	angular diversity receiver
AP	access point
AR	autoregressive
ASM	adaptive spatial modulation
AWGN	additive white Gaussian noise
BER	bit-error ratio
CB	channel busy
CDF	cumulative distribution function
CDMA	code division multiple access
CE	critical elevation
CIR	channel impulse response
CP	cyclic prefix
CQI	channel quality indicator
CSI	channel state information
CSMA/CA	carrier-sense multiple access with collision avoidance
CTS	clear-to-send
DAC	digital to analog converter
DC	direct current
DCF	distributed coordination function
DCO-OFDM	direct-current biased optical orthogonal frequency division multiplexing
DD	direct detection
DIFS	distributed inter-frame space

DSP	digital signal processor
FDD	frequency division duplex
FDMA	frequency-division multiple access
FF	full feedback
FFR	fractional frequency reuse
FFT	fast Fourier transform
FOV	field of view
FR	frequency reuse
FSO	free-space optical
HCPP	hard-core point process
ICI	inter-channel-interference
ICIC	inter-cell interference coordination
IEEE	institute of electrical and electronics engineers
IFFT	inverse fast Fourier transform
IM	intensity modulation
IR	infrared
IrDA	IR data association
ISI	inter-symbol interference
KSD	Kolmogorov-Smirnov distance
LCF	limited-content feedback
LD	laser diodes
LED	light emitting diodes
LF	limited feedback
LFF	limited-frequency feedback
LiFi	light-fidelity
LOS	line-of-sight
LSSA	least-squares spectral analysis
LTI	linear time-invariant
LTE	long term evolution
MA	multiple access
MAC	medium access control

MDR	multi-directional receiver
MDT	multi-directional transmitter
MIMO	multiple-input multiple-output
ML	maximum-likelihood
mmWave	millimeter Wave
NAV	network allocation vector
NLOS	none-line-of-sight
OFDM	orthogonal frequency division multiplexing
OFDMA	orthogonal frequency division multiple access
OOK	on-off keying
OP	optimization problem
ORWP	orientation-based random waypoint
OT	optimum tilt
OWC	optical wireless communication
PAM	pulse amplitude modulation
PD	photodiode
PDF	probability density function
PEP	pairwise error probability
PF	proportional fair
PPM	pulse position modulation
PPP	poisson point process
PSD	power spectral density
PWM	pulse width modulation
QAM	quadrature amplitude modulation
QoS	quality of service
RF	radio frequency
RMS	root mean square
RP	random process
RSI	received signal intensity
RTS	request-to-send
RV	random variable

RWP	random waypoint
SIFS	short inter-frame space
SINR	signal-to-noise-plus-interference ratio
SM	spatial modulation
SNR	signal-to-noise ratio
SR	screen receiver
TDMA	time division multiple access
TIA	transimpedance amplifier
UE	user equipment
VLC	visible light communications
VLCC	visible light communications consortium
W3C	world wide web consortium
WiFi	wireless fidelity
WLAN	wireless local area networks

Nomenclature

$\otimes$	convolution operator
$\mathbb{E}[\cdot]$	the expectation operator
$\mathcal{F}\{\cdot\}$	Fourier transform operator
$\cdot$	inner product
$\|\cdot\|$	the Euclidean norm operator
$(.)^{\mathrm{T}}$	the transpose operator
$(\cdot)^*$	the complex conjugate operator
a	length of the room
A	physical area of the detector
b	width of the room
B	the modulation bandwidth
c	light speed
c_{H}	the probability of being out of FOV due to random orientation
d	the Euclidean distance between the transmitter and receiver
d_n	the total propagation distance of the nth NLOS channel
d_{p}	horizontal distance between users and their UEs
f_0	fitted coefficient
g_{f}	the gain of the optical filter
$g(\psi)$	the optical concentrator
$\mathbf{G}_\rho$	the reflectivity matrix
h	the vertical distance between the UE and the AP
$h(t)$	time-domain channel impulse response
$h_{\mathrm{fe}}(t)$	time-domain channel impulse response of the front-end elements
$h_{\max}$	maximum channel gain
$h_{\min}$	minimum channel gain
$h_{\mathrm{ow}}(t)$	time-domain channel impulse response of the indoor OWC channel
$H(f)$	frequency-domain channel impulse response

H_{b}	height of the blocker
$\mathbf{H}_{\mathrm{e}}(f)$	the frequency-dependent transfer matrix
$H_{\mathrm{fe}}(f)$	frequency-domain channel impulse response of the front-end elements
$H_{\mathrm{ow}}(f)$	frequency-domain channel impulse response of the indoor OWC channel
$H_{\mathrm{LOS}}(f)$	frequency-domain of LOS link
$H_{\mathrm{NLOS}}(f)$	frequency-domain of NLOS link
$\mathbf{I}$	the unity matrix
I_2	the noise bandwidth factor
I_{BG}	the background current
$\mathcal{K}$	total number of subcarriers
k_{B}	Boltzmanns constant
L_{b}	length of the blocker
L_n	Euclidean distance between the $n-1$th and nth waypoints
m	the Lambertian order
M	modulation order
$\mathbb{N}$	set of natural numbers
N_0	noise spectral density
N_{AP}	number of APs
N_{UE}	number of UEs
$\mathbf{n}_{\mathrm{u}}$	normal vector at the receiver
$\mathbf{n}'_{\mathrm{u}}$	normal vector at the receiver after rotation
$\mathbf{n}_{\mathrm{t}}$	normal vector at the transmitter
$n(t)$	noise at the receiver
P_{opt}	transmitted optical power
$P_{\mathrm{opt,Rx}}$	the average received optical power
$\mathbf{P}_n$	nth waypoint
q	the electron charge
$\mathbb{R}$	set of real numbers
$\mathbf{R}$	rotation matrix
$\mathbf{r}(f)$	receiver transfer vector
$\mathbf{R}_\alpha$	rotation matrix w.r.t the z-axis of local coordinate system

$\mathbf{R}_\beta$	rotation matrix w.r.t the x-axis of local coordinate system
$\mathbf{R}_\gamma$	rotation matrix w.r.t the y-axis of local coordinate system
R_{req}	requested data rate
r_{c}	attocell radius
R	optical to electrical responsivity
R_{L}	the load resistance in the receiver circuit
$\mathcal{S}_{\mathrm{d},j,k}$	SNR of jth UE on the kth subcarrier
$\mathcal{S}_{\mathrm{Tx}}$	the average transmit SNR
$\mathcal{S}_{\mathrm{Rx}}$	the average received SNR
T	the absolute temperature in Kelvin
V_n	speed of user during nth movement
v	movement speed
W_{b}	width of the blocker
$x[n]$	output of IFFT module
$x(t)$	transmitted optical signal
$\tilde{x}(t)$	modulated signal
$x_{\mathrm{DC}}(t)$	DC bias
$x_{\mathrm{e}}(t)$	electrical domain signal
$\boldsymbol{X}$	an OFDM frame
$y(t)$	received electrical signal
α	rotation about the z-axis of local coordinate system
β	rotation about the x-axis of local coordinate system
γ	rotation about the y-axis of local coordinate system
η	the conversion factor
θ	polar angle
θ_{ce}	critical elevation angle
κ_{b}	density of a non-user blocker
ρ_i	reflectance of ith reflector
σ^2_{N}	the total noise power
σ^2_{shot}	variance of the shot noise
$\sigma^2_{\mathrm{thermal}}$	variance of the thermal noise

ς	the refractive index
τ_0	propagation delay of LOS link
τ_n	propagation delay of nth NLOS channel
ϕ	the radiance angle with respect to the axis normal to the transmitter surface
$\Phi_{1/2}$	the half-intensity angle
ψ	the incidence angle with respect to the axis normal to the receiver surface
Ψ_{c}	the receiver field of view
ω	azimuth angle
Ω	angle of direction

Chapter 1
Introduction

1.1 Motivation

The increasing demand for wireless data, which is expected to be 49 exabytes by 2021 [1], motivates both academia and industry to invest in alternative techniques. These include millimeter Wave (mmWave), massive multiple-input multiple-output (MIMO), free space optical communication and Light-Fidelity (LiFi) to support the data traffic growth and next-generation high-speed wireless communication systems. Among these technologies, LiFi is a novel bidirectional, high-speed and fully networked wireless communication technology. LiFi uses visible light as the propagation medium in the downlink for the purposes of illumination and communication. It may use infrared in the uplink so that the illumination constraint of a room remains unaffected, and also to avoid interference with the visible light in the downlink [3, 4]. LiFi offers considerable advantages in comparison to radio frequency (RF) systems. These include the very large, unregulated bandwidth available in the visible light spectrum (more than 10^3 times greater than the whole RF spectrum), high energy efficiency, the rather straightforward deployment which uses off-the-shelf light emitting diodes (LED) and photodiode (PD) devices at the transmitter and receiver ends respectively, and enhanced security as light does not penetrate through opaque objects [5]. Furthermore, LiFi can be used in any RF restricted area such as hospitals and airplane cabins. These important benefits of LiFi have made it favorable for recent and future research. Throughout this thesis, the term LiFi refers to a bidirectional wireless communication system with visible light and infrared being used in the downlink and uplink, respectively. Terms optical wireless communication (OWC) and visible light communication (VLC) refer to wireless data communications by means of any optical spectrum and visible light spectrum, respectively, either for downlink or uplink.

In order to realize the full potential of LiFi cellular networks, many aspects of LiFi still need to be carefully studied. One of these aspects originates from the inherent difference of channels

in LiFi and RF. In fact, the LiFi channel is relatively deterministic, which permits a potential improvement of the bidirectional user throughput by reducing the amount of feedback. This is more pivotal in multiuser scenarios where the access point (AP) requires channel state information (CSI) from all users to efficiently allocate the available resources to the users. Device orientation, user mobility and link blockage are the other important aspects of indoor LiFi networks. These factors and in particular, random device orientation can highly affect the system performance and seamless connectivity. Hence, in order to develop effective solutions and support seamless connectivity, they require further analysis. In the following, these aspects are explained more in details.

By employing multiple access (MA) techniques such as time division MA (TDMA), orthogonal frequency-division MA (OFDMA), code division MA (CDMA) and carrier-sense MA with collision avoidance (CSMA/CA), LiFi can support multiuser communications. However, like any other technology for data communication, in order to provide a better user quality of service (QoS), a channel adaptive mechanism is required, which can be realized by means of feedback from users. The channel adaptive mechanism is a well-known technique that brings performance enhancement in user throughput [6]. Channel adaptive methods require information about the channel condition at the transmitter, which is referred to as CSI. Many channel adaptive techniques are considered to be impractical due to necessitating lots of information at the transmitter. The AP in many systems such as frequency division duplex (FDD) where separate frequency bands are used at the downlink and uplink, cannot employ techniques such as training to obtain the CSI. LiFi also due to the separation of frequency band on downlink and uplink, requires an alternative method to be informed about the channel condition at the receiver. The solution is that the receiver frequently sends back the channel information (such as signal-to-noise ratio, interference level or received power) to the AP. This would be at the cost of uplink degradation. The amount of feedback varies for different channel conditions. Generally, the value is greater for channels that often change, while it is smaller for fairly deterministic channels. The other factor that affects the amount of feedback is the MA scheme. For instance, the AP requires the CSI of all subcarriers from all users if OFDMA is employed, which would be a considerable amount especially for large number of subcarriers. However, research has shown that transmitting a small amount of information about the channel can also provide near optimal

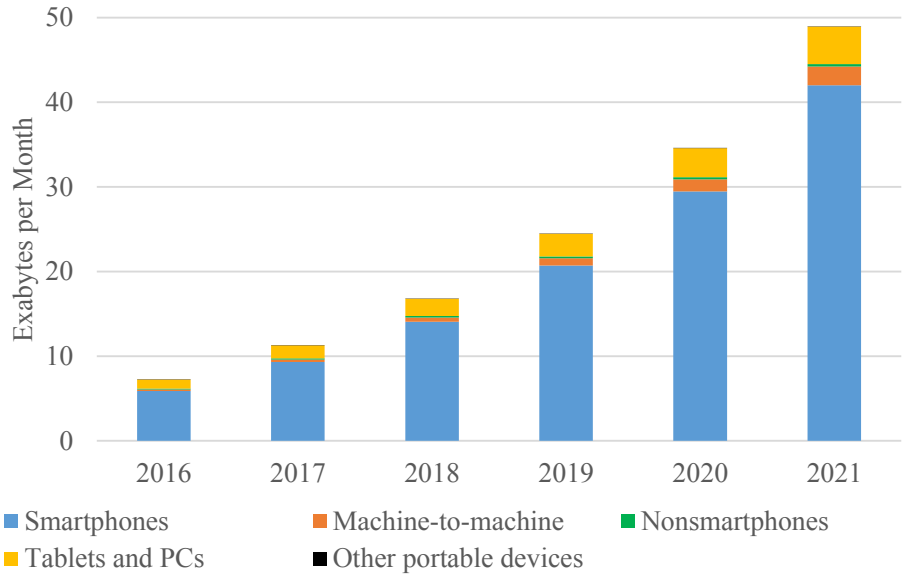

Figure 1.1: *Global Mobile Traffic Growth by Device Type [1].*

channel adaptation [6–9]. These techniques are known as limited feedback methods that can also be employed in LiFi networks. However, in contrast to RF channels, the LiFi channel is relatively deterministic, hence the amount of transmitted feedback can be reduced further without any significant downlink throughput degradation. This motivates us to propose two novel limited feedback schemes for LiFi networks. One is for reducing the content of feedback and the other for decreasing the frequency of feedback transmission, which are called limited-content feedback and limited-frequency feedback schemes, respectively.

Random device orientation is another important factor that can affect the received signal-to-noise ratio (SNR) and as a result the throughput remarkably in mmWave and LiFi networks [10–12]. Both mmWave and LiFi are two promising technologies that are expected to be a part of the future 5th generation (5G) to fulfill its high data rate requirements. However, in both systems, hand-held devices such as smartphones, are prone to random changes in orientation due to hand motion. Smartphones are the most significant and indispensable part of the mobile traffic and thus, they necessitate analysis of random orientation for purposes of resource management and handover protocol design. It is predicted that smartphones generate more than 42 exabytes per month (86% of the mobile data traffic) as shown in figure 1.1 [1]. In order to analyze the effect of random device orientation on the channel gain and received SNR, we need a proper model

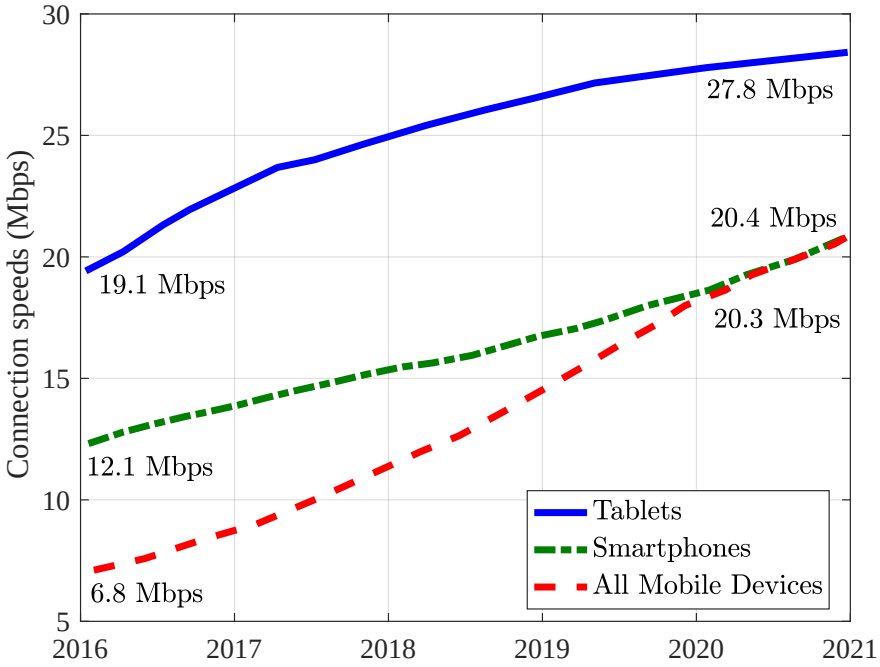

Figure 1.2: *Mobile Speeds by Device [1].*

for the random device orientation. Some studies have been done on device orientation, however, none of them are supported by a valid model through experimental measurements [13–25]. To the best of our knowledge, there is no model for the device orientation, hence, an experiment is conducted to develop a statistical model for the orientation of mobile devices. Based on this model, we are able to find the statistics of the channel gain and SNR in both optical wireless [10] and mmWave systems [11]. In this research, an analyses of device orientation supported by experimental measurements is provided. A new model for device orientation is proposed and its statistics are presented in this work. Based on the proposed model, the effect of random device orientation on the point-to-point communication metrics such as SNR and bit-error ratio (BER) has been studied.

LiFi as a fully networked subset of OWCs should be able to support seamless connectivity for mobile users. According to [1], the connection speed of mobile devices is expected to be about 27.8 Mbps for tablets, and about 20.4 Mbps for smartphones by 2021, as shown in figure 1.2. This growth in connection speed of mobile devices can be supported thanks to the future LiFi-enabled devices. However, due to the small cell radius of LiFi networks, which is in the order of

a few meters, and compared to the average walking speed of human, $v = 1$ m/s [26], a mobile user might only stay in a LiFi cell for a few seconds. Solutions such as integrated RF-based/LiFi networks are proposed in [15, 27, 28]. In these hybrid networks, when the user is static it is served by the LiFi network and when mobile it will be connected to an RF-based network such as wireless fidelity (WiFi) or long term evolution (LTE) networks. In a LiFi standalone cellular network and to support seamless connectivity, the connection has to handed over between APs without loss or interruption of service. However, the challenge facing the employment of conventional handover mechanisms from RF-based cellular networks for LiFi would be frequent handovers because of the user mobility and random device orientation. Due to the inherent difference of LiFi and RF-based networks, it is not appropriate to adopt the same handover protocols from RF networks to LiFi networks. Hence, an analysis of device orientation, mobility and also simultaneous effect of them are required to design an efficient LiFi-capable handover protocol. Another practical solution to support seamless connectivity will be implementing a PD at each side of a smartphone [29] and use all APs for transmitting the same data to the users. However, utilizing all APs for transmitting the same data decreases the spectral efficiency of the system. Spatial modulation (SM) can leverage the spectral efficiency, which can be integrated with the implementation of multiple PDs at the smartphones. This technique is introduced in this research, which is known as multi-directional receiver (MDR). The robust performance of MDR in the presence of random device orientation, user mobility and blockage is shown.

In this research thesis and in order to fully utilize the potential of LiFi cellular networks, the aforementioned aspects and challenges are discussed and effective solutions are provided. The detailed contributions of this research thesis are presented in the next section.

1.2 Contribution

In this thesis, a LiFi network is considered and methods of feedback reduction are introduced. Then, analysis of random user equipment (UE) orientation and user mobility to support seamless connectivity are presented. A new MDR configuration is proposed and its performance is evaluated in the presence of random device orientation, user mobility and link blockage. Theoretical expressions and models are expressed and the accuracy of the analytical models are validated by

Monte-Carlo simulations. In fact, this thesis aims to address the following objectives:

• Reducing the amount of feedback in LiFi networks to improve bidirectional user throughput.

• Providing a model for device orientation supported by experimental measurements.

• Supporting seamless connectivity in LiFi networks in the presence of user mobility, device orientation and blockers in the environment.

Following the first research goal, two techniques for reducing the amount of feedback in LiFi cellular networks are proposed: 1) limited-content feedback scheme based on reducing the content of feedback information and 2) limited-frequency feedback scheme based on the update interval. Furthermore, based on the random waypoint (RWP) mobility model, the optimum update interval, which provides maximum bidirectional user throughput, has been derived. It is noted that to find the optimum update interval feedback time, we only considered the effect of user mobility as it has the dominant effect compared to the random orientation. Referring to the experimental measurements of random device orientation reported in [10], the variation around the mean angle is fairly small. However, the methodology proposed to obtain the optimum update interval can be extended to include the random orientation of UE as well. Furthermore, a modified CSMA/CA protocol for the uplink of LiFi is proposed to address the severe problem of hidden nodes in LiFi networks. The contributions of this work are published in two conference papers *ACM VLCS [30]* and *IEEE PIMRC [31]*, and one journal paper in *IEEE Transactions on Communications [4]*.

With respect to the second research objective, a novel model for device orientation based on experimental measurements of forty participants has been proposed. It is shown that the probability density function (PDF) of the polar angle can be modeled either based on a Laplace (for static users) or a Gaussian (for mobile users) distribution. In addition, a closed-form expression is derived in [10] for the PDF of the cosine of the incidence angle based on which the line-of-sight (LOS) channel gain is described in optical wireless channels. An approximation of this PDF based on the truncated Laplace is proposed and the accuracy of this approximation is confirmed by the Kolmogorov-Smirnov distance (KSD) test. Moreover, the statistics of the LOS channel gain are calculated and the random orientation of a UE is modeled as a random process. The influence of the random orientation on SNR performance of LiFi systems has been

evaluated. By means of the PDF of SNR, the BER of a direct-current biased optical orthogonal frequency division multiplexing (DCO-OFDM) in additive white Gaussian noise (AWGN) channels is evaluated. A closed-form approximation for the BER of the UE with random orientation is presented which shows a close match with Monte-Carlo simulation results. The contributions of this work are in one published journal in *IEEE Transactions on Communications [10]*, one published journal in *IEEE ACCESS [18]* and one accepted conference paper in *IEEE WCNC* [32].

Finally, regarding the third research goal, a new orientation-based random waypoint (ORWP) mobility model is introduced that incorporate the random device orientation with the conventional RWP mobility model. Based on this model, an analysis of handover due to random orientation and user mobility is presented. Next, we consider two configurations for placing the PDs on the UE. The first one is referred to as the screen receiver (SR) whereby all the PDs are located on one face of the UE, e.g., the screen of a smartphone, whereas the other one is an MDR, in which the PDs are located on different sides of the UE. The latter configuration is motivated by the fact that SR exhibited poor performance in the presence of random device orientation and blockage. To improve the spectral efficiency, we adopt SM, which has been shown to be energy efficient as well in many applications, including LiFi. Moreover, an adaptive AP selection scheme for SM is considered where the number of APs are chosen adaptively in an effort to achieve the lowest energy requirement for a target BER and spectral efficiency. The contributions of this work are in one conference paper, *IEEE WCNC* [14], and one submitted journal, *IEEE Journal on Selected Areas in Communications [19]*.

1.3 Thesis Layout

The rest of this thesis is organized as follows. In Chapter 2, the concept of LiFi networks and the channel model are presented. The device orientation, mobility model and blockage are also introduced in this Chapter.

In Chapter 3, two methods to reduce the feedback are introduced. The optimum update interval based on the RWP mobility model is derived that provides maximum bidirectional user throughput. The impact of different parameters such as user velocity and transmitted downlink optical

power on the optimum update interval is studied in this Chapter.

Device orientation models supported by experimental measurements for static and mobile users are proposed in Chapter 4. The effect of random device orientation on the channel gain and SNR has been investigated, where an analytical model for the PDF of channel gain and SNR are developed. Finally, the effect of random orientation on the error performance of point-to-point communication is assessed and a closed-form approximation for the BER of UE with the random orientation is derived.

In Chapter 5, an analysis of handover due to random orientation and user mobility is presented. Then, the effects of mobility, random orientation and blockage on the performance of MDR are investigated while adopting a channel model derived from real-life measurements. Performance metrics such as SNR and BER are considered and the efficiency of MDR is compared to the conventional SR configuration. In addition, an adaptive SM scheme based on AP selection is considered to overcome the effect of random orientation and blockage. It is shown that MDR provides superior performance and can be considered as a practical choice for future LiFi-enabled smartphones.

Chapter 6 summaries the key findings of this research thesis. Conclusions are presented in this Chapter. Additionally, limitations and future work of this research topic are discussed.

1.4 Summary

The rapid growth in mobile data traffic motivates both academia and industry to consider alternative techniques such as mmWave and LiFi. LiFi is a bidirectional and high-speed wireless networked system that offers considerable benefits compared to RF systems. Hence, it has gained a lot of attentions recently. However, to realize the full potential of LiFi systems, the inherent difference of channel in LiFi and RF-based networks needs to be taken into account. Furthermore, to provide seamless connectivity for users, aspects such as random device orientation, user mobility and blockage are required to be studied carefully. In this thesis, the effects of these factors are studied on the system performance and effective solutions are proposed.

Chapter 2
Background

2.1 Introduction

The first experiments that used visible light as a means of communication originated from smoke-beacon systems. Afterwards, in the 19th century, Alexander Graham Bell invented a photophone that could transmit voice messages at a distance of 200 m. The photophone relied on reflected sunlight on a vibrating mirror and a selenium photocell to convey voice via a visible light beam [33, 34]. The British Navy started to communicate through light by means of signal lamps in the late 19th century. These are some examples of initial methods that used visible light as a means of communication. Inspired by these pioneering ideas, the KEIO research group in Japan launched the implementation of data transmission through visible light by using LEDs in 2000 [35]. This was then followed by creation of the visible light communications Consortium (VLCC) in 2003, and the development of the initial and basic concept of the VLC channel model in 2004 [36]. Later, in 2011, Haas introduced LiFi at a TED Global Talk, claiming that unlike VLC, LiFi is a fully-networked bidirectional system, rather than a point-to-point communication technique [3].

In the recent years, especially with the appearance of LiFi with advantages such as providing illumination, high-speed data communication and very accurate indoor localization, LiFi is considered to have a promising market in the future [37]. The optical spectrum can be considered as one of the best resource spectra for wideband wireless communications. It can be performed in the infrared (IR), the visible light and the ultra-violet spectra. The main applications of OWC are free-space optical (FSO) communication for long distance transmission and, IR-based communication and VLC for short-range indoor applications [38]. Wireless IR communication was introduced through the work of Gfeller and Bpst in 1979 [39], where data rates of 100 kbps with a diffuse link were achieved. Later, Kahn and Barry developed channel models for LOS and non-line-of-sight (NLOS) optical wireless links [40]. Visible light as another portion of the

optical spectrum which occupies the frequency spectrum between 400 THz to 790 THz has been recently considered as a potential and promising base for high-speed broadband data communication. The high-speed VLC is in fact a result of recent development in opto-electronics and solid state lighting technology, such as LEDs, laser diodes (LDs) and PDs. LEDs as the future of lighting providers are anticipated to be replaced with the conventional fluorescent lamps in the coming decades due to their energy efficiency. This trend facilitates the use of LEDs in LiFi networks.

LiFi is a novel bidirectional, high-speed and fully-networked OWC system which can be employed as a complementary structure along with RF networks [3]. LiFi utilizes visible light and IR spectra in the downlink and uplink, respectively, and provides high data rates over short distances [4]. Compared to RF networks, LiFi offers notable benefits such as enhanced security, utilizing a very large and unregulated bandwidth and energy efficiency. These advantages have put LiFi in the scope of recent and future research. Therefore, many research and development groups in both academia and industry are currently working on standardization and commercialization of VLC and LiFi.

The first standardization related to VLC was announced by VLCC in Japan [41]. A VLCC specification standard which adopted and developed the IR data association (IrDA) physical layer was published in March 2009. The institute of electrical and electronics engineers (IEEE) issued the "IEEE Standard for Local and Metropolitan Area Networks, Part 15.7: Short-Range Wireless Optical Communication Using Visible Light" in 2011, which covered both the new physical and medium access control (MAC) layers [42]. Later in 2014, a task group called P$802.15.7$r1 was formed to write a revision to the IEEE $802.15.7-$v2011 [43]. In the new draft, some options were included for VLC, namely: i) optical camera communications that utilize flash lights, image and displays sensors as the front-end devices; ii) LED-ID that employs LEDs for the purpose of identification; iii) LiFi as a bidirectional and high-speed wireless network that uses visible light. Moreover, a task group for LiFi in IEEE 802.11 already exists for the standardization of light communication [44].

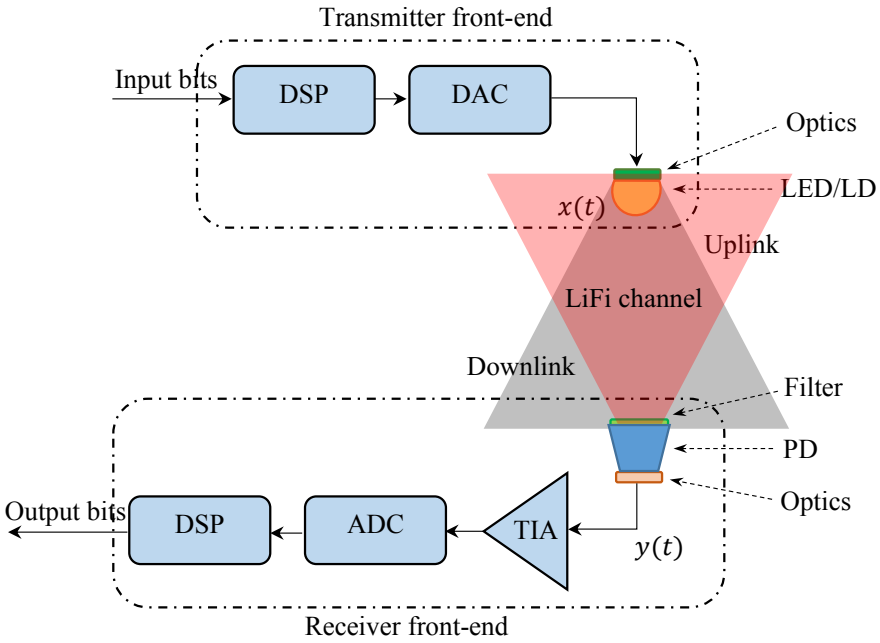

Figure 2.1: *A typical LiFi downlink transmission with commonly used front-end elements at the transmitter and receiver.*

2.2 LiFi Channel

A typical LiFi downlink transmission is shown in figure 2.1. The transmitted optical signal, $x(t)$, after passing through the channel, with the channel impulse response (CIR) of $h(t)$, will be received at the PD. Let's denote the received current at the PD by $y(t)$, then, we have:

$$y(t) = Rh(t) \otimes x(t) + n(t), \tag{2.1}$$

where R is the optical to electrical responsivity of the PD in A/W; and $n(t)$ is the noise at the receiver. The symbol "$\otimes$" stands for a convolution operator. The channel can be described as a baseband linear time-invariant (LTI) system with the frequency response of:

$$H(f) = \int_{-\infty}^{\infty} h(t) e^{-\jmath 2\pi f t} \mathrm{d}t, \tag{2.2}$$

where $H(f) = \mathcal{F}\{h(t)\}$ is the Fourier transform of $h(t)$ and $\jmath = \sqrt{-1}$ is the imaginary number. The CIR, $h(t)$, includes the effect of both front-end elements and the effect of an indoor

liFi channel. Note that front-end elements encompass both transmitter and receiver components such as digital signal processors (DSPs), an analog to digital converter (ADC), a digital to analog converter (DAC) and a transimpedance amplifier (TIA). Therefore, the channel gain can be characterized as:

$$h(t) = h_{\mathrm{fe}}(t) \otimes h_{\mathrm{ow}}(t), \tag{2.3}$$

where $h_{\mathrm{fe}}(t)$ shows the CIR of the front-end elements and $h_{\mathrm{ow}}(t)$ denotes the CIR of the indoor LiFi. Hence, in the frequency domain, we have:

$$H(f) = H_{\mathrm{fe}}(f)H_{\mathrm{ow}}(f), \tag{2.4}$$

where $H_{\mathrm{fe}}(f)$ and $H_{\mathrm{ow}}(f)$ are the Fourier transform of $h_{\mathrm{fe}}(t)$ and $h_{\mathrm{ow}}(t)$, respectively. In the next subsections, we study the CIR of front-end elements and indoor LiFi in detail.

2.2.1 Front-end Elements

As illustrated in figure 2.1, the front-end elements can be classified as transmitter/receiver front-end elements, which are discussed in detail in the following.

2.2.1.1 Transmitter Front-end Elements

At the transmitter, DSP, DAC and LED/LD are used. The DSP component converts the input information bits to digital signals and then, the DAC unit converts the digital signals to analogue current signals. Finally, the analogue current signals are fed into the LED/LD and they are converted into optical light power with various intensities. This is the most favorable and viable modulation for LiFi and is known as intensity modulation (IM). In LiFi systems, LEDs are mainly used as optical source. White LEDs can used for both illumination and communication purposes. Two types of commercial white LEDs are being used. The first one is red-green-blue (RGB) LED. This LED results in white optical light by combining three color components generated by different set of devices [45]. The second type of LEDs with white light is a blue LED chip covered by a yellow-phosphor coating. The emission of narrow blue spectrum can be absorbed and efficiently re-emitted by phosphor coating. The restricting factor of utilizing this

kind of LEDs is that the absorption and re-emission time of phosphor is slow. Hence, the 3-dB bandwidth of these LEDs is in the order of $2 - 10$ MHz [46].

2.2.1.2 Receiver Front-end Elements

At the receiver side, the optical power can be turned into electrical signals by means of various methods such as imaging sensors [47, 48], solar cell panels [49], LEDs [50] and PDs [41]. Among them, PDs are more favorable as they have a shorter response time that leads to a wider bandwidth so that they can provide high-speed data communication. This is the most practical down-conversion method in LiFi known as direct detection (DD). The current signal captured by the optic element at the receiver is then transferred to output voltage via TIA. This analogue voltage signal can be converted to digital signals by ADC and then fed into the DSP unit to recreate the information bits. It is also noted that at the receiver sides of UEs and APs, optical filters are tuned in visible light and IR bands, respectively, to remove unwanted signals.

2.2.1.3 Impulse Response of Front-end Elements

In this subsection, the total effect of both transmitter and receiver front-end elements are considered, which can be modeled as a low-pass filter. A number of experiments have shown that the front-end elements follow low-pass filter characteristics [46, 51, 52]. Therefore, the frequency response of the front-end channel can be modeled by a first order low pass filter as:

$$|H_{\text{fe}}(f)|^2 = e^{-f/f_0}, \tag{2.5}$$

where f_0 is the fitted coefficient. The higher the value of f_0, the wider the 3-dB bandwidth. Typically, the 3-dB bandwidth of the front-end channel is low. Figure 2.2 illustrates the frequency response of front-end elements with fitted coefficient, f_0, of 15.2 MHz, 31.7 MHz and 35.6 MHz given in [46, 51, 52].

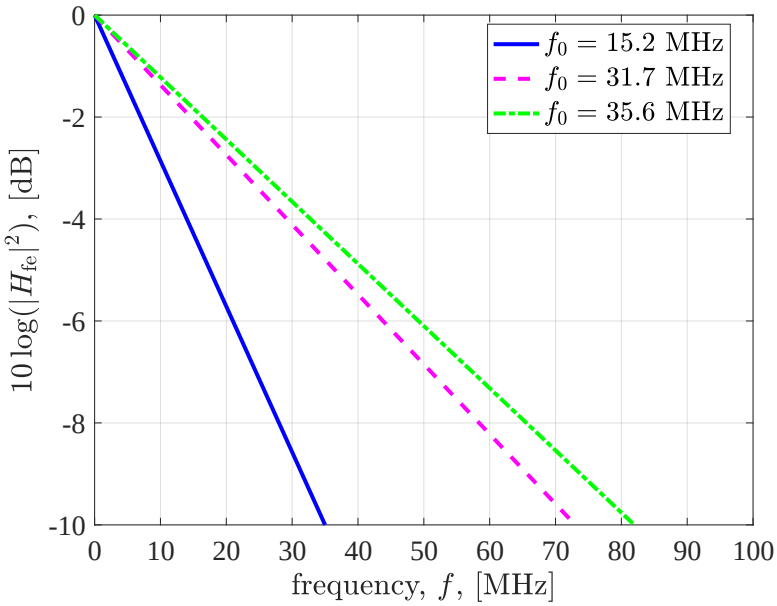

Figure 2.2: *Frequency response of front-end elements with different fitted coefficient,* f_0.

2.2.2 Channel of Indoor LiFi System

The main components of the indoor LiFi channel are a LOS link and a NLOS channel due to reflectors in the environment. The LOS link between the transmitter and the receiver is shown in figure 2.3-(a). The NLOS channel comprises an infinite number of links. Figure 2.3-(b) denotes one of the NLOS links between the transmitter and receiver. In the frequency domain, the indoor LiFi channel can be expressed as:

$$\begin{aligned} H_{\text{ow}}(f) &= H_{\text{LOS}}(f) + H_{\text{NLOS}}(f) \\ &= H_{\text{LOS}}(0)e^{-\jmath 2\pi f \tau_0} + \sum_{n=1}^{\infty} H_{\text{NLOS},n}(0)e^{-\jmath 2\pi f \tau_n}, \end{aligned} \tag{2.6}$$

where $H_{\text{LOS}}(f)$ and $H_{\text{NLOS}}(f)$ are the channel frequency response of the LOS and NLOS components, respectively. The direct current (DC) gain of the LOS link is denoted by $H_{\text{LOS}}(0)$ and the DC gain of the nth NLOS link is shown by $H_{\text{NLOS},n}(0)$ [53]. In (2.6), the propagation link delays between the transmitter and receiver are given as $\tau_0 = d/c$ and $\tau_n = d_n/c$ with d as the Euclidean distance between the transmitter and receiver; d_n as the total propagation distance of the nth NLOS link. The light speed is denoted with c. In the following, the DC gain

components are characterized.

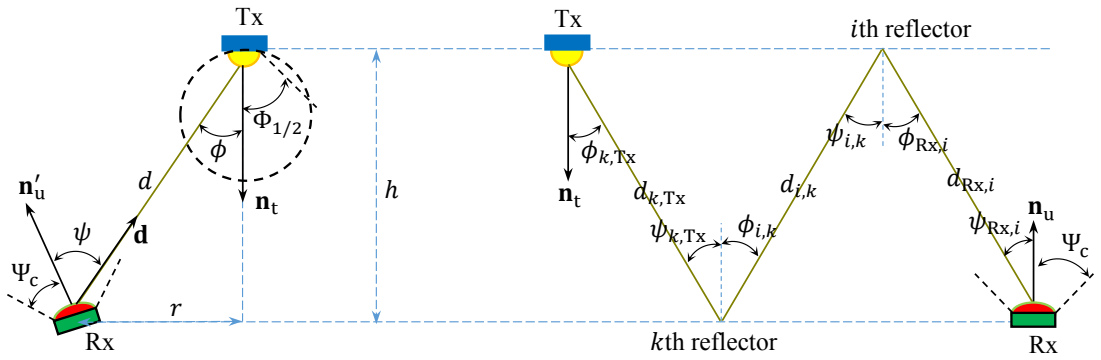

a) LOS link b) The nth NLOS link

Figure 2.3: *The downlink geometry of indoor LiFi channels for (a): LOS link, and (b): one of the NLOS links.*

2.2.2.1 LOS DC Gain

The DC gain of the LOS optical channel between the transmitter and receiver is given by:

$$H_{\text{LOS}}(0) = \frac{(m+1)A}{2\pi d^2} \cos^m \phi \; g_{\text{f}} g(\psi) \cos\psi \; \text{rect}\left(\frac{\psi}{\Psi_{\text{c}}}\right), \tag{2.7}$$

where A, ϕ and ψ are the physical area of the detector, the angle of radiance with respect to the axis normal to the transmitter surface, and the angle of incidence with respect to the axis normal to the receiver surface, respectively. Furthermore, $\text{rect}(\frac{\psi}{\Psi_{\text{c}}}) = 1$ for $0 \leq \psi \leq \Psi_{\text{c}}$ and 0 otherwise. In (2.7), g_{f} is the gain of the optical filter, and Ψ_{c} is the receiver field of view (FOV). The optical concentrator, $g(\psi)$, is given as:

$$g(\psi) = \begin{cases} \dfrac{\varsigma^2}{\sin^2 \Psi_{\text{c}}}, & 0 \leq \psi \leq \Psi_{\text{c}} \\ 0, & \text{o.w} \end{cases}, \tag{2.8}$$

where ς is the refractive index; and also m is the Lambertian order which is:

$$m = -\frac{1}{\log_2(\cos \Phi_{1/2})}, \tag{2.9}$$

where $\Phi_{1/2}$ is the half-intensity angle [54]. The radiance angle ϕ and the incidence angle ψ of the transmitter and the receiver can be calculated using the rules from analytical geometry as:

$$\begin{aligned} \cos\phi &= \frac{-\mathbf{d}\cdot\mathbf{n}_{\mathrm{t}}}{\|\mathbf{d}\|}, \\ \cos\psi &= \frac{\mathbf{d}\cdot\mathbf{n}'_{\mathrm{u}}}{\|\mathbf{d}\|} \end{aligned} \tag{2.10}$$

where $\mathbf{n}_{\mathrm{t}} = [0, 0, -1]^{\mathrm{T}}$ and $\mathbf{n}'_{\mathrm{u}}$ are the normal vectors at the transmitter and the receiver planes, respectively and $\mathbf{d}$ denotes the distance vector from the receiver to the transmitter. The symbols $\cdot$ and $\|\cdot\|$ denote the inner product and the Euclidean norm operators, respectively. Also $(.)^{\mathrm{T}}$ denotes the transpose operator.

2.2.2.2 NLOS Channel

The NLOS component of the optical channel can be calculated based on the method described in [53]. Using the frequency domain instead of the time domain analysis, we are able to consider an infinite number of reflections to have an accurate value of the diffuse link. The environment is segmented into a number of surface elements which reflect light beams. These surface elements are modeled as Lambertian radiators described by (2.9) with $m = 1$. Then, the frequency domain of NLOS channel gain including an infinite number of reflections can be expressed by [53]:

$$H_{\mathrm{NLOS}}(f) = \mathbf{r}^{\mathrm{T}}(f)\mathbf{G}_{\rho}(\mathbf{I} - \mathbf{H}_{\mathrm{e}}(f)\mathbf{G}_{\rho})^{-1}\mathbf{t}(f), \tag{2.11}$$

where $\mathbf{t} = [H_{1,\mathrm{Tx}}(f), H_{2,\mathrm{Tx}}(f), \ldots, H_{N,\mathrm{Tx}}(f)]^{\mathrm{T}}$ is the transmitter transfer vector with the entities given as:

$$H_{k,\mathrm{Tx}}(f) = \frac{(m+1)A_k}{2\pi d_{k,\mathrm{Tx}}^2}\cos^m\phi_{k,\mathrm{Tx}}\cos\psi_{k,\mathrm{Tx}}\, e^{-\jmath 2\pi f\frac{d_{k,\mathrm{Tx}}}{c}}, \quad k = 1, \ldots, N, \tag{2.12}$$

where A_k is the area of the kth reflector element; $\phi_{k,\mathrm{Tx}}$ is the radiance angle to the kth reflector and $\psi_{k,\mathrm{Tx}}$ is the incidence angle with respect to the normal vector of the kth reflector. The Euclidean distance between the kth reflector and the transmitter is denoted by $d_{k,\mathrm{Tx}}$.
In (2.11), $\mathbf{H}_{\mathrm{e}}$ is the LOS transfer matrix of size $N \times N$ for the links between all surface elements.

The frequency-dependent transfer matrix $\mathbf{H}_{\mathrm{e}}(f)$ can be described as:

$$\mathbf{H}_{\mathrm{e}}(f) = \begin{pmatrix} H_{1,1}(f) & \cdots & H_{1,N}(f) \\ \vdots & \ddots & \vdots \\ H_{N,1}(f) & \cdots & H_{N,N}(f) \end{pmatrix}, \tag{2.13}$$

where the entities $H_{i,k}(f)$ are the LOS transfer function between the kth reflector which acts as a transmitter[1] and the ith reflector which acts as a receiving element. These entities can be obtained as:

$$H_{i,k}(f) = \frac{A_i}{\pi d_{i,k}^2} \cos\phi_{i,k} \cos\psi_{i,k}\, e^{-\jmath 2\pi f \frac{d_{i,k}}{c}}, \tag{2.14}$$

for $i, k \in \{1, \cdots, N\}$. Here, $\phi_{i,k}$ and $\psi_{i,k}$ are the radiance and incidence angles between pairs of reflectors i and k with respect to their normal vectors; $d_{i,k}$ is the Euclidean distance between the ith and kth reflectors.

Finally, $\mathbf{r} = [H_{\mathrm{Rx},1}(f), H_{\mathrm{Rx},2}(f), \ldots, H_{\mathrm{Rx},N}(f)]^{\mathrm{T}}$ is the receiver transfer vector with the entities given as:

$$H_{\mathrm{Rx},i}(f) = \frac{A}{\pi d_{\mathrm{Rx},i}^2} \cos\phi_{\mathrm{Rx},i} \cos\psi_{\mathrm{Rx},i}\, \mathrm{rect}\left(\frac{\psi_{\mathrm{Rx},i}}{\Psi_{\mathrm{c}}}\right) e^{-\jmath 2\pi f \frac{d_{\mathrm{Rx},i}}{c}}, \tag{2.15}$$

where A is the PD area; $\phi_{\mathrm{Rx},i}$ and $\psi_{\mathrm{Rx},i}$ are the radiance and incidence angles of the ith reflector and the receiver with respect to their normal vectors, respectively. The Euclidean distance between the ith reflector and the receiver is denoted as $d_{\mathrm{Rx},i}$.

In (2.11), matrix $\mathbf{G}_\rho = \mathrm{diag}(\rho_1, ..., \rho_N)$ is the reflectivity matrix of all N reflectors with ρ_i as the reflectance of the ith reflector; and $\mathbf{I}$ is the unity matrix of size $N \times N$.

2.3 System Configuration

In this section, single input/single output (SISO) configuration and MIMO configurations are discussed. Figure 2.4-(a) represents a single transmit/single receiver, where only one AP transmits data and only one PD detects the signal. On the other hand, in a multiple transmit/multiple

[1] It is assumed the reflectors are modelled as proper Lambertian radiators with $m = 1$.

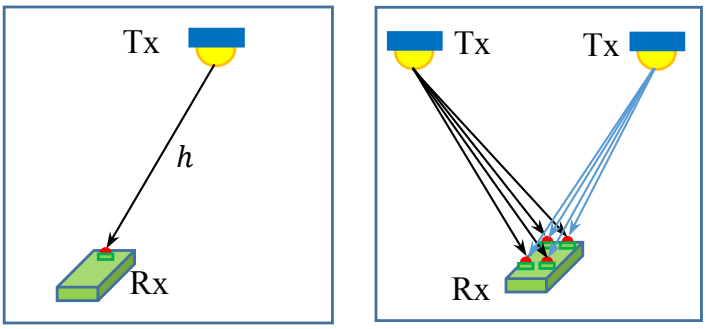

(a) SISO **(b)** MIMO

Figure 2.4: *SISO and MIMO configurations.*

receiver configuration several APs transmit data to the UE and multiple PDs are used to detect the signal. A MIMO configuration with 2 transmitters and 4 PDs is shown in figure 2.4-(b).

2.3.1 SISO Configuration

As shown in figure 2.4, in a SISO configuration, only one AP and transmits data signals to a single PD mounted on the UE. Hence, the received signal at the PD at a specific time instance can be expressed as:

$$y = hx + n \tag{2.16}$$

where h is the channel gain between the AP and the PD, which includes the LOS and NLOS links; x is the transmitted optical signal and n is the noise at the receiver.

2.3.2 MIMO Configuration

In this subsection, an IM/DD LiFi MIMO channel is considered, where N_{t} light sources (e.g. one or more LEDs) can transmit the signal and one UE receives the signal with N_{r} PDs. The resulting channel is described as:

$$\mathbf{y} = \mathbf{H}\mathbf{x} + \mathbf{n}, \tag{2.17}$$

where $\mathbf{x}$ is the transmitted signal vector of size $N_{\mathrm{t}} \times 1$; and $\mathbf{y}$ and $\mathbf{n}$ are $N_{\mathrm{r}} \times 1$ vectors respectively representing the received signal and noise at each PD. The noise here includes all possible noises, such as shot noise and thermal noise and is assumed to be real valued additive white Gaussian

$\mathcal{N}\left(\mathbf{0}_{N_\mathrm{r}}, \sigma_\mathrm{n}^2 \mathbf{I}_{N_\mathrm{r}}\right)$ and independent of the transmitted signal [55]. The variance of the noise is equal to $\sigma_\mathrm{n}^2 = N_0 B$, where N_0 is the single sided power spectral density of noise and B is the bandwidth. The channel matrix $\mathbf{H}$ is given by:

$$\mathbf{H} = \begin{pmatrix} h_{1,1} & \cdots & h_{1,N_\mathrm{t}} \\ \vdots & \ddots & \vdots \\ h_{N_\mathrm{r},1} & \cdots & h_{N_\mathrm{r},N_\mathrm{t}} \end{pmatrix}, \tag{2.18}$$

where the entities $h_{i,j}$ ($i = 1, ..., N_\mathrm{r}$ and $j = 1, ..., N_\mathrm{t}$) are the channel gain of the link between the jth transmitter and the ith PD. In this thesis, two types of MIMO are considered, namely full MIMO and spatial modulation, which are discussed in the following subsections.

2.3.2.1 Full MIMO

In full MIMO, all degrees of freedom in the spatial domain are utilized by transmitting an independent signal by each available transmitter at the same time. The maximum spectral efficiency (assuming $N_\mathrm{r} \geq N_\mathrm{t}$) is achieved in this case that is equal to $N_\mathrm{t} \log_2(M)$ bit/s/Hz for M-PAM. However, the performance of full MIMO depends on the channel matrix, as higher correlation between elements of the channel matrix significantly degrades the performance level.

2.3.2.2 Spatial modulation (SM)

Different variations of SM have been proposed in the literature [56]. We consider the original SM, where each M-PAM modulated symbol is transmitted by one of the available light sources. The active light source is selected according to $\log_2 N_\mathrm{t}$ independent bits. Therefore, the spectral efficiency would be equal to $R_\mathrm{SM} = \log_2(N_\mathrm{t}) + \log_2(M)$ bit/s/Hz. SM benefits from enhanced spectral efficiency compared to SRC, while it is simpler and more immune to inter-channel interference compared to full MIMO. However, the performance of SM also depends on the channel matrix.

2.4 Noise Analysis

Like RF systems, noise can also degrade the system performance in LiFi systems. The noise at the receiver of a LiFi system is comprised of two components: shot noise and thermal noise. In the following, these two primary source of noise at the receiver are described.

2.4.1 Shot Noise

Shot noise is a kind of electronic noise that can be modelled by a Poisson process. Shot noise is caused by the random nature of photon arrivals with an average rate governed by the received optical power. Shot noise may be generated because of many factors in the environment. The major factor is ambient light that includes sunlight, street lights, fluorescent and incandescent lamps [39]. The power of shot noise at the PD is then given by [57]:

$$\sigma^2_{\text{shot}} = 2qRP_{\text{opt,Rx}}B + 2qI_{\text{BG}}I_2B, \tag{2.19}$$

where $P_{\text{opt,Rx}}$ denotes the average received optical power; q is the electron charge which is 1.6×10^{-19} C; B is the modulation bandwidth; I_{BG} is the background current; and I_2 is the noise bandwidth factor.

2.4.2 Thermal Noise

Thermal noise is mainly caused by the random motions of electrons in the circuit due to the temperature fluctuation. The resistance used in the TIA is the primary source of thermal noise at the receiver. The power of thermal noise at the PD is given by [57]:

$$\sigma^2_{\text{thermal}} = \frac{4k_{\text{B}}T}{R_{\text{L}}}B, \tag{2.20}$$

where k_{B} is the Boltzmanns constant which is 1.38×10^{-23} J/K; T is the absolute temperature in Kelvin; R_{L} is the load resistance in the receiver circuit.

The total noise power affecting the photocurrent at the PD is thus given by:

$$\sigma_{\mathrm{N}}^2 = \sigma_{\mathrm{shot}}^2 + \sigma_{\mathrm{thermal}}^2 \,. \tag{2.21}$$

2.5 O-OFDM Based Transmission

Typical modulation techniques that can be used in LiFi systems are categorized into: single carrier modulation techniques and multiple carrier modulation schemes. Pulse position modulation (PPM), unipolar pulse amplitude modulation (PAM), pulse width modulation (PWM) and on-off keying (OOK) are common single carrier modulation techniques. OOK is a simple way of modulating data in LiFi systems, where two optical output power levels, namely low and high, are considered. In PAM modulation, messages are encoded in the amplitude of a series of pulses. In LiFi, only positive levels for PAM. Single carrier modulation techniques are prone to unwanted effects such as inter-symbol interference (ISI) and non-linear signal distortion at the LED [3]. To address the challenges facing single carrier modulation schemes, appropriate equalization methods are needed which require complex digital filters. In comparison to single carrier modulation schemes, multiple carrier modulation techniques are more bandwidth-efficient and can offer higher data rates. Orthogonal frequency division multiplexing (OFDM) is one of the most common and widely used multiple carrier modulation methods. OFDM is one effective solution to combat the effect of ISI in LiFi systems. In LiFi systems, the introduced ISI is as a result of passing the signal through a dispersive optical channel at high-data-rate transmission and also using off-the-shelf limited-bandwidth LEDs [46, 52]. Benefits of using OFDM include: 1) efficient use of spectrum, 2) robustness against frequency selectivity of channel by splitting the channel into narrowband flat fading subcarriers, 3) simple channel equalization by using single-tap equalizer (while adaptive equalization techniques are being used in single carrier modulation schemes), 4) computationally efficient by using fast Fourier transform (FFT) and inverse FFT (IFFT) techniques.

Because of the bipolar and complex signals generated by the OFDM modulator, the conventional OFDM modulator cannot fit the IM/DD requirements where the signals should be positive and real-valued in LiFi systems [58]. Optical-OFDM (O-OFDM) is a unipolar solution that can be

adopted in IM/DD-based transmission. There are several types of O-OFDM that can generate real and non-negative signals. Two of the most well-known and common types of O-OFDM are: DCO-OFDM and asymmetrically clipped optical OFDM (ACO-OFDM) [59]. In the following, these two types of O-OFDM are introduced.

2.5.1 DCO-OFDM

Figure 2.5 shows the block diagram of a DCO-OFDM system and its key elements. In a DCO-OFDM system, first the information bits are mapped to quadrature amplitude modulation (QAM) symbols. Then, each $(\frac{\mathcal{K}}{2}-1)$ consecutive modulated symbols are grouped and converted to parallel frames of OFDM to be used as the input of the IFFT module. An OFDM symbol can be expressed as:

$$\boldsymbol{X} = [X_0, X_1, ..., X_{\mathcal{K}-1}], \tag{2.22}$$

where X_k for $k = 0, \cdots, \mathcal{K}-1$ are modulated data symbols transmitted on kth OFDM subcarrier. To generate real value signals in time domain, Hermitian symmetry is applied to the OFDM symbol, which specifies the following conditions:

$$X_{\mathcal{K}-k} = X_k^* \quad \text{for} \quad 0 < k < \frac{\mathcal{K}}{2}, \tag{2.23a}$$

$$X_0 = X_{\mathcal{K}/2} = 0, \tag{2.23b}$$

where $(\cdot)^*$ denotes the complex conjugate operator. After the IFFT operation, time-domain samples are given as:

$$x[n] = \frac{1}{\sqrt{\mathcal{K}}} \sum_{k=0}^{\mathcal{K}-1} X_k \exp\left(\frac{\jmath 2\pi kn}{\mathcal{K}}\right), \qquad 0 \leq n \leq \mathcal{K}-1. \tag{2.24}$$

After passing through the IFFT module, a cyclic prefix (CP) will be added to the samples in order to combat the ISI due to the dispersive wireless channel. After adding the CP, the samples will be fed into a DAC module. A DC bias will be added to the analog waveform to ensure the modulated signal, $\tilde{x}(t)$, must be positive. The positive constraint is required for optical systems

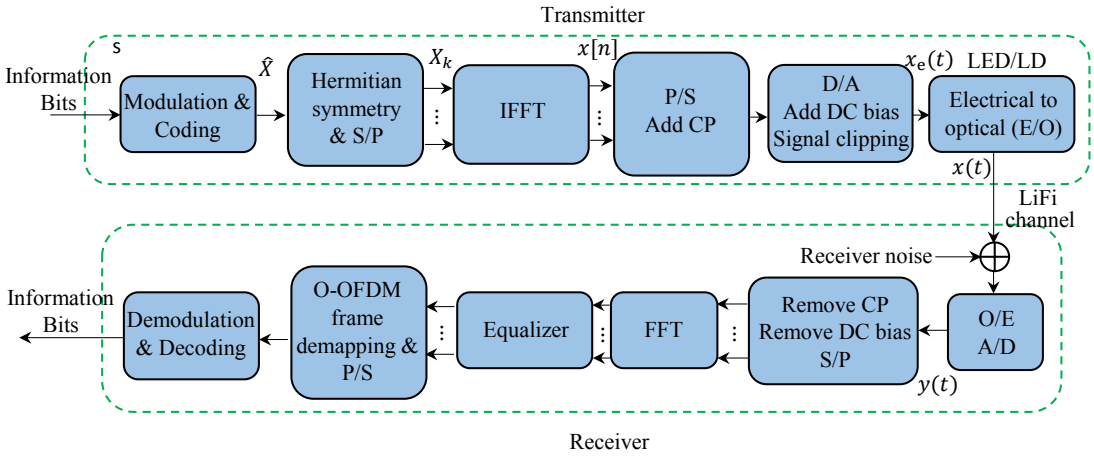

Figure 2.5: *Illustration of a DCO-OFDM system.*

that perform intensity modulation. Therefore,

$$x_{\mathrm{e}}(t) = x_{\mathrm{DC}} + \tilde{x}(t), \tag{2.25}$$

where

$$x_{\mathrm{DC}} = \eta\sqrt{\mathbb{E}[\tilde{x}^2(t)]}, \tag{2.26}$$

and η is the conversion factor. In general, the condition $\eta = 3$ guarantees that less than 1% of the signal is clipped. In this case, the clipping noise is negligible [58]. The current signal $x_{\mathrm{e}}(t)$ derives the LED to generate the optical signal $x(t)$.

2.5.2 ACO-OFDM

ACO-OFDM is another type of energy-efficient O-OFDM that can prevent adding the DC bias to the signal. In ACO-OFDM, only odd subcarriers are used to bear information which results in a loss of spectral efficiency. Hence, the OFDM symbol is $\boldsymbol{X} = [0, X_1, 0, ..., X_{\mathcal{K}-1}]$. Furthermore, the elements of $\boldsymbol{X}$ should fulfill the Hermitian symmetry defined in (2.23a). Compared to DCO-OFDM, half of the spectrum is sacrificed by ACO-OFDM to make the time-domain signal unipolar. Therefore, the signal generated after IFFT is an anti-symmetric real value given as:

$$x[n + \mathcal{K}/2] = -x[n], \qquad 0 < n < \mathcal{K}/2. \tag{2.27}$$

The anti-symmetry property of $x[n]$ guarantees that no information data is lost due to signal clipping at the zero level.

2.6 LiFi Attocell Networks

The coverage area of a typical point-to-point VLC link is in the order of a few square meters. However, to support mobility and seamless connectivity one possible solution is to utilize several LED transmitters or APs and connect them as a networked system. This is known as a LiFi attocell network. A LiFi cellular network consists of several LiFi attocells, which are smaller than RF femtocells. In a LiFi network, AP deployment can be: i) square deployment, ii) hexagonal deployment, iii) Poisson point process (PPP), or iv) hard-core point process (HCPP) [54]. In this research study, we only consider the square network as it is the typical deployment in offices and rooms. The geometric configuration of an indoor LiFi cellular network is shown in figure 2.6.

LiFi is a bidirectional and networked optical wireless system. In the downlink, visible light is utilized for the purpose of both illumination and communication, while in the uplink, data is transmitted through IR light in order to not affect the illumination constraint of the room. As shown in figure 2.6, a LiFi network comprises multiple LED transmitters (i.e., APs) arranged on the vertexes of a square lattice over the ceiling of an indoor network. A PD is installed next to the LED, which is tuned on the IR band for receiving uplink data. At the UE, an IR-LED is used to transmit uplink data and a PD tuned on the visible light band is employed for receiving downlink data. The LEDs are assumed to be point sources with Lambertian emission patterns. To avoid nonlinear distortion effects, the LEDs operate within the linear dynamic range of the current-to-power characteristic curve. In addition, the LEDs are assumed to be oriented vertically downwards, and the UEs are randomly orientated. Only one AP is selected to serve the UE based on the received signal intensity. An optical attocell is then defined as the confined area on the UE plane in which an AP serves the UE.

In order to evaluate the performance of LiFi networks, several QoS metrics are used. In fact, QoS is a qualification or measurement of a service performance met by the users in a network. In order to evaluate and quantify the network QoS several metrics such as BER, bit rate, trans-

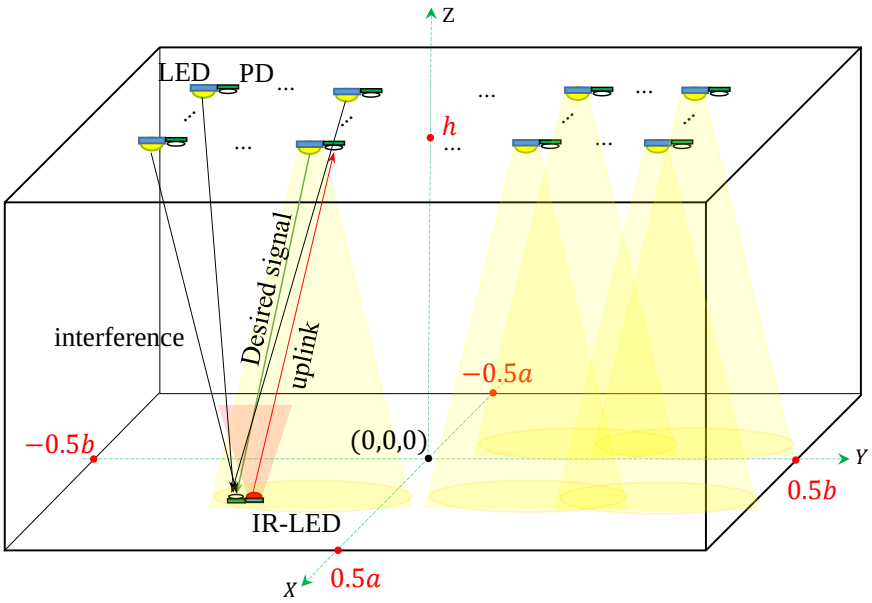

Figure 2.6: *The geometric configuration of an indoor LiFi cellular network.*

mission delay, SNR, and throughput can be used.

2.7 Multiuser Access Techniques

Like in RF networks, LiFi attocell networks should also be capable of supporting multiuser data communications by means of multiple access techniques. In this section, we study three common and widely used multiple access schemes in LiFi cellular networks, which are also considered through this research study. These techniques include TDMA, OFDMA and CSMA/CA.

2.7.1 TDMA

TDMA allows orthogonal access to the whole available modulation bandwidth for all users by assigning various time slots to each of them. Therefore, the users transmit data in rapid successions, one after the other while each uses its own allocated time slot. Figure 2.7-(a) shows the utilization of bandwidth with TDMA.

This multiple access technique can be directly used in a LiFi attocell network, particularly in

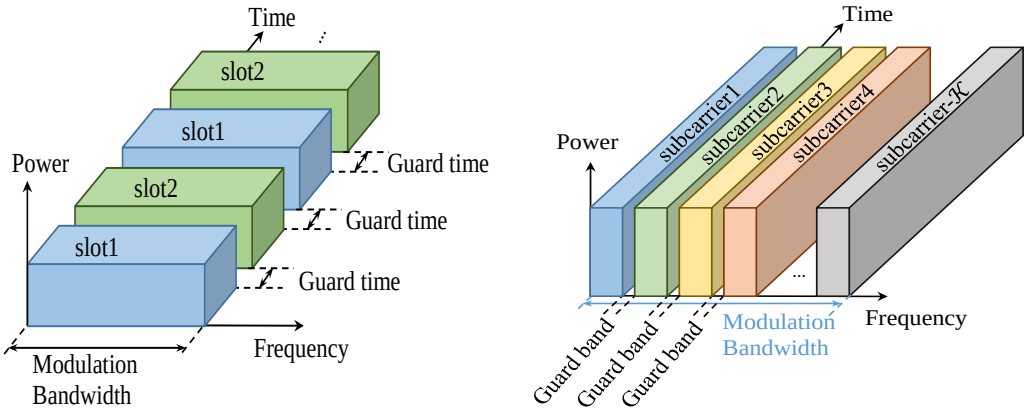

(a) TDMA **(b)** OFDMA

Figure 2.7: *A comparison between TDMA and OFDMA.*

downlink. However, TDMA requires synchronization and it is more difficult for uplink, especially for mobile UEs, due to variation of the timing advance which is required to synchronize the transmission [4]. Moreover, the performance of TDMA can be significantly degraded in LiFi cellular networks due to inter-channel-interference (ICI), that is reported in [3]. Therefore, interference mitigation techniques are required to alleviate the ICI which degrades the cell-edge users' performance.

2.7.2 OFDMA

OFDMA enables users to use frequency resources at different subcarriers and it has been widely considered and implemented in the downlink of LTE systems. Figure 2.7-(b) illustrates the concept of subcarrier utilization by the OFDMA technique. Multiple access can be achieved in OFDMA by allocating subsets of subcarriers to individual users. Note that based on the required QoS, the achievable data rate can be controlled individually for each user. This can be realized through assigning various numbers of subcarriers to different users. Therefore, OFDMA has been recently considered as a promising and practical option for downlink transmission.

2.7.3 CSMA/CA

CSMA/CA is another multiple access method in which nodes try to avoid collision by sensing the channel and then transmitting the data packet if the channel is found to be idle. CSMA/CA can optionally benefit from the request-to-send (RTS) and clear-to-send (CTS) exchange between the transmitter and receiver. This is known as the IEEE 802.11 RTS/CTS handshake mechanism. Implementation of this handshake protocol can help to address the problem of hidden nodes[2] in wireless networks. CSMA/CA is one efficient way of accessing the channel so that whenever a node has data to transmit, it occupies the channel.

2.7.4 CDMA

CDMA is another multiple access scheme, where several a transmitter can send information data of several users simultaneously over a single communication channel. This permits multiple users to share a common bandwidth at the same time. CDMA utilizes spread spectrum approach and a special coding technique (where each user is assigned a specific code) to mitigate the interference [60]. In general, codes are classified into two categories of synchronous (orthogonal codes) and asynchronous (pseudorandom codes). In CDMA, the generated code runs at a much higher rate than the data to be transmitted. Then, the data and the spreading code are combined by bitwise XOR (exclusive OR). The frequency of the transmitted signal varies based on the code, so it can be detected only by a receiver who has the same code. There are plenty of possible frequency-sequencing codes, which improves privacy and security.

2.8 Handover Protocol

In order to provide a seamless connectivity for a mobile UE in cellular networks, the ongoing connection may need to be transferred from one AP to another. This process is called handover. In general, a handover is needed when: 1) the UE is mobile and moves between the neighboring cells, i.e. it exits from the coverage area of one serving AP and enters to the coverage area of an adjacent AP; 2) the channel between the UE and AP is severely degraded as a result of a poten-

[2]Hidden node problem happens when a node is visible to the AP while not to other nodes.

tial rotation of the UE, link blockage or interference; and 3) the serving AP is fully loaded and it cannot provide any further service to the current user as it requests more service. Depending on whether the handover is between the APs of a same technology or between different technologies, two types of handover called horizontal and vertical handover exist. Horizontal handovers occur between APs of a same access technology means in different cells of a same network, for example, between attocells of a LiFi network. In a standalone network, horizontal handovers are typically needed when the serving AP becomes unavailable due to the reasons mentioned above. Horizontal handovers generally use received signal strength (RSS) for handover decisions. On the other side, vertical handover refers to the change of connectivity between different technologies, for instance, from a LiFi network to a WiFi network. Vertical handovers are usually performed to support user mobility.

From the decision point of view, handovers are classified into hard and soft handovers. These two types of handover are explained in the following.

2.8.1 Hard Handover

A hard handover occurs when the previous link is disconnected before a new connection is established. It is also known as “break before make”. Hence, in the hard handover schemes, the user is always served by one AP at a time. Typically, implementation of hard handover schemes are simple and they require low hardware complexity and usage. However, with a hard handover algorithm, a high rate of call drops is expected and the service will be interrupted. Ping-pong effect is one of the other challenges that hard handover schemes face, especially for cell-edge users. This issue is even more severe in LiFi cellular networks, due to the random orientation of a device.

2.8.2 Soft Handover

When considering soft handover, it means that the links are added and broken in a way that the UE always keeps at least one link. This is known as “make before break”. Soft handover methods are used to alleviate the rate fluctuation of hard handover schemes. During the soft handover process, the user is served by two or more APs simultaneously when it is in the intersection

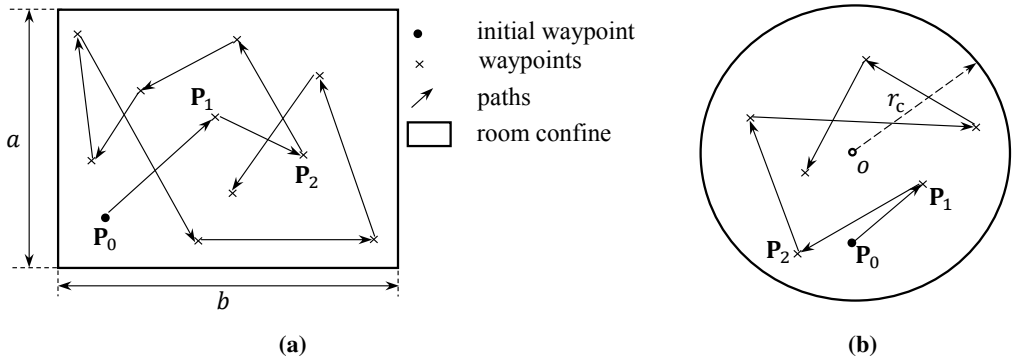

Figure 2.8: *RWP model in (a): a room of size $a \times b$ and (b) an attocell of radius r_c.*

coverage area of the APs, therefore, its data rate does not drop off suddenly. Hence, the reliability of the link connection becomes higher when a soft handover algorithm is performed. It is noted that even though by means of soft handover, the rate of call drops is reduced and it also alleviates the ping-pong effect, they use several channels in the network to support just a single call. This decreases the number of remaining available channels and therefore, reduces the capacity of the network.

2.9 User Behavior Models

In a LiFi cellular network, the user throughput depends on several factors including user mobility, random device orientation and link blockage. There are plenty of mobility models proposed in the literature [61]. Among them, the RWP mobility model is one of the most simple and well-known models that is considered for the simulation of the user mobility either for indoor or outdoor environments. Device orientation and link blockage are the other two significant factors that can affect the user throughput in LiFi networks. In the following, these factors are discussed.

2.9.1 Random Waypoint Mobility Model

The RWP mobility model was initially introduced in [62] to model human movement in a random manner. After that, many studies have focused on the RWP to obtain its statistics, see for

instance [63, 64] and references therein. Figure 2.8-(a) shows the basic concept of the RWP mobility model in a room of size $a \times b$. According to the RWP model, at each waypoint, the UE needs to satisfy a number of properties to move to the next waypoint, these include: i) the random destinations or waypoints are chosen uniformly with probability $1/ab$; ii) the movement path is a straight line; and iii) the speed is constant during the movement between two consecutive waypoints. The RWP mobility model can be mathematically expressed as an infinite sequences of triples: $\{(\mathbf{P}_{n-1}, \mathbf{P}_n, V_n)\}_{n\in\mathbb{N}}$ where n denotes the nth movement period during which the UE moves between the current waypoint $\mathbf{P}_{n-1} = (x_{n-1}, y_{n-1})$ and the next waypoint $\mathbf{P}_n = (x_n, y_n)$ with the constant velocity V_n. The transition length is defined as the Euclidean distance between two consecutive waypoints as the UE progresses, and is given by $L_n = \|\mathbf{P}_n - \mathbf{P}_{n-1}\|$. Here, the transition lengths $\{L_1, L_2, \ldots\}$ are non-negative independent identically distributed (i.i.d) random variables with the PDF given as [63]:

$$f_L(l) = \frac{4l}{a^2 b^2} f_0(l), \tag{2.28}$$

with

$$f_0(l) = \begin{cases} \frac{\pi}{2}ab - al - bl + \frac{1}{2}l^2, & \text{for } 0 \le l \le b \\ ab\sin^{-1}\left(\frac{b}{l}\right) + a\sqrt{l^2 - b^2} - \frac{1}{2}b^2 - al, & \text{for } b < l < a \\ ab\sin^{-1}\left(\frac{b}{l}\right) + a\sqrt{l^2 - b^2} - \frac{1}{2}b^2 - ab\cos^{-1}\left(\frac{a}{l}\right) & \\ +b\sqrt{l^2 - a^2} - \frac{1}{2}a^2 - \frac{1}{2}l^2, & \text{for } a \le l \le \sqrt{a^2 + b^2} \\ 0, & \text{otherwise.} \end{cases} \tag{2.29}$$

For a square room of length a, the mean of transition lengths is given as $\mathbb{E}[L] = 0.5214a$ where $\mathbb{E}[\cdot]$ denotes the expectation operator. Figure 2.8-(b) illustrates the RWP mobility in an attocell of radius r_{c}. According to the RWP model, i) the random destinations or waypoints are chosen uniformly with the probability of $1/(\pi r_{\mathrm{c}}^2)$; ii) the movement path is a straight line; and iii) the speed is constant during the movement. The PDF of transition length within this attocell is given as [63]:

$$f_L(l) = \frac{8}{\pi r_{\mathrm{c}}} \frac{l}{2r_{\mathrm{c}}} \left(\cos^{-1}\left(\frac{l}{2r_{\mathrm{c}}}\right) - \frac{l}{2r_{\mathrm{c}}} \sqrt{1 - \left(\frac{l}{2r_{\mathrm{c}}}\right)^2} \right), \tag{2.30}$$

for $0 \leq l \leq 2r_c$, and 0, otherwise. The mean of transition lengths for this attocell is $\mathbb{E}[L] = 0.9054r_c$.

2.9.2 Device Orientation

Device orientation is another factor that can affect the seamless connectivity of a user. According to the Euler's rotation theorem [65], any rotation in $\mathbb{R}^3$ space can be uniquely achieved by composing three elemental rotations, i.e., the rotations about the axes of a coordinate system. Depending on whether the device (local) or Earth (global) coordinate system is chosen, there are two types of rotations. Intrinsic rotation corresponds to a rotation about the device coordinate system and extrinsic rotation, which conforms to a rotation about the Earth coordinate system. Throughout this thesis, the device and Earth coordinate systems are shown by xyz and XYZ, respectively. The Earth and device coordinates are illustrated in figure 2.9-(a). In the Earth coordinate system, the X and Y axes are in the ground plane and positive towards the East and North pole, respectively, Z is perpendicular to the ground plane and positive upwards. The axes of the local coordinate system are x and y in the screen plane and positive towards the right of the screen and towards the top of the screen, respectively; the z-axis is perpendicular to the screen and positive extending outwards from the screen (the axes are shown in figure 2.9-(a)).

Thanks to the embedded-gyroscope in current smartphones, they are able to report the elemental rotation angles yaw, pitch and roll denoted as α, β and γ, respectively [66]. Here, α represents the rotation about the z-axis, which takes a value in the range of $[0, 360)$; β denotes the rotation angle about the x-axis, that is, tipping the device toward or away from the user, which takes value between -180° and 180°; and γ is the rotation angle about the y-axis, that is, tilting the device right or left, which is chosen from the range $[-90, 90)$. The elemental Euler angles are depicted in figure 2.9-(b) to 2.9-(d).

Depending on the axes order rotations, there are six conventions for Euler angles. The world wide web consortium (W3C) determines the following principles for UE orientation [67]: i) rotations should follow the right-hand rule, this states that the positive rotation about each axis is clockwise when viewing along the positive direction of the axis; ii) the intrinsic rotation of order $z-x'-y''$ is chosen as the standard for the UE orientation, this means the UE is first rotated α degrees about the z-axis. Denoting the new coordinate system as $x'y'z$, then it is rotated β

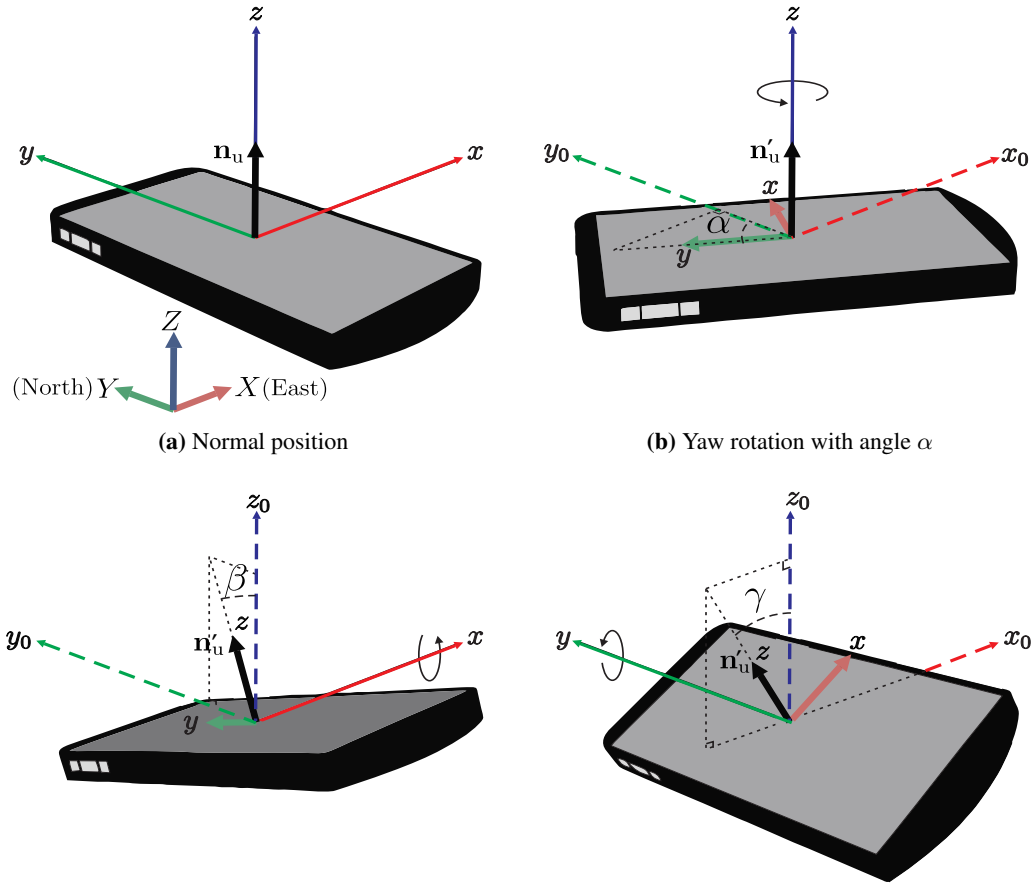

(a) Normal position

(b) Yaw rotation with angle α

(c) Pitch rotation with angle β

(d) Roll rotation with angle γ

Figure 2.9: *Orientations of a mobile device.*

degrees about the x'-axis to get the new coordinate as $x'y''z'$. Finally, the UE is rotated γ degrees about the y''-axis to get the ultimate local coordinate as $x''y''z''$.

Now, we derive the concatenated rotation matrix with respect to the Earth coordinate system. The normal vector $\mathbf{n}_u = [n_1, n_2, n_3]^T$ after rotation can be obtained as:

$$\mathbf{n}'_u = \mathbf{R}\mathbf{n}_u, \tag{2.31}$$

where $\mathbf{n}'_u = [n'_1, n'_2, n'_3]^T$ is the rotated normal vector via the rotation matrix $\mathbf{R}$. The rotation matrix can be decomposed as $\mathbf{R} = \mathbf{R}_\alpha \mathbf{R}_\beta \mathbf{R}_\gamma$, where $\mathbf{R}_\alpha$, $\mathbf{R}_\beta$ and $\mathbf{R}_\gamma$ are the rotation matrices about the z, x' and y'' axes, respectively. Assume that the device and Earth coordinate systems

are initially aligned so that $\mathbf{n}_{\mathrm{u}} = [0, 0, 1]^{\mathrm{T}}$, then, the rotated normal vector, $\mathbf{n}'_{\mathrm{u}}$, via the rotation matrices $\mathbf{R}_\alpha$, $\mathbf{R}_\beta$ and $\mathbf{R}_\gamma$ is given as:

$$\begin{aligned}\mathbf{n}'_{\mathrm{u}} = \mathbf{R}_\alpha \mathbf{R}_\beta \mathbf{R}_\gamma \begin{bmatrix}0\\0\\1\end{bmatrix} &= \begin{bmatrix}\cos\alpha & -\sin\alpha & 0\\ \sin\alpha & \cos\alpha & 0\\ 0 & 0 & 1\end{bmatrix}\begin{bmatrix}1 & 0 & 0\\ 0 & \cos\beta & -\sin\beta\\ 0 & \sin\beta & \cos\beta\end{bmatrix}\begin{bmatrix}\cos\gamma & 0 & \sin\gamma\\ 0 & 1 & 0\\ -\sin\gamma & 0 & \cos\gamma\end{bmatrix}\begin{bmatrix}0\\0\\1\end{bmatrix}\\ &= \begin{bmatrix}\cos\gamma\sin\alpha\sin\beta + \cos\alpha\sin\gamma\\ \sin\alpha\sin\gamma - \cos\alpha\cos\gamma\sin\beta\\ \cos\beta\cos\gamma\end{bmatrix}.\end{aligned} \tag{2.32}$$

The rotated normal vector can be represented in the spherical coordinate system using the azimuth, ω, and polar, θ, angles. That is, $\mathbf{n}'_{\mathrm{u}} = [\sin\theta\cos\omega, \sin\theta\sin\omega, \cos\theta]^{\mathrm{T}}$. As shown in figure 2.10, the polar angle, θ, is the angle between the positive direction of Z-axis and the normal vector $\mathbf{n}'_{\mathrm{u}}$. Moreover, ω is the angle between the projection of $\mathbf{n}'_{\mathrm{u}}$ in the XY-plane and the positive direction of the X-axis. Accordingly,

$$\begin{aligned}&\theta = \cos^{-1}\left(\cos\beta\cos\gamma\right),\\ &\omega = \tan^{-1}\left(\frac{n'_2}{n'_1}\right) = \tan^{-1}\left(\frac{\sin\alpha\sin\gamma - \cos\alpha\cos\gamma\sin\beta}{\cos\gamma\sin\alpha\sin\beta + \cos\alpha\sin\gamma}\right).\end{aligned} \tag{2.33}$$

It is shown in [10] and [68] that the polar angle follows a Laplace distribution, $\theta \sim \mathcal{L}(\mu_\theta, b_\theta)$ where the mean value, μ_θ, and scale parameter, b_θ, depend on whether the user is static or mobile. Furthermore, it is shown that the azimuth angle follows a uniform distribution, $\omega \sim \mathcal{U}[0, 2\pi]$. Let's define the movement direction angle as $\Omega = \omega + \pi$, where Ω provides a better physical concept (compared to ω), as it shows the angle between the movement direction and the X-axis. The geometry of this angle is shown in figure 2.10. The relation between Ω and α depends on whether the UE is being used in the portrait or landscape mode. When the user is working with the cellphone in portrait mode, the angle between the y-axis and North is defined as α, and Ω is specified based on the angle between the y-axis and East. Hence, the relationship between Ω and α can be expressed as:

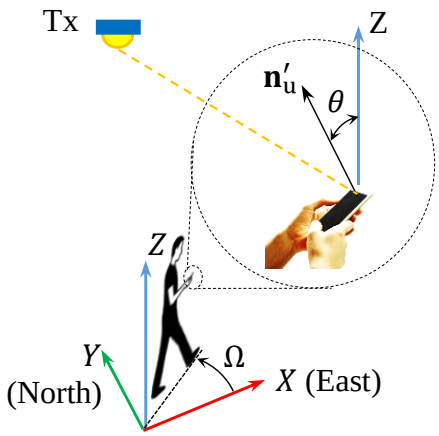

Figure 2.10: *Geometry of θ and Ω angles.*

$$\Omega = \begin{cases} \alpha + \frac{\pi}{2} & \alpha \in (0, \frac{3\pi}{2}] \\ \alpha - \frac{3\pi}{2} & \alpha \in (\frac{3\pi}{2}, 2\pi] \end{cases} . \tag{2.34}$$

Since the difference between portrait mode and landscape mode is just $\pi/2$ which follows the right-hand rule, for landscape mode, we have:

$$\Omega = \begin{cases} \alpha + \pi & \alpha \in (0, \pi] \\ \alpha - \pi & \alpha \in (\pi, 2\pi] \end{cases} . \tag{2.35}$$

2.9.3 Blockage

Due to the nature of LiFi, the link between a pair of the transmitter and receiver can be blocked by an opaque object such as a human body. In this research thesis, we only consider the blockage due to human bodies or other similar objects which can be modeled as rectangular prisms. It is shown in [69, 70] that MIMO can help the optical wireless networks to be robust against the blockage because the transmit or receive diversity is exploited. Here, the model for the link blockage is introduced which is used throughout this thesis.

We model a human body as a rectangular prism of length, L_{b}, width, W_{b}, and height, H_{b}. Two types of blockers are assumed, non-user blockers and user-blockers. The former is due to other people or objects in the room while the latter is due to the user who is using the UE, also known as self-blockage. Thus, one user-blocker is considered in the direction that the user is facing,

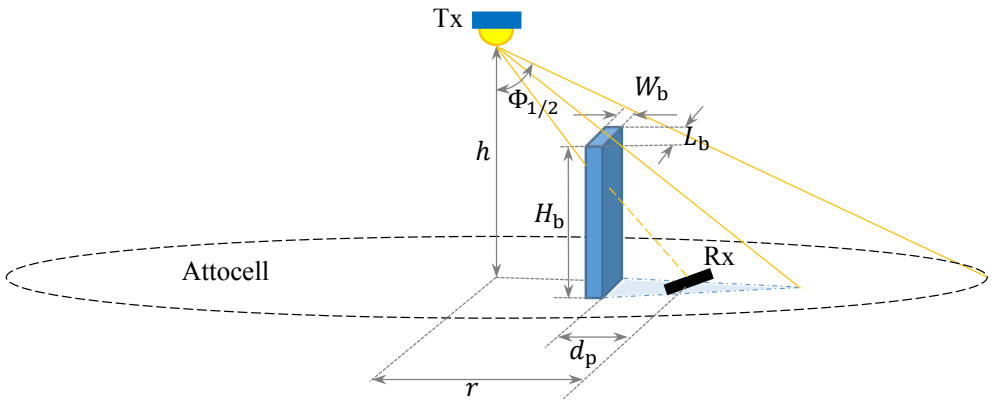

Figure 2.11: *Geometry of the link blockage.*

and other non-user blockers' directions are chosen from a uniform distribution of $\mathcal{U}[0°, 360°]$. Figure 2.11 shows the blockage model and the relevant parameters that are considered in this study. The density of a non-user blocker is denoted by κ_b, which is the number of non-user blockers per room area. It is assumed that non-user blockers are uniformly distributed in the room. The direction and location of the self-blocker are obtained based on the direction and location of the UE. It is assumed that the users keep the UE at a distance of d_p away from themselves.

2.10 Interference Management Techniques

To reduce the interference between the neighboring cells, different inter-cell interference cancellation techniques have been proposed such as the frequency reuse (FR) plan, fractional frequency reuse (FFR) that includes strict FFR and soft-frequency reuse methods. FFR is proposed as an inter-cell interference coordination (ICIC) [3] strategy for OFDMA-based wireless networks [72]. The principle of FR is to guarantee that the mutual interference from adjacent cells remains below a harmful level, with neighboring cells using different frequencies. In fact, a set of different frequencies $f_1, ..., f_{N_c}$ are used for each cluster of N_c adjacent cells. The cluster pattern and the corresponding frequencies are re-used in a regular pattern over the entire service area.

[3] ICIC is a scheme to enhance the network performance by minimizing the experienced interference while maximizing the spatial reuse [71].

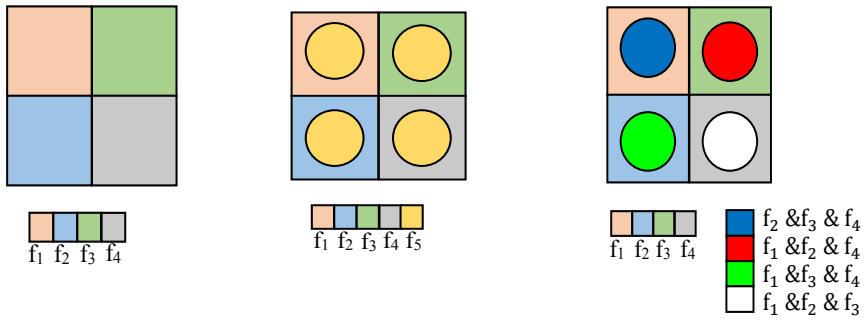

(a) FR **(b)** Strict FFR with $\Delta = 4$ **(c)** Soft FFR with $\Delta = 3$

Figure 2.12: *FR, Strict and Soft FFR schemes in a square network.*

The main principle of FFR is to divide the cell's bandwidth so that i) users close to cell edges do not receive interference from neighboring cells, ii) interior users receive less interference, whereas, iii) they use more total spectrum compared to the traditional FR plans. Users in each cell-interior are assigned a common subband of frequency while for the cell-edge users, the allocated bandwidth is partitioned across cells according to a reuse factor of Δ. Note that FFR plans need a total number of $\Delta + 1$ subbands. Figure 2.12 illustrates a comparison between FR, strict FFR and soft FFR schemes in a square network with four cells. In fact, strict FFR is a modified version of FR plan in which interior users are allocated a separate spectrum, while in the soft FFR interior users are allowed to share the spectrum with cell-edge users of adjacent cells. Further information about strict and soft FFR techniques can be found in [73]. Angular diversity receiver (ADR) is another technique that can be used to mitigate interference [74–76]. An ADR consists of several PDs (with narrow FOV) which are placed on a hemispherical shape at the receiver. In this thesis, FR is used to reduce the inter-cell interference.

2.11 Summary

In this chapter, LiFi including the channel responses of both front-end elements and indoor LiFi have been studied. The LOS and NLOS DC gains have been explained and an analysis of noise encompassing shot noise and thermal noise have been presented. Optical OFDM, which is an effective way of combating the ISI in LiFi networks, is described. The basic concept

of LiFi cellular networks and attocells are provided. Then, TDMA and OFDMA as the most common multiuser access techniques in the downlink and CSMA/CA as a promising option for the uplink are described. The concept of handover is explained, and different types of handover are discussed. Finally, factors which can affect the user throughput such as user mobility, device orientation and link blockage are explained.

Chapter 3

Bidirectional User Throughput Maximization Based on Feedback Reduction in LiFi Networks

3.1 Introduction

It is known that utilizing channel adaptive signalling can bring on enhancement in almost any performance metric. Feedback can realize many kinds of channel adaptive methods that were considered impractical due to the problem of obtaining instantaneous CSI at the AP. Studies have proven that permitting the receiver to transmit a small amount of information or feedback about the channel condition to the AP can provide a near optimal performance [6–9]. Feedback conveys the channel condition, e.g., received power, signal-to-noise-plus-interference ratio (SINR), interference level, channel state and so on. The AP can use the information for scheduling and resource allocation. The practical systems using this strategy, also known as limited-feedback (LF) systems, provide a similar performance to the impractical systems with perfect CSI at the AP.

It is often inefficient and impractical to continuously update the AP with the UE link conditions. However, to support mobility and seamless connectivity, it is also essential to consider the time-varying nature of channels for resource allocation problems to further enhance spectral efficiency. With limited capacity, the assignment of many resources to obtain CSI would evacuate the resources required to transmit actual data, resulting in a reduced overall UE throughput [77]. Therefore, it is common for practical wireless systems to update the CSI less frequently, e.g., only at the beginning of each frame. Many works have been carried out to reduce the amount of feedback in RF networks (see [6] and references therein), however, very few studies are done to lessen the amount of feedback in LiFi networks [4, 30, 31].

An overview of limited feedback in wireless communications has been introduced in [6]. The key role of limited feedback in single-user and multiuser scenarios for narrowband and wideband communications with both single and multiple antennas has been discussed. Two SINR based limited feedback scheduling algorithms for multiuser multiple-input, multiple-output orthogonal frequency-division multiplexing (MIMO-OFDM) in heterogeneous networks are studied in [78] where UEs feed back channel quality information in the form of SINR. UEs at a particular distance from the AP are grouped together and have the same SINR (It is assumed that the UEs have the same multipath profile and shadowing effect). In [79], three limited feedback resource allocation algorithms are evaluated for heterogeneous wireless networks. These resource allocation algorithms try to maximize the weighted sum of instantaneous data rates of all UEs over all cells by jointly optimizing power and subcarrier assignment under power constraints. In order to reduce the feedback signalling, the Lloyd algorithm[1] is utilized to develop the resource allocation scheme into two phases. It is shown that the Lloyd algorithm can provide a close performance to the perfect CSI case. In [81], the authors analyzed the performance of feedback based on the resource-wise SNR quantization and the ordered best-K feedback method, where the K best resources are fed back to the AP. Analytical outage capacity calculations and exact bit error probability expressions are presented for both feedback methods. Results confirm the significant allocation gain achievement with very limited feedback in wideband OFDMA systems. This allocation gain is achieved by combining multiple resource selection and feedback strategies.

In multiuser systems, UEs compete for resources to ensure higher data rates and/or better reliability and QoS. For efficient utilization of resources, opportunistic downlink scheduling has attracted much attention [82]. Opportunistic user allocation based on limited feedback information has been shown to offer remarkable enhancement for wireless multiple access communications. Proportional fair (PF) scheduling, which is one of the opportunistic scheduling schemes, chooses a UE who is able to achieve the highest instantaneous data rate normalized by the average received data rate at each scheduling time. An opportunistic limited feedback technique for PF scheduling in wireless systems has been proposed in [83]. According to this technique, the

[1]The Lloyd algorithm is one of the most popular iterative methods to find evenly spaced sets of points in subsets of Euclidean spaces. [80].

UEs only transmit the feedback information when the probability of being selected to transmit on a subcarrier is high. The same throughput can be achieved by this method similar to a system where each UE feeds back its CSI to the AP, however, with significant feedback reduction per UE.

In order to realize scheduling algorithms for OFDMA in a cellular network, the AP requires knowledge of UEs' SINR conditions on each subcarrier. One solution is to transmit the quantized channel quality indicator (CQI) of subcarriers which is the focus of [84] and [85]. Techniques to tackle the issue of adaptation with unquantized (but outdated or imperfect) CSI at the AP are studied in [86]. More general studies about quantized feedback per subcarrier have been discussed in [87–90]. An optimal strategy to transmit feedback based on outdated channel gain feedbacks and channel statistics for a single-user scenario is proposed in [91]. Four low-complex scheduling algorithms for multiuser case to maximize the sum of the outage capacity of individual UEs have been proposed in [92]. Another solution is the subcarrier clustering method which is developed in [93–95]. Clearly, the required CSI increases proportionally with the number of UEs. This creates challenging problems in practical system implementations when the AP does not have a priori channel information. Another simple and more realizable solution proposed in [96–98] is to inform the AP only if their SINR exceeds a predetermined threshold. This is a very simple approach which is basically a one bit per subcarrier feedback. The one-bit feedback method is very bandwidth efficient and using more feedback can provide slight downlink performance improvement but at the cost of uplink throughput degradation as discussed in [96]. The benefits of employing only one bit feedback per subcarrier and the minor data rate enhancements of downlink using more feedback bits are analyzed in [99]. A one-bit per subcarrier feedback scheme for downlink OFDMA systems has been proposed in [100]. The one-bit feedback specifies whether the channel gain exceeds a predefined threshold or not. Then, UEs are assigned priority weights, and the optimal thresholds are chosen to maximize the weighted sum capacity. One problem linked to the one-bit feedback technique is that there is a low probability that none of the UEs will report their SINR to the AP so the scheduler will be left with no information about the channel condition. This issue can be solved at the expense of some extra feedback and overhead by the multiple-stage version of the threshold-based method proposed in [101].

These limited feedback approaches are all applicable in LiFi networks. However, the channel

in LiFi networks is mostly characterized by the limitations of the receive/transmit devices (i.e., front-end elements) rather than the multipath nature of the channel. The frequency selective characteristics of the front-end elements are relatively deterministic although not frequency flat, and independent of the users position or orientation. However, the average received power is much more dynamic and is significantly dependent on the position and the orientation of the user devices. Therefore, by only updating the average power, a reasonable estimate of the SINR of all the subcarriers can be obtained with a considerably reduced amount of feedback at the AP [30]. In other words, due to the relatively deterministic behavior of LiFi channels, the feedback can be reduced further without any significant downlink throughput degradation. This motivates us to propose two novel limited feedback schemes for LiFi networks. These limited feedback techniques are i) limited-content feedback (LCF) scheme which is based on reducing the content of feedback information and ii) limited-frequency feedback (LFF) scheme based on the update interval. It will be shown that LCF illustrates a close downlink performance to the full-feedback (FF) mechanism and with an even lower overhead compared to the one-bit feedback technique. For the LFF scheme, which is based on the sum-throughput of uplink and downlink maximization, an optimum update interval is derived using the RWP mobility model. These feedback mechanisms will be described after explaining the downlink and uplink access techniques and providing analytical derivations of the downlink and uplink throughput.

The rest of the chapter is organized as follows. In sections 3.2 and 3.3, downlink and uplink throughput of LiFi systems are explained with consideration of OFDMA and CSMA/CA, respectively. Different feedback mechanisms and the proposed limited-feedback schemes are covered in section 3.4. Results and performance comparisons between limited-feedback mechanisms are described in section 3.5. Finally, a summary of this chapter is presented in section 3.6.

3.2 Downlink Throughput Calculation

The channel access protocol in the downlink is assumed to be OFDMA based on DCO-OFDM so as to support downlink multiple access simultaneously. The modulated data symbols of different UEs, X_k, are arranged on $\mathcal{K}$ subcarriers of the OFDMA frame, $\boldsymbol{X}$. Then, the IFFT is applied to the OFDMA frame to obtain the time domain signal $\tilde{x}$. Note that in OFDMA, the number of

modulated subcarriers bearing information is $\mathcal{K}/2-1$.

Let $\mathbf{h}_j=[H_{i,j}]$, for $i=1,2,...,N_{\mathrm{AP}}$, be the downlink channel gain vector from all APs to the jth UE and N_{AP} denotes the total number of APs in the network. The jth UE is connected to the $\imath$th AP based on the maximum channel gain criterion so that $\imath=\arg\max_i(\mathbf{h}_j)$. Afterwards, the embedded scheduling algorithm in the $\imath$th AP allocates a number of subcarriers to the jth UE based on its requested data rate and its link quality. In this study, a fair scheduling method for OFDMA-based wireless systems is considered [102, 103]. The scheduler assigns the kth resource to the j_0th UE according to the following metric:

$$j_0=\arg\max_j\left(\frac{R_{\mathrm{req},j}}{\overline{R}_j}\right), \tag{3.1}$$

where $\overline{R}_j$ is the average data rate of the jth UE before allocating the kth resource, and $R_{\mathrm{req},j}$ is the requested data rate of the jth UE.

Frequency reuse plan is considered to reduce the co-channel interference and also guarantee the cell edge users data rate. It is assumed that the considered LiFi system transmits data based on DCO-OFDM, for which the upper bound on the achievable data rate can be expressed in a Shannon capacity expression form as a function of electrical SINR as shown in [104]. Assuming the effect of clipping noise is negligible, the downlink rate of the jth UE after scheduling can be obtained as:

$$R_{\mathrm{d},j}=\frac{B_{\mathrm{d},n}}{\mathcal{K}}\sum_{k=1}^{\mathcal{K}/2-1}\log_2\left(1+\pi_{j,k}\mathcal{S}_{\mathrm{d},j,k}\right), \tag{3.2}$$

where $\pi_{j,k}=1$ if the kth subcarrier is allocated to the jth UE otherwise $\pi_{j,k}=0$; $\mathcal{S}_{\mathrm{d},j,k}$ is the SINR of the jth UE on the kth subcarrier serving by the $\imath$th AP. Also, $B_{\mathrm{d},n}$ is the downlink bandwidth of the nth FR plan. In communication systems, SINR is defined as the ratio of the desired electrical signal power to the total noise and interference power that corrupts the signal. It is noted that since it is about the signal power only AC is considered and DC bias will finally be removed at the receiver. SINR is an important metric to evaluate the link quality and the transmission data rate. Denoting $P_{\mathrm{elec},\imath,j,k}$ as the received electrical power of the jth UE on the kth subcarrier, then, we have:

$$\mathcal{S}_{\mathrm{d},j,k}=\frac{P_{\mathrm{elec},\imath,j,k}}{\sigma_{\mathrm{N}}^2+P_{\mathrm{int},j}} \tag{3.3}$$

where $\sigma_{\mathrm{N}}^2 = N_0 B_{\mathrm{d},n}/\mathcal{K}$, is the noise power on each subcarrier, and N_0 is the noise power spectral density; $P_{\mathrm{int},j}$ is the interference from other APs at the jth UE. It is assumed that the APs emit the same average optical power and the total transmitted electrical power is equally allocated among $\mathcal{K}-2$ subcarriers so that the received electrical power on the kth subcarrier of the jth UE is equal to:

$$P_{\mathrm{elec},\imath,j,k} = \frac{R^2 P_{\mathrm{d,opt}}^2 H_{\imath,j,k}^2}{\eta^2(\mathcal{K}-2)} \tag{3.4}$$

where $P_{\mathrm{d,opt}}$ is the transmitted optical power. Note that the PDs used in LiFi systems are square law detectors. Therefore, the electrical power is proportional to the square of the optical power input. In other words, since the electrical current is proportional to the optical power and the electrical power, being proportional to the square of current, is proportional to the square of the optical power. In (3.4), R and η are the PD responsivity and conversion factor, respectively. It is noted that η is unitless. Moreover, $H_{\imath,j,k}$ is the frequency response of the optical wireless channel on the kth subcarrier. This includes the effects of both front-end elements and the indoor LiFi channel. Furthermore, the indoor LiFi channel encompasses both LOS and NLOS links. Accordingly, the received SINR of the jth UE on the kth subcarrier can be expressed as:

$$\mathcal{S}_{\mathrm{d},j,k} = \frac{R^2 P_{\mathrm{d,opt}}^2 H_{\imath,j,k}^2}{(\mathcal{K}-2)\eta^2\sigma_{\mathrm{N}}^2 + \sum\limits_{i\in\Xi_{\mathrm{AP},\imath}} R^2 P_{\mathrm{d,opt}}^2 H_{i,j,k}^2}. \tag{3.5}$$

where $\Xi_{\mathrm{AP},\imath}$ is the set of other APs in the room, which use the same frequencies as the $\imath$th AP.

3.3 Uplink Throughput Calculation

3.3.1 Uplink Access Protocol

It is proven that fixed multiple access protocols such as TDMA, FDMA and CDMA become inefficient when the traffic is bursty [105]. In this case, random access protocols perform better for many users, when users only occasionally send a message. CSMA/CA is a random access mechanism that allows UEs to access the channel whenever they have packets for transmission. Here, we employ CSMA/CA as the uplink access protocol. However, a similar study, with the assumption of TDMA in the uplink has been carried out in [31]. CSMA/CA is a multiple access

protocol with a binary slotted exponential backoff strategy being used in wireless local area networks (WLANs) [2]. This is known as the collision avoidance mechanism of the protocol. In CSMA/CA, a UE will access the channel when it has data to transmit. Thus, this access protocol uses the available resources efficiently. Once the UE is allowed to access the channel, it can use the whole bandwidth. However, this access protocol cannot directly be used in LiFi networks, because it results in a severe "hidden node" problem. In contrast to RF networks, the UEs cannot directly hear each other to realize whether the channel is occupied or not in LiFi systems. The reason for this is that the downlink and uplink medium in LiFi are different, i.e., visible light and infrared are used in downlink and uplink, respectively. Therefore, adopting the conventional CSMA/CA for LiFi networks can lead to a drastic degradation in users throughput. To address this issue, we proposed a modified CSMA/CA access protocol for LiFi networks that benefits from transmission of a channel busy (CB) tone [4]. Therefore, we applied two simple modifications to the conventional CSMA/CA to minimize the number of collisions in LiFi networks. Firstly, the RTS/CTS packet transmission scheme, which is optional in RF WLANs should be mandatory in LiFi networks. This is the only way that UEs can notice that the channel is busy in LiFi networks. Because, visible light and infrared are employed in the downlink and uplink of LiFi networks, respectively, which have different wavelengths. Thus, the PD at the UE is tuned for visible light and cannot sense the channel when another UE transmits via infrared. Secondly, the AP transmits a CB tone to inform the other UEs that the channel is busy. This CB tone should be sent simultaneously with the RTS packet transmission. In the following, the conventional and modified CSMA/CA are described in detail.

3.3.2 Conventional CSMA/CA

The main medium access control (MAC) mechanism of IEEE 802.11 is called distributed coordination function (DCF) which is a random access scheme based on the CSMA/CA protocol with a binary slotted exponential backoff [2]. The default scheme of DCF for packet transmission is a two-way handshaking technique known as the basic access mechanism. The second scheme is an optional four-way handshaking technique known as the RTS/CTS mechanism. DCF adopts a slotted binary exponential backoff scheme to reduce collisions due to simultaneous transmission of UEs. This is known as the collision avoidance feature of the protocol.

Hence, prior to transmission, UEs listen to the channel for a time interval called distributed inter-frame space (DIFS). Then, if the channel is found to be idle, the UEs generate a random backoff, $\mathcal{B}_j$, for $j = 1, 2, \ldots, N_{\mathrm{UE}}$, where N_{UE} is the number of competing UEs serving by the considered AP. The value of $\mathcal{B}_j$ is uniformly chosen in the range $[0, w-1]$, where w is the current contention window size. Before the first transmission try, w is set to the minimum contention window, $CW_{\min}$, and after each unsuccessful transmission w is doubled up to the maximum contention window, $CW_{\max}$. Thus, the size of the contention window at lth backoff stage is equal to $w = 2^l CW_{\min}$, for $l = 1, 2, \ldots, M_{\mathrm{r}}$, where M_{r} is the retry limit and it is equal to $M_{\mathrm{r}} = \log_2(CW_{\max}/CW_{\min})$. Let $\boldsymbol{\mathcal{B}} = [\mathcal{B}_j]_{1\times N_{\mathrm{UE}}}$, be the backoff vector of the UEs. After sensing the channel for time interval DIFS, UEs should wait for $\mathcal{B}_j \times t_{\mathrm{slot}}$ seconds, where t_{slot} is the duration of each time slot. Obviously, the UE with the lowest backoff is prior to transmit, i.e., the u_0th UE, where $u_0 = \arg\min_j(\boldsymbol{\mathcal{B}})$. Therefore, the u_0th UE sends the RTS frame to the AP before $N_{\mathrm{UE}} - 1$ other UEs. If the RTS frame is received at the AP successfully, the AP replies after a short inter-frame space (SIFS) with the CTS frame. The u_0th UE only proceeds to transmit the data frame, after the time interval of SIFS, if it receives the CTS frame. Eventually, an acknowledgment (ACK) packet is transmitted after the period of SIFS by the serving AP to notify the successful packet reception. The UEs that can hear the u_0th UE will freeze their backoff counter at the start of RTS transmission. The backoff counter will be reactivated when the channel is sensed to be idle again after the period of DIFS. If the u_1th UE cannot hear the u_0th UE, it will start to send RTS frame after waiting for $\mathcal{B}_{u_1} \times t_{\mathrm{slot}}$ seconds. Here, the u_1th UE is called the hidden node and a collision occurs if $(\mathcal{B}_{u_1} - \mathcal{B}_{u_0}) \times t_{\mathrm{slot}} < t_{\mathrm{RTS}}$, where t_{RTS} is the RTS transmission time which is directly proportional to the length of RTS frame, L_{RTS}, and inversely proportional to the uplink rate, R_{u}, that is $t_{\mathrm{RTS}} = L_{\mathrm{RTS}}/R_{\mathrm{u}}$.

RTS and CTS frames carry a network allocation vector (NAV) field which is a virtual carrier-sensing mechanism. The NAV indicates the number of microseconds that the channel is reserved by a UE. The NAV in an RTS frame includes the CTS frame, the data frame, and the subsequent ACK frame from the AP. Nodes that can hear the RTS frame will set their NAV timers corresponding to the RTS NAV. The CTS frame contains a new NAV updated to the time already elapsed. After the CTS frame is sent, all UEs that can receive the CTS will update their NAV timer and defer transmission until their NAV timers reach zero. This keeps the channel free for

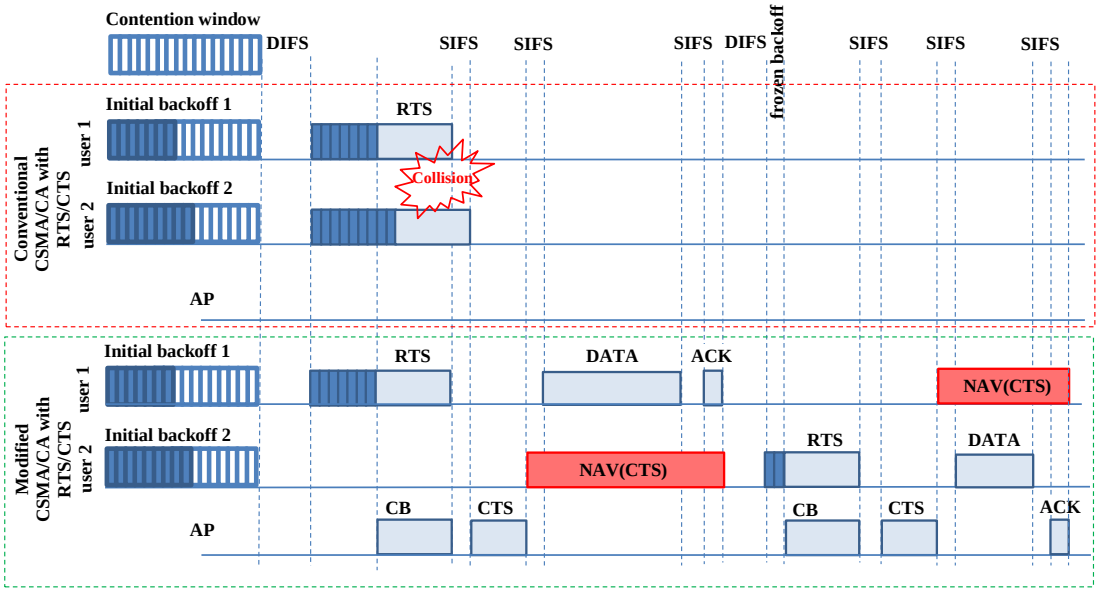

Figure 3.1: *Conventional and modified four-way handshaking RTS/CTS mechanism.*

the u_0th UE to complete the process of transmitting data to the AP and alleviates the problem of hidden nodes. In contrast to RF networks, the UEs cannot hear each other directly in LiFi networks since in the downlink and uplink visible light and IR are employed, respectively. Hence, the downlink filter is tuned in visible light band and cannot sense the uplink transmission of other UEs via IR. Hence, all UEs are hidden for each other and this problem is extreme in LiFi networks. Note that since UEs cannot hear the RTS frame in LiFi networks, they can only set their NAV with the NAV of the CTS frame.

3.3.3 Brief Description of the Modified CSMA/CA Protocol

In the modified CSMA/CA, the AP transmits the CB tone simultaneously with the reception of the RTS packet to notify the other UEs that the channel is already occupied. The UEs that can hear the CB tone will freeze their backoff counters. The backoff counters will be reactivated when the channel is sensed to be idle again after the period of DIFS. If the AP does not transmit the CB tone, the other users will continue to count down their backoff time. Once the backoff time reaches zero, the UEs start to send the RTS packet and in this case it is very probable that a collision occurs. A comparison between the conventional and the modified CSMA/CA with

RTS/CTS mechanism is shown in figure 3.1 when they are adopted in a LiFi network. As it can be seen, for the conventional CSMA/CA in a LiFi network, the RTS of user 2 collides with the RTS of user 1 since user 2 cannot hear user 1. This issue has been solved in the proposed modified CSMA/CA by means of the CB tone. Here, user 2 can hear the CB tone from the AP and it will freeze its backoff counter. Next, the AP transmits the CTS with the NAV. Since user 2 can hear the CTS packet, it defers its transmission for the period of NAV. Hence, the modified CSMA/CA can address the problem of hidden nodes in a LiFi network.

3.3.4 Uplink Throughput

In the modified CSMA/CA for LiFi networks, collision only occurs if the backoff time of at least two UEs reach zero simultaneously. Thus, they transmit at the same time and the packets collide. The analysis of normalized throughput and collision probability is the same as the analysis provided in [106]. In the following, we only provide a summary of the equations and further detail is provided in [106]. The normalized uplink throughput is given as:

$$\widetilde{\mathcal{T}}_{\mathrm{u}} = \frac{P_{\mathrm{t}} P_{\mathrm{s}} \mathbb{E}[t_{\mathrm{D}}]}{(1-P_{\mathrm{t}}) t_{\mathrm{slot}} + P_{\mathrm{t}} P_{\mathrm{s}} \mathbb{E}[t_{\mathrm{s}}] + P_{\mathrm{t}}(1-P_{\mathrm{s}}) t_{\mathrm{c}}}, \tag{3.6}$$

where $P_{\mathrm{t}} = 1-(1-P_{\mathrm{w}})^{N_{\mathrm{UE}}}$ is the probability of at least one transmission in the considered backoff time slot, $P_{\mathrm{s}} = N_{\mathrm{UE}} P_{\mathrm{w}} (1-P_{\mathrm{w}})^{N_{\mathrm{UE}}-1} / P_{\mathrm{t}}$ is the probability of successful transmission, and $P_{\mathrm{w}} = \frac{2}{w+1}$ is the probability that a UE transmits on a randomly chosen time slot. In (3.6), $\mathbb{E}[t_{\mathrm{D}}], \mathbb{E}[t_{\mathrm{s}}]$ and t_{c} are the average transmission time of data packets, the average successful transmission time and the collision time, respectively. Assuming that all data packets have the same length, then:

$$\begin{aligned} \mathbb{E}[t_{\mathrm{s}}] = t_{\mathrm{s}} =& t_{\mathrm{RTS}} + t_{\mathrm{SIFS}} + t_{\mathrm{dely}} + t_{\mathrm{CTS}} + t_{\mathrm{SIFS}} + t_{\mathrm{dely}} + t_{\mathrm{HDR}} + t_{\mathrm{D}} + t_{\mathrm{SIFS}} \\ & + t_{\mathrm{dely}} + t_{\mathrm{ACK}} + t_{\mathrm{DIFS}} + t_{\mathrm{dely}}, \\ \mathbb{E}[t_{\mathrm{D}}] =& t_{\mathrm{D}}, \\ t_{\mathrm{c}} =& t_{\mathrm{RTS}} + t_{\mathrm{DIFS}} + t_{\mathrm{dely}}, \end{aligned} \tag{3.7}$$

where t_{dely} is the propagation delay. Also, t_{CTS} and t_{ACK} are the transmission time of CTS and ACK packets, respectively. Furthermore, t_{SIFS} and t_{DIFS} are the duration of SIFS and DIFS,

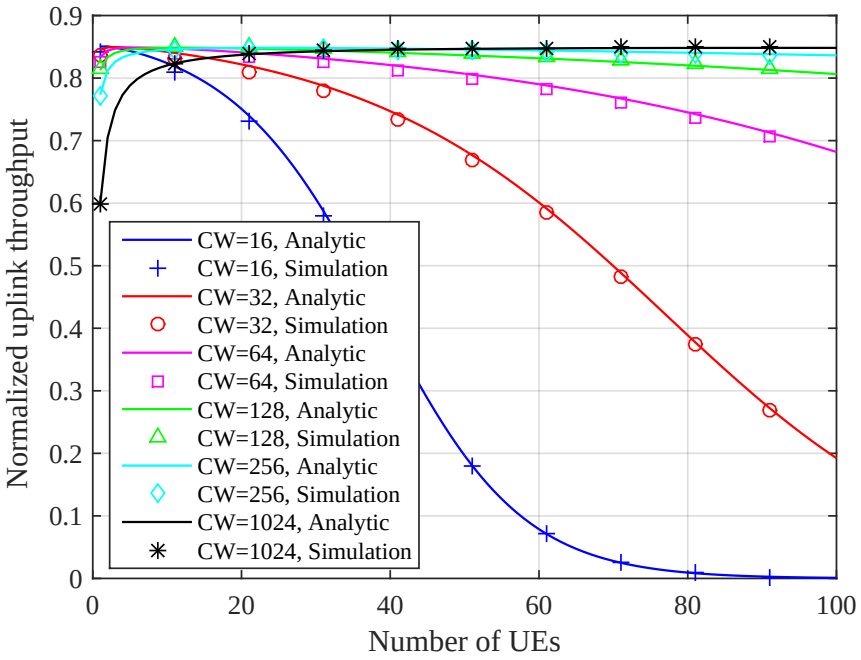

Figure 3.2: *Normalized uplink throughput using modified RTS/CTS access protocol versus different number of UEs in a LiFi attocell for various sizes of contention window.*

respectively. Note that the packet header includes both physical and MAC headers.

Finally, the uplink throughput of the jth UE can be obtained as follows:

$$R_{\mathrm{u},j} = \frac{\widetilde{\mathcal{T}}_{\mathrm{u}} B_{\mathrm{u},n}}{N_{\mathrm{UE}}} \log_2 \left(1 + \mathcal{S}_{\mathrm{u},j}\right). \tag{3.8}$$

where $B_{\mathrm{u},n}$ is the uplink bandwidth of the nth FR plan and $\mathcal{S}_{\mathrm{u},j}$ is the SINR at the AP when communicating with the jth UE and it is given as:

$$\mathcal{S}_{\mathrm{u},j} = \frac{\left(RP_{\mathrm{u,opt}} H_{\imath,j}\right)^2}{\eta^2 N_0 B_{\mathrm{u},n} + \sum_{j \in \Pi} \left(RP_{\mathrm{u,opt}} H_{i,j}\right)^2}, \tag{3.9}$$

where Π is the set of other UEs using the same bandwidth as the jth UE and communicating with the $\imath$th AP, $(\imath \neq \imath)$ simultaneously with the jth UE; and $P_{\mathrm{u,opt}}$ is the transmitted uplink power which is assumed to be the same for all UEs.

The analytical results based on (3.6) and Monte-Carlo simulation results of the normalized up-

Parameter	Symbol	Value
Average length of uplink payload	L_{D}	2000 B
Physical header	H_{PHY}	128 b
MAC header	H_{MAC}	272 b
RTS packet size	L_{RTS}	288 b
CTS packet size	L_{CTS}	240 b
ACK packet size	L_{ACK}	240 b
SIFS	t_{SIFS}	16 μs
DIFS	t_{DIFS}	32 μs
Backoff slot duration	t_{slot}	8 μs
Propagation delay	t_{delay}	1 μs

Table 3.1: *Uplink simulation parameters [2].*

link throughput versus different number of UEs in a LiFi attocell with an RTS/CTS access protocol are shown in figure 3.2. Note that since the aim of these results is to show the effect of contention window size on the uplink throughput, we assume all UEs transmit packets with the same data rate of 1 Mbps. The results are presented for various sizes of contention window with the parameters given in Table 3.1. As we can see from figure 3.2, when there are few UEs in the network, the contention window with smaller size outperforms. The reason for this is that the header caused by their backoff time is lower and the UEs do not need to wait for a long time to transmit data. However, as the number of UEs increases, the probability of collision also increases which leads to throughput degradation. Therefore, for crowded networks, the probability of collision can be reduced by increasing the size of the contention window. In fact, by increasing the size of the contention window, the probability of having two or more UEs with the same backoff time reduces, which ensures a low collision probability.

3.4 Feedback Mechanism

Over the last few years, studies have repeatedly illustrated that permitting the receiver to send some information bits about the channel conditions to the transmitter can allow effective resource allocation and downlink throughput enhancement. This feedback information is usually the SINR at the receiver [6, 79]. However, sending this information is at the cost of uplink throughput degradation. Therefore, there is a trade-off between downlink and uplink through-

put when the amount of feedback varies. Let's define the feedback ratio, ϵ, as the ratio of total feedback time and total transmission time as:

$$\epsilon = \frac{\sum t_{\mathrm{fb}}}{t_{\mathrm{tot}}}, \tag{3.10}$$

where t_{fb} is the feedback duration. Figure 3.3-(a) denotes a general feedback mechanism, in which feedback information is transmitted periodically after an interval of t_{u}. Denoting that the denominator of (3.10) is the total transmission time which is equal to $t_{\mathrm{tot}} = (N_{\mathrm{D}} + N_{\mathrm{f}})t_{\mathrm{fr}}$, where N_{D} and N_{f} are the number of data and feedback frames in the total transmission time. The total feedback time is $\Sigma t_{\mathrm{fb}} = N_{\mathrm{f}} t_{\mathrm{fb}}$. Replacing these equations in (3.10), the feedback ratio can be obtained as:

$$\epsilon = \frac{N_{\mathrm{f}} t_{\mathrm{fb}}}{(N_{\mathrm{D}} + N_{\mathrm{f}})t_{\mathrm{fr}}} = \frac{t_{\mathrm{fb}}}{\left(1 + \frac{N_{\mathrm{D}}}{N_{\mathrm{f}}}\right) t_{\mathrm{fr}}}. \tag{3.11}$$

Since $t_{\mathrm{tot}} = (N_{\mathrm{D}} + N_{\mathrm{f}})t_{\mathrm{fr}} = N_{\mathrm{f}} t_{\mathrm{u}}$, then $1 + \dfrac{N_{\mathrm{D}}}{N_{\mathrm{f}}} = \dfrac{t_{\mathrm{u}}}{t_{\mathrm{fr}}}$, and substituting it in (3.11), it can be simplified as:

$$\epsilon = \frac{t_{\mathrm{fb}}}{t_{\mathrm{u}}}. \tag{3.12}$$

Then, the uplink throughput of the jth UE in consideration of feedback is given by:

$$R_{\mathrm{u},j} = \left(1 - \frac{t_{\mathrm{fb}}}{t_{\mathrm{u}}}\right) \frac{\widetilde{\mathcal{T}}_{\mathrm{u}} B_{\mathrm{u},n}}{N_{\mathrm{UE}}} \log_2 \left(1 + \mathcal{S}_{\mathrm{u,j}}\right). \tag{3.13}$$

Due to the use of DCO-OFDM modulation, the AP requires the SINR information of $\mathcal{K}/2 - 1$ subcarriers. The extreme and least cases for sending the SINR information are full feedback and one-bit fixed-rate feedback, respectively. These schemes are shown in figure 3.3-(b) and figure 3.3-(c). In the FF scheme, UEs send the SINR of all subcarriers at the beginning of each data frame. Obviously, this impractical method produces a huge amount of feedback. According to the one-bit feedback technique, the AP sets a threshold for all UEs. Each UE compares the value of its SINR to this threshold. When the SINR exceeds the threshold, a '1' will be transmitted to the AP; otherwise a '0' will be sent. The AP receives feedback from all UEs and then randomly selects a UE whose feedback bit was '1'. If all the feedback bits received by the AP are zero, then no signal is transmitted in the next time interval. However, in this case

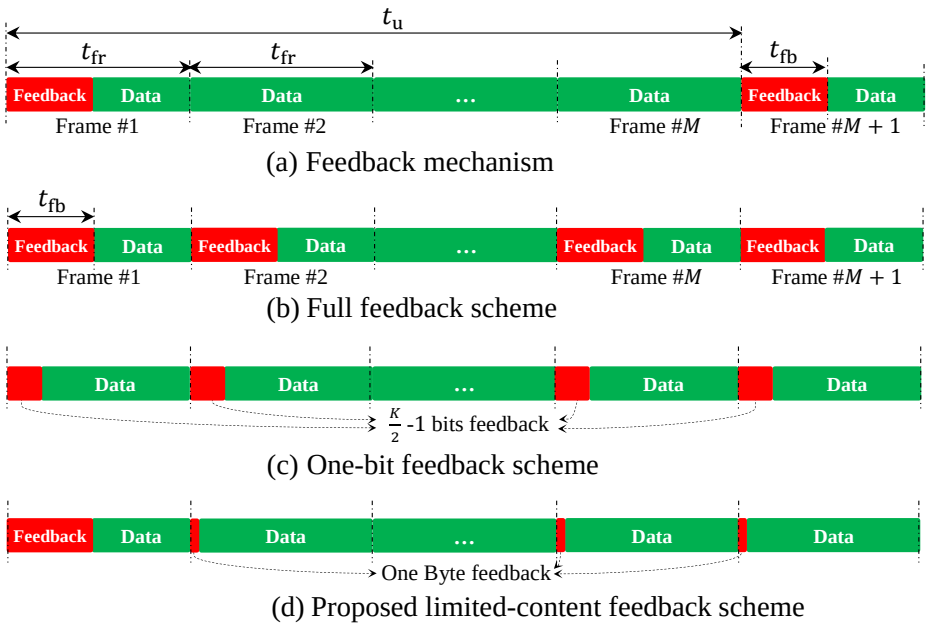

Figure 3.3: *Feedback schemes.*

the AP can also randomly choose a UE for data transmission. For a large number of UEs this solution has a vanishing benefit over no data transmission when all the received feedback bits are '0' [107].

As can be induced from (3.12), the feedback ratio can generally be reduced by means of either decreasing the content of feedback or increasing the update interval. In the following, we propose the LCF and LFF techniques. The former is based on reducing the feedback information in each frame and the latter is based on increasing the update interval.

3.4.1 Proposed LCF Scheme

Unlike RF wireless and optical diffused channels, the frequency selectivity of the channel in LiFi networks is mostly characterized by the limitations of the front-end devices, rather than the multipath nature of the channel [54]. In order to assess the frequency response of the indoor LiFi channel, computer simulations are conducted. The simulations are performed for a network size of $10 \times 10 \times 2.15$ m^3. The network area is divided equally into nine quadrants with one AP located at the center of each. It is assumed that the center of the XY-plane is located in

Parameter	Symbol	Value
Network space	–	$10 \times 10 \times 2.15$ m^3
Number of APs	N_{AP}	9
Cell radius	r_{c}	2.35 m
LED half-intensity angle	$\Phi_{1/2}$	60°
Receiver FOV	Ψ_{c}	90°
Physical area of a PD	A	1 cm^2
Gain of optical filter	g_{f}	1
Refractive index	ς	1
PD responsivity	R	1 A/W
Reflection coefficient of walls	ρ_{w}	0.85
Reflection coefficient of floor	ρ_{f}	0.2
Number of subcarriers	$\mathcal{K}$	2048
Transmitted optical power	$P_{\mathrm{d,opt}}$	8 W
Downlink FR bandwidth	$B_{\mathrm{d},n}$	10 MHz
Fitted coefficient	f_0	7.2 MHz
Conversion factor	η	3
Noise power spectral density	N_0	10^{-21} A^2/Hz

Table 3.2: *Downlink simulation parameters.*

the center of the room. The other parameters are listed in Table 3.2. The normalized frequency response of the channel gain, $\frac{|H(f)|^2}{|H_{\mathrm{LOS}}(0)|^2}$, for a UE placed at different positions in the room is depicted in figure 3.4. As can be seen, the normalized frequency response fluctuates around the LOS component and the variation of the fluctuation is less than 1 dB. Moreover, the channel gain variation is less significant for UEs that are further away from the walls of the room, due to the dominant effect of the LOS link compared to the NLOS channel [108]. Accordingly, the frequency selectivity of LiFi channels is mainly confined by front-end components, and the frequency selectivity of the front-end elements are relatively deterministic although not frequency flat. The average received power at the UE is much more dynamic and is significantly dependent on the position of the UE. Therefore, by only updating the average power, a reasonable estimate of the SINR of all the subcarriers can be obtained. This idea forms the foundation of our proposed LCF scheme.

Figure 3.3-(d) represents the principal working mechanism of our proposed LCF scheme. According to the LCF scheme, when a UE connects to an AP, it sends the SINR information of all subcarriers only once at the beginning of the first frame. For the following frames and as long

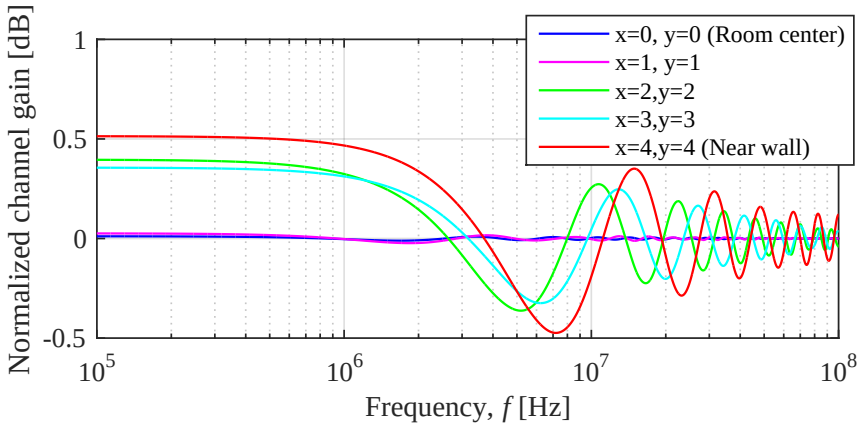

Figure 3.4: *Normalized channel gain,* $\frac{|H(f)|^2}{|H_{\mathrm{LOS}}(0)|^2}$*, for different room positions.*

as the UE is connected to the same AP, it only updates the scheduler on its received average power (i.e., the DC channel component). Once the UE connects to a new AP, it will transmit the SINR information of all subcarriers again. The proposed LCF scheme then simply scales the individual SINR values received in the next frames such that the total average power matches the updated average power [30]. Thus, the estimated SINR on the kth subcarrier of the jth UE at time instance t is given as:

$$\hat{\mathcal{S}}_{\mathrm{d},j,k}(t) \approx \mathcal{S}_{\mathrm{d},j,k}(0)\frac{\mathcal{S}_{\mathrm{d},j,0}(t)}{\mathcal{S}_{\mathrm{d},j,0}(0)}, \tag{3.14}$$

where $\mathcal{S}_{\mathrm{d},j,k}(0)$ is the downlink SINR of the jth UE on the kth subcarrier at $t = 0$. The scheduler uses this estimated SINR information for subcarrier allocation according to (3.1).

The most significant difference between the LCF technique and one-bit feedback method is that the AP does not have any knowledge about the SINR value of each subcarrier and it just knows that the SINR is above or lower than a predetermined threshold for the one-bit feedback technique. However, thanks to the use of LCF approach, the AP can have an estimation of the SINR value for each subcarrier.

3.4.2 LFF Scheme to Support Mobility

Due to the slowly-varying nature of the indoor LiFi channels, the UE can update the AP about its channel condition less frequently, especially when the UE is immobile or it moves slowly [31]. Mobility is one of the main factors that can lead to a considerable channel variation of a UE. Therefore, in order to maintain the required QoS and support seamless connectivity, mobile UEs are needed to update the AP every t_{u} seconds about their channel conditions. In the following, we first introduce the RWP mobility model that is considered in the analysis of the proposed LFF mechanism. Then, the LFF scheme is described in detail. Note that the RWP model is just an example of a mobility model, which does not affect the general idea of the proposed LFF scheme. Another point is that as soon as the UE changes the attocell, it is required to update the new AP with its channel condition. The average time that a UE spends in an attocell before leaving it, depends on the cell radius. This average time is called sojourn time [109]. For the typical LiFi attocells, this sojourn time is much greater than the update interval within an attocell. Hence, in the analysis of LFF, we can only focus on the mobility of the UE within one attocell.

We consider a FR plan in both downlink and uplink to reduce the co-channel interference and also guarantee the cell edge users data rate. Furthermore, hard handover with threshold is assumed with the decision metric of $|\mathcal{S}_\imath - \mathcal{S}_i| < \alpha_{\mathrm{Th}}$, where $\mathcal{S}_\imath$ and $\mathcal{S}_i$ are the SINR of the serving AP and adjacent APs, respectively; and α_{Th} is the handover threshold. According to the considered soft handover scheme, when the difference of SINR from two APs goes below the threshold, handover will occur.

As shown in figure 3.5, the UE distance at time instance t from the AP is $d(t) = \left(r^2(t) + h^2\right)^{1/2}$, where $r(t) = (r_0^2 + v^2t^2 - 2r_0vt\cos\hat{\theta})^{1/2}$ with $\hat{\theta} = \pi - \cos^{-1}\left(\frac{\vec{\boldsymbol{r_0}}\cdot\vec{\boldsymbol{v}}}{|\vec{\boldsymbol{r_0}}||\vec{\boldsymbol{v}}|}\right)$; $\vec{\boldsymbol{r_0}}$ is the initial UE distance vector from the cell center at $t = 0$ with $|\vec{\boldsymbol{r_0}}| = r_0$; and $\vec{\boldsymbol{v}}$ is the vector of the UE's velocity with $|\vec{\boldsymbol{v}}| = v$. Here, r_0 has the PDF of $f_{\mathcal{R}_0}(r_0) = 2r_0/r_{\mathrm{c}}^2$ and $\hat{\theta}$ follows a uniform distribution with the PDF of $f_{\Theta}(\hat{\theta}) = 1/2\pi$. For notation simplicity, the dependency of the equations to time is omitted unless it is confusing.

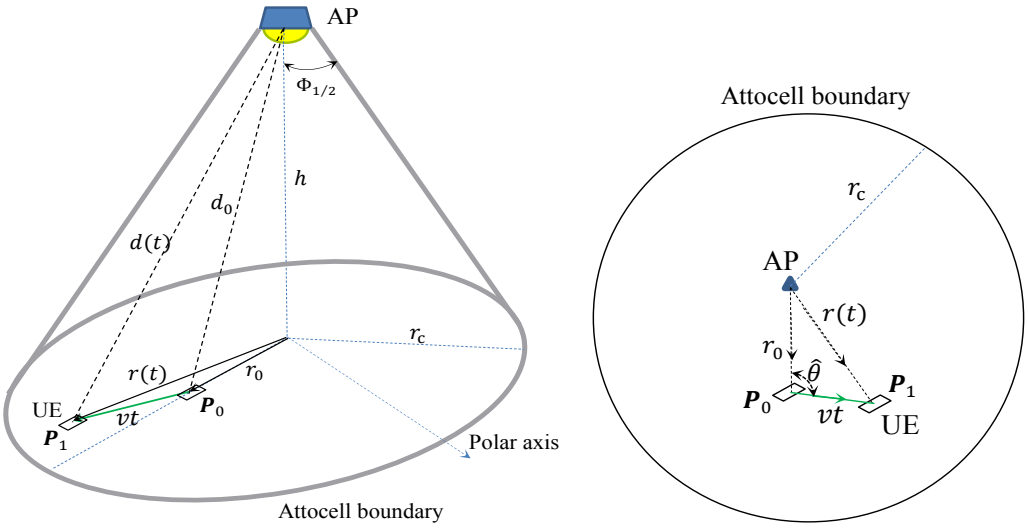

Figure 3.5: *RWP movement model.*

3.4.2.1 LFF Scheme

Based on the UE's velocity, we aim to find the appropriate channel update interval, t_{u}, so that the expected weighted average sum throughput of uplink and downlink per user is maximized. Weighted sum throughput maximization is commonly used to optimize the overall throughput for bidirectional communications [110], [111]. The optimization problem (OP) is formulated as:

$$\max_{t_{\mathrm{u}}} \left(\mathbb{E}_{[\boldsymbol{r_0}],[\hat{\boldsymbol{\theta}}]} \left[\frac{1}{N_{\mathrm{UE}}} \sum_{j=1}^{N_{\mathrm{UE}}} \left(w_{\mathrm{d}} \overline{R}_{\mathrm{d},j}(t_{\mathrm{u}}) + w_{\mathrm{u}} \overline{R}_{\mathrm{u},j}(t_{\mathrm{u}}) \right) \right] \right), \tag{3.15}$$

where $\overline{R}_{\mathrm{d},j}$ and $\overline{R}_{\mathrm{u},j}$ are the average downlink and uplink throughput of the jth UE, respectively, with the corresponding weights w_{d} and w_{u}, both take values from the range $[0, 1]$. Note that $[\boldsymbol{r_0}] = [r_{01}, \cdots, r_{0N_{\mathrm{UE}}}]$ and $[\hat{\boldsymbol{\theta}}] = [\hat{\theta}_1, \cdots, \hat{\theta}_{N_{\mathrm{UE}}}]$ are random variable vectors with independent and identically distributed (i.i.d) entities; $\mathbb{E}_{[\boldsymbol{r_0}],[\hat{\boldsymbol{\theta}}]}[\cdot]$ is the expectation with respect to the joint PDF $f([\boldsymbol{r_0}], [\hat{\boldsymbol{\theta}}]) = f(r_{01}, \cdots, r_{0N_{\mathrm{UE}}}, \hat{\theta}_1, \cdots, \hat{\theta}_{N_{\mathrm{UE}}})$. Since r_{0j}'s and $\hat{\theta}_j$'s are i.i.d, we have $f([\boldsymbol{r_0}], [\hat{\boldsymbol{\theta}}]) = f_{\mathcal{R}_0}(r_{0j}) f_{\Theta}(\hat{\theta}_j) \prod_{i \neq j} f_{\mathcal{R}_0}(r_{0i}) f_{\Theta}(\hat{\theta}_i)$. The expectation can go inside the summation, then, we have $\mathbb{E}_{[\boldsymbol{r_0}],[\hat{\boldsymbol{\theta}}]}\left[\overline{R}_{\mathrm{d},j}(t_{\mathrm{u}})\right] = \mathbb{E}_{r_{0j},\hat{\theta}_j}\left[\overline{R}_{\mathrm{d},j}(t_{\mathrm{u}})\right]$ for downlink and

$\mathbb{E}_{[\boldsymbol{r_0}],[\hat{\boldsymbol{\theta}}]}\left[\overline{R}_{\mathrm{u},j}(t_{\mathrm{u}})\right] = \mathbb{E}_{r_{0j},\hat{\theta}_j}\left[\overline{R}_{\mathrm{u},j}(t_{\mathrm{u}})\right]$ for uplink. Since r_{0j}'s and $\hat{\theta}_j$'s are i.i.d, then:

$$\mathbb{E}_{r_{01},\hat{\theta}_1}\left[\overline{R}_{\mathrm{d},1}(t_{\mathrm{u}})\right] = \cdots = \mathbb{E}_{r_{0N_{\mathrm{UE}}},\hat{\theta}_{N_{\mathrm{UE}}}}\left[\overline{R}_{\mathrm{d},N_{\mathrm{UE}}}(t_{\mathrm{u}})\right] \triangleq \mathbb{E}_{r_0,\hat{\theta}}\left[\overline{R}_{\mathrm{d}}(t_{\mathrm{u}})\right]$$
$$\mathbb{E}_{r_{01},\hat{\theta}_1}\left[\overline{R}_{\mathrm{u},1}(t_{\mathrm{u}})\right] = \cdots = \mathbb{E}_{r_{0N_{\mathrm{UE}}},\hat{\theta}_{N_{\mathrm{UE}}}}\left[\overline{R}_{\mathrm{u},N_{\mathrm{UE}}}(t_{\mathrm{u}})\right] \triangleq \mathbb{E}_{r_0,\hat{\theta}}\left[\overline{R}_{\mathrm{u}}(t_{\mathrm{u}})\right].$$

After substituting the above equations in (3.15) and some manipulations, the OP can be expressed as:

$$\max_{t_{\mathrm{u}}} \left(\overline{\mathcal{T}} = w_{\mathrm{u}}\mathbb{E}_{r_0,\hat{\theta}}\left[\overline{R}_{\mathrm{u}}(t_{\mathrm{u}})\right] + w_{\mathrm{d}}\mathbb{E}_{r_0,\hat{\theta}}\left[\overline{R}_{\mathrm{d}}(t_{\mathrm{u}})\right]\right), \tag{3.16}$$

The average is calculated over one update interval, since it is assumed that the UE feeds back its velocity information to the AP after each update interval. It is noted that $\overline{\mathcal{T}}$ is the average result of all UEs. The opposite behaviour of $\overline{R}_{\mathrm{u}}$ and $\overline{R}_{\mathrm{d}}$ with respect to the update interval (the former directly and the latter inversely are proportional to the update interval), results in an optimum point for $\overline{\mathcal{T}}$. In the following, $\overline{R}_{\mathrm{u}}$ and $\overline{R}_{\mathrm{d}}$ are calculated with some simplifying assumptions.

The exact and general state of SINR at the receiver is provided in (3.5). However, for ease of analytical derivations, it can be simplified under some reasonable assumptions including: *i*) the interference from other APs can be neglected due to employing FR plan, *ii*) $H_{i,j,k} \approx H_{\mathrm{LOS},i,j}H_{\mathrm{fe},k}$. The latter assumption is based on the fact that in LiFi systems, $H_{\mathrm{LOS},i,j} >> H_{\mathrm{NLOS},i,j}$. Moreover, H_{fe} is assumed to be the same for all UEs. It was shown in figure 3.4 that the variation of the frequency response fluctuation around the LOS component is less than 1 dB. For a vertically upward UE, $\cos\phi_{ij} = \cos\psi_{ij} = h/d_{ij}$, can be substituted in (2.7), then, the DC gain of the LOS channel is $H_{\mathrm{LOS},i,j} = G_0/d_{ij}^{m+3}$, where $G_0 = \frac{(m+1)A}{2\pi\sin^2\Psi_{\mathrm{c}}} g_{\mathrm{f}}\varsigma^2 h^{m+1}$. Hence, the approximate and concise equation of SINR at the kth subcarrier of the jth UE is given by:

$$\mathcal{S}_{j,k} \approx \frac{G e^{\frac{-2kB_{\mathrm{d},n}}{\mathcal{K}f_0}}}{\left(r_j^2 + h^2\right)^{m+3}}, \tag{3.17}$$

where $G = \frac{\mathcal{K}G_0^2 R^2 P_{\mathrm{d,opt}}^2}{(\mathcal{K}-2)\eta^2 N_0 B_{\mathrm{d},n}}$ and r_j is the distance between the jth UE and the center of the cell.

Substituting (3.17) in (3.2), the downlink throughput is given as:

$$R_{\mathrm{d},j} = \frac{B_{\mathrm{d},n}}{\mathcal{K}} \sum_{k=1}^{\frac{\mathcal{K}}{2}-1} \log_2 \left(1 + \pi_{j,k} \frac{G e^{\frac{-2kB_{\mathrm{d},n}}{\mathcal{K}f_0}}}{\left(r_j^2 + h^2\right)^{m+3}} \right). \tag{3.18}$$

Noting that for SINR values of larger than 10 dB, we have:

$$R_{\mathrm{d},j} \cong \frac{B_{\mathrm{d},n}}{\mathcal{K}} \sum_{k=1}^{\frac{\mathcal{K}}{2}-1} \pi_{j,k} \log_2 \left(\frac{G e^{\frac{-2kB_{\mathrm{d},n}}{\mathcal{K}f_0}}}{\left(r_j^2 + h^2\right)^{m+3}} \right). \tag{3.19}$$

The same approximations can be also considered for uplink throughput. Define $G_{\mathrm{u}} = \frac{(G_0 R P_{\mathrm{u,opt}})^2}{\eta^2 N_0 B_{\mathrm{u},n}}$, then, the SINR at the AP is $\mathcal{S}_{\mathrm{u},j} = G_{\mathrm{u}}/(r_j^2 + h^2)^{m+3}$. Substituting it in (3.13), the uplink throughput of the jth UE can approximately be obtained as:

$$R_{\mathrm{u},j} \cong \left(1 - \frac{t_{\mathrm{fb}}}{t_{\mathrm{u}}}\right) \frac{\widetilde{\mathcal{T}}_{\mathrm{u}} B_{\mathrm{u},n}}{N_{\mathrm{UE}}} \log_2 \left(\frac{G_{\mathrm{u}}}{\left(r_j^2 + h^2\right)^{m+3}} \right). \tag{3.20}$$

Without loss of generality and for ease of notations, we consider one of the UEs for the rest of the derivations and remove the subscript j. The average uplink throughput over one update interval is given as:

$$\begin{aligned}
\overline{R}_{\mathrm{u}} &= \left(1 - \frac{t_{\mathrm{fb}}}{t_{\mathrm{u}}}\right) \frac{\widetilde{\mathcal{T}}_{\mathrm{u}} B_{\mathrm{u},n}}{N_{\mathrm{UE}}} \frac{1}{t_{\mathrm{u}}} \int_0^{t_{\mathrm{u}}} \log_2 \left(\frac{G_{\mathrm{u}}}{(r^2(t) + h^2)^{m+3}} \right) \mathrm{d}t \\
&= \frac{2(m+3)\widetilde{\mathcal{T}}_{\mathrm{u}} B_{\mathrm{u},n}}{N_{\mathrm{UE}}} \left(1 - \frac{t_{\mathrm{fb}}}{t_{\mathrm{u}}}\right) \left(\frac{1}{2(m+3)} \log_2 \left(\frac{G_{\mathrm{u}}}{(r^2(t_{\mathrm{u}}) + h^2)^{m+3}} \right) \right. \\
&+ \frac{r_0 \cos\hat{\theta}}{2vt_{\mathrm{u}}} \log_2 \left(\frac{r^2(t_{\mathrm{u}}) + h^2}{r_0^2 + h^2} \right) + \frac{1}{\ln(2)} - \frac{(h^2 + r_0^2 \sin^2\hat{\theta})^{\frac{1}{2}}}{vt_{\mathrm{u}} \ln(2)} \tan^{-1} \left(\frac{vt_{\mathrm{u}} - r_0 \cos\hat{\theta}}{(h^2 + r_0^2 \sin^2\hat{\theta})^{\frac{1}{2}}} \right) \\
&\left. - \frac{(h^2 + r_0^2 \sin^2\hat{\theta})^{\frac{1}{2}}}{vt_{\mathrm{u}} \ln(2)} \tan^{-1} \left(\frac{r_0 \cos\hat{\theta}}{(h^2 + r_0^2 \sin^2\hat{\theta})^{\frac{1}{2}}} \right) \right).
\end{aligned} \tag{3.21}$$

The average downlink throughput over one update interval can be obtained as:

$$\begin{aligned}\overline{R}_{\mathrm{d}} &= \frac{B_{\mathrm{d},n}}{\mathcal{K}t_{\mathrm{u}}}\int_0^{t_{\mathrm{u}}}\sum_{k=1}^{k_{\mathrm{req}}}\log_2\left(\frac{Ge^{\frac{-2kB_{\mathrm{d},n}}{\mathcal{K}f_0}}}{(r^2(t)+h^2)^{m+3}}\right)\mathrm{d}t \\ &= \frac{k_{\mathrm{req}}B_{\mathrm{d},n}}{\mathcal{K}t_{\mathrm{u}}}\int_0^{t_{\mathrm{u}}}\log_2\left(\frac{Ge^{-(k_{\mathrm{req}}+1)B_{\mathrm{d},n}/\mathcal{K}f_0}}{(r^2(t)+h^2)^{m+3}}\right)\mathrm{d}t \\ &= \frac{2(m+3)k_{\mathrm{req}}B_{\mathrm{d},n}}{\mathcal{K}}\left(\frac{1}{2(m+3)}\log_2\left(\frac{Ge^{-(k_{\mathrm{req}}+1)B_{\mathrm{d},n}/\mathcal{K}f_0}}{(r^2(t_{\mathrm{u}})+h^2)^{m+3}}\right)\right. \\ &+\frac{r_0\cos\hat{\theta}}{2vt_{\mathrm{u}}}\log_2\left(\frac{r^2(t_{\mathrm{u}})+h^2}{r_0^2+h^2}\right)+\frac{1}{\ln(2)}-\frac{(h^2+r_0^2\sin^2\hat{\theta})^{\frac{1}{2}}}{vt_{\mathrm{u}}\ln(2)}\tan^{-1}\left(\frac{vt_{\mathrm{u}}-r_0\cos\hat{\theta}}{(h^2+r_0^2\sin^2\hat{\theta})^{\frac{1}{2}}}\right) \\ &\left.-\frac{(h^2+r_0^2\sin^2\hat{\theta})^{\frac{1}{2}}}{vt_{\mathrm{u}}\ln(2)}\tan^{-1}\left(\frac{r_0\cos\hat{\theta}}{(h^2+r_0^2\sin^2\hat{\theta})^{\frac{1}{2}}}\right)\right).\end{aligned} \tag{3.22}$$

where k_{req} is the required number of subcarriers to be allocated to the UE at $t=0$. With the initial and random distance of r_0 from the cell center, the required number of subcarriers can approximately be obtained as:

$$k_{\mathrm{req}} \cong \frac{\mathcal{K}R_{\mathrm{req}}}{B_{\mathrm{d},n}\log_2\left(G/(r_0^2+h^2)^{m+3}\right)}. \tag{3.23}$$

The proof of (3.23) is given in Appendix A.

From a practical point of view, with adaptive modulation and coding (AMC) level described in [54], the requested data rate can be satisfied by allocating k_{req} subcarriers to the user. Thus, the achieved data rate would be

$$R_{\mathrm{achieved}} = \frac{B_{\mathrm{d},n}}{\mathcal{K}}\sum_{k=1}^{k_{\mathrm{req}}}\varepsilon_k \tag{3.24}$$

where ε_k is the spectral efficiency (bits/symbol) of the kth subcarrier. Note that for the case of uncoded M-QAM modulation, we have $\varepsilon_k = \log_2(M)$.

Both the average uplink and downlink throughput given in (3.21) and (3.22), respectively, are continuous and derivative in the range $(0, 2r_{\mathrm{c}}/v)$. Therefore, we can express the following proposition to find the optimal update interval that results in the maximum sum-throughput.

Proposition. *Let t_{u} be continuous in the range of $(0, 2r_{\mathrm{c}}/v)$. The optimal solution to the OP given in* (3.16) *can be obtained by solving the following equation:*

$$\mathbb{E}_{r_0,\hat{\theta}}\left[\frac{\partial\overline{\mathcal{T}}}{\partial t_{\mathrm{u}}}\right] = w_{\mathrm{u}}\mathbb{E}_{r_0,\hat{\theta}}\left[\frac{\partial\overline{\mathcal{T}}_{\mathrm{u}}}{\partial t_{\mathrm{u}}}\right] + w_{\mathrm{d}}\mathbb{E}_{r_0,\hat{\theta}}\left[\frac{\partial\overline{\mathcal{T}}_{\mathrm{d}}}{\partial t_{\mathrm{u}}}\right] = 0. \tag{3.25}$$

For $vt_{\mathrm{u}} \ll h$, the root of (3.25) *can be well approximated as:*

$$\widetilde{t}_{\mathrm{u,opt}} \cong \left(\frac{\frac{3\ln(2)}{2(m+3)} w_{\mathrm{u}} t_{\mathrm{fb}} \widetilde{\mathcal{T}}_{\mathrm{u}} B_{\mathrm{u},n} C_1}{w_{\mathrm{d}} v^2 N_{\mathrm{UE}} R_{\mathrm{req}} + C_2 w_{\mathrm{u}} v^2 \widetilde{\mathcal{T}}_{\mathrm{u}} B_{\mathrm{u},n}}\right)^{\frac{1}{3}}, \tag{3.26}$$

where

$$\begin{aligned} C_1 &= \frac{\mathbb{E}_{r_0}\left[\log_2\left(\frac{G_{\mathrm{u}}}{(r_0^2+h^2)^{m+3}}\right)\right]\mathbb{E}_{r_0}\left[\log_2\left(\frac{G}{(r_0^2+h^2)^{m+3}}\right)\right]}{\mathbb{E}_{r_0,\hat{\theta}}\left[\frac{(h^2+r_0^2\sin^2\hat{\theta})^2}{(h^2+r_0^2)^3}\right]}, \\ C_2 &= \mathbb{E}_{r_0}\left[\log_2\left(\frac{G}{(r_0^2+h^2)^{m+3}}\right)\right]. \end{aligned} \tag{3.27}$$

Proof: See Appendix B.

As can be seen from (3.26), the optimum update interval depends on both physical and MAC layer parameters. Among them, the UE velocity affects the update interval more than others. Let's fix the other parameters, then $\widetilde{t}_{\mathrm{u,opt}} = C_{\mathrm{const}}/v^{\frac{2}{3}}$, where $C_{\mathrm{const}} = \left(\frac{\frac{3\ln(2)}{2(m+3)} w_{\mathrm{u}} t_{\mathrm{fb}} \widetilde{\mathcal{T}}_{\mathrm{u}} B_{\mathrm{u},n} C_1}{w_{\mathrm{d}} R_{\mathrm{req}} + C_2 w_{\mathrm{u}} \widetilde{\mathcal{T}}_{\mathrm{u}} B_{\mathrm{u},n}}\right)^{\frac{1}{3}}$.

3.5 Results and Comparison of Limited-Feedback Schemes

In order to compare the downlink performance of FF, one-bit feedback and LCF, Monte-Carlo simulations are executed. The simulation tests are carried out 10^3 times per various number of UEs, and with the parameters given in Table 3.2. In each run, the UEs' locations are chosen uniformly random in the room. Once they settle in the new locations, they update the AP about their subcarrier SINR as explained. Then, the AP, reschedules the resources based on (3.1). The request data rate of all UEs are assumed to be the same. Figure 3.6 illustrates the average downlink throughput versus the different number of UEs for LCF, FF and one-bit feedback schemes. As can be seen from the results, the performance of the LCF is better than the one-bit

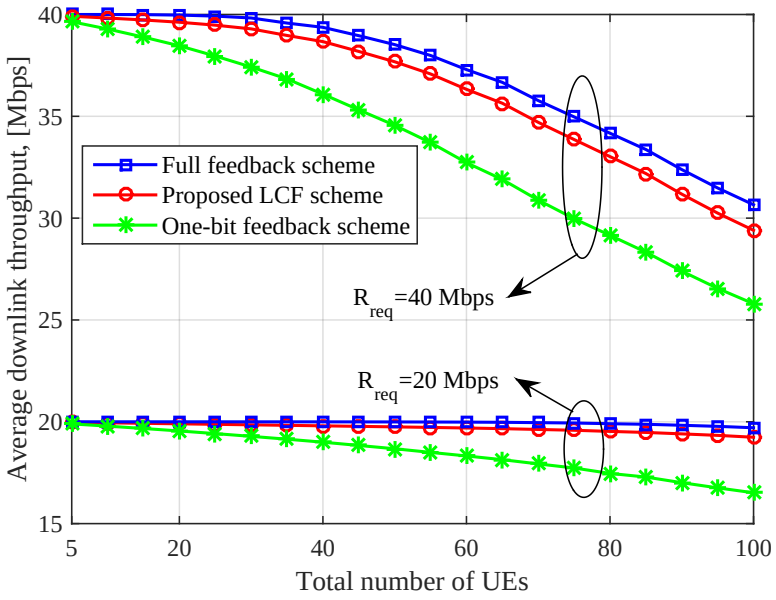

Figure 3.6: *Average downlink throughput for different feedback schemes (average request data rate: 20 Mbps and 40 Mbps).*

feedback scheme and the gap between LCF and FF schemes is less than 1 Mbps. As the number of UEs increases, the gap between the considered feedback schemes increases. However, the LCF follows the FF fairly well, especially for a low data request rate. Moreover, compared to the one-bit feedback technique, the LCF scheme occupies a smaller portion of the uplink bandwidth.

We study the effect of the UE's velocity and transmitted downlink optical power on the update interval as illustrated in figure 3.7. Analytical and Monte-Carlo simulations are presented for $w_{\mathrm{u}} = w_{\mathrm{d}}$, $N_{\mathrm{UE}} = 5$ and with the downlink and uplink simulation parameters given in Table 3.1, Table 3.2 and Table 3.3. For a fixed t_{u}, Monte-Carlo simulations are accomplished 10^4 times, where in each run, the UE's initial position and destinations are randomly chosen. Then, for the considered t_{u}, the expected sum-throughput, $\overline{\mathcal{T}}$, can be obtained by averaging out over 10^4 runs. Afterwards, Monte-Carlo simulations are repeated for different t_{u} varying in the range $0 < t_{\mathrm{u}} < 2r_{\mathrm{c}}/v$. The optimal update interval corresponds to the maximum sum-throughput. The effect of the UE's velocity on the optimal update interval for $R_{\mathrm{req}} = 5$ Mbps and $R_{\mathrm{req}} = 20$ Mbps is shown in figure 3.7-(a). Here, we can see that the optimal update interval decreases rapidly as the UE's speed increases, according to $v^{-2/3}$. Furthermore, Monte-Carlo simulations

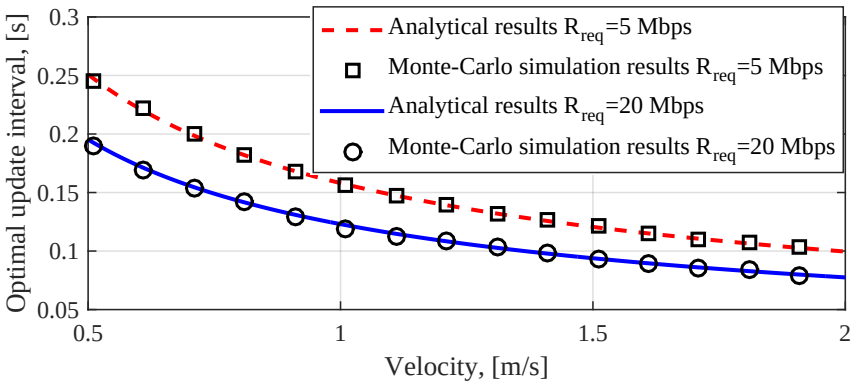

(a) The effect of UE's velocity on the optimal update interval with $P_{\mathrm{d,opt}} = 8$ W.

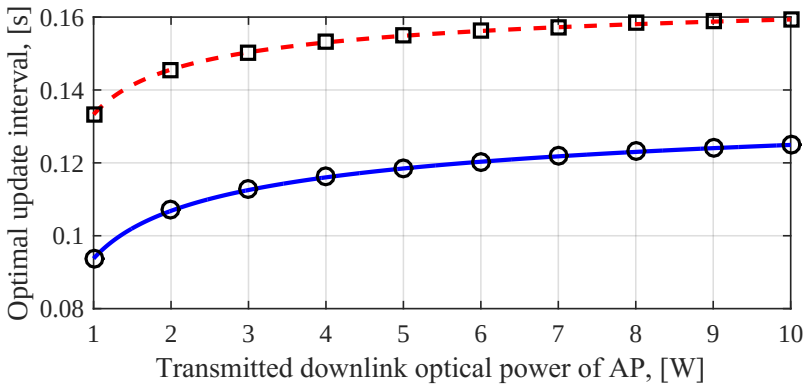

(b) The effect of transmitted downlink optical power on the optimal update interval ($v = 1$ m/s).

Figure 3.7: *The effects of UE's velocity and downlink optical power on optimal update interval for* $R_{\mathrm{req}} = 5$ *Mbps and* $R_{\mathrm{req}} = 20$ *Mbps, and* $N_{\mathrm{UE}} = 5$.

confirm the accuracy of the analytical results provided in (3.26). Figure 3.7-(b) illustrates the saturated effect of transmitted optical power on $\widetilde{t}_{\mathrm{u,opt}}$. As can be observed, the variation of the optimal update interval due to alterations of $P_{\mathrm{d,opt}}$ is less than 30 ms. From both figure 3.7-(a) and figure 3.7-(b), it can be deduced the lower R_{req}, the higher $\widetilde{t}_{\mathrm{u,opt}}$.

Now, let's consider an overloaded multiuser scenario with N_{UE} users. The fair scheduler introduced in (3.1) tries to equalize the rate of all UEs. For a high number of subcarriers, the UEs achieve approximately the same data rate. Accordingly, the average achieved data rate of UEs in an overloaded network for a high number of subcarriers would nearly be λR_{req}, where $0 < \lambda < 1$. This system is equivalent to a non-overloaded multiuser system where all UEs have

Parameter	Symbol	Value
Transmitted uplink optical power	$P_{\mathrm{u,opt}}$	0.2 W
Uplink FR bandwidth	$B_{\mathrm{u},n}$	5 MHz
Feedback time	t_{fb}	0.8 ms

Table 3.3: *Uplink simulation parameters.*

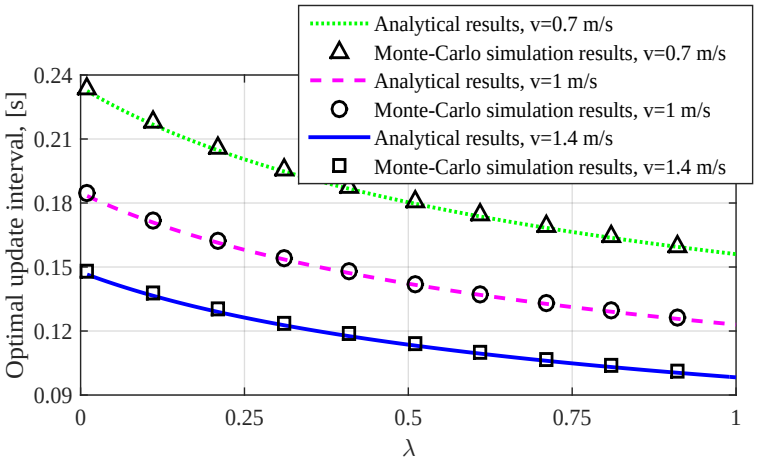

Figure 3.8: *Optimal update interval versus overload parameter, λ, for different UE's velocity* ($N_{\mathrm{UE}} = 5$).

achieved an average data rate of λR_{req}. Then, the approximate optimal update interval that results in near-maximum sum-throughput is given as:

$$\widetilde{t}_{\mathrm{u,opt}} \cong \left(\frac{\frac{3\ln(2)}{2(m+3)} w_{\mathrm{u}} t_{\mathrm{fb}} \widetilde{\mathcal{T}}_{\mathrm{u}} B_{\mathrm{u},n} C_1}{w_{\mathrm{d}} v^2 N_{\mathrm{UE}} \lambda R_{\mathrm{req}} + C_2 w_{\mathrm{u}} v^2 \widetilde{\mathcal{T}}_{\mathrm{u}} B_{\mathrm{u},n}} \right)^{\frac{1}{3}}. \tag{3.28}$$

Analytical and Monte-Carlo simulations of an overloaded system are shown in figure 3.8. Three speed values are chosen around the average human walking speed which is 1.4 m/s [26]. Note that to obtain an overloaded system either the number of UEs or their request data rate can be increased. In the results shown in figure 3.8, we fixed the number of UEs to $N_{\mathrm{UE}} = 5$ and increase their R_{req}. As can be inferred from these results, as the network becomes more overloaded, the optimal update interval should be increased. The reason for this is that updating the AP frequently is useless and it wastes the uplink resources due to lack of enough resources in an overloaded network.

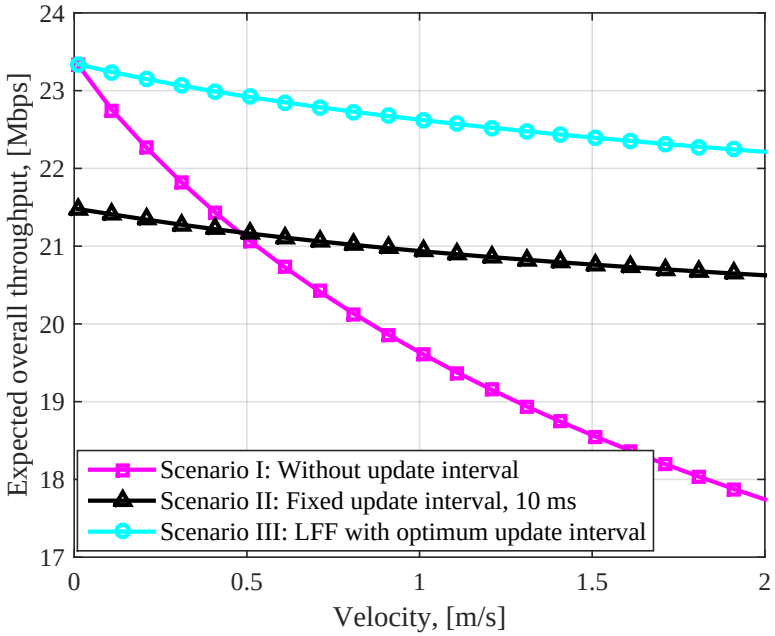

Figure 3.9: *Expected overall throughput versus UE's velocity for three scenarios; and* $R_{\mathrm{req}} = 20$ *Mbps,* $w_{\mathrm{u}} = w_{\mathrm{d}} = 1$.

To verify the significance of update interval in practical systems, three scenarios have been considered. Scenario I: a system without any update interval; Scenario II: a system with the conventional fixed update interval but without looking at the UE's velocity; Scenario III: a system with the proposed update interval and adjustable with the UE's velocity. For these scenarios, Monte-Carlo simulation results of the expected sum-throughput versus different UE's velocity have been obtained and presented in figure 3.9. In scenario I, the UEs only update the AP once at the start of the connection by transmission of the SINR information of $\mathcal{K}/2 - 1$ subcarriers. For scenario II, the fixed update interval is considered to be $t_{\mathrm{u}} = 10$ ms and independent of UE's velocity. A fixed update interval is currently used in LTE systems with $t_{\mathrm{u}} = 10$ ms by transmission of one-bit feedback information at the beginning of every frame [112]. It is worth mentioning that for practical wireless systems, it is common to transmit feedback frequently, e.g., at the beginning of each frame regardless of the UE channel variation and its velocity. As can be seen from the results, the proposed LFF scheme outperforms the conventional method with a fixed update interval. For low speeds (up to 0.5 m/s), the conventional fixed update interval even falls behind the system without any update interval. This is due to redundant feedback

Scheme	Overhead
Full feedback	$\mathscr{B}(\mathcal{K}/2-1)$ bpf
One-bit feedback	$(\mathcal{K}/2-1)$ bpf
Proposed LCF	$\mathscr{B}$ bpf
Proposed LFF	$\mathscr{B}(\mathcal{K}/2-1)/M$ bpf

Table 3.4: *Comparison of feedback schemes in terms of overhead.*

information being sent to the AP. The gap between LFF and scenario II with a fixed update interval is due to both higher uplink and downlink throughput of LFF. LFF provides higher uplink throughput thanks to the transmission of lower feedback compared to the fixed update interval scheme. Also, in scenario II, the UEs after 10 ms update the AP with one bit per subcarrier, and the AP does not know the SINR value of each subcarrier to allocate them efficiently to the UEs.

A comparison between the FF, one-bit feedback, LCF and LFF schemes in case of transmitted overhead is given in Table 3.4. It is assumed that the SINR on each subcarrier can be fed back to the AP using $\mathscr{B}$ bits, and $M = [\widetilde{t}_{\mathrm{u,opt}}/t_{\mathrm{fr}}]$. Note that for $M \geq (\mathscr{B}+1)$, the overhead per frame of the LFF scheme is lower than the one-bit feedback technique. Also, for $M \geq \mathcal{K}/2$, LFF scheme produces lower overhead per frame in comparison to LCF. For $N_{\mathrm{UE}} = 5$, $\mathscr{B} = 10$, $t_{\mathrm{fr}} = 1.6$ ms and $R_{\mathrm{req}} = 5$ Mbps the overhead per frame versus different numbers of subcarriers are illustrated in figure 3.10. The rest of the parameters are the same as those given in Table 3.1, Table 3.2 and Table 3.3. As can be observed from figure 3.10, the FF scheme generates a huge amount of feedback overhead especially for a high number of subcarriers. The practical one-bit feedback reduces the overhead by a factor of $\mathscr{B}$. As can be seen, the LCF always falls below the one-bit feedback method. The gap between the LCF and one-bit feedback becomes remarkable for higher numbers of subcarriers. The overhead results of the LFF have been also presented for a stationary UE and a UE with low and normal speeds. Clearly, the LFF generates the lower feedback overhead per frame as the UE's velocity tends to zero. The expected sum-throughput of different feedback schemes with the same parameters as mentioned above are summarized in Table. 3.5. As we expected, the LFF outperforms the other schemes when the UEs are stationary. However, the sum-throughput of the LCF method is higher for mobile UEs.

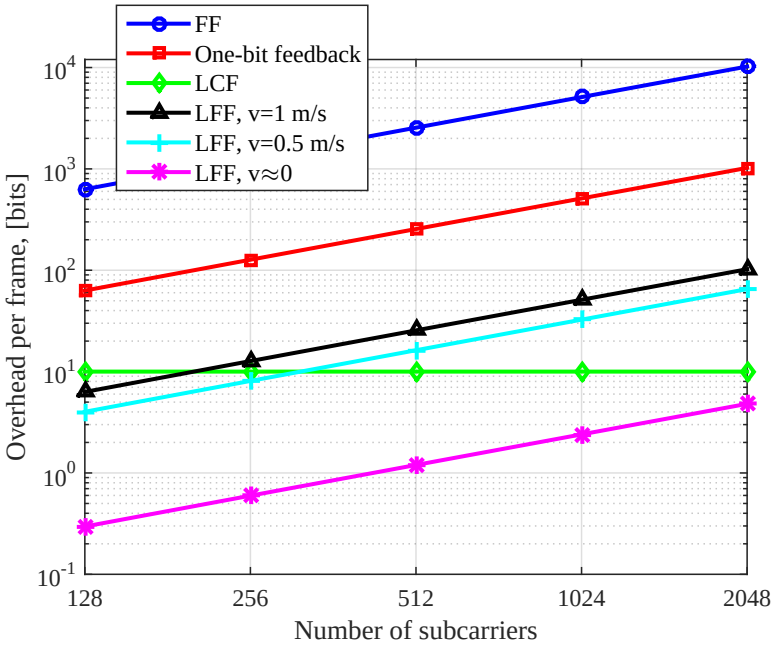

Figure 3.10: *Transmitted overhead versus different number of subcarriers.*

Scheme	Expected sum-throughput ($v = 0$ m/s)	Expected sum-throughput ($v = 1$ m/s)
Full feedback	6.67 Mbps	6.67 Mbps
One-bit feedback	7.64 Mbps	7.47 Mbps
Proposed LCF	8.33 Mbps	8.33 Mbps
Proposed LFF	8.35 Mbps	8.08 Mbps

Table 3.5: *Comparison of feedback schemes in case of expected sum-throughput,* $N_{\mathrm{UE}} = 5$, $R_{\mathrm{req}} = 5$ *Mbps and* $w_{\mathrm{u}} = w_{\mathrm{d}} = 1$.

3.6 Summary

In this chapter, two methods for reducing the feedback cost were proposed: i) the LCF scheme, and ii) the LFF method. The former is based on reducing the content of feedback information by only sending the SINR of the first subcarrier and estimating the SINR of other subcarriers at the AP. The latter is based on the less frequent transmission of feedback information. The optimal update interval was derived, which results in the maximum expected sum-throughput of uplink and downlink. The Monte-Carlo simulations confirmed the accuracy of the analytical results. The effect of different parameters on the optimum update interval was studied. It was

also shown that the proposed LCF and LFF schemes provide an improvement of 0.86 and 0.61 Mbps, respectively, sum-throughput for mobile users with average speed of $v = 1$ m/s compared to the practical one-bit feedback method. Furthermore, both LCF and LFF while transmit a lower amount of feedback in comparison to the one-bit feedback technique. Therefore, both LCF and LFF schemes can be used to support mobility and seamless connectivity in a LiFi cellular network.

Chapter 4

Modeling the Random Orientation of Mobile Devices: Measurement and Analysis

4.1 Introduction

Device orientation is an important factor that can affect the system performance significantly. The knowledge of device orientation statistics at the AP can help to improve system performance such as user throughput. The device orientation information can be fed back through limited-feedback mechanism discussed in the previous chapter. In LiFi systems, smartphones are more prone to device random device orientation and requires a deep analysis.

Smartphones are the most significant and indispensable part of the wireless network generating about 86% of mobile data traffic [1]. LiFi as part of the future 5G can handle this immense data traffic thanks to future LiFi-enabled smartphones. Hence, an analysis of device orientation is required for purposes of resource allocation and handover management. Generally, users tend to work with their smartphones in a comfortable manner which is not necessarily vertically upward. Smartphones are equipped with a gyroscope that can measure the device orientation. This orientation information can be fed back to the AP via limited-feedback methods described in the previous chapter [4, 30, 31]. Then, the AP can use the orientation information for resource allocation and handover management purposes. Many previous studies in LiFi networks assumed that the receiver is vertically upward and fixed for simplicity purposes and also due to the lack of a proper model for device orientation. However, there are few studies that have considered the effect of device orientation in their analysis [13–25, 113, 114]. Nevertheless, none of these studies have considered the actual statistics of device orientation and have mainly assumed a uniform or Gaussian distribution with hypothetical moments for device orientation. In this chapter,

based on experimental measurements from forty participants, a new statistical model for device orientation has been proposed.

In [13], the authors consider three standard angles similar to those used in mobile devices to model the device orientation; namely yaw, pitch and roll. Based on this model, the effect of arbitrary orientation on users' throughput and network load balancing is investigated. The problem of handover due to device rotation for downlink in an indoor optical attocell network was first proposed in [14]. The handover probability has been obtained for both sitting and mobile users while considering device orientation. In [15], the handover probability in hybrid LiFi/RF-based networks is evaluated assuming randomly-oriented devices. The impact of the receiver's tilted angle on the channel capacity of VLC is investigated in [16]. The lower and upper bounds of the channel capacity for the VLC are presented and by considering an optimization problem the channel capacity has been improved by tilting the receiver plane properly. In [17], a theoretical expression of the BER for input-dependent noise of VLC using on-off keying has been derived. Then, a convex optimization problem is formulated based on the derived BER expression to minimize the BER performance by tilting the receiver plane. The impact of device orientation on BER performance of DCO-OFDM and OOK modulation has been evaluated in [18] and [32], respectively. A closed form approximation for BER of randomly-orientated UEs is derived. In [19, 115], the effect of random orientation on BER performance of spatial modulation is evaluated for both stationary and mobile users.

The effect of device orientation on positioning has been investigated in several studies [20–23]. By using the accelerometer sensor, the positioning technique proposed in [20] can be used for any arbitrary device orientation. Downlink and uplink indoor positioning techniques based on VLC while considering the tilting of the device have been developed in [21] and [22], respectively. It is shown that the tilting angle can affect the positioning error significantly. Therefore, device orientation should be considered in the positioning analysis [23]. The SNR and spectral efficiency improvement of OFDM signals for indoor LiFi systems by optimally tilting the receiver plane is proposed in [24]. In [25], the effect of random orientation on the LOS channel gain for a randomly located UE has been investigated. The statistical distribution of the channel gain has been derived for a single LED and extended to a scenario with double LEDs. The effect of device orientation has been studied on sojourn time of LiFi systems in [113]. The SNR

statistics of mobile users with random orientations in an indoor LiFi system, where the mobility of users are modeled based on RWP, are derived in [114]. We note that none of these studies are supported by any experimental data. A measurement of the random orientations of mobile devices has been made in [116], but the authors only measure the statistics of the pace of change of the device orientation. Their results, therefore, do not describe the statistical model of the randomly-oriented devices in general. Our recent works in [10, 68] report some initial results based on the experimental data from 40 participants. The effect of randomly-oriented devices has been studied and a statistical model of the LiFi channel considering the random orientation is proposed. In the following, further detail about experimental measurements as well as device orientation analysis are provided.

The rest of the chapter is organized as follows. In section 4.2, an experimental setup is explained and based on that the statistics of mobile device orientation have been obtained. In section 4.3, an analysis of random orientation effect on channel gain is discussed. The statistics of channel gain is then obtained in section 4.4 and the analysis of device orientation impact on channel gain is presented in section 4.5. The effect of device orientation on error performance is evaluated in section 4.6. Finally, a summary of this chapter is presented in section 4.7.

4.2 Mobile Device Orientation Statistics

An experiment is designed to study mobile users behavior and to develop a statistical model for the orientation of mobile devices that act as the receiver for wireless communication systems. During the experiment, 40 participants were asked to use their cellphones normally, which created 222 datasets for orientation. They were asked to use the cellphone in both portrait and landscape modes for one minute. In the portrait mode, the users were asked to do activities such as texting and browsing while in the portrait mode they were asked to watch a short video of length 1 minute. We asked them to work in portrait and landscape mode for two times. It is noted that both sitting and walking activities were recorded in an indoor environment. The orientation data is measured for both sitting and mobile users. In the experimental measurement, the application Physics Toolbox Sensor Suite has been used as it can provide instantaneous rotation angles, α, β and γ [117]. This application can run in the background while the participants

can perform activities that require data connection, e.g., browsing or watching streaming videos. This application can sample data with a resolution of 1 millisecond. Below is a summary of the experimental setup:

- Activities while sitting:
  1. Browsing twice in portrait mode,
  2. Watching streaming videos twice in landscape mode,
- Activities while walking following a certain path:
  1. Browsing in portrait mode,
  2. Watching streaming videos in landscape mode.

The path that the participants took was in a straight corridor with dimensions of 40 m $\times 1.5$ m. The participants were asked to walk down the corridor once. We note that the shape of the test area should not affect the experimental results and the model for the elevation angle since it mostly depends on the posture and physical attributes of typical users rather than the environment. This has been confirmed with sets of uncontrolled data collections from participants using their device in different environments [11].

Measurement and Analysis

The statistics of the azimuth and polar angles can be measured based on the collected experimental data set. In order to evaluate the similarity of measurement data with a particular distribution, we consider KSD, skewness and kurtosis. The two-sample KSD is the maximum absolute distance between the cumulative distribution functions (CDFs) of two data vectors, which can be obtained as [118]:

$$D = \max_{x} \left(\left| \hat{F}_1(x) - \hat{F}_2(x) \right| \right), \tag{4.1}$$

where $\hat{F}_1(x)$ and $\hat{F}_2(x)$ are the CDFs of the first and second data vectors, respectively. Smaller values of KSD correspond to more similarity of the distributions. Skewness is another metric to evaluate the similarity of two distributions. It is described as a measure of the symmetry

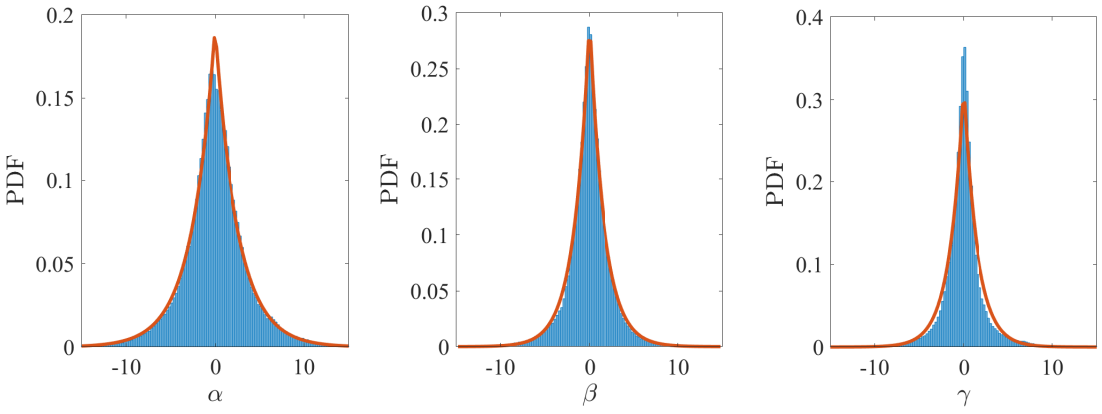

(a) Yaw **(b)** Pitch **(c)** Roll

Figure 4.1: *Histograms of orientation angles α, β, and γ for sitting activities obtained from experimental measurements.*

or asymmetry of a probability distribution. A perfectly symmetrical distribution will have a skewness of 0. For example, the Gaussian and Laplace distributions both have a skewness of 0. Mathematically, the skewness of a random variable (RV) X is defined as [119]:

$$\text{Skew}[X] = \frac{\mathbb{E}\left[(x - \mu_{\text{x}})^3\right]}{\sigma_{\text{x}}^3}, \tag{4.2}$$

where μ_{x} and σ_{x}^2 are the mean and variance of the distribution X. The other metric that we considered is Kurtosis, which is a measure of the tailedness of a probability distribution. It is given as:

$$\text{Kurt}[X] = \frac{\mathbb{E}\left[(x - \mu_{\text{x}})^4\right]}{\sigma_{\text{x}}^4}. \tag{4.3}$$

The kurtosis of Laplace, Gaussian and Uniform distributions are 6, 3 and 1.8, respectively.

The histograms for angles α, β, and γ, obtained from experimental measurements, along with the Laplace and Gaussian fitted distributions are shown in Figs. 4.1 and 4.2, respectively for sitting and walking activities. It can be seen that the distributions are well fitted with a Laplace distribution for sitting activities while histograms are more close to a Gaussian distribution for walking activities. The mean and variance for each case is noted in Table 4.1. The statistics given in Table 4.1 can be used to model the random device orientation. The parameter Ω shows the user direction as explained in 2.9.2.

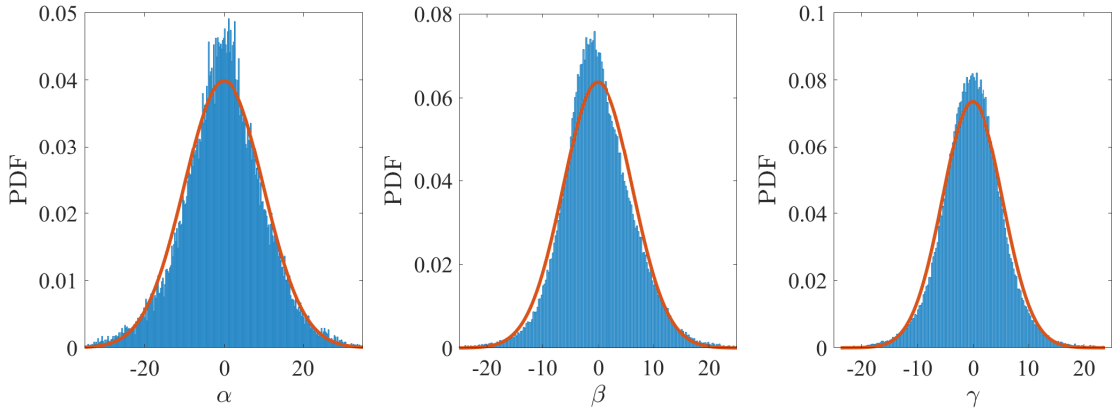

(a) Yaw **(b)** Pitch **(c)** Roll

Figure 4.2: *Histograms of orientation angles α, β, and γ for walking activities obtained from experimental measurements.*

For these angles, α, β and γ, we model them with Laplace and Gaussian distributions taking into account the first and second laws of error. According to the first law of error proposed by Laplace in 1774, the frequency of an error can be represented as an exponential function of the numerical magnitude of the error, regardless of the sign as $f_X(x) = \frac{k_c}{2} e^{-k_c|x-x_q|}$, where x and x_q are the measured data and actual value, respectively and k_c is a constant [120]. The second law of error was also proposed by Laplace four years later and it states that the frequency of error is an exponential function of the square of the error, that is, $f_X(x) = \frac{1}{\sqrt{2\pi}\sigma_x} e^{-\frac{(x-x_q)^2}{2\sigma_x^2}}$ with σ_x^2 as the variance of measured data. This is also called the normal distribution or Gauss law of error [120].

The PDF of α, β and γ, are estimated based on a set of almost uncorrelated data samples taken from the measurement data. Since the acquired data from the application are unevenly-spaced in time, we first generate a set of sufficiently separated data in time to ensure that samples taken from an individual user are almost uncorrelated. To define the proper separation between uncorrelated samples, we need to calculate the coherence lag between the samples that can be acquired by the autocorrelation function (ACF). However, due to the uneven distribution of samples in time, the classical Fourier analysis is no longer valid. In fact, interpolation can be used to generate evenly spaced data samples but this would affect the autocorrelation by removing higher frequencies [121, 122]. Another solution would be to use least-squares spectral

	Sitting			Walking		
	α	β	γ	α	β	γ
Mean	Ω-90	40.78	-0.84	Ω-90	28.81	-1.35
Standard deviation	3.67	2.39	2.21	10	3.26	5.42
Kurtosis	6.12	7.97	11.82	3.47	3.84	4.06
Gaussian KSD	0.07	0.09	0.13	0.02	0.03	0.02
Laplace KSD	0.01	0.01	0.04	0.04	0.06	0.05
Coherence Time	0.342	0.377	0.331	0.131	0.176	0.142

Table 4.1: *Statistics of orientation measurement.*

analysis (LSSA) [123, 124]. Based on the LSSA method, we first calculate the power spectral density (PSD) of the unevenly spaced samples and then, the ACF can be estimated by calculating the inverse Fourier transform of the PSD. This technique has been explained in detail in our recent paper [125]. The results show that the coherence time of the elevation angle is in the order of few hundred milliseconds. This is in accordance with the results presented in Table 4.1.

Note that using (2.33), the orientation of device can be expressed in the spherical coordinate system based on polar angle, θ and azimuth angle, ω. Therefore, we can have tractable analysis of device orientation. The sample PDF of the azimuth angle for sitting and walking activities are represented in figure 4.3-(a) and figure 4.3-(b), respectively. As can be seen, the azimuth angle closely follows a uniform distribution, i.e., $\omega \sim \mathcal{U}[-\pi, \pi)$, with the skewness of -0.03, kurtosis of 1.68 and KSD of 0.034 for sitting activities. Also it is shown that walking activities have a skewness of -0.0045, kurtosis of 1.85 and KSD of 0.019. Note that the peaks in the PDFs (more visible for sitting) are due to the limited number of users, therefore, the azimuth angle is correlated for each sitting user along with the direction of the chair they used.

The histogram of θ is shown in figure 4.3-(c) for sitting activities and in figure 4.3-(d) for walking activities. The KSD is used to measure the distance between the Gaussian or Laplace distributions and the collection of datasets. The skewness and kurtosis of the collection of datasets are also calculated. These values are given in Table 4.2. From this table, the kurtosis of the polar angle, θ, for sitting activities is 6.36 which is closer to the kurtosis of the Laplace distribution than the Gaussian distribution, whereas for walking activities the kurtosis of empirical data is 3.77 which confirms a greater similarity to the Gaussian distribution compared to the Laplace distribution. Hence, for sitting activities, the Laplace distribution closely matches the distri-

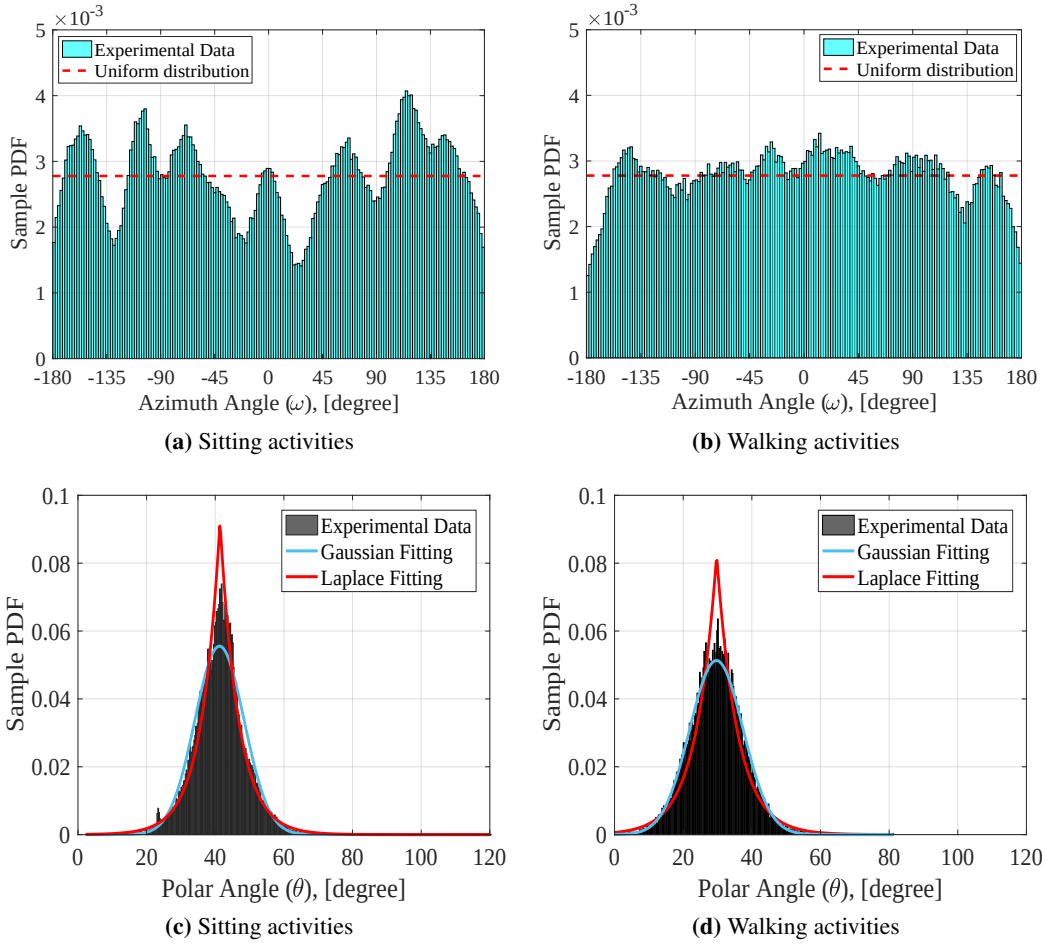

(a) Sitting activities

(b) Walking activities

(c) Sitting activities

(d) Walking activities

Figure 4.3: *Samples PDFs of azimuth and polar angles with their distribution fitting.*

bution of the experimental measurements in comparison with the Gaussian distribution when considering both KSD and kurtosis metrics. For walking activities, however, the Gaussian distribution matches the experimental data more closely. The reason for this is because when the users are static, they tend to put their hands on the desk and keep the smartphone with almost a fixed orientation. Hence, some variations around a high peak in the pdf are expected. While if they are mobile and working with their smartphone, the peak is expected to be lower with more variations around it. In the following, we mainly focus on the sitting activities and therefore the derivations are based on the Laplace distribution for the polar angle. However, one can readily apply a similar methodology to obtain the analytical results for the Gaussian distribution. The other important observation here is in regards to the moments of the measured data. The mean

	Polar Angle (θ) [degree]							
	Empirical Data		The Gaussian Fitting			The Laplacian Fitting		
	Skewness	Kurtosis	μ_{G}	σ_{G}	KSD	μ_{L}	σ_{L}	KSD
Sitting	0.21	6.36	41.23	7.18	0.04	41.39	7.68	0.04
Walking	0.13	3.77	29.67	7.78	0.02	29.74	8.59	0.05

Table 4.2: *Statistical model of the orientation of mobile devices.*

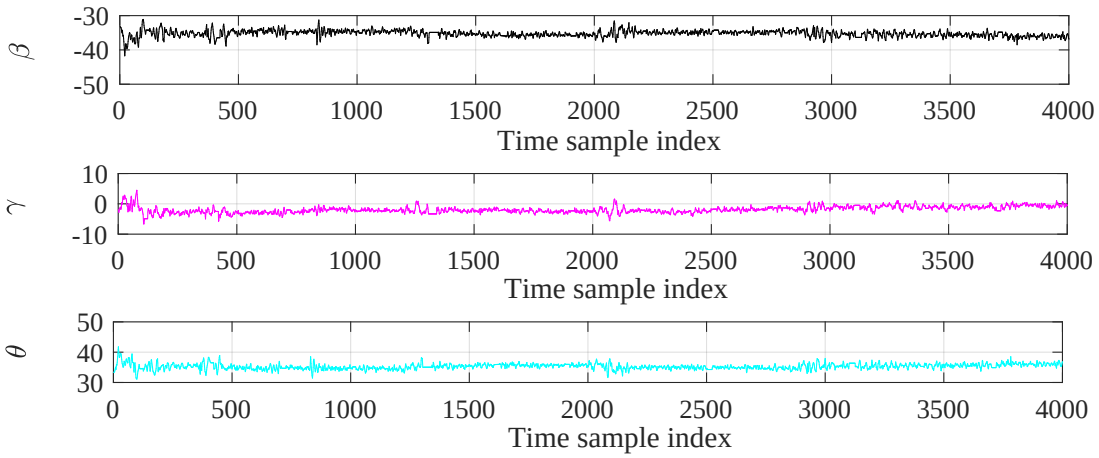

Figure 4.4: *Representation of one ensemble of the stochastic RPs, β, γ and θ for three UE locations at $(-2,-2)$, $(3,3)$ and $(0,0)$. Here, $\Omega = \frac{\pi}{4}$ and the sampling time is $T_{\mathrm{s}} = 13$ ms.*

of the sitting and walking activities are about 41° and 30°, respectively and both with a standard deviation of less than 9°.

Figure 4.4 illustrates one ensemble of the stochastic processes β, γ and θ. As can be seen, the pitch angle, β, varies around the mean value of $\mathbb{E}[\beta] = -35.81^\circ$ and the roll angle, γ, fluctuates around its mean value which is zero. This means that the user tends to hold their cellphone with a pitch angle of -35.81° and a roll angle of zero. However, due to the random nature of users behavior, fluctuations are observed in pitch, roll and consequently in polar angles. The variations in the pitch and roll angles also affect the LOS channel gain.

To characterize the temporal behavior of the random device orientation as a random process, the coherence time of the channel needs to be known. Autocorrelation is one common way to calculate the coherence time of a stochastic random process. Denoting the autocorrelation of θ

as $\mathcal{R}_\theta(t)$, the coherence time of the polar angle stochastic process denoted by $T_{\mathrm{c},\theta}$ represents the time it takes for the random process to become uncorrelated with its initial value and can be defined as $\mathcal{R}_\theta(T_{\mathrm{c},\theta}) = 0.05\mathcal{R}_\theta(0) = 0.05$ [126]. Our experimental results show that the coherence time of the angle θ is in the order of a few hundreds of milliseconds [125]. However, the coherence time of the LOS channel gain highly depends on the UE's location and direction (determined by the angle Ω), which is in the order of a few tens of milliseconds. Accordingly, the effect of random orientation may be modeled as a slow large-scale fading effect as the coherence time of the channel variation due to random orientation, $T_{\mathrm{c,H}}$, is very large compared to the typical symbol period in LiFi. This implies that the channel gain can be presumed as roughly constant over a large number of transmitted symbols [126].

Based on the experimental results, the PDF of $f_\theta(\theta)$ can be properly fitted with the truncated Laplace distribution. Mathematically, $\theta \in [0, \pi]$, however, as shown by the experimental measurements, the samples of the angle θ are restricted to the range $[0, \frac{\pi}{2}]$. Therefore, the PDF of θ can be conveniently denoted as:

$$f_\theta(\theta) = \frac{\exp\left(-\frac{|\theta-\mu_\theta|}{b_\theta}\right)}{2b_\theta\left(G(\frac{\pi}{2}) - G(0)\right)}, \quad 0 \le \theta \le \frac{\pi}{2}, \tag{4.4}$$

where $b_\theta = \sqrt{\sigma_{\mathrm{L}}^2/2} > 0$. The mean and scale parameters are set to the values from Table 4.2. That is, $\mu_\theta = \mu_{\mathrm{L}}$ and $b_\theta = b_{\mathrm{L}}$. Furthermore, $G(0) = \frac{1}{2}\exp\left(\frac{-\mu_\theta}{b_\theta}\right)$ and $G(\frac{\pi}{2}) = 1 - \frac{1}{2}\exp\left(-\frac{\frac{\pi}{2}-\mu_\theta}{b_\theta}\right)$. Note that with the parameters for μ_θ and b_θ given in Table 4.2, we have $G(\frac{\pi}{2}) \approx 1$ and $G(0) \approx 0$. Thus, (4.4) can be simplified as:

$$\tilde{f}_\theta(\theta) \cong \frac{\exp\left(-\frac{|\theta-\mu_\theta|}{b_\theta}\right)}{2b_\theta}, \quad 0 \le \theta \le \frac{\pi}{2}, \tag{4.5}$$

where $\int_0^{\frac{\pi}{2}} \tilde{f}_\theta(\theta)\,\mathrm{d}\theta \approx 1$. The CDF of θ is also given as:

$$\tilde{F}_\theta(\theta) \cong \begin{cases} \frac{1}{2}\exp\left(\frac{\theta-\mu_\theta}{b_\theta}\right), & \theta < \mu_\theta \\ 1 - \frac{1}{2}\exp\left(-\frac{\theta-\mu_\theta}{b_\theta}\right), & \theta \ge \mu_\theta \end{cases}. \tag{4.6}$$

4.3 Analysis of Random Orientation Effect on Channel Gain

The downlink geometry of a LOS link in an indoor LiFi system is shown in figure 2.3. Let's denote the locations of a UE and an AP position by the vectors $(x_{\mathrm{u}}, y_{\mathrm{u}}, z_{\mathrm{u}})$ and $(x_{\mathrm{a}}, y_{\mathrm{a}}, z_{\mathrm{a}})$, respectively. From figure 2.3 and the LOS DC gain given in (2.7), it is clear that for a particular UE position, the statistics of the LOS highly depend on the device orientation. In order to develop the statistics of the LOS channel gain, the statistics of $\cos\psi$ should first be determined based on the statistics of the device orientation discussed in section 4.2. We note that the radiance angle, ϕ, is not affected by the random orientation and we always have $\cos\phi = -\mathbf{n}_{\mathrm{t}} \cdot \mathbf{d}/\|\mathbf{d}\|$. It should be mentioned that in this section, we focus on the effect of UE's random orientation in our analyses and do not consider the possible movements in the user's hands that may change the distance d. Note that such random changes in the distance would be small compared to the average distance between the AP and the UE. Furthermore, if an analysis of the random movement of the UE is of interest, our results can be readily used as the conditional statistics of the channel gain for a given location of the UE to develop the joint statistics assuming that the statistics of the random movement is available. This is similar to how we analyze the effect of random orientation in a mobile scenario in section 5.2.5 where the random movement is modeled based on the random waypoint model.

4.3.1 The PDF of $\cos\psi$

Throughout this chapter, we calculate the PDF of $\cos\psi$ conditioned on ω. Let the vector $\mathbf{d}$ be the distance vector from the UE to the AP. Noting that the vector $\mathbf{n}'_{\mathrm{u}}$ given in (2.31), denotes the normal vector of the UE receiver after rotation, the cosine of the incidence angle, ψ, can be obtained as:

$$\cos\psi = \frac{\mathbf{n}'_{\mathrm{u}} \cdot \mathbf{d}}{d} = \left(\frac{x_{\mathrm{a}} - x_{\mathrm{u}}}{d}\right)\sin\theta\cos\omega + \left(\frac{y_{\mathrm{a}} - y_{\mathrm{u}}}{d}\right)\sin\theta\sin\omega + \left(\frac{z_{\mathrm{a}} - z_{\mathrm{u}}}{d}\right)\cos\theta, \tag{4.7}$$

where ω is given in (2.33) and depends on α, β and γ. According to the experimental data, the standard deviation of γ in portrait mode for sitting and walking activities is 0.072 and 0.113 radian, respectively. The standard deviation of β in landscape mode for sitting and walking ac-

tivities is 0.044 and 0.091 radian, respectively. These small values of standard deviation confirm that when a user is working with the cellphone in portrait mode, the roll angle, γ, is almost zero. Whereas, when the user works with the cellphone in landscape mode, the pitch angle, β, is close to zero. Hence, substituting $\gamma = 0$ in (2.33), it can be simplified as $\hat{\omega} = \tan^{-1}\left(\frac{-\cos\alpha}{\sin\alpha}\right)$. Therefore, for portrait mode, we have:

$$\hat{\omega} = \begin{cases} \alpha - \frac{\pi}{2} & \alpha \in (0, \frac{3\pi}{2}] \\ \alpha - \frac{5\pi}{2} & \alpha \in (\frac{3\pi}{2}, 2\pi] \end{cases} . \tag{4.8}$$

Similarly for landscape mode, we have:

$$\hat{\omega} = \begin{cases} \alpha & \alpha \in (0, \pi] \\ \alpha - 2\pi & \alpha \in (\pi, 2\pi] \end{cases} . \tag{4.9}$$

Comparing Ω given in (2.34) and (2.35), with the above equations for $\hat{\omega}$, one can easily deduce $\Omega = \hat{\omega} + \pi$. Note that, based on the measurements, the mean absolute error of approximating the angles ω as $\hat{\omega}$ is about 0.09 and 0.14 radian respectively for sitting and mobile users, which confirms a relatively good accuracy of the approximation. For the rest of this study, we consider the angle Ω in the equations since it has a better physical interpretation compared to the angles $\hat{\omega}$ or ω. As noted before, the angle Ω represents the angle of direction the user is facing and the X-axis of the Earth coordinate system. Therefore, (4.7) can be approximated as $\cos\psi \cong -\left(\frac{x_\mathrm{a}-x_\mathrm{u}}{d}\right)\sin\theta\cos\Omega - \left(\frac{y_\mathrm{a}-y_\mathrm{u}}{d}\right)\sin\theta\sin\Omega + \left(\frac{z_\mathrm{a}-z_\mathrm{u}}{d}\right)\cos\theta$. For simplicity of notation, this equation can be rewritten as:

$$g(\theta) \triangleq \cos\psi = \lambda_1 \sin\theta + \lambda_2 \cos\theta, \tag{4.10}$$

where

$$\begin{aligned} \lambda_1 &= -\left(\frac{x_\mathrm{a} - x_\mathrm{u}}{d}\right)\cos\Omega - \left(\frac{y_\mathrm{a} - y_\mathrm{u}}{d}\right)\sin\Omega, \\ \lambda_2 &= \left(\frac{z_\mathrm{a} - z_\mathrm{u}}{d}\right). \end{aligned} \tag{4.11}$$

The coefficients λ_1 and λ_2 play a prominent role in the analysis of $\cos\psi$ so it is worth investigating them in detail to help readers intuitively understand them. Throughout this study, the AP

is always located above the UE, i.e., $\lambda_2 > 0$. The coefficient λ_1 can be rewritten as:

$$\lambda_1 = \sqrt{\frac{(x_\mathrm{a} - x_\mathrm{u})^2 + (y_\mathrm{a} - y_\mathrm{u})^2}{d^2}} \cos\left(\Omega - \tan^{-1}\left(\frac{y_\mathrm{u} - y_\mathrm{a}}{x_\mathrm{u} - x_\mathrm{a}}\right)\right),$$

Fixing the AP location, the peak of the coefficient λ_1 only depends on the position of the UE. Meanwhile, the sign of the coefficient λ_1 is negative if the UE does not face the AP (opposite direction to the AP). For example, if the AP is located in the position $(0, 0, 2)$, and the UE is located in $(-1, 0, 0)$, then λ_1 will be negative if $\frac{-\pi}{2} < \Omega < \frac{\pi}{2}$. In addition, the coefficients λ_1 and λ_2 should satisfy the following inequalities:

$$-1 < \lambda_1 < 1,\ 0 < \lambda_2 \leq 1,\ \text{and}\ \lambda_2 \leq \sqrt{\lambda_1^2 + \lambda_2^2} \leq 1. \tag{4.12}$$

Based on the sign of λ_1, the term $\cos\psi$ may be a monotonically decreasing function of θ (**Case 1**) or it may be a concave downward function with one peak (**Case 2**). These two cases are explained next and the PDF of $\cos\psi$ is derived for each case. The detailed derivations are provided in Appendix C.

1) *For $\lambda_1 < 0$ (**Case 1**)*: If $\lambda_1 < 0$, $\lambda_2 > 0$ and $0 < \theta < \frac{\pi}{2}$, it can be seen from (4.10) that $\cos\psi$ is a monotonically decreasing function of θ. Using the fundamental theorem to calculate the PDF of a function of an RV given in [127], we get the PDF of $\cos\psi$ as:

$$f_{\cos\psi}(\tau) = \frac{f_\theta\left(-\sin^{-1}\left(\frac{\tau}{\sqrt{\lambda_1^2+\lambda_2^2}}\right) - \tan^{-1}\left(\frac{\lambda_2}{\lambda_1}\right)\right)}{\sqrt{\lambda_1^2 + \lambda_2^2 - \tau^2}},\ \lambda_1 < \tau < \lambda_2, \tag{4.13}$$

where τ denotes the realization of the RV $\cos\psi$. Let's define:

$$\mathrm{ss}_f \triangleq \sup \mathrm{supp}\left(f_{\cos\psi}\right) \tag{4.14}$$

as "sup supp" stands for supremum of the support of $f_{\cos\psi}$. This metric is presented to emphasize that ss_f is not always 1. For $\lambda_1 < 0$, $\mathrm{ss}_f = \lambda_2$ which is strictly less than 1.

2) *For $\lambda_1 \geq 0$ (**Case 2**)*: If $\lambda_1 \geq 0$, $\lambda_2 > 0$, and $0 < \theta < \frac{\pi}{2}$, (4.10) is a concave downward

function. Then, the maximum value of (4.10) is at the point θ^* given as follows:

$$\theta^* = \underset{0 < \theta < \frac{\pi}{2}}{\arg\max} \left(\lambda_1 \sin\theta + \lambda_2 \cos\theta\right) = \tan^{-1}\left(\frac{\lambda_1}{\lambda_2}\right). \tag{4.15}$$

For this case, the PDF of $\cos\psi$ has been derived in detain in Appendix C. Note that for $\lambda_1 \geq 0$, $\mathrm{ss}_f = \sqrt{\lambda_1^2 + \lambda_2^2} \leq 1$. It is worth noting that the PDF expressions given for the two cases do not particularly depend on whether θ is Laplace or Gaussian distributed so one can apply either of the distributions into these PDFs ((4.13) and (C.3) of Appendix C) and calculate the distribution of $\cos\psi$.

4.3.2 Approximate PDF of $\cos\psi$

In order to make the performance analysis of LiFi systems with random orientation tractable, one would be interested in approximating the closed-form PDF equations (4.13) and (C.3) of Appendix C with simpler expressions. In this section, we show that the truncated Laplace distribution can be used to approximate the PDF of cosine of the incidence angle, $f_{\cos\psi}$ for the sitting scenario. Assuming a walking scenario, an approximation of the exact PDF as a truncated Gaussian distribution can be made similarly.

Note that the non-zero mean random variable θ can be expressed as $\theta = \mu_\theta + \theta'$, where θ' follows a zero mean Laplace distribution with the same variance as θ. Substituting $\theta = \mu_\theta + \theta'$ in (4.10), and expanding the cosine and sine functions, we have:

$$\cos\psi = \lambda_1 \sin\theta' \cos\mu_\theta + \lambda_1 \sin\mu_\theta \cos\theta' + \lambda_2 \cos\theta' \cos\mu_\theta - \lambda_2 \sin\theta' \sin\mu_\theta. \tag{4.16}$$

Under the condition of a small variance for θ, and employing the first-order Taylor series approximation ($\sin\theta' \cong \theta'$ and $\cos\theta' \approx 1$), then, (4.16) can be approximated as:

$$\begin{aligned} \cos\psi &\cong \lambda_1 \theta' \cos\mu_\theta + \lambda_1 \sin\mu_\theta + \lambda_2 \cos\mu_\theta - \lambda_2 \theta' \sin\mu_\theta \\ &= \left(\lambda_1 \cos\mu_\theta - \lambda_2 \sin\mu_\theta\right)\theta' + \lambda_1 \sin\mu_\theta + \lambda_2 \cos\mu_\theta. \end{aligned} \tag{4.17}$$

Noting that $\cos\psi$ is a linear function of θ' and $\hat{\tau}_{\min} \leq \cos\psi \leq \hat{\tau}_{\max}$, the PDF of $\cos\psi$ can be

expressed based on the truncated Laplace distribution given as follows:

$$\tilde{f}_{\cos\psi}(\hat{\tau}) = \frac{f_{\theta'}(\hat{\tau})}{F_{\theta'}(\hat{\tau}_{\max}) - F_{\theta'}(\hat{\tau}_{\min})}, \quad \hat{\tau}_{\min} \leq \hat{\tau} \leq \hat{\tau}_{\max}, \tag{4.18}$$

where $\hat{\tau}_{\min} = -1$ and taking into account the supremum of the support of $f_{\cos\psi}$, then, $\hat{\tau}_{\max} = \lambda_2$ for $\lambda_1 < 0$ and $\hat{\tau}_{\max} = \sqrt{\lambda_1^2 + \lambda_2^2}$ for $\lambda_1 \geq 0$. In (4.18), θ' follows a Laplace distribution with the following parameters:

$$\hat{\mu}_\theta = \lambda_1 \sin\mu_\theta + \lambda_2 \cos\mu_\theta, \tag{4.19}$$

$$\hat{b}_\theta = b_\theta \left|\lambda_1 \cos\mu_\theta - \lambda_2 \sin\mu_\theta\right|. \tag{4.20}$$

Substituting $\hat{\tau}_{\min}$ and $\hat{\tau}_{\max}$ in (4.18), the truncated Laplace distribution of $\cos\psi$ conditioned on Ω is given as:

$$\tilde{f}_{\cos\psi}(\hat{\tau}) = \frac{1}{\Delta(\hat{\mu}_\theta, \hat{b}_\theta, \hat{\tau}_{\max})} \exp\left(-\frac{|\hat{\tau} - \hat{\mu}_\theta|}{\hat{b}_\theta}\right), \tag{4.21}$$

where $\Delta(\hat{\mu}_\theta, \hat{b}_\theta, \hat{\tau}_{\max}) = 2\hat{b}_\theta \left(1 - \frac{1}{2}\exp\left(\frac{\hat{\mu}_\theta - \hat{\tau}_{\max}}{\hat{b}_\theta}\right) - \frac{1}{2}\exp\left(\frac{-1-\hat{\mu}_\theta}{\hat{b}_\theta}\right)\right)$ and the support range of $\tilde{f}_{\cos\psi}$ is $-1 \leq \hat{\tau} \leq \hat{\tau}_{\max}$. Furthermore, the corresponding CDF can be obtained by simplifying the $\tilde{F}_{\cos\psi}(\hat{\tau}) = \int_{-1}^{\hat{\tau}} \tilde{f}_{\cos\psi}(x)\mathrm{d}x$, as follows:

$$\tilde{F}_{\cos\psi}(\hat{\tau}) = \begin{cases} \frac{\hat{b}_\theta}{\Delta(\hat{\mu}_\theta, \hat{b}_\theta, \hat{\tau}_{\max})}\left(\exp\left(\frac{\hat{\tau}-\hat{\mu}_\theta}{\hat{b}_\theta}\right) - \exp\left(\frac{-1-\hat{\mu}_\theta}{\hat{b}_\theta}\right)\right), & \hat{\tau} < \hat{\mu}_\theta \\ \frac{\hat{b}_\theta}{\Delta(\hat{\mu}_\theta, \hat{b}_\theta, \hat{\tau}_{\max})}\left(2 - \exp\left(\frac{\hat{\mu}_\theta-\hat{\tau}}{\hat{b}_\theta}\right) - \exp\left(\frac{-1-\hat{\mu}_\theta}{\hat{b}_\theta}\right)\right), & \hat{\tau} \geq \hat{\mu}_\theta \end{cases} \tag{4.22}$$

In order to evaluate the accuracy of our proposed truncated Laplace model based on the first-order Taylor series, we have calculated the average KSD with respect to the experimental data over different positions in a room of size 10×10 m^2. The average KSD for sitting activities of the proposed model given in (4.21) and the exact PDF given in (4.13) and (C.3) of Appendix C are 0.055 and 0.026, respectively. These values are relatively small so that our exact derived PDF and the proposed approximation based on the first order Taylor series show a close similarity with the sample PDF from the experimental measurements. Note that, as indicated before, an approximation of the exact PDF for the walking scenario as a truncated Gaussian distribution can be made similarly using the linear relationship of $\cos\psi$ and θ' in (4.17).

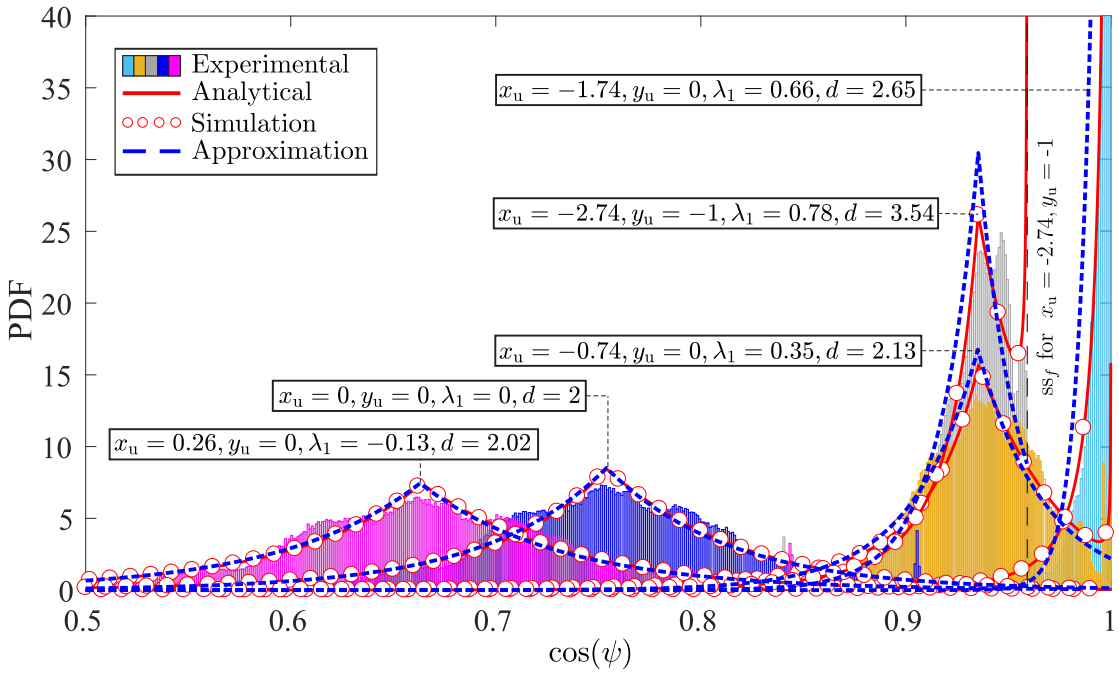

Figure 4.5: *Comparisons between sample PDF of experimental measurements, the closed-form PDFs and the approximation expression for different locations of UE and with fixed* $(x_a, y_a, z_a) = (0, 0, 2)$, $z_u = 0$, $\Omega = \pi$. *The users are assumed to be stationary.*

Figure 4.5 presents a comparison between the PDF of $\cos\psi$ given in (4.13) and (C.3) of Appendix C with the approximate PDF expressed in (4.21) for different positions of the UE with θ following the Laplace distribution. The UE is assumed to be stationary with $\Omega = \pi$ and located in the XY-plane, i.e., $z_u = 0$. The AP location is $(x_a, y_a, z_a) = (0, 0, 2)$. As can be seen, the first-order Taylor approximate PDF provides a well-matched approximation with the experimental measurements. Taking a close look at the results, it can be inferred that for $\lambda_1 \leq 0$, $f_{\cos\psi}$ is still closely Laplace distributed. Although, for $\lambda_1 > 0$ and especially when it is close to 1, the shape of $f_{\cos\psi}$ does not resemble a Laplace distribution, however, it still can be approximated with a truncated Laplace distribution.

Let's define $\mathcal{C}_w = \{(x_u, y_u) | \lambda_1 \cos\mu_\theta = \lambda_2 \sin\mu_\theta\}$. It can be inferred from (4.20) that when $(x_u, y_u) \in \mathcal{C}_w$, then, $\hat{b}_\theta = 0$. To give readers a context, the set $\mathcal{C}_w$ is a line (a hyperline in $\mathbb{R}^2$) at which the orientation of the UE faces the AP. In other words, when $(x_u, y_u) \in \mathcal{C}_w$ the channel attenuation is small. Under this condition, the PDF of the approximation method turns into a

probability mass function, i.e., it becomes a discrete RV. In this case, we observe a sudden jump in the KSD value [68]. In fact, this anomaly only occurs when $(x_{\rm u}, y_{\rm u}) \in \mathcal{C}_{\rm w}$. However, the area of the line $\mathcal{C}_{\rm w}$ in $\mathbb{R}^2$ is zero and so this is a negligible part of the typical indoor room area. Furthermore, we will show that if $(x_{\rm u}, y_{\rm u}) \in \mathcal{C}_{\rm w}$, the BER performance is less sensitive to the random orientation [18].

4.4 The Statistics of Channel Gain

After justifying the proposed approximation for the PDF of $\cos\psi$, we can use the simple equation given in (4.21) instead of the more complicated equations given in (4.13) and (C.3) of Appendix C to calculate the LOS channel gain and further related derivations. Note that the PDF of the channel gain derived in this section is the conditional PDF given the location and direction of the UE. Therefore, having the statistics of the user location, the joint PDF of the channel gain with respect to both UE orientation and location can be readily obtained. In the next chapter, we use this approach to develop an orientation-based random waypoint model to analyze mobile wireless systems.

The DC gain of the LOS optical channel can be expressed as $H_{\rm LOS} = \frac{H_0 \cos\psi}{d^{m+2}}$ for $0 \le \psi \le \Psi_{\rm c}$ and $H_{\rm LOS} = 0$ for $\psi \ge \Psi_{\rm c}$, where $H_0 = \frac{(m+1) g_{\rm f} \varsigma^2 A h^m}{2\pi \sin^2 \Psi_{\rm c}}$. Thus, for any given position $(x_{\rm u}, y_{\rm u}, z_{\rm u})$, the PDF of H can be expressed as follows:

$$f_{\rm H}(\hbar) = \frac{1}{h_{\rm n}} f_{\cos\psi}\left(\frac{\hbar}{h_{\rm n}}\right) + F_{\cos\psi}\left(\cos\Psi_{\rm c}\right)\delta(\hbar) \tag{4.23}$$

where $\delta(\hbar)$ is the Dirac delta function, taking 1 if $\hbar = 0$, and 0 otherwise; $h_{\rm n} = \frac{H_0}{d^{m+2}}$ is the normalizing factor. The support range of $f_{\rm H}(\hbar)$ is $h_{\min} \le \hbar \le h_{\max}$, where $h_{\min}$ and $h_{\max}$ are given as:

$$h_{\min} = \begin{cases} \dfrac{H_0}{d^{m+2}} \cos\Psi_{\rm c}, & \text{if} \quad \cos\psi < \cos\Psi_{\rm c} \\ \dfrac{H_0}{d^{m+2}} \min\{\lambda_1, \lambda_2\}, & \text{o.w} \end{cases} \tag{4.24}$$

$$h_{\max} = \begin{cases} \dfrac{H_0}{d^{m+2}} \lambda_2, & \text{if} \quad \lambda_1 < 0 \\ \dfrac{H_0}{d^{m+2}} \sqrt{\lambda_1^2 + \lambda_2^2}, & \text{if} \quad \lambda_1 \ge 0 \end{cases} \tag{4.25}$$

Parameter	Symbol	Value
LED half-intensity angle	$\Phi_{1/2}$	60°
Receiver FOV	Ψ_{c}	90°
Physical area of a PD	A	1 cm^2
Gain of optical filter	g_{f}	1
Refractive index	ς	1
Vertical distance of UE and AP	h	2 m

Table 4.3: *Simulation parameters of channel gain.*

The proof of (4.23) is provided in Appendix D. After some manipulations and using $\tilde{f}_{\cos\psi}$, (4.23) can be rewritten for the sitting scenario (i.e., Laplace distribution assumption for θ) as:

$$f_{\mathrm{H}}(\hbar) = \frac{\exp\left(-\frac{|\hbar-\mu_{\mathrm{H}}|}{b_{\mathrm{H}}}\right)}{b_{\mathrm{H}}\left(2-\exp\left(-\frac{h_{\max}-\mu_{\mathrm{H}}}{b_{\mathrm{H}}}\right)\right)} + F_{\cos\psi}\left(\cos\Psi_{\mathrm{c}}\right)\delta(\hbar), \tag{4.26}$$

with the support range of $h_{\min} \leq \hbar \leq h_{\max}$; The parameters μ_{H} and b_{H} are given as:

$$\mu_{\mathrm{H}} = \frac{H_0}{d^{m+2}}\left(\lambda_1 \sin\mu_\theta + \lambda_2 \cos\mu_\theta\right), \tag{4.27}$$

$$b_{\mathrm{H}} = \frac{H_0}{d^{m+2}} b_\theta |\lambda_1 \cos\mu_\theta - \lambda_2 \sin\mu_\theta|. \tag{4.28}$$

Moreover, for the special case of $b_{\mathrm{H}} \approx 0$, we have $f_{\mathrm{H}}(\hbar) \cong \delta(\hbar - h_{\max})$ and for the case that $\Pr(\psi < \Psi_{\mathrm{c}}) \approx 0$, the PDF would be $f_{\mathrm{H}}(\hbar) \cong \delta(\hbar)$.

The CDF of the LOS channel gain can be also obtained by calculating the integral of (4.26), which is given as:

$$F_{\mathrm{H}}(\hbar) = c_{\mathrm{H}} + \begin{cases} \dfrac{\exp\left(\frac{\hbar-\mu_{\mathrm{H}}}{b_{\mathrm{H}}}\right) - \exp\left(\frac{h_{\min}-\mu_{\mathrm{H}}}{b_{\mathrm{H}}}\right)}{\left(2-\exp\left(-\frac{h_{\max}-\mu_{\mathrm{H}}}{b_{\mathrm{H}}}\right)\right)}, & h_{\min} \leq \hbar \leq \mu_{\mathrm{H}} \\ \dfrac{2-\exp\left(\frac{h_{\min}-\mu_{\mathrm{H}}}{b_{\mathrm{H}}}\right) - \exp\left(-\frac{\hbar-\mu_{\mathrm{H}}}{b_{\mathrm{H}}}\right)}{\left(2-\exp\left(-\frac{h_{\max}-\mu_{\mathrm{H}}}{b_{\mathrm{H}}}\right)\right)}, & h_{\min} \leq \mu_{\mathrm{H}} \leq \hbar \\ \dfrac{\exp\left(-\frac{h_{\min}-\mu_{\mathrm{H}}}{b_{\mathrm{H}}}\right) - \exp\left(-\frac{\hbar-\mu_{\mathrm{H}}}{b_{\mathrm{H}}}\right)}{\left(2-\exp\left(-\frac{h_{\max}-\mu_{\mathrm{H}}}{b_{\mathrm{H}}}\right)\right)}, & \mu_{\mathrm{H}} \leq h_{\min} \leq \hbar \end{cases} . \tag{4.29}$$

where $c_{\mathrm{H}} = F_{\cos\psi}\left(\cos\Psi_{\mathrm{c}}\right)$. In fact, c_{H} shows the probability of being out of UE's FOV due to

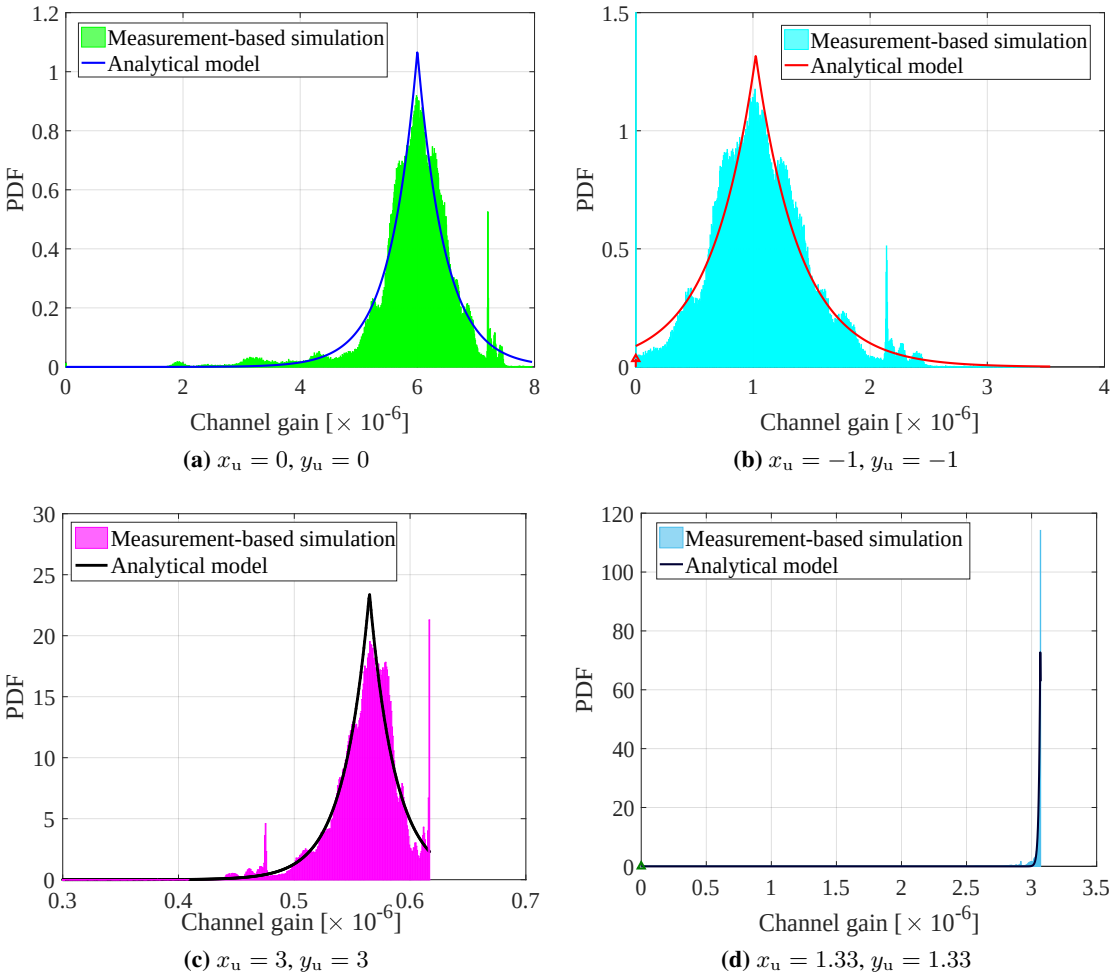

(a) $x_{\mathrm{u}} = 0, y_{\mathrm{u}} = 0$ **(b)** $x_{\mathrm{u}} = -1, y_{\mathrm{u}} = -1$

(c) $x_{\mathrm{u}} = 3, y_{\mathrm{u}} = 3$ **(d)** $x_{\mathrm{u}} = 1.33, y_{\mathrm{u}} = 1.33$

Figure 4.6: *Comparison between measurement-based simulations and analytical results of PDF of channel gain for different locations in the room with* $\Omega = \frac{\pi}{4}$.

random orientation.

Figure 4.6 represents the PDF of the LOS channel gain obtained from analytical results given in (4.26) and the measurement-based simulations. The results are provided for different positions in the room with $\Omega = \frac{\pi}{4}$. The simulation parameters are provided in Table 4.3. The results show the accuracy of the derived analytical PDF. The magnitude of the Dirac delta term is almost zero in figure 4.6-(a) and figure 4.6-(c) while it is 0.0336 and 0.006 in figure 4.6-(b) and figure 4.6-(d), respectively. Figure 4.6-(a) and figure 4.6-(b) illustrate two positions that correspond to $\lambda_1 = 0$ and $\lambda_1 < 0$, respectively while figure 4.6-(c) and figure 4.6-(d) present the positions associated

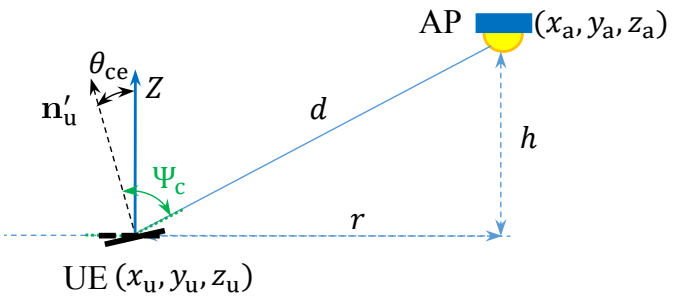

Figure 4.7: *Geometry of critical elevation angle.*

to $\lambda_1 > 0$. As can be seen, for $\lambda_1 \leq 0$, the analytical derivation of the LOS channel gain and the measurement-based simulations match very well. For $\lambda_1 > 0$, we still observe a good accommodation between the analytical and simulation results and in fact the difference happens at $\hbar = h_{\max}$ as shown in figure 4.6-(c) and figure 4.6-(d). We also observe that the distribution of the channel gain significantly changes from the Laplacian shape as $\lambda_1 \longrightarrow 1$ or equivalently (x_u, y_u) approaches to the $\mathcal{C}_w$ region as shown in figure 4.6-(d). As it can be seen from figure 4.3-(c), there is a small peak around $\theta = 25°$. This peak in the PDF of polar angle results in the observed small peak in the channel gain of figures 4.6-(a), 4.6-(b) and 4.6-(c) around channel gains of 7.5×10^{-6}, 2.1×10^{-6} and 0.47×10^{-6}, respectively. The peak at the channel gain of 6.2×10^{-6} in figure 4.6-(c) is because the UE is faced toward the AP. This is more obvious in figure 4.6-(d) since the UE is almost aligned to the AP (mathematically, $\psi \approx 0$).

4.5 Analysis of Orientation on Channel Gain

Before analyzing user's performance metrics such as average SNR and BER, let us define the critical elevation (CE), θ_{ce}, which defines the elevation angle at the boundary of the FOV of the receiver. As shown in figure 4.7, the CE angle for a given position of UE, (x_u, y_u), and user's direction, Ω, is the elevation angle for which $\psi = \Psi_c$, where Ψ_c is the UE's FOV. Thus, $\theta \geq \theta_{ce}$ results in $\psi \geq \Psi_c$, and the channel gain would be zero. This angle depends on both the UE position and its direction, Ω which is given as follows:

$$\theta_{ce} = \cos^{-1}\left(\frac{\cos\Psi_c}{\sqrt{\lambda_1^2 + \lambda_2^2}}\right) + \tan^{-1}\left(\frac{\lambda_1}{\lambda_2}\right), \tag{4.30}$$

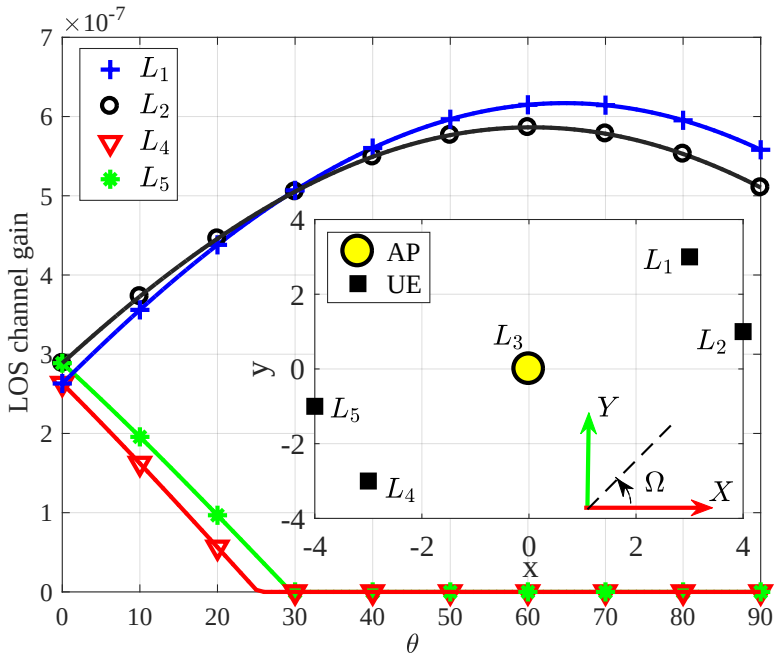

Figure 4.8: *The effect of changing* θ *on* $\cos\psi$ *for different locations of the UE with fixed* $\Omega = 45°$ *and* $\Psi_c = 90°$.

where the coefficients λ_1 and λ_2 are given in (4.11). Proof of (4.30) is provided in Appendix E. As can be seen from (4.11), the parameter λ_1 contains the direction angle, Ω. The physical concept of positive λ_1 is that the UE is facing to the AP while if it is not facing to the AP, λ_1 is negative. On the other hand, since always $z_u < z_a$, we have $\lambda_2 > 0$. It should be mentioned that the acceptable range for θ_{ce} is $[0, 90]$ similar to the polar angle, θ, which takes values between $0°$ and $90°$. Note that for a given location of UE, the minimum CE angle, θ_{th}, is obtained for $\Omega = \pi + \tan^{-1}\left(\frac{y_u - y_a}{x_u - x_a}\right) \triangleq \Omega_{th}$ which is given as:

$$\theta_{th} = \Psi_c + \sin^{-1}\left(\frac{h}{d}\right) - \frac{\pi}{2}. \tag{4.31}$$

The effect of changing the elevation angle, θ, on the LOS channel gain for different locations of the UE with a fixed direction angle, $\Omega = 45°$ and $\Psi_c = 90°$, is shown in figure 4.8. Other parameters are presented in Table 4.3. It can be seen that for the UE's locations of $L_4 = (-3, -3)$ and $L_5 = (-4, -1)$ by increasing the elevation angle, the LOS channel gain decreases. After $\theta_{ce} = 25.24°$ and $\theta_{ce} = 29.5°$ for L_4 and L_5, respectively, the AP is out of the UE's FOV and

hence the LOS channel gains are zero. However, with the same $\Omega = 45^\circ$ if the UE is located at $L_1 = (3, 3)$ or $L_2 = (4, 1)$, the LOS channel gain does not become zero if the elevation angle changes between 0° and 90°. This means that the AP would be always in the UE's FOV.

It is noted that under the condition of $\theta < \theta_{\rm th}$ the AP is always within the UE's FOV for any direction of Ω. For a given UE's location, we are also interested in the range of Ω for which the LOS channel is active. Let's denote this range as $\mathcal{R}_{\Omega,\theta}$. This range can be determined according to the following Proposition.

Proposition. For a given UE's location, the range of Ω for which the LOS channel gain is non-zero is $[0, 2\pi]$ if θ is smaller than or equal to a threshold angle $\theta_{\rm th} = \Psi_{\rm c} + \sin^{-1}\left(\frac{h}{d}\right) - \frac{\pi}{2}$. Otherwise it is given as follows:

$$\mathcal{R}_{\Omega,\theta} = \begin{cases} [0, \Omega_{\rm r1}) \bigcup (\Omega_{\rm r2}, 2\pi], & \text{if } \Lambda'(\Omega_{\rm r1}) < 0 \\ (\Omega_{\rm r1}, \Omega_{\rm r2}), & \text{if } \Lambda'(\Omega_{\rm r1}) \geq 0 \end{cases}, \tag{4.32}$$

where $\Lambda'(\Omega) = -\kappa_1 \sin\left(\Omega - \tan^{-1}\left(\frac{y_{\rm u}-y_{\rm a}}{x_{\rm u}-x_{\rm a}}\right)\right) + \kappa_2$ with:

$$\kappa_1 = \frac{\sqrt{(x_{\rm u}-x_{\rm a})^2 + (y_{\rm u}-y_{\rm a})^2}}{d} \sin\theta \qquad \text{and} \qquad \kappa_2 = \frac{(z_{\rm a}-z_{\rm u})}{d} \cos\theta. \tag{4.33}$$

Also $\Omega_{\rm r1} = \min\{\Omega_1, \Omega_2\}$ and $\Omega_{\rm r2} = \max\{\Omega_1, \Omega_2\}$, where:

$$\begin{aligned} \Omega_1 &= \cos^{-1}\left(\frac{\cos\Psi_{\rm c} - \kappa_2}{\kappa_1}\right) + \tan^{-1}\left(\frac{y_{\rm u}-y_{\rm a}}{x_{\rm u}-x_{\rm a}}\right), \\ \Omega_2 &= -\cos^{-1}\left(\frac{\cos\Psi_{\rm c} - \kappa_2}{\kappa_1}\right) + \tan^{-1}\left(\frac{y_{\rm u}-y_{\rm a}}{x_{\rm u}-x_{\rm a}}\right). \end{aligned} \tag{4.34}$$

Proof: See Appendix F.

The LOS channel gain versus Ω for locations of L_1 and L_5 (see the inset of figure 4.8) with $\theta = \theta_{\rm th}$ (dash line) and $\theta = 41^\circ \geq \theta_{\rm th}$ (solid line) are shown in figure 4.9. Note that for L_1 and L_5, we have $\theta_{\rm th} = 25.24^\circ$ and $\theta_{\rm th} = 25.88^\circ$, respectively. As can be seen, if $\theta < \theta_{\rm th}$, then, $\forall\Omega \in [0, 360)$, LOS channel gain is always non-zero (dash lines). Based on the proposition, the range of Ω for which the LOS channel gain is non-zero with $\theta = 41^\circ > \theta_{\rm th}$ is $[0, 167.8) \cup (282.2, 360]$

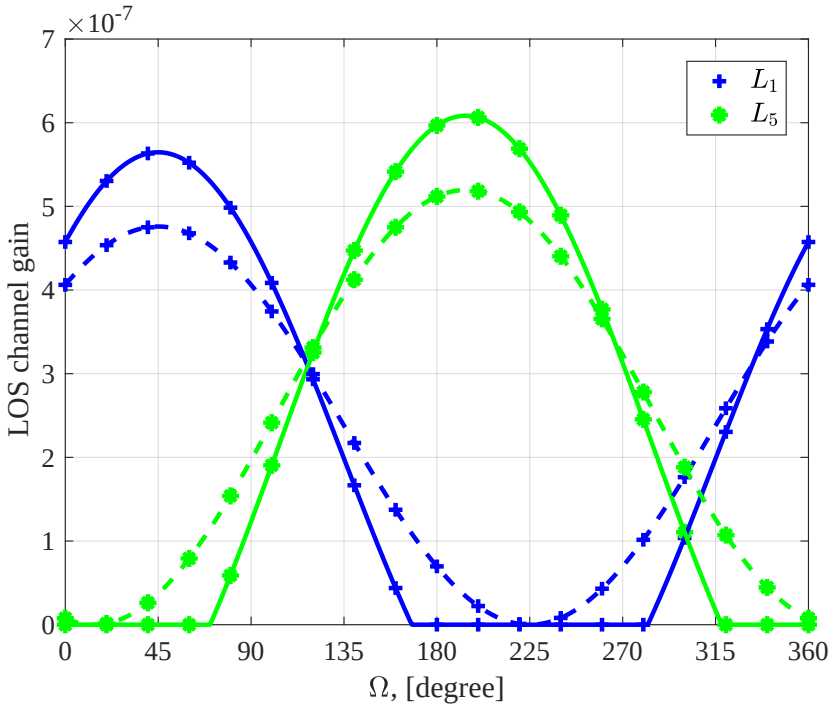

Figure 4.9: *The effect of changing Ω and θ on the LOS channel gain with $\Psi_{\rm c} = 90°$, for different positions and elevation angles $\theta = 41°$ (solid lines) and $\theta = \theta_{\rm th}$ (dash lines).*

for L_1 and $[70.1, 318]$ for L_2.

It can be inferred form the Proposition that for a given UE's location and θ, the probability that the LOS link is not within the UE's FOV (due to change of Ω) is $\Pr\{H = 0\} = 1 - \Pr\{\Omega \in \mathcal{R}_{\Omega,\theta}\}$. Figure 4.10 shows the $\Pr\{H = 0\}$ versus the horizontal distance between the UE and the AP, r, for different UE's FOV. The results are obtained by changing Ω from $0°$ to $360°$ for each r with $\theta = 41°$. As can be observed, $\Pr\{H = 0\} = 1$, for UEs with a narrow FOV (i.e., $\Psi_{\rm c} = 30°$ and $40°$) when they are located in the vicinity below the AP. As the horizontal distance, r, increases, $\Pr\{H = 0\}$ first decreases and then it increases as it goes away from the AP. For wide FOVs (i.e., $\Psi_{\rm c} = 60°$, $80°$ and $90°$), $\Pr\{H = 0\}$ is zero when the UE is in the vicinity below the AP, and then it starts to increase at a certain r. This can be derived based on (4.31) for $\Psi_{\rm c} \geq \theta$ that is $r \geq h \tan(\Psi_{\rm c} - \theta)$. Note that the high probability of losing the LOS link particularly for narrower FOVs is due to the fact that a single AP is considered and the effect of reflections are ignored. A study of such effects has been presented in our recent work [125].

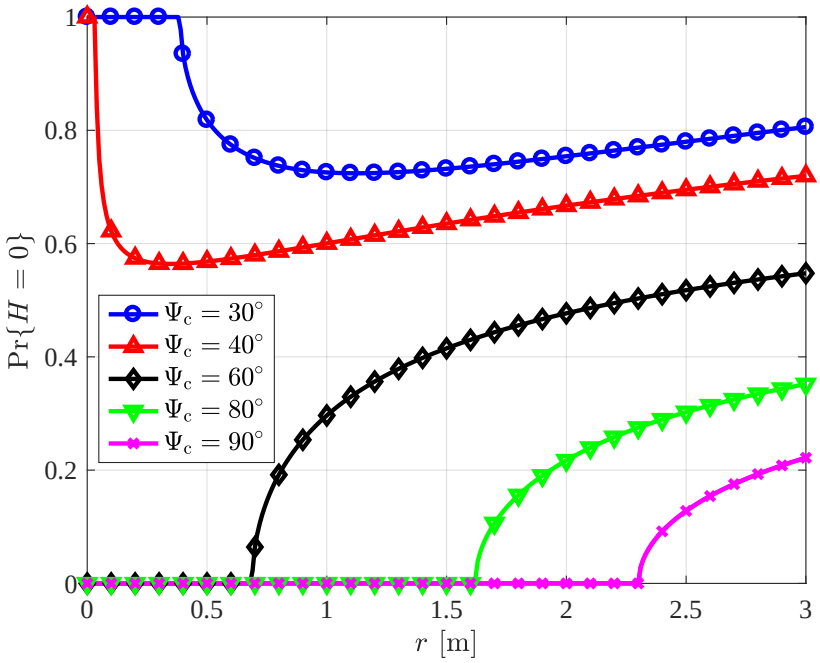

Figure 4.10: *The effect of different FOV on having a zero LOS,* $\Pr\{H = 0\}$.

Let $\mathcal{R}_\Omega$ denote the range for which the LOS channel gain is always non-zero regardless of θ, i.e., $\forall\theta \in [0, 90]$. The range, $\mathcal{R}_\Omega$, can be determined according to the following Corollary.

Corollary. For a given UE's location, the range of Ω for which the LOS channel gain is non-zero for all $\theta \in [0, 90]$ can be obtained as:

$$\mathcal{R}_\Omega = \mathcal{R}_{\Omega,\theta}|_{\text{For } \theta=90}. \tag{4.35}$$

Proof of this corollary is similar to the proof of Proposition 1. Noting that the worst elevation angle that leads to the smallest range of Ω is $\theta = 90°$. The physical concept of $\mathcal{R}_\Omega$ is that when the UE faces the AP, we have $\Omega \in \mathcal{R}_\Omega$. Otherwise, if the UE faces the opposite direction of the AP, $\Omega \notin \mathcal{R}_\Omega$. In fact, $\mathcal{R}_\Omega$ provides a stable range for which the user can change the elevation angle between 0 and 90 without experiencing the AP out of its FOV. In the next section, we will show that under the condition of $\Omega \notin \mathcal{R}_\Omega$, the BER performance is very sensitive to the random orientation of UE. We note that the range given in (4.35) is valid if $\Psi_c \geq \cos^{-1}\left(\frac{r}{d}\right)$ (this condition can be readily seen by substituting $\theta = 90°$ in (4.33) and then replacing the results in (4.34)).

4.6 Bit-Error Ratio Performance

In this section, we evaluate the BER performance of DCO-OFDM in LiFi networks. We initially derive the SNR statistics on each subcarrier, then based on the derived PDF of SNR, the BER performance is assessed. Note that the PDF of the SNR derived in this study is the conditional PDF given the location and direction of the UE. Therefore, having the statistics of the user location, the joint PDF of the SNR with respect to both UE orientation and location can be readily obtained.

4.6.1 SNR Statistics

The received electrical SNR on the kth subcarrier of a LiFi system can be acquired as:

$$\mathcal{S} = \frac{R^2 H_{\mathrm{LOS}}^2 P_{\mathrm{opt}}^2}{(\mathcal{K}-2)\eta^2 \sigma_{\mathrm{N}}^2}, \tag{4.36}$$

where the photodiode (PD) responsivity is denoted by R; H_{LOS} is the LOS channel gain given in (2.7); P_{opt} is the transmitted optical power; $\mathcal{K}$ is the total number of subcarriers with $\mathcal{K}/2-1$ subcarriers bearing information. Furthermore, η is the conversion factor [128]. As mentioned, the condition $\eta = 3$ can guarantee that less than 1% of the signal is clipped so that the clipping noise is negligible [4, 129]. In (4.36), $\sigma_{\mathrm{N}}^2 = N_0 B/\mathcal{K}$ is the noise power on the kth subcarrier where N_0 stands for the noise spectral density and B is the modulation bandwidth. The PDF of the LOS channel gain, H_{LOS}, is given in (4.26). Using the fundamental theorem of determining the distribution of a random variable [130], the PDF of SNR can be obtained as follows:

$$f_{\mathcal{S}}(s) = \frac{f_H(\sqrt{s/\mathcal{S}_0})}{2\mathcal{S}_0\sqrt{s/\mathcal{S}_0}} = \frac{\exp\left(-\frac{|\sqrt{s}-\sqrt{\mathcal{S}_0}\mu_{\mathrm{H}}|}{\sqrt{\mathcal{S}_0}b_{\mathrm{H}}}\right)}{2b_{\mathrm{H}}\sqrt{\mathcal{S}_0 s}\left(2-\exp\left(-\frac{h_{\max}-\mu_{\mathrm{H}}}{b_{\mathrm{H}}}\right)\right)} + c_{\mathrm{H}}\delta(s), \tag{4.37}$$

where $\mathcal{S}_0 = \frac{R^2 P_{\mathrm{opt}}^2}{(\mathcal{K}-2)\eta^2\sigma_{\mathrm{N}}^2}$ and with the support range of $s \in (s_{\min}, s_{\max})$, where $s_{\min} = \mathcal{S}_0 h_{\min}^2$ and $s_{\max} = \mathcal{S}_0 h_{\max}^2$, with $h_{\min}$ and $h_{\max}$ given in (4.24) and (4.25), respectively. Moreover, $c_{\mathrm{H}} = F_{\cos\psi}(\cos\Psi_{\mathrm{c}})$.

By calculating the integral, $F_{\mathcal{S}}(s) = \int_{s_{\min}}^{s} f_{\mathcal{S}}(s)\mathrm{d}s$, the CDF of SNR on the kth subcarrier can be obtained. The CDF of SNR can be also acquired by substituting $\hbar = \sqrt{\frac{s}{\mathcal{S}_0}}$ in (4.29), i.e.,

Parameter	Symbol	Value
AP location	$(x_{\mathrm{a}}, y_{\mathrm{a}}, z_{\mathrm{a}})$	$(0, 0, 2)$
Downlink bandwidth	B	10 MHz
PD responsivity	R	1 A/W
Number of subcarriers	$\mathcal{K}$	1024
Noise power spectral density	N_0	10^{-21} A^2/Hz
LED half-intensity angle	$\Phi_{1/2}$	60°
Receiver FOV	Ψ_{c}	90°
Physical area of a PD	A	1 cm^2
Gain of optical filter	g_{f}	1
Refractive index	ς	1
Vertical distance of UE and AP	h	2 m
Transmitted optical power	P_{opt}	3 W
Conversion factor	η	3
Mean value of polar angle	μ_θ	41°
Scaling parameter of polar angle	b_θ	5.43°

Table 4.4: *Simulation parameters.*

$F_{\mathcal{S}}(s) = F_H(\sqrt{\frac{s}{\mathcal{S}_0}})$.

Figure 4.11 shows the PDF and CDF of the received SNR obtained from analytical results compared with the Monte-Carlo simulation results. The UE is located at position $L_1 = (3, 3)$ and the transmitted optical power is 3 W. The results are provided for two directions: $\Omega = 45^\circ$ and $\Omega = 225^\circ$. Other simulation parameters are given in Table 4.4. As it can be seen, the analytical models for both PDF and CDF of the received SNR match the simulation results. The factor c_{H} for $\Omega = 45^\circ$ is 0. This factor for $\Omega = 225^\circ$ is 0.975 for simulation results and 0.979 for the analytical model. These results confirm the accuracy of the analytical model.

4.6.2 BER Performance

In this subsection, we aim to evaluate the effect of UE orientation on the BER performance of a LiFi-enabled device as one use case. BER is one of the common metrics to evaluate the point-to-point communication performance. Assuming the M-QAM DCO-OFDM modulation, the average BER per subcarrier of the communication link can be obtained as [38]:

$$\bar{P}_{\mathrm{e}} = \int_{s_{\min}}^{s_{\max}} P_{\mathrm{e}}(s)\, f_{\mathcal{S}}(s) \mathrm{d}s, \tag{4.38}$$

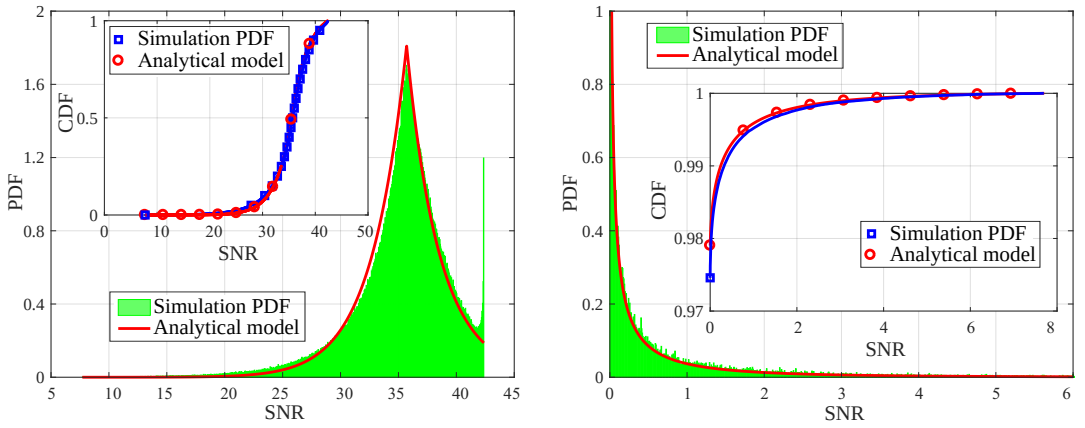

(a) $\Omega = 45°$ **(b)** $\Omega = 225°$

Figure 4.11: *Comparison between simulation and analytical results of PDF and CDF of received SNR for UE's location* $L_1 = (3, 3)$ *with* $\Omega = 45°$ *and* $\Omega = 225°$.

where P_{e} determines the BER of M-QAM DCO-OFDM in AWGN channels, which can be obtained approximately as [131]:

$$P_{\mathrm{e}}(s) \approx \frac{4}{\log_2 M}\left(1 - \frac{1}{\sqrt{M}}\right) Q\left(\sqrt{\frac{3s}{M-1}}\right), \tag{4.39}$$

where $Q(\cdot)$ is the Q-function. Substituting (4.37) and (4.39) into (4.38) and calculating the integral from $s_{\min}$ to $s_{\max}$, we get the average BER of the M-QAM DCO-OFDM in AWGN channels with randomly-orientated UEs. After calculating the integral and some simplifications, the approximated average BER is given as:

$$\bar{P}_{\mathrm{e}} \approx \begin{cases} -\Delta_0 + \frac{1}{2} c_{\mathrm{H}} c_{\mathrm{M}}, & \mu_{\mathrm{H}} \leq h_{\min} \\ P_{\mathrm{e}}(\mathcal{S}_0 \mu_{\mathrm{H}}^2) + \frac{1}{2} c_{\mathrm{H}} c_{\mathrm{M}}, & h_{\min} < \mu_{\mathrm{H}} \leq h_{\max} \end{cases}, \tag{4.40}$$

where

$$\Delta_0 = \frac{\frac{2}{\log_2 M}\left(1 - \frac{1}{\sqrt{M}}\right) \exp\left(\frac{\mu_{\mathrm{H}} - h_{\min}}{b_{\mathrm{H}}}\right)}{\left(2 - \exp\left(-\frac{h_{\max} - \mu_{\mathrm{H}}}{b_{\mathrm{H}}}\right)\right)},$$

$$c_{\mathrm{M}} = \frac{4}{\log_2 M}\left(1 - \frac{1}{\sqrt{M}}\right).$$

The proof is provided in Appendix G.

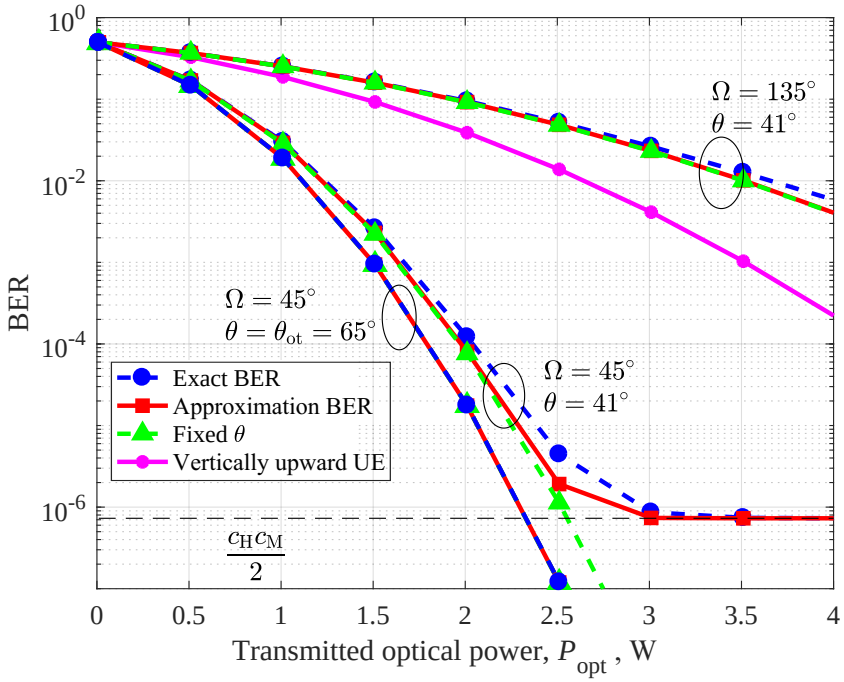

Figure 4.12: *BER performance of point-to-point communications for a UE located at* $L_1 = (3, 3)$. *Three scenarios are considered: i) vertically upward UE, ii) UE with the fixed polar angle without random orientation, and iii) real scenario with a random orientation (Laplace distribution) for polar angle.*

Note that if the UE is tilted optimally towards the AP, the BER is minimum. For any arbitrary location and direction of UE, the optimum tilt (OT) angle is defined as the angle that provides the maximum channel gain [16, 17, 23]. This angle is $\theta_{\text{ot}} = \tan^{-1}\left(\frac{\lambda_1}{\lambda_2}\right)$ and the average BER for this tilt angle is $\bar{P}_{\text{e}} \approx P_{\text{e}}(\mathcal{S}_0\mu_{\text{H}}^2)$ (since $c_{\text{H}} = 0$).

Figure 4.12 illustrates the BER performance of 4-QAM DCO-OFDM for three scenarios: i) a vertically upward UE, ii) a UE with a fixed polar angle and without random orientation, iii) a realistic scenario in which the polar angle follows a Laplace distribution that considers the random orientation, i.e., $\theta \sim \mathcal{L}(\mu_\theta, b_\theta)$. Here, we assume $\mu_\theta = 41^\circ$ and $b_\theta = 5.43^\circ$ as obtained based on the experimental measurements. Other simulation parameters are given in Table 4.4. The results are provided for the UE's location of $L_1 = (3, 3)$. For this location, $\theta_{\text{ot}} \approx 65^\circ$. Some interesting observations can be seen from the results shown in this figure. For the case of $\theta = 41^\circ$ and $\Omega = 135^\circ$, the vertically upward UE outperforms the other two scenarios. Also

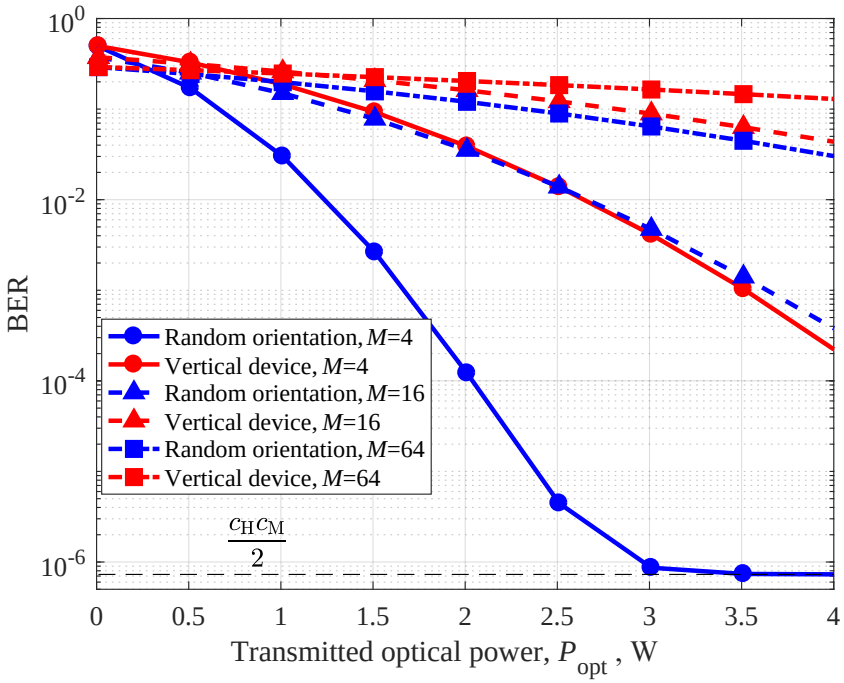

Figure 4.13: *BER performance of different modulation orders, M, for vertically upward and randomly-orientated UEs located at $L_1 = (3, 3)$ with $\Omega = 45°$ and $\theta = \theta_{ot}$.*

the gap between the exact and approximate BER is small especially for low transmission power. By changing Ω from $\Omega = 135°$ to $\Omega = 45°$, the BER of the second and third scenarios change significantly and now outperform the vertically upward UE. The reason for this is because, in this case, the PD faces the AP. One interesting observation is that after $P_{opt} > 3$ W, the BER does not decrease and is saturated. This is due to the constant term in (4.40), i.e., $\frac{1}{2} c_H c_M$, will be dominant compared to the power-dependent term, i.e., $P_e(\mathcal{S}_0 \mu_H^2)$. In other words, due to the random orientation, there are cases that the LOS link is out of the UE's FOV and data is lost. The BER performance of the second and third scenarios can still be better if $\theta = \theta_{ot} \approx 65°$. For $\theta = \theta_{ot}$ the maximum LOS channel gain is achieved and under this condition the BER is minimum. This fact underlines that the device orientation is not always destructive. Furthermore, with $\theta = \theta_{ot}$ the UE's random orientation has the minimum effect on the BER. We note that for a given location and Ω, the $\bar{P}_e$ given in (4.40) is always upper bounded to the BER of $P_e(s)$ obtained for $\theta = \theta_{ot}$ as it provides the maximum LOS channel gain.

Figure 4.13 illustrates the BER performance comparison of vertically upward and randomly orientated UEs for different modulation orders. For these results, the UE is again located at $L_1 = (3, 3)$ with $\Omega = 45^\circ$ and the elevation angle is set to the optimum tilt angle, $\theta = \theta_{\text{ot}} = 65^\circ$. Other parameters are the same as given in Table 4.4. As can be seen, randomly-oriented UEs are highly affected by the increase of the modulation order compared to vertically upward UEs. As the ratio of BER for modulation orders of $M = 4$ and $M = 16$ at $P_{\text{opt}} = 3$ W for randomly-orientated UEs is 5×10^3 while this ratio for vertically upward UEs is just 22. The other observation is that randomly-orientated UEs with higher modulation order of $M = 16$ and with $\theta = \theta_{\text{ot}}$ have still better performance than the vertically upward UEs with $M = 4$.

4.7 Summary

A new model for device orientation based on the experimental measurements is proposed. It is shown that the PDF of the polar angle follows a Laplace distribution for static users while it is better fitted to a Gaussian distribution for mobile users. We proposed an approximation PDF using the truncated Laplace distribution and the accuracy of this approximated method was confirmed by the KSD test. The LOS channel gain statistics are calculated and it is described as a random process for which the coherence time was discussed. We analyzed the device orientation and assessed its importance on system performance. The PDF of SNR for a randomly-orientated device is derived, and based on the derived PDF, the BER performance of DCO-OFDM in AWGN channels with randomly-orientated UEs is evaluated. An approximation for the average BER of randomly-oriented UEs is calculated that closely matches the exact one. It is shown that the random orientation should not be neglected, which might lead to an error floor at some specific locations. We also observed that by orientating the device with the optimum tilt angle, the transmitted optical power can be reduced around 0.7 W at a BER of 10^{-6}.

Chapter 5
Efficient LiFi Networking in the Presence of User Mobility, Random Orientation and Blockage

5.1 Introduction

In the previous chapter, we assessed the impact of random device orientation on the point-to-point communication metrics such as received SNR and BER. In this chapter, we will evaluate the effect of device orientation and user mobility on the system performance of a LiFi network. Handover is one of the most common methods to measure the network performance. We will propose a new MDR to support seamless connectivity in a LiFi network. The proposed MDR structure shows a robust performance compared to the conventional SR (for which all photo-diodes are placed on one side of a smartphone) in the presence of random device orientation, user mobility and link blockage. It should be noted that the MDR can improve the performance of any MIMO technique. However, in this chapter, we focus on the performance of SM as a use case. SM is a type of MIMO structure that offers enhanced spectral efficiency compared to non-MIMO systems. It is shown in [132] that SM has lower complexity when compared to full MIMO (i.e., spatial multiplexing while using all available transmitters).

For the subject of handover in indoor LiFi networks, there are a number of studies in published research [133]– [134]. In [133], a handover procedure is proposed based on a pre-handover scheme to initiate broadcasting the UE data on the target cell. The procedure relies on position estimation obtained by visible light positioning and motion tracking with the Kalman filter. In [135], a handover management approach is proposed based on the received signal intensity (RSI). The spatial distribution of the received data rate is studied using software simulations for both overlapping and non-overlapping lighting scenarios. In [136], power-based and frequency-based soft handover methods are proposed to reduce data rate fluctuations as the UE moves from

one cell to another. The statistical distribution of the received data rate is also studied using computer simulations. In [134], a handover algorithm is proposed with the aim of extending the transmission bandwidth by minimizing the multipath induced dispersion of the VLC channel. For a cellular network, the algorithm deactivates those cells that do not cover the UE to decrease the overall root mean square (RMS) delay spread.

The above studies, however, have significant shortcomings. In principle, they do not focus on modeling and analysis of the underlying handover mechanism in LiFi networks. Also, the lack of a standard mobility model for mobile UE devices is evident in these studies. In addition, they assume that the UE devices are always oriented vertically upward. This assumption may not be true for LiFi networks, since the UE devices (for example smartphones) have random orientation while moving. This fact was shown through the experimental measurement as presented in the previous chapter. Here, we therefore attempt to provide a fundamental modeling approach required for understanding and analysis of handover in downlink optical attocell networks, considering the effects of both mobility and change of UE's orientation. Initially, the RWP model in [63] is adopted for the UE movement, then, we introduce the ORWP model which considers the change of UE's orientation during movement. It should be noted that the ORWP model has been developed based on the experimental measurements. The handover rate due to the movement and rotation of the receiver are separately calculated and studied using Monte-Carlo simulations.

The rest of the chapter is organized as follows. In section 5.2, handover in LiFi systems due to device orientation and user mobility has been studied. In section 5.3, the MDR configuration is proposed and its performance has been evaluated in Section 5.4. Finally, a summary of this chapter is presented in section 5.5.

5.2 Handover Assessment

5.2.1 Handover Criterion

In order to support seamless connectivity for a mobile UE, the downlink connection has to be handed over between APs without loss or interruption of service. In this section, the RSI of the

optical signal is considered as the criterion for handover. Thus, a handover decision is made when there is a new AP in the receiver FOV whose RSI is greater than that of the primary AP. Note that all APs transmit the same power, and the RSI from an AP is directly proportional to the DC gain of the corresponding VLC channel. Therefore, the focus is on the DC gains of the channel for handover assessment.

Let H_i, for $i = 1, 2, \ldots, N_{\text{AP}}$, be the DC gain for the VLC channels from APs to the UE receiver at the current time sample, where N_{AP} is the total number of APs. The UE receiver is connected to the kth AP based on the maximum DC gain criterion so that $k = \arg\max_i(H_i)$. The DC gains are updated at each time sample while the UE evolves (i.e., moves or rotates) within the network. For the next time sample, denoting k' as the updated index of the AP with the maximum DC gain, a handover occurs if $k' \neq k$.

From the point of view of handover protocols, a certain amount of time is required for processing the handover request before the connection can be completely transferred from one AP to another. Denote this time by t_{ho}, and denote the time that it takes for a UE to pass across or rotate through an attocell by t_{mo}. Note that if $t_{\text{ho}} > t_{\text{mo}}$, then the handover does not occur or it may fail. Throughout this chapter, it is assumed that $t_{\text{ho}} \ll t_{\text{mo}}$.

5.2.2 Probability of Handover Due to Receiver Rotation

Here, the probability of handover due to rotation, denoted as P_{rot}, of the UE located at the point (x, y) is derived. The rotation may occur for each of the two angles θ and Ω (see figure 2.10) independently and randomly with the PDFs $f_\theta(\theta)$ and $f_\Omega(\Omega)$. This in turn causes a random DC gain for the VLC channel. To define the handover event, suppose that the UE is initially connected to AP$_j$, for $j = 1, 2, \ldots, N_{\text{AP}}$. Any random rotation of the UE leads to a handover if there is AP$_i$, $i \neq j$, in the receiver FOV after rotation such that $H_i > H_j$. Hence, the handover probability is obtained as:

$$P_{\text{rot}} = \Pr\left(\bigcup_{i \neq j} \{H_i > H_j\}\right) = 1 - \Pr\left(\bigcap_{i \neq j} \{H_i < H_j\}\right). \tag{5.1}$$

To further evaluate the probability in (5.1), H_i and H_j need to be expanded in terms of the coordinates and orientation angles of the UE. Using figure 2.3, $\cos\phi_i = -\mathbf{d}_i \cdot \mathbf{n}_\mathrm{t}/\|\mathbf{d}_i\| = h/d_i$ can be substituted in (2.7), where $\mathbf{d}_i = [x_{\mathrm{a},i} - x_\mathrm{u}, y_{\mathrm{a},i} - y_\mathrm{u}, h]^\mathrm{T}$ is the distance vector from the UE located at $(x_\mathrm{u}, y_\mathrm{u}, z_\mathrm{u})$ and the ith AP located at $(x_{\mathrm{a},i}, y_{\mathrm{a},i}, z_{\mathrm{a},i})$. Also, $h = z_{\mathrm{a},i} - z_\mathrm{u}$ is the same for all APs. Hence, $d_i = \|\mathbf{d}_i\| = \sqrt{(x_{\mathrm{a},i} - x_\mathrm{u})^2 + (y_{\mathrm{a},i} - y_\mathrm{u})^2 + h^2}$. With this result, and after normalizing H_i and H_j to the common term $G_0 = (m+1)Ah^m g_\mathrm{f}/2\pi$, (5.1) is simplified as:

$$P_\text{rot} = 1 - \Pr\left(\bigcap_{i\neq j}\left\{\frac{\cos\psi_i}{d_i^{m+2}}g(\psi_i) < \frac{\cos\psi_j}{d_j^{m+2}}g(\psi_j)\right\}\right). \tag{5.2}$$

The probability of handover due to the receiver rotation as a function of (x, y) can be expressed as:

$$P_\text{rot}(x,y) = 1 - \iint\limits_{\mathcal{R}(x,y)} f_{\theta,\Omega}(\theta,\Omega)\,\mathrm{d}\theta\mathrm{d}\Omega, \tag{5.3}$$

where $f_{\theta,\Omega}$ is the joint PDF of the random variables (θ, Ω) given by $f_{\theta,\Omega}(\theta,\Omega) = f_\theta(\theta)f_\Omega(\Omega)$, since θ and Ω are independent [68]. Furthermore,

$$\mathcal{R}(x,y) = \{(\theta,\Omega) \mid w_i(x,y) < w_j(x,y)\ \forall i \neq j\}, \tag{5.4}$$

is the integration region where $w_i(x,y) = g(\psi_i)\cos\psi_i/d_i^{m+2}$. Note that $\cos\psi_i = \mathbf{d}_i \cdot \mathbf{n}'_\mathrm{u}/\|\mathbf{d}_i\|$ after rotation, where $\mathbf{n}'_\mathrm{u}$ is given in (2.32). This yields:

$$\cos\psi_i = \frac{1}{d_i}\Big[-(x_{\mathrm{a},i} - x_\mathrm{u})(\sin\theta\cos\Omega) - (y_{\mathrm{a},i} - y_\mathrm{u})(\sin\theta\sin\Omega) + (z_{\mathrm{a},i} - z_\mathrm{u})\cos\theta\Big]. \tag{5.5}$$

Case Study I: Handover Probability Due to Change of Direction

Assume $\Omega \sim \mathcal{U}[0, 2\pi)$ and $\theta = \theta_0$. In other words, a zero roll and a non-zero constant pitch are assumed for the UE orientation while the direction of the user is a uniform random variable distributed between 0 and 2π. Here, since Ω is the only random variable, the double integral in (5.3) reduces to a single integral and by using $f_\Omega(\Omega) = 1/2\pi$, the handover probability is

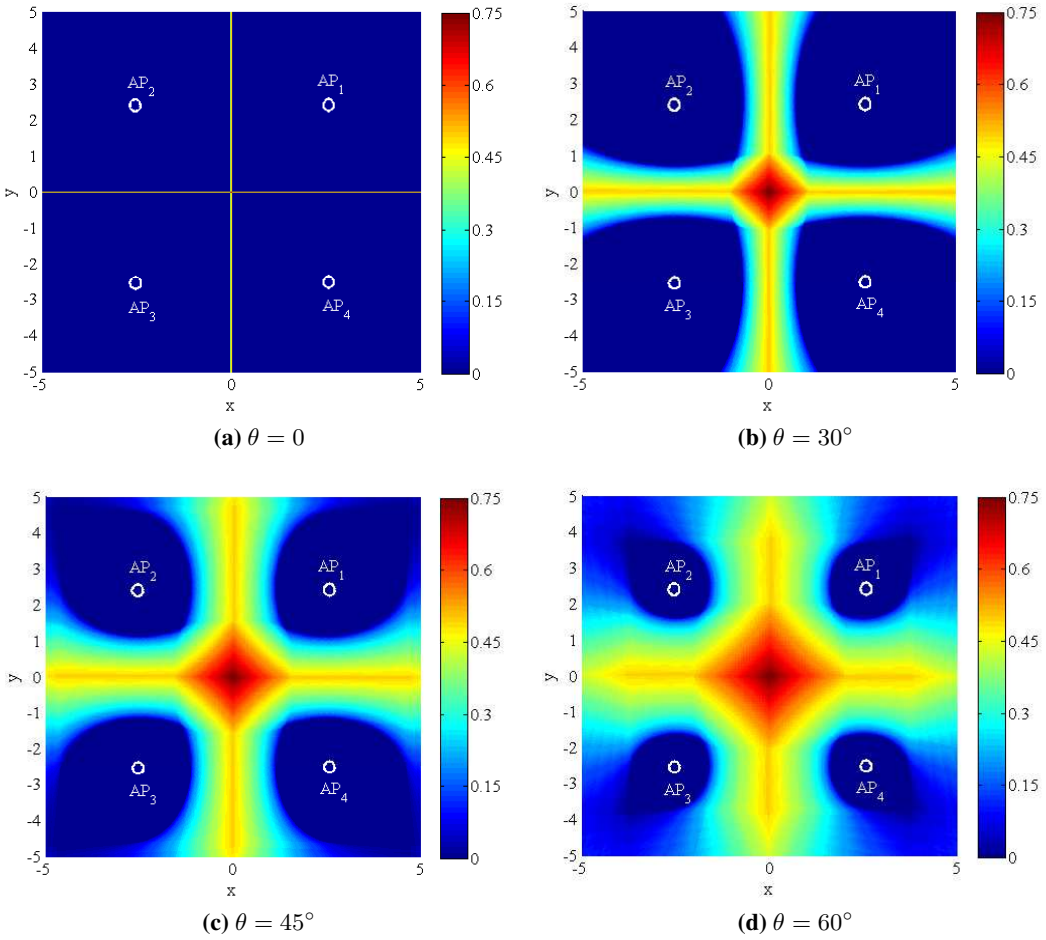

(a) $\theta = 0$ **(b)** $\theta = 30°$

(c) $\theta = 45°$ **(d)** $\theta = 60°$

Figure 5.1: *Handover probability at different positions in the network due to changes of UE direction for* $\theta = 0, 30°, 45°, 60°$.

calculated as:

$$P_{\text{rot}}(x, y) = 1 - \int_{\mathcal{R}_0(x,y)} \frac{1}{2\pi} \mathrm{d}\Omega = 1 - \frac{L_0(x, y)}{2\pi}, \tag{5.6}$$

where $\mathcal{R}_0(x, y) = \{\Omega \mid w_i(x, y) < w_j(x, y)\ \forall i \neq j\}$ by using (5.4); and $L_0(x, y)$ is the length of the linear subspace defined by $\mathcal{R}_0(x, y)$. Figure 5.1 illustrates the handover probability at different positions in the network considering a uniform distribution for Ω in $[0, 2\pi)$ and $\theta = 0, \pi/6, \pi/4, \pi/3$. Table 5.1 lists the parameters used for simulation. With four APs in this setup, the network area is divided into four quadrants with one AP at the center of each quadrant as shown in figure 5.1. In each quadrant, the UE is assumed to be initially connected

Parameter	Symbol	Value
Network space	–	$10 \times 10 \times 2.15$ m^3
LED half-intensity angle	$\Phi_{1/2}$	60°
Receiver FOV	Ψ_{c}	90°
Number of APs	N_{AP}	4
Locations of APs	–	$(\pm 2.5, \pm 2.5, 2.15)$ m

Table 5.1: *Simulation parameters of handover.*

to the corresponding AP denoted as AP$_j$ for $j = 1, 2, 3, 4$. For every position in the network, the handover probability is calculated based on (5.6). It is observed that by change of the user direction, depending on the initial position of the UE, the downlink connection is handed over either one of the three neighboring APs including AP$_i$ $\forall i \neq j$, with probability shown in figure 5.1. Specifically, the handover probability is equal to zero under each AP and it approaches 0.75 as the UE position moves toward the network center. Note that the maximum probability of handover is equal to 0.75 at the network center. The reason for this is that three out of four APs are equally likely to be available for handover at the network center, which yields a probability of 0.75. It is also observed from figure 5.1.(a)–(d) that the areas with a higher probability of handover are extended by increasing θ. This is especially evident for the red area in the network center that holds the highest probability of handover. Moreover, there is a blue zone in the center of each quadrant where the handover probability is equal to zero, and the UE is connected to the corresponding AP for that quadrant regardless of any value for Ω. Also, the blue zone is smaller for larger values of θ.

5.2.3 Probability of Handover Due to Receiver Movement

Here, the probability of handover due to movement, denoted as P_{mov}, of the UE moving from the initial waypoint (x_0, y_0) to the destination waypoint (x, y) is derived. The random waypoint (RWP) mobility model described in section 2.9.1 is employed. The room size is assumed to be $a \times a$ m^2. Let $\mathcal{Z} : \mathcal{A} \mapsto \mathcal{J}$ such that $\mathcal{Z}(x, y) = j$, be defined as the function which takes the UE coordinates on the xy-plane and returns the index of the serving AP; $\mathcal{A} = \{(x, y) \in \mathbb{R}^2 | \ |x| < 0.5a, |y| < 0.5a\}$ is the set for all positions in the network and $\mathcal{J} = \{1, 2, \ldots, N_{\mathrm{AP}}\}$. The handover probability can be calculated as:

$$P_{\text{mov}} = \sum_{j=1}^{N_{\text{AP}}} \Pr(\mathcal{Z}(x,y) \neq j |\ \mathcal{Z}(x_0,y_0) = j) \Pr(\mathcal{Z}(x_0,y_0) = j). \tag{5.7}$$

The probability that the UE stays in the coverage area of AP_j can be expressed and obtained as:

$$\Pr(\mathcal{Z}(x,y) = j |\ \mathcal{Z}(x_0,y_0) = j) = \Pr(\mathcal{Z}(x,y) = j), \tag{5.8}$$

because the UE randomly chooses the destination waypoint (x, y) independent of the initial waypoint (x_0, y_0), according to the RWP model. Using (2.7), and with a similar approach used in Section 5.2.2 to express H_i in terms of the spherical angles, θ and Ω, then, $\mathcal{A}_j$ is defined as the set for all positions included within the coverage area of AP_j such that:

$$\mathcal{A}_j(\theta,\Omega) = \{(x,y) \in \mathcal{A} \mid H_j(\theta,\Omega) > H_i(\theta,\Omega)\ \forall i \neq j\}, \tag{5.9}$$

which is a function of the orientation angles (θ, Ω). With this definition, (5.8) is simplified as $\Pr(\mathcal{Z}(x,y) = j) = S_j/a^2$, where S_j is the area of $\mathcal{A}_j$. Thus, $\Pr(\mathcal{Z}(x_0,y_0) = j) = S_j/a^2$. Inserting these in (5.7), the probability of handover due to the receiver movement as a function of (θ, Ω) is obtained as:

$$P_{\text{mov}}(\theta,\Omega) = \sum_{j=1}^{N_{\text{AP}}} \left(1 - \frac{S_j(\theta,\Omega)}{a^2}\right) \frac{S_j(\theta,\Omega)}{a^2}. \tag{5.10}$$

Before presenting the results for handover due to movement, it is instructive to look at the coverage area of each AP in the network and how it changes with orientation angles of the UE. Figure 5.2 shows a number of example realizations of coverage areas for the four APs considered in Case Study I, assuming the same simulation parameters in Table 5.1. The coverage areas $\mathcal{A}_j$, for $j = 1, 2, 3, 4$, are obtained based on (5.9). It is observed that the coverage areas significantly deviate from their square shapes whereby each one covers a quadrant of the network for $\theta = 0$, compared with figure 5.1.(a). In fact, figure 5.1 reveals how a UE device with given orientation angles is served by a specific AP in each position of the network. It is also observed from figure 5.2.(c) and figure 5.2.(d) that there is a blue region which is not covered by any of the APs. This is because only the LOS connections with the APs are considered.

Figure 5.3 illustrates the handover probability due to the random movement of UE within the

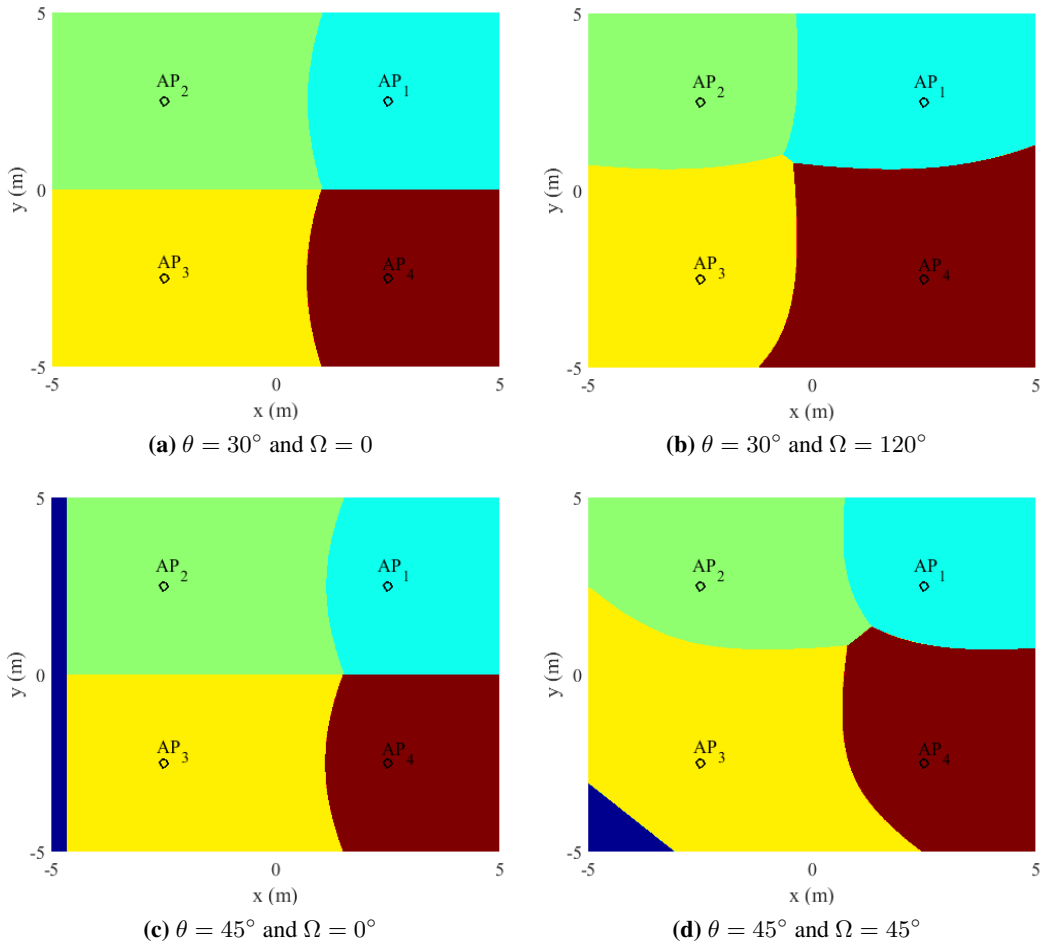

(a) $\theta = 30^\circ$ and $\Omega = 0$

(b) $\theta = 30^\circ$ and $\Omega = 120^\circ$

(c) $\theta = 45^\circ$ and $\Omega = 0^\circ$

(d) $\theta = 45^\circ$ and $\Omega = 45^\circ$

Figure 5.2: *Coverage areas of the four APs for a number of orientation angles.*

network. Here, it is assumed that the UE is initially connected to AP_1 (i.e., the UE picks an initial waypoint from the cyan area as shown in figure 5.2). Also, the angle Ω varies according to the direction of movement, assuming that the user keeps the UE device in the direction of movement when traveling between two consecutive waypoints. This means $\Omega = \tan^{-1}((y_n - y_{n-1})/(x_n - x_{n-1}))$. Given the value for θ, the handover probability is calculated by averaging (5.10) for many random realizations of the waypoints. It is observed from figure 5.3 that the handover probability decreases as the elevation angle increases. The reason for this is that by increasing θ the attocell coverage areas become asymmetric and as a result the handover probability decreases. Note that (5.10) is maximized when the coverage area of all attocells are the same. Further increase of θ, will result in the increase of the blue area (as

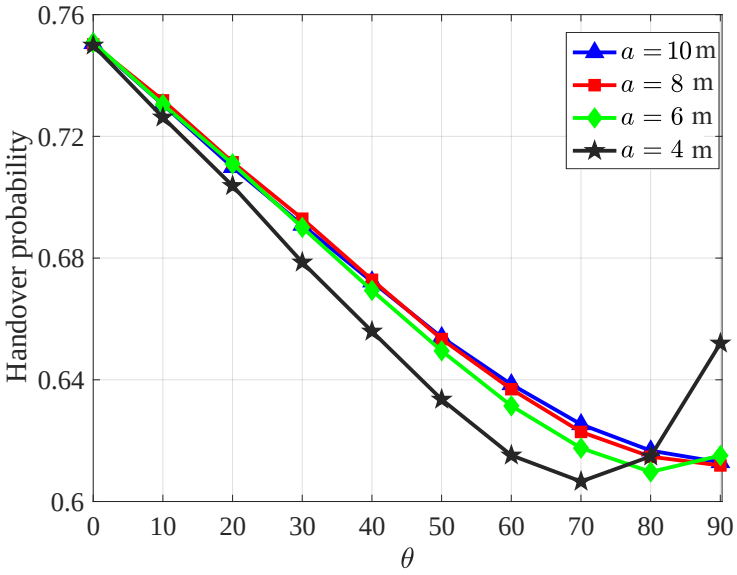

Figure 5.3: *Handover probability due to the random movement of UE within the network as a function of θ for different room lengths.*

shown in figure 5.1-(c) and figure 5.1-(d)) which leads to an increase in the handover rate after a certain point. In other words, the effective areas of other attocells reduce, so according to (5.10), the handover probability due to movement increases. This is more obvious for smaller room sizes. As shown in figure 5.3, for a room size of 4×4 m^2, by increase of the elevation angle, the handover probability decreases initially, then after $\theta = 70^\circ$, the handover probability increases as the area of the blue region increases as well. Note that in Case Study I, it is assumed that the UE is static and does not move, and figure 5.1 shows the average handover probability performance in different positions of the network when Ω is uniformly distributed between 0 and 2π. In contrast, here in figure 5.3, since Ω changes in the direction of movement the effect of Ω is averaged out through the large number of random realizations for different paths that the UE may take within the network area.

5.2.4 Handover Rate

The handover probability gives an idea for how probable the occurrence of handover is at the destination, yet it does not show how many handovers may occur while the UE is on the move. Alternatively, handover rate is a widely used metric in mobile networks to measure how frequent the handovers occur during the movement, and is used in this section. The handover rate is

defined as [63]:

$$\mathcal{H} = \frac{\mathbb{E}[N_{\text{ho}}]}{\mathbb{E}[T_{\text{p}}]}, \tag{5.11}$$

where N_{ho} is the number of handovers occurred during the movement; and T_{p} is the corresponding transition time. The expected number of handovers $\mathbb{E}[N_{\text{ho}}]$ can be calculated as:

$$\mathbb{E}[N_{\text{ho}}] = \mathbb{E}_{X_0,Y_0}\left[\mathbb{E}_{X,Y|X_0,Y_0}\left[N_{\text{ho}}((X,Y)|(X_0,Y_0))\right]\right], \tag{5.12}$$

where $N_{\text{ho}}((X,Y)|(X_0,Y_0))$ denotes the number of handovers occurred between two random waypoints (X_0,Y_0) and (X,Y); $\mathbb{E}_{X,Y|X_0,Y_0}[\,]$ is the expectation with respect to the conditional joint PDF of $(X,Y)|(X_0,Y_0)$; and $\mathbb{E}_{X_0,Y_0}[\,]$ is the expectation with respect to the joint PDF of (X_0,Y_0). Based on the RWP mobility model, the random waypoints (X_0,Y_0) and (X,Y) are independent of each other. Therefore, the above conditional expectation reduces to the expectation with respect to (X,Y). Also, the joint PDFs of (X_0,Y_0) and (X,Y) are given as $f_{X_0,Y_0}(x_0,y_0) = f_{X,Y}(x,y) = 1/a^2$. These simplify (5.12) as:

$$\mathbb{E}[N_{\text{ho}}] = \frac{1}{a^4}\int_{-\frac{a}{2}}^{\frac{a}{2}}\int_{-\frac{a}{2}}^{\frac{a}{2}}\int_{-\frac{a}{2}}^{\frac{a}{2}}\int_{-\frac{a}{2}}^{\frac{a}{2}} N_{\text{ho}}((x,y)|(x_0,y_0))\mathrm{d}x\mathrm{d}y\mathrm{d}x_0\mathrm{d}y_0. \tag{5.13}$$

The transition time in (5.11) is given by $T_{\text{p}} = L/v$, where v is the constant speed; and L is the random transition length [63]. The expected transition time can then be obtained as:

$$\mathbb{E}[T_{\text{p}}] = \frac{\mathbb{E}[L]}{v} = \frac{0.5214a}{v}. \tag{5.14}$$

Case Study II: Handover Rate for $\theta = 0^\circ$

The angle Ω varies according to the direction of movement. Note that this is the special case where the UE receiver is oriented vertically upward. The system configuration and simulation parameters are the same as in Case Study I. Suppose that the UE is initially located in attocell 1. If it moves to either attocell 2 or attocell 4, only one handover occurs, whereas if it moves to attocell 3, two handovers occur. But if the UE takes its path to attocell 3 via the origin then only one handover occurs. However, the probability of such an event is zero. Therefore, $N_{\text{ho}} \in \{1,2\}$, depending on the choice for destination waypoint. Using (5.13), the expected

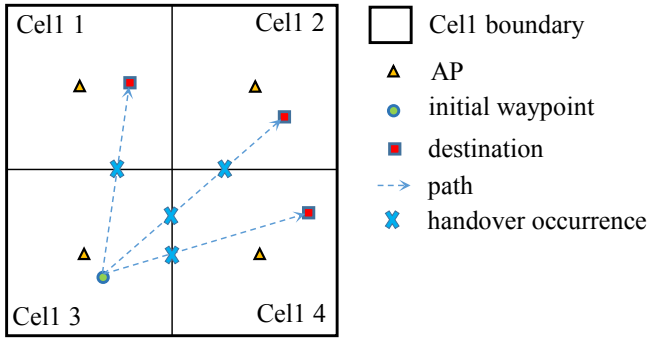

Figure 5.4: *Possible cases of handover when a user is moving from cell 3 to other cells.*

number of handovers in this case is obtained as:

$$\mathbb{E}[N_{\text{ho}}] = \frac{4}{a^4}\left(\int_0^{\frac{a}{2}}\int_{-\frac{a}{2}}^{0}\int_0^{\frac{a}{2}}\int_0^{\frac{a}{2}} \mathrm{d}x_0\mathrm{d}y_0\mathrm{d}x\mathrm{d}y + \int_{-\frac{a}{2}}^{0}\int_0^{\frac{a}{2}}\int_0^{\frac{a}{2}}\int_0^{\frac{a}{2}} \mathrm{d}x_0\mathrm{d}y_0\mathrm{d}x\mathrm{d}y + \int_{-\frac{a}{2}}^{0}\int_{-\frac{a}{2}}^{0}\int_0^{\frac{a}{2}}\int_0^{\frac{a}{2}} 2\mathrm{d}x_0\mathrm{d}y_0\mathrm{d}x\mathrm{d}y\right), \tag{5.15}$$

$$\mathbb{E}[N_{\text{ho}}] = \frac{4}{a^4}\left(\frac{a^4}{16} + \frac{a^4}{16} + \frac{2a^4}{16}\right) = 1. \tag{5.16}$$

In order to make (5.16) more understandable, figure 5.4 shows the possible cases of handover when a user is moving from an initial waypoint in cell 3 to other cells. As it can be seen, 1, 2, 1 and 0 handovers occur if the destination is in cell 1, cell 2, cell 4 or cell 3, respectively. Hence, the expected number of handover can be obtained as:

$$\mathbb{E}[N_{\text{ho}}] = \frac{1}{4}(1+2+1+0) = 1, \tag{5.17}$$

where the factor $1/4$ is because the probability that the UE is going to any other cells is $1/4$ including cell 3.

Combining (5.14) and (5.16) with (5.11), the final expression of the handover rate for this special case is derived as:

$$\mathcal{H} = \frac{1}{0.5214a}v. \tag{5.18}$$

Figure 5.5 shows the handover rate versus the side length a of the network area for different values of the UE speed. The results are obtained based on (5.18) and verified by Monte-Carlo

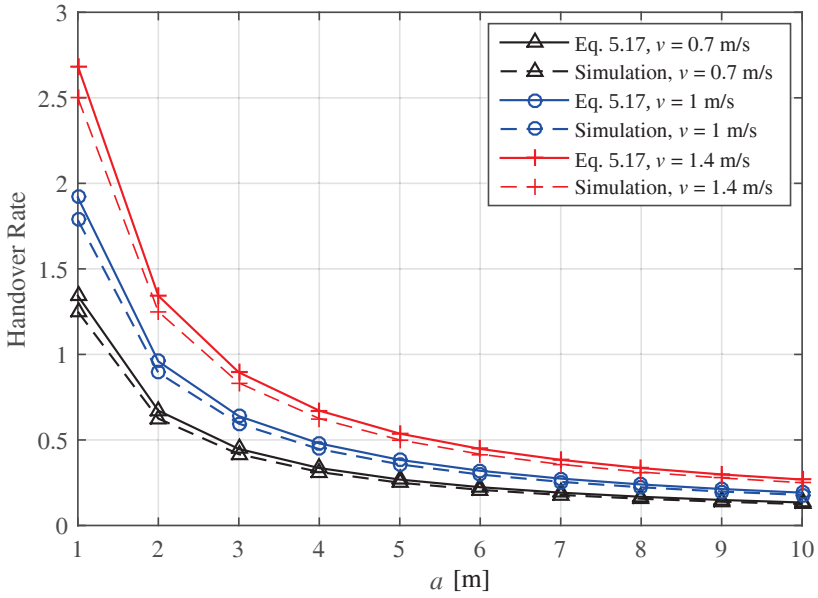

Figure 5.5: *Handover rate as a function of room length, a, for $\theta = 0$.*

simulations. There are three speed values chosen around the average human walking speed which is 1.4 m/s [137]. In figure 5.5, the simulation results closely follow (5.18). The handover rate is decreasing overall, with an increase in the network dimensions. In contrary, as the speed increases, the handover rate increases. This is more significant when the network dimensions are smaller. For $v = 1.4$ m/s, the handover rate is equal to 0.26 in a room of length $a = 10$ m.

5.2.5 Orientation-based Random Waypoint

In the context of LiFi as well as mmWave cellular networks, the effect of a UE's orientation on the performance of the system is significant. In fact, a major change in the UE's orientation, whether individually or combined with the mobility of the user, can lead to a handover that would not normally happen for UEs with a constant orientation. So in order to provide a framework to analyze the performance of mobile wireless networks more realistically, we need to combine the conventional RWP with the random orientation model. The ORWP can be modeled as an infinite sequence of quadruple: $\{(\mathbf{P}_{n-1}, \mathbf{P}_n, v_n, \theta_n)\}_{n\in\mathbb{N}}$, where θ_n is the nth generation of UE's polar angle from waypoint $\mathbf{P}_{n-1}$ to waypoint $\mathbf{P}_n$. More discussions about how to generate these sequences are presented in the next section and the ORWP is summarized in Algorithm 1.

Algorithm 1 Orientation-based random waypoint

Initialization: $n \longleftarrow 1$; $k \longleftarrow 1$;

denote $\mathbf{P}_n = (x_n, y_n)$ as the nth location of UE and $\mathbf{P}_0 = (x_0, y_0)$ as the initial UE's position;

N_{r} as the number of runs;

v as the speed of UE;

$T_{\mathrm{c},\theta}$ as the coherence time of the polar angle;

for $k = 1 : N_{\mathrm{r}}$ **do**

  Choose a random position $\mathcal{P}_k = (x_k, y_k)$

  Compute $\mathcal{D}_k = \|\mathcal{P}_k - \mathcal{P}_{k-1}\|$

  Compute $\Omega = \tan^{-1}\left(\frac{y_k - y_{k-1}}{x_k - x_{k-1}}\right)$

  $t_{\mathrm{move}} \longleftarrow 0$;

  while $t_{\mathrm{move}} \leq \frac{\mathcal{D}_k}{v}$ **do**

    Compute $\mathbf{P}_n = (x_n, y_n)$ with

    $x_n = x_{n-1} + vT_{\mathrm{c},\theta}\cos\Omega$ and $y_n = y_{n-1} + vT_{\mathrm{c},\theta}\sin\Omega$

    Generate θ_n based on the AR(1) model

    Return $(\mathbf{P}_{n-1}, \mathbf{P}_n, v, \theta_n)$ as ORWP specifications

    $n \longleftarrow n + 1$

    $t_{\mathrm{move}} \longleftarrow t_{\mathrm{move}} + T_{\mathrm{c},\theta}$

  end while

  if $t_{\mathrm{move}} \neq \frac{\mathcal{D}_n}{v} - T_{\mathrm{c},\theta}$ & $t_{\mathrm{move}} \geq \lfloor \frac{\mathcal{D}_n}{v} \rfloor T_{\mathrm{c},\theta} - T_{\mathrm{c},\theta}$ **then**

    Generate θ_n based on the AR(1) model

    $\mathbf{P}_n \longleftarrow \mathcal{P}_k$

    Return $(\mathbf{P}_{n-1}, \mathbf{P}_n, v, \theta_n)$ as ORWP specifications

    $n \longleftarrow n + 1$

  end if

  $k \longleftarrow k + 1$

end for

5.2.5.1 Correlated Gaussian Random Process

As shown in section 4.2, the polar angle for walking activities follows a Gaussian distribution. The experimental measurements also illustrate that the adjacent samples of the RP, θ, are correlated. Therefore, in order to incorporate the orientation with the RWP mobility model, it is required to generate a correlated Gaussian RP that statistically matches the experimental measurements. Possible ways of generating a correlated Gaussian RP can be found in [138–142] and references therein. A simple method to generate a correlated Gaussian RP is to pass a white noise through a LTI filter. A straightforward approach to produce a correlated Gaussian RP with a desired ACF is the use of the linear autoregressive (AR) model. Let's denote the white noise by w, then, after passing it through the LTI filter, the nth time sample of the correlated Gaussian RP, θ, is given as:

$$\theta[n] = c_0 + \sum_{i=1}^{p} c_i \theta[n-i] + w[n], \tag{5.19}$$

where c_0 determines the biased level and c_i for $i = 1, \cdots, p$ are constant factors of the AR order of p, AR(p). Note that AR(p) contains $p+2$ unknown parameters including: $c_0, c_1, \cdots, c_p, \sigma_w^2$, where σ_w^2 is the variance of white noise RP, w. Here, we assume $p = 1$ and consider the first-order AR model to generate the correlated Gaussian RP. Thus, the nth sample of the AR(1) model can be expressed as:

$$\theta[n] = c_0 + c_1 \theta[n-1] + w[n], \tag{5.20}$$

where c_1 should meet the condition $|c_1| < 1$ to guarantee the RP, θ, is wide-sense stationary. Noting that for AR(1), the mean, variance and ACF are given as [143]:

$$\mathbb{E}[\theta] = \frac{c_0}{1-c_1}, \qquad \sigma_\theta^2 = \frac{\sigma_a^2}{1-c_1^2}, \qquad \mathcal{R}_\theta(\ell) = c_1^\ell.$$

Using above equations and noting that $\mathcal{R}_\theta(\frac{T_{\mathrm{c},\theta}}{T_\mathrm{s}}) = 0.05$, we have:

$$c_0 = (1-c_1)\mathbb{E}[\theta], \qquad \sigma_a^2 = (1-c_1^2)\sigma_\theta^2, \qquad c_1 = 0.05^{\frac{T_\mathrm{s}}{T_{\mathrm{c},\theta}}}, \tag{5.21}$$

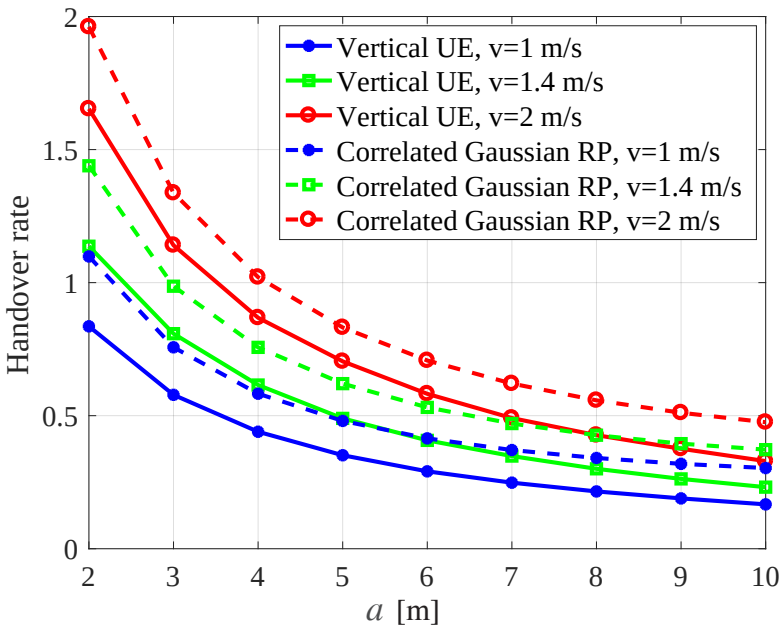

Figure 5.6: *Comparison of handover rate as a function of room length, a, for vertically upward UE and a UE with correlated Gaussian RP for θ.*

where $T_{\mathrm{c},\theta}$ and T_{s} are the coherence time of θ and sampling time, respectively. Once the parameters of the AR(1) model are determined, the nth time sample of the correlated Gaussian RP, θ, can be specified according to (5.20).

Using the method described above, the ORWP is presented in Algorithm 1.

Case Study III: Handover Rate with ORWP

Here, we investigate the effect of the UE's orientation on the handover rate as a case study. Figure 5.6 shows the Monte-Carlo simulations of handover rate as a function of room length for a UE moving at a speed of $v = 1$ m/s, $v = 1.4$ m/s and $v = 2$ m/s. In this simulation setup, four APs are assumed to divide the network area into four separate quadrants (attocells) with one AP at the center of each attocell. The UE is assumed to be initially connected to the corresponding AP denoted as AP_j for $j = 1, 2, 3, 4$. We compared a vertically upward UE (shown by the solid lines in the figure 5.6) with a UE that follows the orientation-based RWP

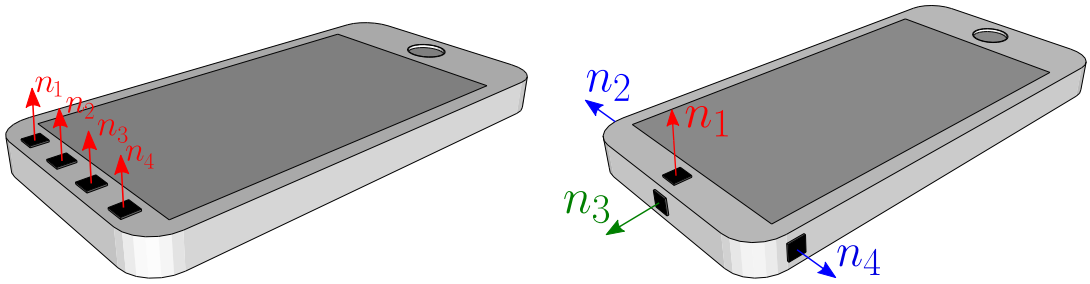

(a) SR **(b)** MDR

Figure 5.7: *The SR and MDR structures for hand-held smartphone.*

mobility model in which the random orientation of the UE is generated based on the correlated Gaussian RP (shown by the dotted line). As can be seen from figure 5.6, the handover rate is decreasing overall with an increase in the network dimensions. On the other hand, as the UE's speed increases, the handover rate increases. This is more remarkable when the network dimensions are smaller. The other observation is that smaller network sizes are more affected by the random orientation of the UE and it leads to more handover rate. That is, as the room length is smaller, the gap between the random orientation and vertically upward scenarios are more.

5.3 Multi-directional Receiver Configuration

In the literature, usually it is assumed that one or multiple PDs are placed on one side of the UE, which can lead to a satisfactory performance level when the UE is placed vertically upward. This conventional design is shown in figure 5.7-(a). Note that PDs may be placed on the screen side of the smartphone with configurations other than the one shown in figure 5.7-(a). In this paper, we assume the configuration shown in figure 5.7-(a) without loss of generality and name it as the SR. Particularly for MIMO, this design is not favorable because the resulting channel matrix is likely to be highly ill-conditioned, and also, the probability that all PDs suffer from poor channel gain at the same time is high.

As we observed in the previous section and also chapter 4, the random orientation and mobility are two important factors that can affect the system performance. In order to support seamless connectivity for mobile users with smartphones, here, we introduce a new MDR configuration.

The MDR configuration can be employed in MIMO optical wireless channels and provides a significant performance improvement. In the conventional configuration, it is assumed that all PDs are placed on the screen of a smartphone, as shown in figure 5.7-(a). However, this results in poor performance due to two issues. First, the resulting channel matrix is likely to have highly correlated entities because PDs are placed close to each other. Second, it is highly likely that some of the transmitters are out of the FOV of all PDs since usually the smartphone is held with an orientation other than upward. These issues are addressed in MDR structure by placing PDs on the screen and three other sides as shown in figure 5.7-(b). Note that another PD can be placed at the back and can be activated instead of the one on the screen for situations where the user is lying on a horizontal surface. We investigate the performance of both structures later. We refer to the structure in figure 5.7-(a) as the SR. It should be noted that, in either structure, since the PDs are located at the top of the smartphone, there is a very low probability that they will be covered by the user's hand when the smartphone is being used.

5.3.1 SNR and BER

It should be mentioned that the MDR configuration can be evaluated in any MIMO system, however, in this thesis, we evaluate the performance of MDR using a SM technique which can provide the spectral and energy efficiency fulfillment of the next generation wireless communications. Moreover, an important benefit of SM is the absence of interference from other transmitter units. Furthermore, a full MIMO system is also considered and the performance of MDR and SR are compared. Following the basic principles of SM, the spatially distributed light sources are utilized to carry data along with the transmitted signal. In the original SM format [144], only one light source is turned on at each time instant. Let $N_{\mathrm{a}} \leq N_{\mathrm{t}}$ be the number of used LEDs, chosen out of N_{t} LEDs. Thus, by activating only one LED at each channel use, $\log_2(N_{\mathrm{a}})$ bits (the spatial information) are transmitted by SM. The transmitted symbol by an individual LED is also encoded by an M-ary PAM (M-PAM) constellation. Therefore, the spectral efficiency is $R = \log_2(M) + \log_2(N_{\mathrm{a}})$ bits/sec/Hz. Note that, unlike spatial multiplexing (i.e., full MIMO), even one PD can be sufficient for signal detection because only differences between all possible symbols determine the system performance. This highlights the benefit of SM which is simple and is capable of potentially satisfying communication requirements when some PDs are

blocked and not available.

Here, we consider activating one of the available N_{a} LEDs with an M-PAM modulation format, which results in a total of $K = MN_{\mathrm{a}}$ symbols. The intensity levels of M-PAM are given by:

$$I_m = \frac{2P_{\mathrm{opt}}}{M+1}m, \quad \text{for } m = 1, \ldots, M, \tag{5.22}$$

where P_{opt} is the average emitted optical power. Therefore, one of the available N_{a} LEDs transmits one of the M levels at each channel use, and the input vector $\mathbf{x} = \mathbf{s}_k$, $k = 1, ..., K$, is chosen from the columns of the $N_{\mathrm{a}} \times K$ matrix $\mathbf{S} = [I_1\mathbf{I}_{N_{\mathrm{a}}}\ I_2\mathbf{I}_{N_{\mathrm{a}}}\ \cdots I_M\mathbf{I}_{N_{\mathrm{a}}}]$, where $\mathbf{I}_{N_{\mathrm{a}}}$ is the square unity matrix of size N_{a}. At the Rx, Maximum-Likelihood (ML) detection is performed. An error occurs whenever a transmitted vector $\mathbf{s}_1$ is detected mistakenly as another vector $\mathbf{s}_2$. The pairwise error probability (PEP) is defined as [55]:

$$\mathrm{PEP} = Q\left(\sqrt{\frac{\mathcal{S}_{\mathrm{Tx}}}{4P_{\mathrm{opt}}^2}\|\mathbf{H}(\mathbf{s}_1 - \mathbf{s}_2)\|^2}\right), \tag{5.23}$$

where $\mathcal{S}_{\mathrm{Tx}}$ is the average transmit SNR, and $\mathrm{Q}(\cdot)$ is the Q-function. The transmit SNR is defined as $\mathcal{S}_{\mathrm{Tx}} = \frac{E_{\mathrm{s}}}{N_0}$, where E_{s} is the mean emitted electrical energy. Note that in (5.23), $\mathbf{s}_k$'s include P_{opt}. We define the received SNR $\mathcal{S}_{\mathrm{Rx}}$ by considering the received signal energy as the total received signal energies at all N_{r} PDs. Therefore, the received SNR can be expressed as [55]:

$$\mathcal{S}_{\mathrm{Rx}} = \frac{\mathcal{S}_{\mathrm{Tx}}}{N_{\mathrm{a}}^2}\sum_{i=1}^{N_{\mathrm{r}}}\left(\sum_{j=1}^{N_{\mathrm{a}}} h_{i,j}\right)^2. \tag{5.24}$$

The upper bound on the BER can be derived using the union bound method as [55]:

$$\mathrm{BER}\left(M, E_{\mathrm{s}}, \mathbf{H}\right) \simeq \frac{1}{K\log_2(K)}\sum_{k_1=1}^{K}\sum_{k_2=1}^{K}\mathrm{d_H}(b_{k_1}, b_{k_2})Q\left(\sqrt{\frac{\mathcal{S}_{\mathrm{Tx}}}{4P_{\mathrm{opt}}^2}||\mathbf{H}(\mathbf{s}_{k_1} - \mathbf{s}_{k_2})||^2}\right), \tag{5.25}$$

where $\mathrm{d_H}(b_{k_1}, b_{k_2})$ is the Hamming distance between the two bit allocations of b_{k_1} and b_{k_2} corresponding to signal vectors $\mathbf{s}_{k_1}$ and $\mathbf{s}_{k_2}$. It has been shown in the literature [55] and later in this chapter that (5.25) is a tight bound at high SNR. It can be seen from (5.23) and (5.25) that the error performance of SM directly depends on the channel matrix which determines the

Parameter	Symbol	Value	Parameter	Symbol	Value
Receiver FOV	Ψ	60°	Ceiling height	h_{z}	3 m
LED half-power semiangle	Φ	60°	Reflectivity factor of walls	ρ_{w}	0.6
PD responsivity	R_{PD}	1 A/W	Reflectivity factor of the floor	ρ_{f}	0.2
Physical area of a PD	A	0.25 cm^2	Reflectivity factor of the ceiling	ρ_{c}	0.8
UE height (sitting)	h_{r}	0.8 m	Length of the blockers	L_{b}	0.7 m
UE height (walking)	h_{r}	1.4 m	Width of the blockers	W_{b}	0.2 m
Light source height	h_{t}	2.95 m	Height of the blockers	H_{b}	1.75 m
Room dimensions	$h_{\mathrm{x}} \times h_{\mathrm{y}}$	5 m×5 m	UE distance from user	d_{p}	0.3 m

Table 5.2: *Downlink simulation parameters.*

differentiability between signal vectors.

5.3.2 Mobility Evaluation

Performance analysis with consideration of user mobility is crucial in the design of wireless communication networks. In order to provide a more realistic framework for analyzing the performance of mobile wireless networks in LiFi, we consider the ORWP mobility model that was introduced in section 5.2.5, where the elevation angle of the UE is included during user's movement. An altered version of ORWP (where α, β and γ are encompassed) is used in this section to evaluate the system performance metrics (such as received SNR) for mobile users having several PDs on different sides of the smartphone. The ORWP can be modeled as an infinite sequence of quadruples, $\left\{(\mathbf{P}_{n-1}, \mathbf{P}_n, v_n, \mathbf{\Theta}_n) \,\middle|\, n \in \mathbb{N}\right\}$, where $\mathbf{\Theta}_n = (\alpha_n, \beta_n, \gamma_n)$ is a random vector process describing the UE's orientation during the movement from waypoint $\mathbf{P}_{n-1}$ to waypoint $\mathbf{P}_n$. The entities, α, β and γ are random processes. The ORWP is summarized in Algorithm 2.

It is shown in Section 4.2 that α, β and γ for walking activities follow a Gaussian distribution with the parameters given in Table 4.1. According to the experimental measurements, the adjacent samples of the RPs α, β and γ are correlated. Hence, to incorporate the device orientation with the RWP mobility model, a correlated Gaussian RP which statistically follows the experimental measurements should be generated. It should be noted that the random orientation process considered here can be applied to any other mobility models. Here, we use the moments

obtained through experimental measurements. Hence, a first-order AR model is sufficient to be considered for generating the correlated Gaussian RP as the mean and variance of the produced samples match the measurement results. The kth sample of the AR(1) model is given as:

$$\alpha[k] = c_0 + c_1\alpha[k-1] + w[k]. \tag{5.26}$$

To guarantee the RP α is wide-sense stationary, the condition $|c_1| < 1$ should be fulfilled. The mean, variance and autocorrelation function of AR(1) are given respectively as [143]:

$$\mu_\alpha = \frac{c_0}{1-c_1}, \qquad \sigma_\alpha^2 = \frac{\sigma_w^2}{1-c_1^2}, \qquad \mathcal{R}_\alpha(k) = c_1^k.$$

Note that $\mathcal{R}_\alpha(\frac{T_{\mathrm{c},\alpha}}{T_\mathrm{s}}) = 0.05$ where $T_{\mathrm{c},\alpha}$ is the coherence time of α and T_s is the sampling time [10]. Using the above equations:

$$c_0 = (1-c_1)\mu_\alpha, \qquad \sigma_w^2 = (1-c_1^2)\sigma_\alpha^2, \qquad c_1 = 0.05^{\frac{T_\mathrm{s}}{T_{\mathrm{c},\alpha}}}. \tag{5.27}$$

Then, the kth time sample of the correlated Gaussian RP, α, can be obtained based on (5.26) and using the parameters of the AR(1) model given in (5.27). The same approach can be applied to both β and γ to determine the kth time sample of the device orientation, $\mathbf{\Theta}_n[k] = (\alpha_n[k], \beta_n[k], \gamma_n[k])$. According to the approach explained above, the ORWP is described in Algorithm 2.

Algorithm 2 ORWP for MDR

Initialization: $n \longleftarrow 1$; $k \longleftarrow 1$;
Denote $\mathbf{P}_n = (x_n, y_n)$ and $\mathbf{P}_0 = (x_0, y_0)$ as the nth and initial UE's positions, respectively; N as the number of simulation runs; v as the average speed of UE; $T_{\mathrm{c},\alpha}$, $T_{\mathrm{c},\beta}$ and $T_{\mathrm{c},\gamma}$ as the coherence time of α, β and γ, respectively; Set $T_{\mathrm{c}} = \min\{T_{\mathrm{c},\alpha}, T_{\mathrm{c},\beta}, T_{\mathrm{c},\gamma}\}$;
μ_α, μ_β and μ_γ as the mean and σ_α^2, σ_β^2 and σ_γ^2 as the variance of Gaussian RPs α, β and γ;
for $n = 1 : N$ **do**
  Choose a random location $\mathcal{P}_n = (x_n, y_n)$
  Compute $\mathcal{D}_n = \|\mathcal{P}_n - \mathcal{P}_{n-1}\|$
  Compute $\Omega = \tan^{-1}\left(\frac{y_n - y_{n-1}}{x_n - x_{n-1}}\right)$
  $t_{\mathrm{move}} \longleftarrow 0$;
  while $t_{\mathrm{move}} \leq \frac{\mathcal{D}_n}{v}$ **do**
    Compute $\mathbf{P}_k = (x_k, y_k)$ with $x_k = x_{k-1} + vT_{\mathrm{c}}\cos\Omega$ and $y_k = y_{k-1} + vT_{\mathrm{c}}\sin\Omega$
    Generate $\mathbf{\Theta}_k = (\alpha_k, \beta_k, \gamma_k)$ based on the AR(1) model
    Return $(\mathbf{P}_{k-1}, \mathbf{P}_k, v, \mathbf{\Theta}_k)$ as ORWP specifications
    $k \longleftarrow k + 1$
    $t_{\mathrm{move}} \longleftarrow t_{\mathrm{move}} + T_{\mathrm{c}}$
  end while
  if $t_{\mathrm{move}} \neq \frac{\mathcal{D}_n}{v} - T_{\mathrm{c}}$ & $t_{\mathrm{move}} \geq \lfloor \frac{\mathcal{D}_n}{v} \rfloor T_{\mathrm{c}} - T_{\mathrm{c}}$ **then**
    Generate $\mathbf{\Theta}_k = (\alpha_k, \beta_k, \gamma_k)$ based on the AR(1) model
    $\mathbf{P}_k \longleftarrow \mathcal{P}_n$
    Return $(\mathbf{P}_{k-1}, \mathbf{P}_k, v, \mathbf{\Theta}_k)$ as ORWP specifications
    $k \longleftarrow k + 1$
  end if
  $n \longleftarrow n + 1$
end for

5.4 Simulation Results

We consider a typical indoor environment. Although the results may change slightly in other scenarios, it is expected that the same behavior will be observed provided that the main charac-

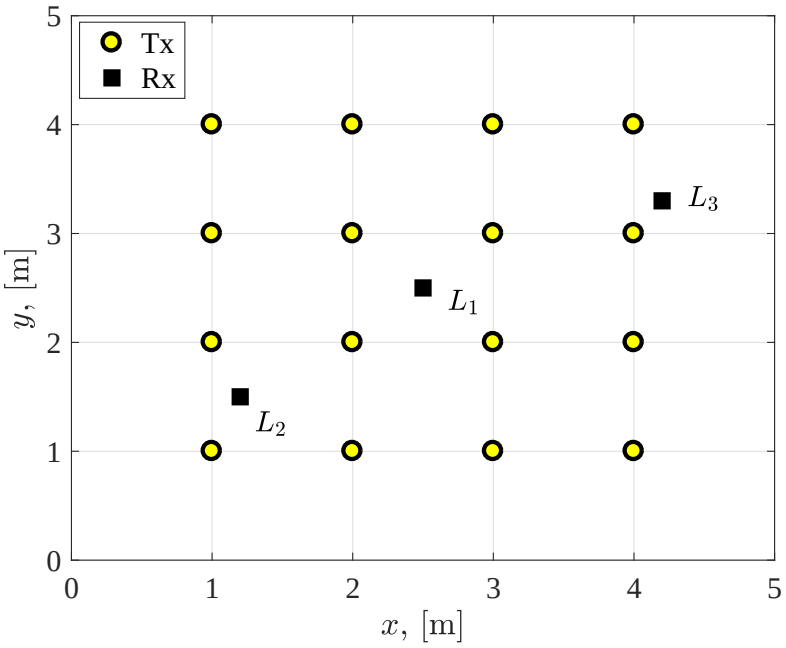

Figure 5.8: *Room geometry and transmitters arrangement.*

teristics of the environment, such as transmitter separation, the room dimensions and the ceiling height, etc., do not vary dramatically. Figure 5.8 shows the geometric configuration of the transmitters which are arranged on the vertexes of a square lattice over the ceiling of an indoor environment. We use this configuration for the rest of this chapter, where 16 LED transmitters are considered in a room of $5 \times 5 \times 3$ m^3. Transmitters are oriented vertically downward, while the receivers may have a random orientation. The rest of the simulation parameters are given in Table 5.2. It is noted that the FOV is set to 60° in this chapter, however, this will not affect the generality of the results and final conclusions. The dimensions of the smartphone are $14 \times 7 \times 1$ cm^3. As shown in figure 5.7, the PDs on the screen are placed 1 cm from the top edge, one PD for MDR at the center is considered, and 4 PDs for SR are uniformly distributed. For MDR, the PD associated with $\mathbf{n}_3$ is placed at the center of the corresponding side, and PDs shown by $\mathbf{n}_2$ and $\mathbf{n}_4$ are placed 1.5 cm from the top edge of the smartphone.

5.4.1 The Effect of Blockage and Random Orientation

Here, we investigate the effect of low and high density receiver blockage, fixed orientation versus random orientation, and the effect of the NLOS channel component. The density of a non-user blocker is denoted by κ_{b}. First, an example scenario is considered at the middle of the room (i.e., location L_1 in figure 5.8) with fixed AP allocation with $N_{\mathrm{a}} = 4$ and spectral efficiency $R = 5$ bits/sec/Hz. The user direction is $\Omega = 90^{\circ}$. The APs are determined by measuring the received power from each AP, and the strongest $N_{\mathrm{a}} = 4$ APs, i.e., the ones corresponding to the highest received power at the user position, are selected. The results are shown in figure 5.9 for both BER approximation in (5.25) (solid lines) and Monte-Carlo simulations (markers). Note that the statistics of random orientation for sitting activities are used according to Table 4.1 for Laplace distribution.

It is observed in figure 5.9 that the simulation results match the BER approximation at around $\mathrm{BER} \geq 10^{-2}$ for both cases. The performance of both SR and MDR is significantly degraded when the NLOS channel gains are ignored because it is highly likely that the channel gains for some of the APs are zero due to blockage or limited FOV. In such a case, the information will be lost, and the BER saturates at high SNR. The BER approximation (5.25) is not valid in this case and is not shown in figure 5.9. When the NLOS gain is included, the performance of MDR is always better than SR with SNR gains up to 12 dB at target BER 3.8×10^{-3}. For SR, the performance with random orientation is slightly worse than the fixed orientation with blockage parameter $\kappa_{\mathrm{b}} = 0.2$. This happens because the strongest links are chosen at each random orientation, and in the middle of the room some "good" links are almost always found which lead to this performance. However, when the blockage parameter is increased, the BER also degrades for SR. On the other hand, both random orientation and increased blockage are beneficial for MDR since the induced randomness increases the differentiability between spatial symbols, which consequently leads to better performance. Overall, it can be seen that the proposed MDR structure is robust against random orientation and blockage, and exhibits superior performance compared to the conventional SR.

Another location, L_3 in figure 5.8, is also considered with user direction $\Omega = 180^{\circ}$. In this case the user is facing the room and the UE screen is facing the wall. The results are shown

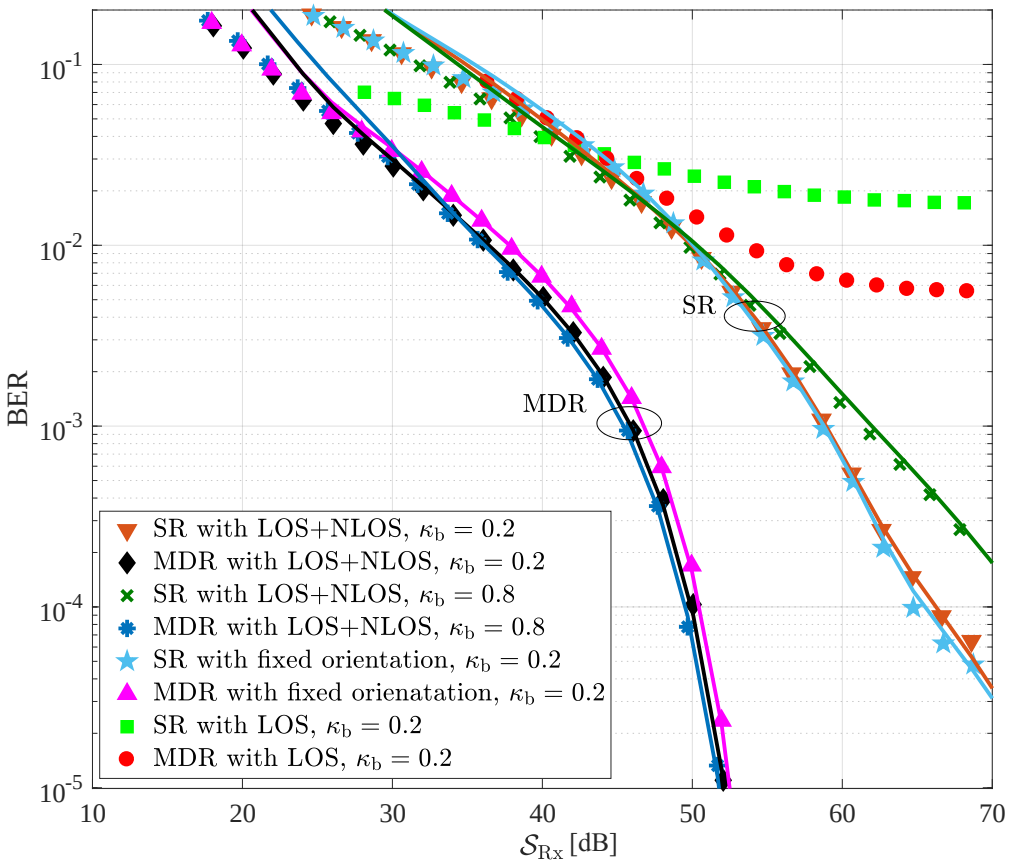

Figure 5.9: *Performance comparison of SR and MDR for UE's location of L_1 and direction of $\Omega = 90^\circ$ versus the required SNR, $\mathcal{S}_{\mathrm{RX}}$. Marks denote Monte-Carlo simulation results and solid lines are based on the BER upper bound given in* (5.25).

in figure 5.10. In this scenario the effect of the NLOS channel gain is much more significant. Note that, unlike L_1, the channel matrix is non-symmetric at L_3, which generally leads to better performance compared to L_1. For SR, both random orientation and higher blockage density cause worse performance, and this is severe because "good" links are limited in the vicinity of the walls. Again, MDR outperforms SR in any condition, and demonstrates a robust performance against random orientation and blockage. In figure 5.10, the random orientation has a negligible effect on the performance of MDR, but the link blockage adversely affects the BER performance. This happens because the channel matrix is already non-symmetric, and blockage slightly worsens the channel matrix. The results shown in Figs. 5.9 and 5.10 confirm that the

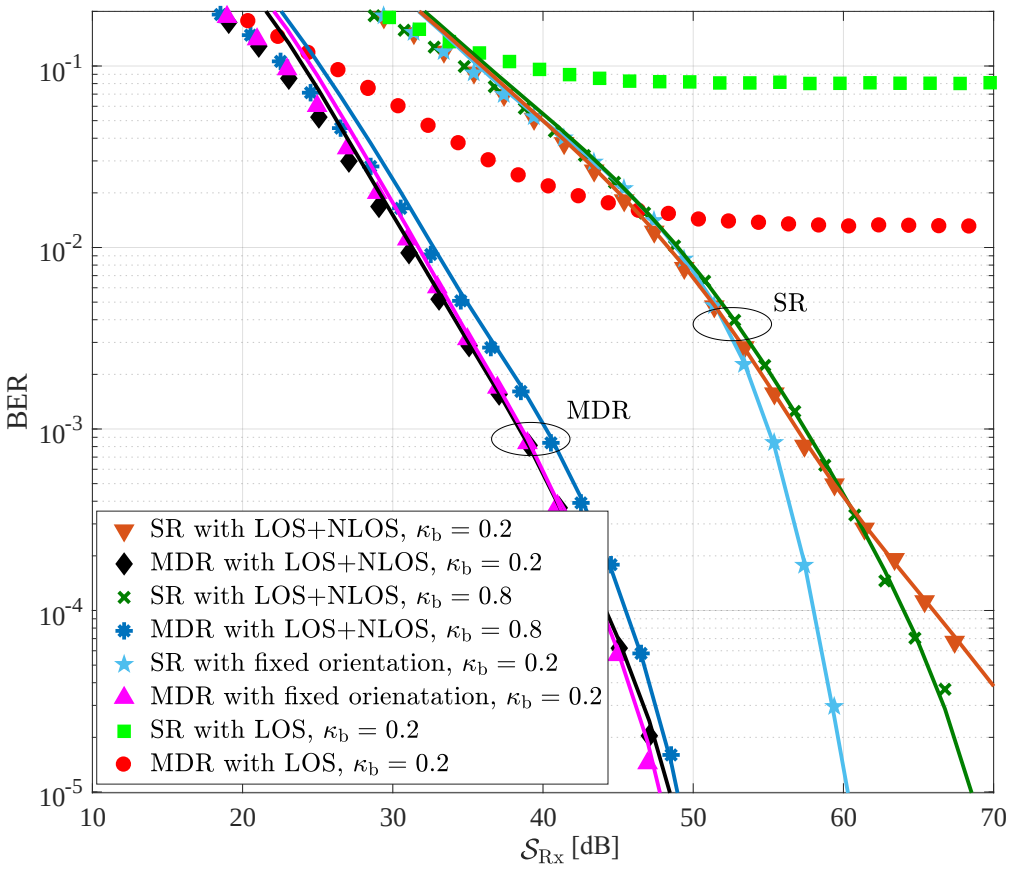

Figure 5.10: *Performance comparison of SR and MDR for UE's location of L_3 and direction of $\Omega = 180°$ versus the required SNR, $\mathcal{S}_{\mathrm{RX}}$. Marks denote Monte-Carlo simulation results and solid lines are based on the BER upper bound given in* (5.25).

proposed MDR outperforms SR and is robust against random orientation and blockage. However, the exact performance depends on the user location. This will be investigated later, but first the effect of AP selection is studied in the next subsection.

5.4.2 AP Selection

In the previous subsection, the number of selected APs was fixed and the APs were selected based on the received power at the UE location, user direction and UE orientation. It is expected that the choice of parameter N_{a} can affect the performance of the system with fixed target BER and spectral efficiency. Therefore, the BER performance of MDR and SR are shown in figure

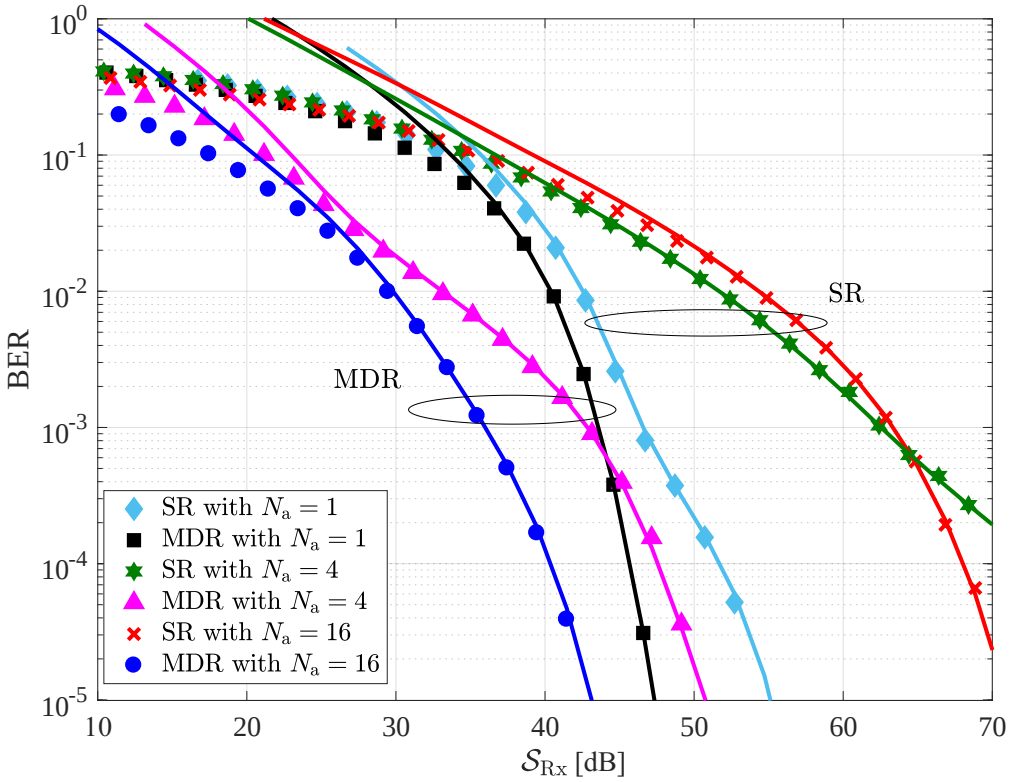

Figure 5.11: *Performance comparison of SR and MDR for UE's location of L_2 and direction of $\Omega = 0°$ versus the required SNR, $\mathcal{S}_{\mathrm{RX}}$. Markers denote Monte-Carlo simulation and solid lines are based on the BER approximation given in* (5.25).

5.11 for position L_2 (see figure 5.8) with $\Omega = 0°$ for $R = 5$ bits/sec/Hz for $N_{\mathrm{a}} = 1, 4, 16$. It is observed that the BER varies for each choice of N_{a}. For MDR, $N_{\mathrm{a}} = 16$ achieves the best performance while $N_{\mathrm{a}} = 1$ is the best choice for SR in this specific scenario.

Figure 5.11 is an example which highlights the importance of AP selection. A simple method is proposed based on this observation, and an adaptive SM (ASM) is defined. The parameter N_{a} is determined at each user position, direction, and UE orientation in order to select the one associated with the minimum energy requirement at the target BER 3.8×10^{-3}. This simple method is performed by calculating the required $\mathcal{S}_{\mathrm{RX}}$ based on BER approximation (5.25) which is a tight approximation for the target BER.

In order to evaluate the performance of the proposed adaptive SM, the room area is divided

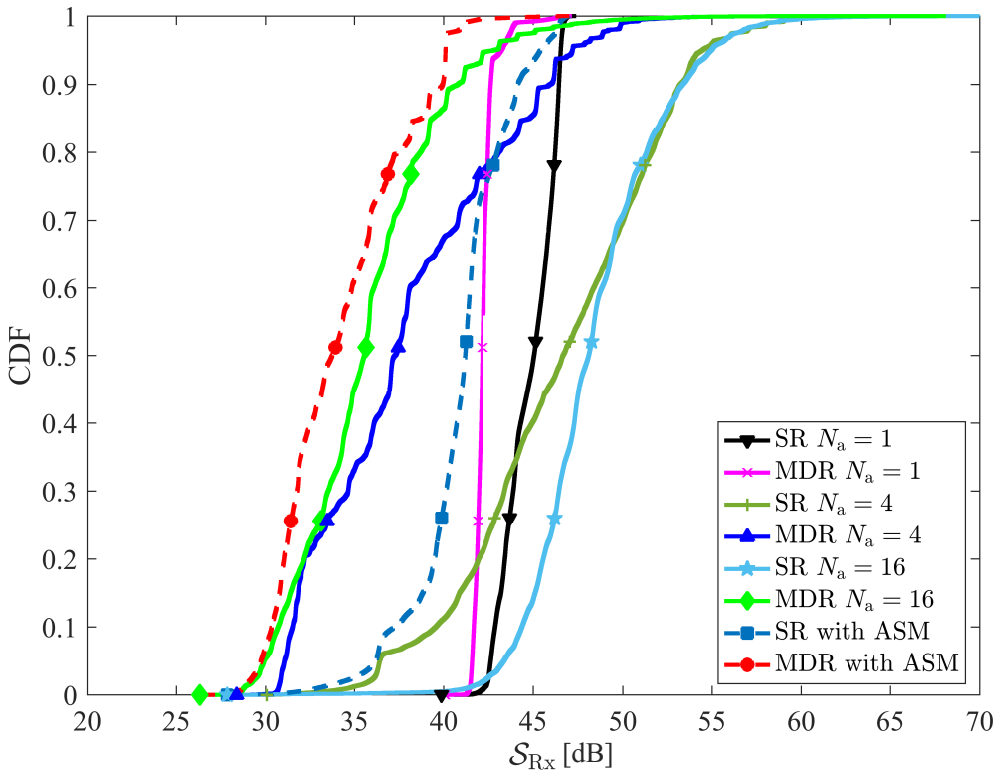

Figure 5.12: *Performance comparison of SR and MDR for all UE's locations and directions in the room versus the required SNR,* $\mathcal{S}_{\mathrm{RX}}$.

into uniformly distributed points that are 25 cm apart in x and y directions. At each point, 24 user directions (every 15°) are used, and 500 random orientation angles are generated for each user position and direction. The CDF of the required received SNR over the room is demonstrated in figure 5.12 for MDR and SR structures. Fixed AP numbers of $N_{\mathrm{a}} = 1$, 4 and 16 are depicted along with the adaptive method, in which the optimum number is determined from $N_{\mathrm{a}} \in \{1, 2, 4, 8, 16\}$ for each user position, direction, and UE orientation. As expected, the minimum energy consumption is achieved by using this simple adaptive method, and MDR significantly outperforms SR. However, it can be seen that the CDF of the received SNR for ASM with the MDR method is close to a fixed $N_{\mathrm{a}} = 16$. This indicates that whenever the complexity is a limiting factor, fixing $N_{\mathrm{a}} = 16$ can be used for MDR. However, a similar statement is not applicable to SR.

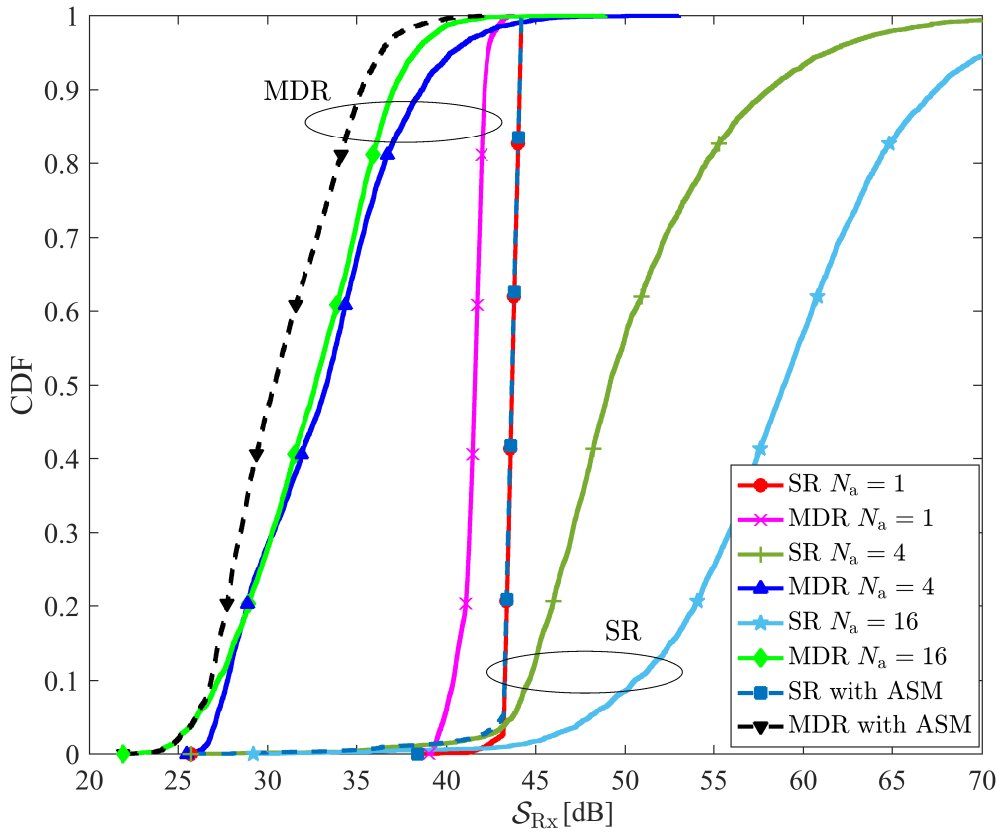

Figure 5.13: *Performance comparison of SR and MDR for mobile users based on RWP mobility model versus the required SNR, $\mathcal{S}_{\mathrm{RX}}$.*

The simple adaptive algorithm used for the sitting scenario before is also incorporated here in conjunction with the ORWP model. About 500 random waypoints are generated and the user walks between these points with a constant speed of 1 m/s (the choice of $v = 1$ m/s is because of the average walking speed of human [26]). The required received SNRs are calculated along the user's route for $N_{\mathrm{a}} \in \{1, 2, 4, 8, 16\}$ and the adaptive scheme for a target BER of 3.8×10^{-3} and spectral efficiency of $R = 5$ bits/sec/Hz. The results are shown in figure 5.13 for $N_{\mathrm{a}} = 1, 4, 16$ and ASM. Note that ASM is carried out with the choice of $N_{\mathrm{a}} \in \{1, 2, 4, 8, 16\}$ for each channel realization. It can be seen that once again the MDR method significantly improves the performance. The ASM for SR does not change the required SNR value compared to $N_{\mathrm{a}} = 1$, and therefore, $N_{\mathrm{a}} = 1$ is almost optimal for SR in the walking scenario. However, MDR with ASM improves the performance by about 2 dB as compared to a fixed $N_{\mathrm{a}} = 16$.

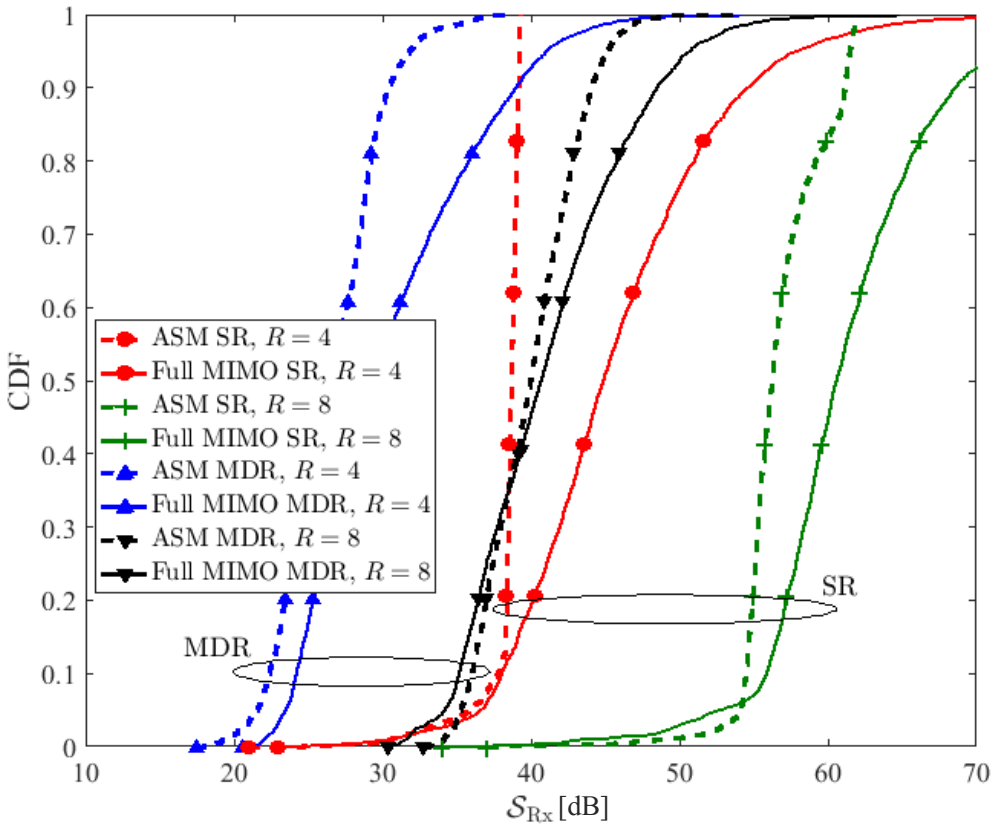

Figure 5.14: *Performance comparison of SR and MDR for mobile users with ASM and full MIMO utilization versus the required SNR,* $\mathcal{S}_{\mathrm{RX}}$.

In figure 5.14, the CDF of the required received SNR is simulated for ASM for MDR and SR for two different spectral efficiency values, namely, $R = 4$ and 8 bits/sec/Hz. Moreover, a 4×4 full MIMO (i.e., spatial multiplexing) is also considered with both structures. For the full MIMO, the strongest 4 APs are selected for each channel realization, and the required received SNR is calculated using the union bound method for the BER approximation [55]. Interestingly, it is observed that the proposed ASM method outperforms the full MIMO system. As expected, a higher spectral efficiency demands more received SNR in any case. However, by using MDR, $R = 8$ bits/sec/Hz can be achieved at similar SNRs compared to SR with $R = 4$ bits/sec/Hz at the target BER. This confirms the advantage of using MDR. By increasing the spectral efficiency, the difference between the ASM and full MIMO system reduces. Clearly, the full MIMO system also benefits from the improved channel condition in MDR. Thus, in high spectral efficiencies

the full MIMO can be the adopted modulation scheme as it uses spatial degrees of freedom more efficiently [145].

5.5 Summary

Handover performance for indoor LiFi cellular networks was evaluated. It was found that the receiver rotation and user mobility have a significant effect on the handover performance. Then, the effects of mobility, random orientation and blockage on indoor optical MIMO were investigated while adopting a channel model derived from real-life measurements. A new user device configuration, called MDR was proposed to overcome the problems such as random device orientation, blockage and high channel correlation. In addition, an adaptive SM scheme based on AP selection for downlink was proposed to reduce power consumption with the consideration of random device orientation, mobility and blockage. It was shown that MDR structures provide a superior performance in terms of SNR, BER and energy efficiency and significantly outperform their counterpart SR configurations.

Chapter 6
Conclusions, Limitations and Future Research

6.1 Summary and Conclusions

In this research thesis, an analysis of user mobility and device orientation in LiFi networks to support seamless connectivity was presented. It was observed that LiFi channels are relatively deterministic. This feature permits the users to not only transmit a low amount of feedback to the AP but also transmit the feedback information infrequently. The lack of a proper model for device orientation motivated us to carry out a set of experimental measurements to provide a new model for device orientation. In this thesis, the orientation model was assessed in a LiFi network and its effect has been evaluated on the LOS channel gain, SNR and BER. It should be noted that this model can be also used in mmWave networks as the device orientation can affect the user's QoS. It was shown that besides user mobility, device orientation is also one of the main factors of handover in a LiFi network. In order to provide a more realistic mobility model for LiFi systems, we proposed the ORWP mobility model that includes the random device orientation during the user's movement. An analysis of handover with user mobility, device orientation and the ORWP model was presented in this research. Finally, an MDR configuration was proposed to address the challenges of user mobility, device orientation and link blockage. The robustness of the MDR configuration was confirmed and it can be considered as a promising solution to provide seamless connectivity in LiFi networks. In summary the three main findings of this research thesis are mentioned as follow.

• Reducing the amount of feedback in LiFi networks to improve bidirectional user throughput. Specifically, two limited-feedback mechanisms called LCF and LFF are proposed. The former is based on reducing the content of feedback information while the latter is based on the update interval.

• Providing a model for device orientation supported by experimental measurements. The statis-

tics of device orientation for both sitting and walking activities are derived. This allows us to calculate the statistics of channel gain and SNR in LiFi systems.

• Supporting seamless connectivity in LiFi networks in the presence of user mobility, device orientation and blockers in the environment. A new configuration called MDR structure to support seamless connectivity is proposed. In MDR, PDs are placed on different sides of a smartphone. The performance of MDR is compared with the conventional configuration in which the PDs are located on one side of a smartphone, e.g., on screen side.

In chapter 2, the relevant background related to LiFi channels and networks was presented. We first provided a brief introduction and history of VLC and LiFi systems. Then, the LiFi channel model was described, which included the effect of both front-end elements and the effect of an indoor LiFi channel. The LOS and NLOS gains have been explained and an analysis of noise encompassing shot noise and thermal noise have been presented. O-OFDM, which is an effective way of combating the ISI in LiFi networks, was described. DCO-OFDM and ACO-OFDM as two of the most well-known and common types of O-OFDM were explained. The basic concept of LiFi cellular networks and attocells were provided. Then, TDMA and OFDMA as the most common multiuser access techniques in the downlink and CSMA/CA as a promising option for the uplink were described. The concept of handover was explained, and different types of handover were discussed. Finally, factors which can affect the user throughput in a LiFi system such as user mobility, device orientation and blockage were explained.

In the third chapter, a modified CSMA/CA for uplink was proposed, in which the AP transmits a CB tone to inform other users that the channel is already occupied. It was shown that the CB tone can alleviate the problem of severe hidden nodes in LiFi networks. Then, based on the relatively deterministic feature of LiFi channels, two methods for reducing the feedback cost were proposed: i) the LCF scheme, and ii) the LFF method. The former was based on reducing the content of feedback information by only sending the SINR of the first subcarrier and estimating the SINR of other subcarriers at the AP. The latter was based on the less frequent transmission of feedback information. The optimal update interval was derived, which results in a maximum expected sum-throughput of uplink and downlink. The effect of different parameters on the optimum update interval was studied. It was also shown that the proposed LCF and LFF schemes provide better sum-throughput while transmitting a lower amount of feedback

compared to the practical one-bit feedback method.

In chapter 4, a new model for device orientation based on the experimental measurements was proposed. The experimental measurements were taken from 40 participants creating 222 datasets for device orientation. It was shown that the PDF of the polar angle follows a Laplace distribution for static users while it is better fitted to a Gaussian distribution for mobile users. A similar observation was confirmed through PDF fitting and KSD test for the elemental rotation angles, i.e., α, β and γ. We proposed an approximation PDF using the truncated Laplace distribution and the accuracy of this approximated method was confirmed by using the KSD test. The LOS channel gain statistics were calculated. Then, we analyzed the device orientation and assessed its importance on channel gain. The PDF of SNR for a randomly-orientated device was derived, and based on the derived PDF, the BER performance of DCO-OFDM in AWGN channels with a randomly-orientated UE was evaluated. An approximation for the average BER of randomly-oriented UEs was calculated that closely matches the exact one. The role of the CE angle that guarantees having LOS link in the UEs FOV was investigated. Furthermore, the impact of being optimally tilted towards the AP on the BER performance was shown. Finally, the channel gain was described as a random process for which the coherence time was discussed.

In the fifth chapter, handover modeling for indoor LiFi cellular networks was proposed. We investigated the effect of both user mobility and device orientation on the handover probability and handover rate. It was found that the receiver orientation has a significant effect on the handover performance. By means of the AR(1) model, a new ORWP mobility model was proposed that considers the random orientation of a device during user's movement. Then, to support seamless connectivity, a new user device configuration, called MDR was proposed, in which the photodiodes are located on different sides of the UE. The effects of mobility, random orientation and blockage on the received SNR and BER performance of the MDR configuration in MIMO systems were investigated while adopting a channel model based on the experimental measurements of device orientation. In addition, an adaptive SM scheme based on AP selection was proposed to overcome the effect of random orientation and blockage and to reduce power consumption. It was shown that MDR provides superior performance in terms of SNR and BER, and significantly outperforms its counterpart SR configuration.

6.2 Limitations and Future Research

In chapter 3, the feedback information is assumed to be the SINR at the receiver. However, other metrics such as interference level, user location and/or device orientation may be also considered as the feedback information. It is noted that the major factor for update interval calculation is the user mobility and that is why the device orientation and blockage are not considered. LFF with random orientation and blockage is another topic for future research. Furthermore, the combination of the LCF with the update interval can be considered as another topic of future studies.

In chapter 4, since there is no built-in LiFi receiver in smartphones yet, we had to start one step behind by measuring and analyzing the device orientation and its statistics. However, a future vision would be measuring the channel gain with random orientation of the device, once a LiFi-enabled smartphone is available. Developing a framework for analyical derivations of NLOS channel gain statistics is also one of the other future research study. In fact, using the frequency domain analysis as explained in chapter 2, the statistics of infinite number of reflection orders can be obtained. Next, to have a vision about the similarity of the analysis and experimental measurements, one can also plan to measure the NLOS channel gain through the experiments. Moreover, the combination of LOS and NLOS statistics can provide an accurate model for SNR and BER analysis, which can be compared with the experimental measurements of the SNR and BER. This could also be a future research topic.

It is noted that even though we considered DCO-OFDM for analysis of BER, the methodology could be readily extended to other modulation schemes, which could be the focus of future studies. Furthermore, other performance metrics such as outage probability, throughput and users quality of service can also be assessed under random device orientation.

In chapter 5, the extended analysis of the RSI-based and bandwidth-based handover mechanisms in LiFi networks can be considered for future research. Soft-handover protocols can further help to improve seamless connectivity. Therefore, development of a new handover protocol based on soft-handover mechanisms that can reduce the ping-pong effect due to random orientation for cell-edge users is another future perspective.

Regarding the MDR configuration, a future extension could be a joint optimization of the uplink and downlink, especially if the channel gains are available at the transmitter. On the other hand,

recall that the performance of MDR in this thesis was investigated for an indoor communication system. Therefore, the validity of the obtained results for outdoor environments should also be considered in future work. Moreover, incorporating the multiuser scenario and SM will be another direction that one can explore for future studies. The optimum locations of the PDs on the sides of smartphone can be also considered as another research topic.

List of Publications

The list of published papers are included here.

1. Journal Papers

M. D. Soltani, X. Wu, M. Safari, and H. Haas, "Bidirectional User Throughput Maximization Based on Feedback Reduction in LiFi Networks," *IEEE Transactions on Communications*, vol. 66, no. 7, pp. 3172–3186, July 2018.

M. D. Soltani, A. A. Purwita, Z. Zeng, H. Haas, and M. Safari, "Modeling the Random Orientation of Mobile Devices: Measurement, Analysis and LiFi Use Case," *IEEE Transactions on Communications*, vol. 67, no. 3, pp. 2157-2172, March 2019.

M. D. Soltani, I. Tavakkolnia, A. A. Purwita, H. Haas, and M. Safari, "Impact of Device Orientation on Error Performance of LiFi Systems," *IEEE Access*, vol. 7, pp. 41690-41701, 2019.

M. D. Soltani, M. A. Arfaoui, I. Tavakkolnia, A. Ghrayeb, M. Safari, C. Assi, M. Hasna, and H. Haas, "Bidirectional Optical Spatial Modulation for Mobile Users: Towards a Practical Design for LiFi Systems," *Submitted to IEEE Journal on Selected Areas in communications*, Dec. 2018.

2. Conference Papers

M. D. Soltani, X. Wu, M. Safari, and H. Haas, "On Limited Feedback Resource Allocation for Visible Light Communication Networks," *in Proc. 2015 ACM 2nd Int. Workshop on Visible Light Communications Systems (VLCS)*, pp. 27–32.

M. D. Soltani, X. Wu, M. Safari, and H. Haas, "Access Point Selection in Li-Fi Cellular Networks with Arbitrary Receiver Orientation," *IEEE 27th Annual International Symposium on Personal, Indoor, and Mobile Radio Communications (PIMRC)*, Valencia, Spain, Sept 2016, pp. 1–6.

M. D. Soltani, H. Kazemi, M. Safari, and H. Haas, "Handover Modeling for Indoor Li-Fi Cellular Networks: The Effects of Receiver Mobility and Rotation," *IEEE Wireless Communications and Networking Conference (WCNC)*, San Francisco, USA, March 2017, pp. 1–6.

M. D. Soltani, M. Safari, and H. Haas, "On Throughput Maximization Based on Optimal Update Interval in LiFi Networks," *IEEE 28th Annual International Symposium on Personal, Indoor, and Mobile Radio Communications (PIMRC)*, Montreal, QC, Canada, Oct. 2017, pp. 1–6.

M. D. Soltani, Z. Zeng, I. Tavakkolnia, H. Haas, and M. Safari, "Random Receiver Orientation Effect on Channel Gain in LiFi Systems," *IEEE Wireless Communications and Networking Conference (WCNC)*, Marrakech, Morocco, April 2019, pp. 1–6.

Appendix A

Proof of Required Number of Subcarriers

According to the RWP mobility model, the UE is initially located at $\mathbf{P}_0$ with the distance r_0 from cell center. The scheduler at the AP is supposed to allocate the resources to the UEs as much as they require. Thus, the achievable data throughput of the UE at $t = 0$ is equal to the requested data rate, i.e., $R(0) = R_{\text{req}}$. Hence, k_{req} can be obtained by solving the following equation:

$$
\begin{aligned}
R_{\text{req}} &= \frac{B_{\text{d},n}}{\mathcal{K}} \sum_{k=1}^{k_{\text{req}}} \log_2 \left(\frac{G e^{\frac{-2kB_{\text{d},n}}{\mathcal{K}f_0}}}{(h^2 + r_0^2)^{m+3}} \right) \\
&= \frac{B_{\text{d},n}}{\mathcal{K}} \sum_{k=1}^{k_{\text{req}}} \log_2 \left(\frac{G}{(h^2 + r_0^2)^{m+3}} \right) + \frac{B_{\text{d},n}}{\mathcal{K}} \sum_{k=1}^{k_{\text{req}}} \log_2 \left(e^{\frac{-2kB_{\text{d},n}}{\mathcal{K}f_0}} \right) \\
&= \frac{k_{\text{req}} B_{\text{d},n}}{\mathcal{K}} \log_2 \left(\frac{G}{(h^2 + r_0^2)^{m+3}} \right) - \frac{2}{f_0} \left(\frac{B_{\text{d},n}}{\mathcal{K}} \right)^2 \log_2 e \sum_{k=1}^{k_{\text{req}}} k \\
&= \frac{k_{\text{req}} B_{\text{d},n}}{\mathcal{K}} \log_2 \left(\frac{G}{(h^2 + r_0^2)^{m+3}} \right) - \frac{1}{f_0} \left(\frac{B_{\text{d},n}}{\mathcal{K}} \right)^2 (\log_2 e) k_{\text{req}} (k_{\text{req}} + 1) \\
&\Rightarrow k_{\text{req}}^2 + \left(1 - \frac{\log_2 \left(\frac{G}{(h^2 + r_0^2)^{m+3}} \right)}{\frac{B_{\text{d},n}}{\mathcal{K}f_0} \log_2 e} \right) k_{\text{req}} + \frac{R_{\text{req}}}{\frac{1}{f_0} \left(\frac{B_{\text{d},n}}{\mathcal{K}} \right)^2 \log_2 e} = 0.
\end{aligned}
\tag{A.1}
$$

The above equation is a quadratic equation and it has two roots where the acceptable k_{req} can be obtained as follows:

$$k_{\mathrm{req}} = \frac{\left(\frac{\log_2\left(\frac{G}{(h^2+r_0^2)^{m+3}}\right)}{\frac{B_{\mathrm{d},n}}{\mathcal{K}f_0}\log_2 e} - 1\right) - \sqrt{\left(1 - \frac{\log_2\left(\frac{G}{(h^2+r_0^2)^{m+3}}\right)}{\frac{B_{\mathrm{d},n}}{\mathcal{K}f_0}\log_2 e}\right)^2 - \frac{4R_{\mathrm{req}}}{\frac{1}{f_0}\left(\frac{B_{\mathrm{d},n}}{\mathcal{K}}\right)^2 \log_2 e}}}{2}. \tag{A.2}$$

If $R_{\mathrm{req}} \ll \frac{f_0}{4}\log_2\left(\frac{G}{(h^2+r_0^2)^{m+3}}\right)$, the approximate number of required subcarriers is:

$$k_{\mathrm{req}} \cong \frac{\mathcal{K}R_{\mathrm{req}}}{B_{\mathrm{d},n}\log_2\left(\frac{G}{(h^2+r_0^2)^{m+3}}\right)}. \tag{A.3}$$

With the parameters given in Table 3.2, the constraint on the requested data rate would be $R_{\mathrm{req}} << 350$ Mbps.

Appendix B
Proof of Update Interval

The optimal solution of the optimization problem (OP) given in (3.16) can be obtained by finding the roots of its derivation that is $\frac{\partial \mathbb{E}_{r_0,\hat{\theta}}[\overline{\mathcal{T}}]}{\partial t_\mathrm{u}} = w_\mathrm{u}\frac{\partial \mathbb{E}_{r_0,\hat{\theta}}[\overline{R}_\mathrm{u}]}{\partial t_\mathrm{u}} + w_\mathrm{d}\frac{\partial \mathbb{E}_{r_0,\hat{\theta}}[\overline{R}_\mathrm{d}]}{\partial t_\mathrm{u}} = 0$. The expectation value of the average downlink throughput is $\mathbb{E}_{r_0,\hat{\theta}}[\overline{R}_\mathrm{d}] = \iint_{r_0,\hat{\theta}} \overline{R}_\mathrm{d} f_{\mathcal{R}_0}(r_0) f_\Theta(\hat{\theta})\mathrm{d}\hat{\theta}\mathrm{d}r_0$ and its derivation is equal to $\frac{\partial \mathbb{E}_{r_0,\hat{\theta}}[\overline{R}_\mathrm{d}]}{\partial t_\mathrm{u}} = \frac{\partial}{\partial t_\mathrm{u}} \iint_{r_0,\hat{\theta}} \overline{R}_\mathrm{d} f_{\mathcal{R}_0}(r_0) f_\Theta(\hat{\theta})\mathrm{d}\hat{\theta}\mathrm{d}r_0$. Since the function inside the integral is derivative on the range $(0, 2r_\mathrm{c}/v)$, the derivation operator can go inside the integral as $\iint_{r_0,\hat{\theta}} \frac{\partial \overline{R}_\mathrm{d}}{\partial t_\mathrm{u}} f_{\mathcal{R}_0}(r_0) f_\Theta(\hat{\theta})\mathrm{d}\hat{\theta}\mathrm{d}r_0$ [146], and this is the expectation value of the derivation of the average downlink throughput, i.e., $\mathbb{E}_{r_0,\hat{\theta}}[\frac{\partial \overline{R}_\mathrm{d}}{\partial t_\mathrm{u}}]$. Thus, we can conclude that $\frac{\partial \mathbb{E}_{r_0,\hat{\theta}}[\overline{R}_\mathrm{d}]}{\partial t_\mathrm{u}} = \mathbb{E}_{r_0,\hat{\theta}}[\frac{\partial \overline{R}_\mathrm{d}}{\partial t_\mathrm{u}}]$. Using the same methodology for uplink throughput, we have $\frac{\partial \mathbb{E}_{r_0,\hat{\theta}}[\overline{R}_\mathrm{u}]}{\partial t_\mathrm{u}} = \mathbb{E}_{r_0,\hat{\theta}}[\frac{\partial \overline{R}_\mathrm{u}}{\partial t_\mathrm{u}}]$. Then, the derivation of (3.16) can be expressed as:

$$\mathbb{E}_{r_0,\hat{\theta}}\left[\frac{\partial \overline{\mathcal{T}}}{\partial t_\mathrm{u}}\right] = w_\mathrm{u}\mathbb{E}_{r_0,\hat{\theta}}\left[\frac{\partial \overline{R}_\mathrm{u}}{\partial t_\mathrm{u}}\right] + w_\mathrm{d}\mathbb{E}_{r_0,\hat{\theta}}\left[\frac{\partial \overline{R}_\mathrm{d}}{\partial t_\mathrm{u}}\right]. \tag{B.1}$$

Hence, the root of $\mathbb{E}_{r_0,\hat{\theta}}[\frac{\partial \overline{\mathcal{T}}}{\partial t_\mathrm{u}}] = 0$ will be the same as the root of $\frac{\partial \mathbb{E}_{r_0,\hat{\theta}}[\overline{\mathcal{T}}]}{\partial t_\mathrm{u}} = 0$.

Using the Leibniz integral rule the derivation of (3.21) can be obtained as:

$$\begin{aligned}
\frac{\partial \overline{R}_\mathrm{u}}{\partial t_\mathrm{u}} = {} & \frac{-2(m+3)\widetilde{\mathcal{T}}_\mathrm{u} B_{\mathrm{u},n}}{N_\mathrm{UE} t_\mathrm{u}^2}\left(1 - \frac{2t_\mathrm{fb}}{t_\mathrm{u}}\right)\left(\frac{t_\mathrm{u}}{2(m+3)}\log_2\left(\frac{G_\mathrm{u}}{(r^2(t_\mathrm{u})+h^2)^{m+3}}\right)\right. \\
& + \frac{r_0\cos\hat{\theta}}{2v}\log_2\left(r^2(t_\mathrm{u})+h^2\right) - \frac{(h^2 + r_0^2\sin^2\hat{\theta})^{\frac{1}{2}}}{v\ln(2)}\tan^{-1}\left(\frac{vt_\mathrm{u} - r_0\cos\hat{\theta}}{(h^2+r_0^2\sin^2\hat{\theta})^{\frac{1}{2}}}\right) \\
& - \frac{(h^2 + r_0^2\sin^2\hat{\theta})^{\frac{1}{2}}}{v\ln(2)}\tan^{-1}\left(\frac{r_0\cos\hat{\theta}}{(h^2+r_0^2\sin^2\hat{\theta})^{\frac{1}{2}}}\right) - \frac{r_0\cos\hat{\theta}}{2v}\log_2\left(r_0^2+h^2\right) + \left.\frac{t_\mathrm{u}}{\ln(2)}\right) \\
& + \frac{\widetilde{\mathcal{T}}_\mathrm{u} B_{\mathrm{u},n}}{N_\mathrm{UE} t_\mathrm{u}}\left(1 - \frac{t_\mathrm{fb}}{t_\mathrm{u}}\right)\log_2\left(\frac{G_\mathrm{u}}{(r^2(t_\mathrm{u})+h^2)^{m+3}}\right).
\end{aligned} \tag{B.2}$$

Using the sum of inverse tangents formula, $\tan^{-1}(a) + \tan^{-1}(b) = \tan^{-1}\left(\frac{a+b}{1-ab}\right)$, (B.2) can

be further simplified as:

$$\begin{aligned}\frac{\partial \overline{R}_{\mathrm{u}}}{\partial t_{\mathrm{u}}} = \frac{-2(m+3)\widetilde{\mathcal{T}}_{\mathrm{u}} B_{\mathrm{u},n}}{N_{\mathrm{UE}} t_{\mathrm{u}}^2}\left(1-\frac{2t_{\mathrm{fb}}}{t_{\mathrm{u}}}\right)\left(\frac{r_0\cos\hat{\theta}}{2v}\log_2\left(\frac{r^2(t_{\mathrm{u}})+h^2}{r_0^2+h^2}\right)\right.\\ -\frac{(h^2+r_0^2\sin^2\hat{\theta})^{\frac{1}{2}}}{v\ln(2)}\tan^{-1}\left(\frac{\frac{vt_{\mathrm{u}}}{(h^2+r_0^2\sin^2\hat{\theta})^{\frac{1}{2}}}}{1-\frac{r_0\cos\hat{\theta}(vt_{\mathrm{u}}-r_0\cos\hat{\theta})}{h^2+r_0^2\sin^2\hat{\theta}}}\right)+\left.\frac{t_{\mathrm{u}}}{\ln(2)}\right)\\ +\frac{\widetilde{\mathcal{T}}_{\mathrm{u}} B_{\mathrm{u},n} t_{\mathrm{fb}}}{N_{\mathrm{UE}} t_{\mathrm{u}}}\log_2\left(\frac{G_{\mathrm{u}}}{(r^2(t_{\mathrm{u}})+h^2)^{m+3}}\right).\end{aligned} \tag{B.3}$$

This is the exact derivation of the average uplink achievable throughput respect to t_{u}, however, for $vt_{\mathrm{u}} \ll h$, this equation can be further simplified. Substituting $r(t_{\mathrm{u}}) = (r_0^2 + v^2t_{\mathrm{u}}^2 - 2r_0vt_{\mathrm{u}}\cos\hat{\theta} + h^2)^{1/2}$ in logarithm term, ignoring the small terms and using the approximation $\ln(1+x) \cong x$ for small values of x, we arrive $\log_2\left(1+\frac{v^2t_{\mathrm{u}}^2-2r_0vt_{\mathrm{u}}\cos\hat{\theta}}{r_0^2+h^2}\right) \cong \log_2\left(1-\frac{2r_0vt_{\mathrm{u}}\cos\hat{\theta}}{r_0^2+h^2}\right) \cong \frac{-2r_0vt_{\mathrm{u}}\cos\hat{\theta}}{\ln(2)\left(r_0^2+h^2\right)}$. Considering the rule of small-angle approximation for inverse tangent, it can also be approximated by its first two terms of Taylor series as $\tan^{-1}(x) \cong x - x^3/3$ for small x. Noting that $t_{\mathrm{fb}} \ll t_{\mathrm{u}}$, the approximate derivation is given as follows:

$$\begin{aligned}\frac{\partial \overline{R}_{\mathrm{u}}}{\partial t_{\mathrm{u}}} \cong \frac{-2(m+3)\widetilde{\mathcal{T}}_{\mathrm{u}} B_{\mathrm{u},n}}{\ln(2) N_{\mathrm{UE}} t_{\mathrm{u}}^2}\left(1-\frac{2t_{\mathrm{fb}}}{t_{\mathrm{u}}}\right)\left(\frac{(vt_{\mathrm{u}})^3(h^2+r_0^2\sin^2\hat{\theta})^2}{3v(h^2+r_0^2)^3}+t_{\mathrm{u}}\right.\\ \left.-\frac{r_0^2\cos^2\hat{\theta}t_{\mathrm{u}}}{r_0^2+h^2}-\frac{t_{\mathrm{u}}(h^2+r_0^2\sin^2\hat{\theta})}{h^2+r_0^2}\right)+\frac{\widetilde{\mathcal{T}}_{\mathrm{u}} B_{\mathrm{u},n} t_{\mathrm{fb}}}{N_{\mathrm{UE}} t_{\mathrm{u}}^2}\log_2\left(\frac{G_{\mathrm{u}}}{(r_0^2+h^2)^{m+3}}\right)\\ = -\frac{2(m+3)\widetilde{\mathcal{T}}_{\mathrm{u}} B_{\mathrm{u},n} v^2(h^2+r_0^2\sin^2\hat{\theta})^2 t_{\mathrm{u}}}{3N_{\mathrm{UE}}\ln(2)(h^2+r_0^2)^3}+\frac{\widetilde{\mathcal{T}}_{\mathrm{u}} B_{\mathrm{u},n} t_{\mathrm{fb}}}{N_{\mathrm{UE}} t_{\mathrm{u}}^2}\log_2\left(\frac{G_{\mathrm{u}}}{(r_0^2+h^2)^{m+3}}\right)\end{aligned} \tag{B.4}$$

Using the Leibniz integral rule to calculate the derivation of the average downlink throughput, and the sum of inverse tangents formula to simplify it, the derivation of average downlink throughput is given as:

$$\frac{\partial \overline{R}_{\mathrm{d}}}{\partial t_{\mathrm{u}}} = \frac{-2(m+3)k_{\mathrm{req}}B_{\mathrm{d},n}}{\mathcal{K}t_{\mathrm{u}}^2}\left(\frac{r_0\cos\hat{\theta}}{2v}\log_2\left(\frac{r^2(t_{\mathrm{u}})+h^2}{r_0^2+h^2}\right)+\frac{t_{\mathrm{u}}}{\ln(2)}\right.$$
$$\left.-\frac{(h^2+r_0^2\sin^2\hat{\theta})^{\frac{1}{2}}}{v\ln(2)}\tan^{-1}\left(\frac{\frac{vt_{\mathrm{u}}}{(h^2+r_0^2\sin^2\hat{\theta})^{\frac{1}{2}}}}{1-\frac{r_0\cos\hat{\theta}(vt_{\mathrm{u}}-r_0\cos\hat{\theta})}{(h^2+r_0^2\sin^2\hat{\theta})}}\right)\right). \tag{B.5}$$

This is the exact derivation of average downlink achievable throughput respect to t_{u}, however, using the approximation rules for $vt_{\mathrm{u}} \ll h$, the well-approximated derivation is given as follows:

$$\frac{\partial \overline{R}_{\mathrm{d}}}{\partial t_{\mathrm{u}}} \cong \frac{-2(m+3)k_{\mathrm{req}}B_{\mathrm{d},n}}{\mathcal{K}t_{\mathrm{u}}^2}\left(-\frac{r_0^2\cos^2\hat{\theta}t_{\mathrm{u}}}{\ln(2)(r_0^2+h^2)}-\frac{t_{\mathrm{u}}(h^2+r_0^2\sin^2\hat{\theta})}{\ln(2)(h^2+r_0^2)}\right.$$
$$\left.+\frac{(vt_{\mathrm{u}})^3(h^2+r_0^2\sin^2\hat{\theta})^2}{3v\ln(2)(h^2+r_0^2)^3}+\frac{t_{\mathrm{u}}}{\ln(2)}\right)=\frac{-2(m+3)k_{\mathrm{req}}B_{\mathrm{d},n}v^2t_{\mathrm{u}}(h^2+r_0^2\sin^2\hat{\theta})^2}{3\mathcal{K}\ln(2)(h^2+r_0^2)^3}. \tag{B.6}$$

The exact optimum time, $t_{\mathrm{u,opt}}$, can be obtained numerically by solving (3.25) after substituting $\frac{\partial \overline{R}_{\mathrm{d}}}{\partial t_{\mathrm{u}}}$ and $\frac{\partial \overline{R}_{\mathrm{u}}}{\partial t_{\mathrm{u}}}$ given in (B.2) and (B.5). However, we can approximately obtain a closed form for optimum update interval denoted as $\widetilde{t}_{\mathrm{u,opt}}$ by using (B.4) and (B.6). Taking into account that $vt_{\mathrm{u}} \ll h$ the closed form solution for optimum update interval is given as:

$$\widetilde{t}_{\mathrm{u,opt}} \cong \left(\frac{\frac{3\ln(2)}{2(m+3)}w_{\mathrm{u}}t_{\mathrm{fb}}\widetilde{\mathcal{T}}_{\mathrm{u}}B_{\mathrm{u},n}C_1}{w_{\mathrm{d}}v^2N_{\mathrm{UE}}R_{\mathrm{req}}+C_2w_{\mathrm{u}}v^2\widetilde{\mathcal{T}}_{\mathrm{u}}B_{\mathrm{u},n}}\right)^{\frac{1}{3}},$$

where

$$C_1 = \frac{\mathbb{E}_{r_0}\left[\log_2\left(\frac{G_{\mathrm{u}}}{(r_0^2+h^2)^{m+3}}\right)\right]\mathbb{E}_{r_0}\left[\log_2\left(\frac{G}{(r_0^2+h^2)^{m+3}}\right)\right]}{\mathbb{E}_{r_0,\hat{\theta}}\left[\frac{(h^2+r_0^2\sin^2\hat{\theta})^2}{(h^2+r_0^2)^3}\right]},$$
$$C_2 = \mathbb{E}_{r_0}\left[\log_2\left(\frac{G}{(r_0^2+h^2)^{m+3}}\right)\right].$$

Appendix C
Proof of PDF of $\cos\psi$ Case 2

(The derivations of this appendix are taken from our paper [10].)

For case 2, we need the intervals of the domain of $\cos\psi$ such that the transformation (4.10) is one-to-one. Using (4.10) and (4.15), we have two intervals which are $g(0) < \cos\psi < g(\theta^*)$ and $g(\frac{\pi}{2}) < \cos\psi \leq g(\theta^*)$. The inverse functions are denoted by:

$$\theta = \begin{cases} \sin^{-1}\left(\frac{\cos\psi}{\sqrt{a^2+b^2}}\right) - \tan^{-1}\left(\frac{b}{a}\right), & g(0) < \cos\psi < g(\theta^*) \\ \pi - \sin^{-1}\left(\frac{\cos\psi}{\sqrt{a^2+b^2}}\right) - \tan^{-1}\left(\frac{b}{a}\right), & g(\frac{\pi}{2}) < \cos\psi \leq g(\theta^*). \end{cases} \tag{C.1}$$

Note that both the inverse functions have the same Jacobian of the transformation which is

$$|J| = 1/\sqrt{a^2 + b^2 - \cos^2\psi}. \tag{C.2}$$

Combining the Jacobian of transformation, (4.4), and (C.1), we get (C.3). Therefore, the PDF of $\cos\psi$ can be expressed as in (C.3a) for $g(0) \leq g(\frac{\pi}{2})$ or in (C.3b) for $g(\frac{\pi}{2}) < g(0)$, which are given at the top of the next page. Note that for $a \geq 0$, $\text{ss}_f = \sqrt{a^2+b^2} \leq 1$.

$$f_{\cos\psi}(\tau) = \begin{cases} \frac{f_\theta\left(\sin^{-1}\left(\frac{\tau}{\sqrt{a^2+b^2}}\right) - \tan^{-1}\left(\frac{b}{a}\right)\right)}{\sqrt{a^2+b^2-\tau^2}}, & g(0) < \tau < g(\frac{\pi}{2}) \\ \frac{f_\theta\left(\sin^{-1}\left(\frac{\tau}{\sqrt{a^2+b^2}}\right) - \tan^{-1}\left(\frac{b}{a}\right)\right)}{\sqrt{a^2+b^2-\tau^2}} & \\ + \frac{f_\theta\left(-\sin^{-1}\left(\frac{\tau}{\sqrt{a^2+b^2}}\right) - \tan^{-1}\left(\frac{b}{a}\right) + \pi\right)}{\sqrt{a^2+b^2-\tau^2}}, & g(\frac{\pi}{2}) < \tau \leq g(\theta^*) \end{cases} \tag{C.3a}$$

$$f_{\cos\psi}(\tau) = \begin{cases} \frac{f_\theta\left(-\sin^{-1}\left(\frac{\tau}{\sqrt{a^2+b^2}}\right) - \tan^{-1}\left(\frac{b}{a}\right) + \pi\right)}{\sqrt{a^2+b^2-\tau^2}}, & g(\frac{\pi}{2}) < \tau < g(0) \\ \frac{f_\theta\left(\sin^{-1}\left(\frac{\tau}{\sqrt{a^2+b^2}}\right) - \tan^{-1}\left(\frac{b}{a}\right)\right)}{\sqrt{a^2+b^2-\tau^2}} & \\ + \frac{f_\theta\left(-\sin^{-1}\left(\frac{\tau}{\sqrt{a^2+b^2}}\right) - \tan^{-1}\left(\frac{b}{a}\right) + \pi\right)}{\sqrt{a^2+b^2-\tau^2}}, & g(0) < \tau \leq g(\theta^*) \end{cases} \tag{C.3b}$$

Appendix D
Proof of the PDF of LOS Channel Gain

The CDF of the LOS channel gain, $H = H_0 \cos\psi / d^{m+2} \mathrm{rect}\left(\frac{\psi}{\Psi_\mathrm{c}}\right)$ is given as:

$$\begin{aligned} F_H(\hbar) &= \Pr\{H_0 \cos\psi / d^{m+2} \mathrm{rect}\left(\frac{\psi}{\Psi_\mathrm{c}}\right) < \hbar\} \\ &= \Pr\{H_0 \cos\psi / d^{m+2} < \hbar, 0 \le \psi \le \Psi_\mathrm{c}\} \\ &\quad + \Pr\{\hbar > 0, \cos\psi < \cos\Psi_\mathrm{c}\} \\ &= \Pr\left\{\cos\psi < \frac{\hbar d^{m+2}}{H_0}, 0 \le \psi \le \Psi_\mathrm{c}\right\} \\ &+ \Pr\{\cos\psi < \cos\Psi_\mathrm{c}, \hbar > 0\} \\ &= F_{\cos\psi}\left(\frac{\hbar d^{m+2}}{H_0}\right) + F_{\cos\psi}\left(\cos\Psi_\mathrm{c}\right) \mathrm{rect}\left(\hbar\right). \end{aligned} \tag{D.1}$$

with the support range of $h_{\min} \le \hbar \le h_{\max}$. Then, the corresponding PDF can be obtained as follows:

$$\begin{aligned} f_H(\hbar) &= \frac{\partial}{\partial \hbar} F_H(\hbar) = \frac{d^{m+2}}{H_0} f_{\cos\psi}\left(\frac{\hbar d^{m+2}}{H_0}\right) + F_{\cos\psi}\left(\cos\Psi_\mathrm{c}\right) \delta(\hbar) \\ &= \frac{c_\mathrm{N}}{h_\mathrm{n}} f_{\cos\psi}\left(\frac{\hbar}{h_\mathrm{n}}\right) + F_{\cos\psi}\left(\cos\Psi_\mathrm{c}\right) \delta(\hbar). \end{aligned} \tag{D.2}$$

where in the last equation, we define $h_\mathrm{n} \triangleq H_0 / d^{m+2}$. The Dirac delta function comes out due to the discontinuity of CDF given in (D.1) at $\hbar = 0$. To ensure that the $\int_{h_{\min}}^{h_{\max}} f_H(\hbar) \mathrm{d}\hbar = 1$, the normalizing factor should be $c_\mathrm{N} = 1$. This completes the proof of (4.23).

Appendix E
Proof of Critical Elevation Angle

Recalling that $\cos\psi = \mathbf{d}\cdot\mathbf{n}'_{\mathrm{u}}/d$, replacing for $\mathbf{d} = [x_{\mathrm{a}}-x_{\mathrm{u}}, y_{\mathrm{a}}-y_{\mathrm{u}}, z_{\mathrm{a}}-z_{\mathrm{u}}]^{\mathrm{T}}$ and $\mathbf{n}'_{\mathrm{u}} = [\sin\theta\cos\omega, \sin\theta\sin\omega, \cos\theta]^{\mathrm{T}}$ and also noting that $\omega = \Omega+\pi$, we have:

$$\begin{aligned}\cos\psi =& \frac{(x_{\mathrm{u}}-x_{\mathrm{a}})\sin\theta\cos\Omega + (y_{\mathrm{u}}-y_{\mathrm{a}})\sin\theta\sin\Omega - (z_{\mathrm{u}}-z_{\mathrm{a}})\cos\theta}{\sqrt{(x_{\mathrm{u}}-x_{\mathrm{a}})^2+(y_{\mathrm{u}}-y_{\mathrm{a}})^2+(z_{\mathrm{u}}-z_{\mathrm{a}})^2}} \\ =& \frac{\sqrt{(x_{\mathrm{u}}-x_{\mathrm{a}})^2+(y_{\mathrm{u}}-y_{\mathrm{a}})^2}\sin\theta\cos\left(\Omega-\tan^{-1}\left(\frac{y_{\mathrm{u}}-y_{\mathrm{a}}}{x_{\mathrm{u}}-x_{\mathrm{a}}}\right)\right) - (z_{\mathrm{u}}-z_{\mathrm{a}})\cos\theta}{\sqrt{(x_{\mathrm{u}}-x_{\mathrm{a}})^2+(y_{\mathrm{u}}-y_{\mathrm{a}})^2+(z_{\mathrm{u}}-z_{\mathrm{a}})^2}}.\end{aligned} \tag{E.1}$$

For a given location of user equipment (UE) and a fixed angle of Ω, by using the simple triangular rules, $\cos\psi$ can be represented as:

$$\cos\psi = \lambda_1\sin\theta + \lambda_2\cos\theta = \sqrt{\lambda_1^2+\lambda_2^2}\cos\left(\theta-\tan^{-1}\left(\frac{\lambda_1}{\lambda_2}\right)\right), \tag{E.2}$$

where λ_1 and λ_2 are given as:

$$\begin{aligned}\lambda_1 &= \frac{\sqrt{(x_{\mathrm{u}}-x_{\mathrm{a}})^2+(y_{\mathrm{u}}-y_{\mathrm{a}})^2}\cos\left(\Omega-\tan^{-1}\left(\frac{y_{\mathrm{u}}-y_{\mathrm{a}}}{x_{\mathrm{u}}-x_{\mathrm{a}}}\right)\right)}{\sqrt{(x_{\mathrm{u}}-x_{\mathrm{a}})^2+(y_{\mathrm{u}}-y_{\mathrm{a}})^2+(z_{\mathrm{u}}-z_{\mathrm{a}})^2}}, \\ \lambda_2 &= \frac{(z_{\mathrm{a}}-z_{\mathrm{u}})}{\sqrt{(x_{\mathrm{u}}-x_{\mathrm{a}})^2+(y_{\mathrm{u}}-y_{\mathrm{a}})^2+(z_{\mathrm{u}}-z_{\mathrm{a}})^2}}.\end{aligned} \tag{E.3}$$

According to the definition of critical elevation angle, if $\theta = \theta_{\mathrm{ce}}$, then, $\cos\psi = \cos\Psi_{\mathrm{c}}$. Therefore, (E.2) results in:

$$\theta_{\mathrm{ce}} = \cos^{-1}\left(\frac{\cos\Psi_{\mathrm{c}}}{\sqrt{\lambda_1^2+\lambda_2^2}}\right) + \tan^{-1}\left(\frac{\lambda_1}{\lambda_2}\right). \tag{E.4}$$

This completes the proof of the derivation of CE angle.

Appendix F
Proof of Proposition

For a given location of UE and a fixed elevation angle, one other representation of $\cos\psi$ given in (E.1) would be as a function of Ω:

$$\cos\psi = \kappa_1 \cos\left(\Omega - \tan^{-1}\left(\frac{y_\mathrm{u}-y_\mathrm{a}}{x_\mathrm{u}-x_\mathrm{a}}\right)\right) + \kappa_2 \triangleq \Lambda(\Omega), \tag{F.1}$$

where the coefficients κ_1 and κ_2 are given as:

$$\kappa_1 = \frac{\sqrt{(x_\mathrm{u}-x_\mathrm{a})^2+(y_\mathrm{u}-y_\mathrm{a})^2}}{d}\sin\theta, \quad \kappa_2 = \frac{(z_\mathrm{a}-z_\mathrm{u})}{d}\cos\theta. \tag{F.2}$$

Note that since $\theta \in [0, 90]$ and $z_\mathrm{a} > z_\mathrm{u}$, we have $\kappa_1 \geq 0$ and $\kappa_2 \geq 0$. As mentioned for $\theta = \theta_\mathrm{ce}$, we have $\cos\psi = \cos\Psi_\mathrm{c}$. Then, solving $\Lambda(\Omega) - \cos\Psi_\mathrm{c} = 0$ for Ω, the roots are $\Omega_{\mathrm{r}1} = \min\{\Omega_1, \Omega_2\}$ and $\Omega_{\mathrm{r}2} = \max\{\Omega_1, \Omega_2\}$, where Ω_1 and Ω_2 are given as follow:

$$\begin{aligned}
\Omega_1 &= \cos^{-1}\left(\frac{\cos\Psi_\mathrm{c}-\kappa_2}{\kappa_1}\right) + \tan^{-1}\left(\frac{y_\mathrm{u}-y_\mathrm{a}}{x_\mathrm{u}-x_\mathrm{a}}\right), \\
\Omega_2 &= -\cos^{-1}\left(\frac{\cos\Psi_\mathrm{c}-\kappa_2}{\kappa_1}\right) + \tan^{-1}\left(\frac{y_\mathrm{u}-y_\mathrm{a}}{x_\mathrm{u}-x_\mathrm{a}}\right).
\end{aligned} \tag{F.3}$$

Using the sinuous function properties if $\Lambda(\Omega) \leq 0$ for $\Omega \in [\Omega_{\mathrm{r}1}, \Omega_{\mathrm{r}2}]$, then the derivative of $\Lambda(\Omega)$ at $\Omega = \Omega_{\mathrm{r}1}$ is negative, i.e., $\frac{\partial\Lambda(\Omega)}{\partial\Omega}|_{\Omega=\Omega_{\mathrm{r}1}} < 0$. For simplicity of notation, let's denote $\Lambda'(\Omega) = \frac{\partial\Lambda(\Omega)}{\partial\Omega}$. Using (F.1), we have $\Lambda'(\Omega) = -\kappa_1 \sin\left(\Omega - \tan^{-1}\left(\frac{y_\mathrm{u}-y_\mathrm{a}}{x_\mathrm{u}-x_\mathrm{a}}\right)\right) + \kappa_2$. Therefore, the range of $\mathcal{R}_{\Omega,\theta}$ that guarantees $\Lambda(\Omega) > 0$ would be $[0, \Omega_{\mathrm{r}1}) \bigcup (\Omega_{\mathrm{r}2}, 360]$. Similarly, if $\Lambda(\Omega) \geq 0$ for $\Omega \in [\Omega_{\mathrm{r}1}, \Omega_{\mathrm{r}2}]$, then the derivative of $\Lambda(\Omega)$ at $\Omega = \Omega_{\mathrm{r}1}$ is positive, i.e., $\frac{\partial\Lambda(\Omega)}{\partial\Omega}|_{\Omega=\Omega_{\mathrm{r}1}} > 0$. Consequently, in this case the range of $\mathcal{R}_{\Omega,\theta}$ that ensures $\Lambda(\Omega) > 0$ would be $[\Omega_{\mathrm{r}1}, \Omega_{\mathrm{r}2}]$. This completes the proof of Proposition.

Appendix G
Proof of BER Approximation

Substituting (4.37) and (4.39) into (4.38), we have:

$$\begin{aligned}\bar{P}_{\mathrm{e}} = c_0 \int_{s_{\min}}^{s_{\max}} Q\left(\sqrt{\frac{3s}{M-1}}\right) \frac{1}{\sqrt{s}} \exp\left(-\frac{|\sqrt{s}-\sqrt{\mathcal{S}_0}\mu_{\mathrm{H}}|}{\sqrt{\mathcal{S}_0}b_{\mathrm{H}}}\right) \mathrm{d}s \\ + c_{\mathrm{H}}c_{\mathrm{M}} \int_{s_{\min}}^{s_{\max}} Q\left(\sqrt{\frac{3s}{M-1}}\right) \delta(s)\mathrm{d}s\end{aligned} \tag{G.1}$$

with c_0 and c_{M} given as:

$$\begin{aligned}c_0 &= \frac{c_{\mathrm{M}}}{2b_{\mathrm{H}}\sqrt{\mathcal{S}_0}\left(2-\exp\left(-\frac{h_{\max}-\mu_{\mathrm{H}}}{b_{\mathrm{H}}}\right)\right)}, \\ c_{\mathrm{M}} &= \frac{4}{\log_2 M}\left(1-\frac{1}{\sqrt{M}}\right).\end{aligned} \tag{G.2}$$

Note that if $s_{\min}=0$, the second integral in (G.1) is $c_{\mathrm{H}}c_{\mathrm{M}}Q(0)=\frac{c_{\mathrm{H}}c_{\mathrm{M}}}{2}$, and referring to the definition of c_{H}, it is zero for $s_{\min}>0$. Thus, the second integral can be expressed as $\frac{c_{\mathrm{H}}c_{\mathrm{M}}}{2}$ and we need to simplify the first integral. For simplicity of notation, let define $c_1=\sqrt{\frac{3}{M-1}}$, $c_2=\sqrt{\mathcal{S}_0}\mu_{\mathrm{H}}$ and $c_3=\sqrt{\mathcal{S}_0}b_{\mathrm{H}}$. Furthermore, let $x=\sqrt{s}$, thus, the first integral in (G.1) can be rewritten as:

$$\begin{aligned}&\int_{\sqrt{s_{\min}}}^{\sqrt{s_{\max}}} Q(c_1x)e^{-\frac{|x-c_2|}{c_3}}\mathrm{d}x \\ &= \begin{cases}\int_{\sqrt{s_{\min}}}^{\sqrt{s_{\max}}} Q(c_1x)e^{-\frac{x-c_2}{c_3}}\mathrm{d}x, & c_2 \le \sqrt{s_{\min}} \\ \int_{\sqrt{s_{\min}}}^{c_2} Q(c_1x)e^{\frac{x-c_2}{c_3}}\mathrm{d}x + \int_{c_2}^{\sqrt{s_{\max}}} Q(c_1x)e^{-\frac{x-c_2}{c_3}}\mathrm{d}x, & \sqrt{s_{\min}} < c_2 \le \sqrt{s_{\max}}\end{cases},\end{aligned} \tag{G.3}$$

The right side of (G.3) is based on the behavior of PDF of SNR. It can be either single exponential (if $c_2 \ge \sqrt{s_{\min}}$) or double exponential (if $\sqrt{s_{\min}} < c_2 \le \sqrt{s_{\max}}$), for example, see results

shown in Fig. 4.11. Noting that

$$\int Q(c_1 x) e^{\frac{x}{c_3}} \mathrm{d}x = c_3 e^{\frac{x}{c_3}} Q(c_1 x) + \frac{c_3}{2} e^{\frac{1}{4c_1^2 c_3^2}} \left(1 - 2Q\left(c_1 x - \frac{1}{2c_1 c_3}\right)\right),$$

also for given values of c_1, c_2 and c_3, we have $Q(c_1 c_2) \approx Q(c_1\sqrt{s_{\max}})$ and also since $\mu_{\mathrm{H}} >> b_{\mathrm{H}}$, then, $e^{-\frac{c_2}{c_3}} \approx 0$. Hence, $\bar{P}_{\mathrm{e}}$ can be approximated by:

$$\bar{P}_{\mathrm{e}} \approx \begin{cases} -c_0 c_3 + \frac{c_{\mathrm{H}} c_{\mathrm{M}}}{2}, & c_2 \leq \sqrt{s_{\min}} \\ 2c_0 c_3 Q(c_1 c_2)\left(2 - e^{\frac{c_2 - \sqrt{s_{\max}}}{c_3}}\right) + \frac{c_{\mathrm{H}} c_{\mathrm{M}}}{2}, & \sqrt{s_{\min}} < c_2 \leq \sqrt{s_{\max}} \end{cases}. \tag{G.4}$$

By substituting for the values of c_0, c_1, c_2, c_3 and noting that $\sqrt{s_{\min}} = \sqrt{\mathcal{S}_0} h_{\min}$ and $\sqrt{s_{\max}} = \sqrt{\mathcal{S}_0} h_{\max}$ (G.4) can be rewritten as:

$$\bar{P}_{\mathrm{e}} \approx \begin{cases} -\dfrac{\frac{2}{\log_2 M}\left(1 - \frac{1}{\sqrt{M}}\right) e^{\frac{\mu_{\mathrm{H}} - h_{\min}}{b_{\mathrm{H}}}}}{\left(2 - \exp\left(-\frac{h_{\max} - \mu_{\mathrm{H}}}{b_{\mathrm{H}}}\right)\right)} + \dfrac{c_{\mathrm{H}} c_{\mathrm{M}}}{2}, & \mu_{\mathrm{H}} \leq h_{\min} \\ \dfrac{4\left(1 - \frac{1}{\sqrt{M}}\right)}{\log_2 M} Q\left(\sqrt{\dfrac{3\mathcal{S}_0 \mu_{\mathrm{H}}^2}{M-1}}\right) + \dfrac{c_{\mathrm{H}} c_{\mathrm{M}}}{2}, & h_{\min} < \mu_{\mathrm{H}} \leq h_{\max} \end{cases}. \tag{G.5}$$

This completes the proof of (4.40).

Bibliography

[1] Cisco, "Cisco Visual Networking Index: Global Mobile Data Traffic Forecast Update, 2016–2021 White Paper," *white paper at Cisco.com*, Mar. 2017.

[2] *IEEE 802.11: Wireless LAN Medium Access Control (MAC) and Physical Layer (PHY) Specifications*, IEEE-SA Std., Rev. 2012.

[3] H. Haas, L. Yin, Y. Wang, and C. Chen, "What is LiFi?" *Journal of Lightwave Technology*, vol. 34, no. 6, pp. 1533–1544, 2016.

[4] M. D. Soltani, X. Wu, M. Safari, and H. Haas, "Bidirectional User Throughput Maximization Based on Feedback Reduction in LiFi Networks," *IEEE Transactions on Communications*, vol. 66, no. 7, pp. 3172–3186, July 2018.

[5] S. Wu, H. Wang, and C.-H. Youn, "Visible Light Communications for 5G Wireless Networking Systems: From Fixed to Mobile Communications," *IEEE Network*, vol. 28, no. 6, pp. 41–45, 2014.

[6] D. J. Love, R. W. Heath, V. K. Lau, D. Gesbert, B. D. Rao, and M. Andrews, "An Overview of Limited Feedback in Wireless Communication Systems," *IEEE Journal on Selected Areas in Communications*, vol. 26, no. 8, pp. 1341–1365, 2008.

[7] X. Chen *et al.*, "Performance Analysis and Optimization for Interference Alignment Over MIMO Interference Channels With Limited Feedback," *IEEE Transactions on Signal Processing*, vol. 62, no. 7, pp. 1785–1795, 2014.

[8] R. Bhagavatula and R. W. Heath, "Adaptive Limited Feedback For Sum-rate Maximizing Beamforming in Cooperative Multicell Systems," *IEEE Transactions on Signal Processing*, vol. 59, no. 2, pp. 800–811, 2011.

[9] D. J. Ryan, I. B. Collings, I. V. L. Clarkson, and R. W. Heath, "Performance of Vector Perturbation Multiuser MIMO Systems With Limited Feedback," *IEEE Transactions on Communications*, vol. 57, no. 9, 2009.

[10] M. D. Soltani, A. A. Purwita, Z. Zeng, H. Haas, and M. Safari, "Modeling the Random Orientation of Mobile Devices: Measurement, Analysis and LiFi Use Case," *IEEE Transactions on Communications*, vol. 67, no. 3, pp. 2157–2172, March 2019.

[11] Z. Zeng, M. D. Soltani, H. Haas, and M. Safari, "Orientation Model of Mobile Device for Indoor Visible Light Communication and Millimetre Wave Systems," *Submitted to the 2018 IEEE 88nd Vehicular Technology Conference (VTC2018-Fall)*, Chicago, USA, August 2018.

[12] M. Alimadadi, A. Mohammadi, and M. D. Soltani, "Throughput Analysis of Ad-Hoc Networks with Directional Antenna at 60 GHz," *Journal of Electromagnetic Waves and Applications*, vol. 28, no. 2, pp. 228–241, 2014.

[13] M. D. Soltani, X. Wu, M. Safari, and H. Haas, "Access Point Selection in Li-Fi Cellular Networks with Arbitrary Receiver Orientation," in *IEEE 27th Annual International Symposium on Personal, Indoor, and Mobile Radio Communications (PIMRC)*, Valencia, Spain, Sept 2016, pp. 1–6.

[14] M. D. Soltani, H. Kazemi, M. Safari, and H. Haas, "Handover Modeling for Indoor Li-Fi Cellular Networks: The Effects of Receiver Mobility and Rotation," in *IEEE Wireless Communications and Networking Conference (WCNC)*, San Francisco, USA, March 2017, pp. 1–6.

[15] A. A. Purwita, M. D. Soltani, M. Safari, and H. Haas, "Handover Probability of Hybrid LiFi/RF-based Networks with Randomly-Oriented Devices," in *2018 87nd Vehicular Technology Conference (VTC2018-Spring)*, Porto, Portugal, June 2018.

[16] J. Y. Wang, Q. L. Li, J. X. Zhu, and Y. Wang, "Impact of Receiver's Tilted Angle on Channel Capacity in VLCs," *Electronics Letters*, vol. 53, no. 6, pp. 421–423, Mar. 2017.

[17] J. Y. Wang, J. B. Wang, B. Zhu, M. Lin, Y. Wu, Y. Wang, and M. Chen, "Improvement of BER Performance by Tilting Receiver Plane for Indoor Visible Light Communications with Input-Dependent Noise," in *2017 IEEE International Conference on Communications (ICC)*, Paris, France, May 2017, pp. 1–6.

[18] M. D. Soltani, I. Tavakkolnia, A. A. Purwita, H. Haas, and M. Safari, "Impact of Device Orientation on Error Performance of LiFi Systems," *IEEE Access*, vol. 7, pp. 41 690–41 701, 2019.

[19] M. D. Soltani, M. A. Arfaoui, I. Tavakkolnia, A. Ghrayeb, M. Safari, C. Assi, M. Hasna, and H. Haas, "Bidirectional optical spatial modulation for mobile users: Towards a practical design for lifi systems," *Submitted to IEEE Journal on Selected Areas in communications*, Dec. 2018.

[20] P. Huynh and M. Yoo, "VLC-based Positioning System for an Indoor Environment Using an Image Sensor and an Accelerometer Sensor," *Sensors*, vol. 16, no. 6, p. 783, 2016.

[21] L. Wang, C. Guo, P. Luo, and Q. Li, "Indoor Visible Light Localization Algorithm Based on Received Signal Strength Ratio with Multi-Directional LED Array," in *2017 IEEE International Conference on Communications Workshops (ICC Workshops)*, Paris, France, May 2017, pp. 138–143.

[22] L. Yin, X. Wu, and H. Haas, "Indoor Visible Light Positioning with Angle Diversity Transmitter," in *2015 IEEE 82nd Vehicular Technology Conference (VTC2015-Fall)*, Boston, USA, Sept 2015, pp. 1–5.

[23] E.-M. Jeong, S.-H. Yang, H.-S. Kim, and S.-K. Han, "Tilted Receiver Angle Error Compensated Indoor Positioning System Based on Visible Light Communication," *Electronics Letters*, vol. 49, no. 14, pp. 890–892, 2013.

[24] Z. Wang, C. Yu, W.-D. Zhong, and J. Chen, "Performance Improvement by Tilting Receiver Plane in M-QAM OFDM Visible Light Communications," *Optics express*, vol. 19, no. 14, pp. 13 418–13 427, 2011.

[25] Y. S. Eroglu, Y. Yapici, and I. Guvenc, "Impact of Random Receiver Orientation on Visible Light Communications Channel," *IEEE Transactions on Communications*, vol. 67, no. 2, pp. 1313–1325, Feb 2019.

[26] R. W. Bohannon, "Comfortable and Maximum Walking Speed of Adults Aged 20–79 Years: Reference Values and Determinants," *Age and ageing*, vol. 26, no. 1, pp. 15–19, 1997.

[27] Y. Wang, D. A. Basnayaka, X. Wu, and H. Haas, "Optimization of Load Balancing in Hybrid LiFi/RF Networks," *IEEE Transactions on Communications*, vol. 65, no. 4, pp. 1708–1720, April 2017.

[28] Y. Wang, X. Wu, and H. Haas, "Load Balancing Game With Shadowing Effect for Indoor Hybrid LiFi/RF Networks," *IEEE Transactions on Wireless Communications*, vol. 16, no. 4, pp. 2366–2378, April 2017.

[29] C. Chen, R. Bian, and H. Haas, "Omnidirectional transmitter and receiver design for wireless infrared uplink transmission in LiFi," in *Proc. IEEE ICC*, Kansas City, MO, USA, May. 2018.

[30] M. D. Soltani, X. Wu, M. Safari, and H. Haas, "On Limited Feedback Resource Allocation for Visible Light Communication Networks," in *Proc. 2015 ACM 2nd Int. Workshop on Visible Light Communications Systems (VLCS)*, pp. 27–32.

[31] M. D. Soltani, M. Safari, and H. Haas, "On Throughput Maximization Based on Optimal Update Interval in LiFi Networks," in *IEEE 28th Annual International Symposium on Personal, Indoor, and Mobile Radio Communications (PIMRC)*, Montreal, QC, Canada, Oct 2017, pp. 1–6.

[32] M. D. Soltani, Z. Zeng, I. Tavakkolnia, H. Haas, and M. Safari, "Random Receiver Orientation Effect on Channel Gain in LiFi Systems," in *IEEE Wireless Communications and Networking Conference (WCNC)*, Marrakech, Morocco, April 2019, pp. 1–6.

[33] A. G. Bell, "Selenium and the Photophone," *Nature*, vol. 22, no. 569, pp. 500–503, Sep. 1880.

[34] R. Zhang, J. Wang, Z. Wang, Z. Xu, C. Zhao, and L. Hanzo, "Visible Light Communications in Heterogeneous Networks: Paving the Way for User-Centric Design," *IEEE Wireless Communications*, vol. 22, no. 2, pp. 8–16, April 2015.

[35] Y. Tanaka, S. Haruyama, and M. Nakagawa, "Wireless Optical Transmissions with White Colored LED for Wireless Home Links," in *11th IEEE International Symposium on Personal Indoor and Mobile Radio Communications. PIMRC 2000. Proceedings (Cat. No.00TH8525)*, vol. 2, London, UK, Sept 2000, pp. 1325–1329 vol.2.

[36] T. Komine and M. Nakagawa, "Fundamental Analysis for Visible-Light Communication System Using LED Lights," *IEEE Transactions on Consumer Electronics*, vol. 50, no. 1, pp. 100–107, Feb 2004.

[37] M. Uysal, C. Capsoni, Z. Ghassemlooy, A. Boucouvalas, and E. Udvary, *Optical Wireless Communications: An Emerging Technology*. Springer, 2016.

[38] Z. Ghassemlooy, W. Popoola, and S. Rajbhandari, *Optical Wireless Communications: System and Channel Modelling with Matlab*. CRC press, 2012.

[39] F. R. Gfeller and U. Bapst, "Wireless in-house data communication via diffuse infrared radiation," *Proceedings of the IEEE*, vol. 67, no. 11, pp. 1474–1486, Nov 1979.

[40] J. M. Kahn and J. R. Barry, "Wireless Infrared Communications," *Proceedings of the IEEE*, vol. 85, no. 2, pp. 265–298, Feb 1997.

[41] H. Elgala, R. Mesleh, and H. Haas, "Indoor Optical Wireless Communication: Potential and State-of-the-Art," *IEEE Communications Magazine*, vol. 49, no. 9, pp. 56–62, September 2011.

[42] IEEE Std. 802.15.7-2011, *IEEE Standard for Local and Metropolitan Area Networks, Part 15.7: Short-Range Wireless Optical Communication Using Visible Light*, IEEE Std., 2011.

[43] *IEEE 802.15 WPANTM 15.7 Revision: Short-Range Optical Wireless Communications Task Group (TG 7r1)*, IEEE-SA Std., Apr. 2018.

[44] *IEEE 802.11bb Standard for Information Technology-Telecommunications and Information Exchange Between Systems Local and Metropolitan Area Networks-Specific Requirements, Part 11: Wireless LAN Medium Access Control (MAC) and Physical Layer (PHY) Specifications Amendment: Light Communications*, IEEE-SA Std., Jul. 2018.

[45] K. H. Lee and S. W. R. Lee, "Process Development for Yellow Phosphor Coating on Blue Light Emitting Diodes (LEDs) for White Light Illumination," in *2006 8th Electronics Packaging Technology Conference*, Singapore, Singapore, Dec 2006, pp. 379–384.

[46] D. Tsonev, H. Chun, S. Rajbhandari, J. J. D. McKendry, S. Videv, E. Gu, M. Haji, S. Watson, A. E. Kelly, G. Faulkner, M. D. Dawson, H. Haas, and D. O'Brien, "A 3-Gb/s Single-LED OFDM-Based Wireless VLC Link Using a Gallium Nitride μLED," *IEEE Photonics Technology Letters*, vol. 26, no. 7, pp. 637–640, April 2014.

[47] J. Liu, W. Noonpakdee, H. Takano, and S. Shimamoto, "Foundational Analysis of Spatial Optical Wireless Communication Utilizing Image Sensor," in *2011 IEEE International Conference on Imaging Systems and Techniques*, May 2011, pp. 205–209.

[48] P. Djahani and J. M. Kahn, "Analysis of Infrared Wireless Links Employing Multibeam Transmitters and Imaging Diversity Receivers," *IEEE Transactions on Communications*, vol. 48, no. 12, pp. 2077–2088, Dec 2000.

[49] Z. Wang, D. Tsonev, S. Videv, and H. Haas, "On the Design of a Solar-Panel Receiver for Optical Wireless Communications With Simultaneous Energy Harvesting," *IEEE Journal on Selected Areas in Communications*, vol. 33, no. 8, pp. 1612–1623, Aug 2015.

[50] S. Schmid, G. Corbellini, S. Mangold, and T. R. Gross, "An LED-to-LED Visible Light Communication System with Software-Based Synchronization," in *2012 IEEE Globecom Workshops*, Dec 2012, pp. 1264–1268.

[51] H. L. Minh, D. O'Brien, G. Faulkner, L. Zeng, K. Lee, D. Jung, Y. Oh, and E. T. Won, "100-Mb/s NRZ Visible Light Communications Using a Postequalized White LED," *IEEE Photonics Technology Letters*, vol. 21, no. 15, pp. 1063–1065, Aug 2009.

[52] A. M. Khalid, G. Cossu, R. Corsini, P. Choudhury, and E. Ciaramella, "1-Gb/s Transmission Over a Phosphorescent White LED by Using Rate-Adaptive Discrete Multitone Modulation," *IEEE Photonics Journal*, vol. 4, no. 5, pp. 1465–1473, Oct 2012.

[53] H. Schulze, "Frequency-Domain Simulation of the Indoor Wireless Optical Communication Channel," *IEEE Transactions on Communications*, vol. 64, no. 6, pp. 2551–2562, Jun. 2016.

[54] C. Chen, D. A. Basnayaka, and H. Haas, "Downlink Performance of Optical Attocell Networks," *Journal of Lightwave Technology*, vol. 34, no. 1, pp. 137–156, Jan. 2016.

[55] T. Fath and H. Haas, "Performance comparison of MIMO techniques for optical wireless communications in indoor environments," *IEEE Transactions on Communications*, vol. 61, no. 2, pp. 733–742, Feb. 2013.

[56] M. Di Renzo, H. Haas, A. Ghrayeb, S. Sugiura, and L. Hanzo, "Spatial modulation for generalized MIMO: Challenges, opportunities, and implementation," *Proc. IEEE*, vol. 102, no. 1, pp. 56–103, Jan. 2014.

[57] J. M. Kahn and J. R. Barry, "Wireless Infrared Communications," *Proc. IEEE*, vol. 85, no. 2, pp. 265–298, Feb. 1997.

[58] S. Dimitrov and H. Haas, "Optimum Signal Shaping in OFDM-Based Optical Wireless Communication Systems," in *2012 IEEE Vehicular Technology Conference (VTC Fall)*, Sept 2012, pp. 1–5.

[59] J. Armstrong, "OFDM for Optical Communications," *Journal of Lightwave Technology*, vol. 27, no. 3, pp. 189–204, Feb 2009.

[60] A. J. Viterbi, *CDMA: principles of spread spectrum communication*. Addison Wesley Longman Publishing Co., Inc., 1995.

[61] F. Bai and A. Helmy, "A Survey of Mobility Models," *Wireless Adhoc Networks. University of Southern California, USA*, vol. 206, p. 147, 2004.

[62] J. Broch, D. A. Maltz, D. B. Johnson, Y.-C. Hu, and J. Jetcheva, "A Performance Comparison of Multi-hop Wireless Ad Hoc Network Routing Protocols," in *Proceedings of the 4th Annual ACM/IEEE International Conference on Mobile Computing and Networking*, ser. MobiCom '98. New York, NY, USA: ACM, 1998, pp. 85–97.

[63] C. Bettstetter, H. Hartenstein, and X. Perez-Costa, "Stochastic Properties of the Random Waypoint Mobility Model," *ACM Wireless Netw.*, vol. 10, no. 5, pp. 555–567, Sep. 2004.

[64] E. Hyytiä and J. Virtamo, "Random Waypoint Mobility Model in Cellular Networks," *Wireless Networks*, vol. 13, no. 2, pp. 177–188, 2007.

[65] J. B. Kuipers, *Quaternions and rotation sequences*. Princeton university press Princeton, 1999, vol. 66.

[66] C. Barthold, K. P. Subbu, and R. Dantu, "Evaluation of Gyroscope-Embedded Mobile Phones," in *Proc. IEEE Int. Conf. Syst. Man Cybernetics (SMC)*, Oct. 2011, pp. 1632–1638.

[67] World Wide Web Consortium (W3C), "Device Orientation Event Specification," *specification at w3c.github.io*, Jul. 2016.

[68] A. A. Purwita, M. D. Soltani, M. Safari, and H. Haas, "Impact of Terminal Orientation on Performance in LiFi Systems," in *IEEE Wireless Communications and Networking Conference (WCNC)*, Barcelona, Spain, April 2018.

[69] S. Jivkova and M. Kavehrad, "Shadowing and Blockage in Indoor Optical Wireless Communications," in *Proc. IEEE Globecom*, San Francisco, USA, Dec. Dec. 2003, pp. 3269–3273.

[70] C. Chen, M. D. Soltani, M. Safari, A. A. Purwita, X. Wu, and H. Haas, "An Omnidirectional User Equipment Configuration to Support Mobility in LiFi Networks," in *Proc. IEEE ICC*, Shanghai, China, May. 2019, pp. 1–6.

[71] G. Boudreau, J. Panicker, N. Guo, R. Chang, N. Wang, and S. Vrzic, "Interference Coordination and Cancellation for 4G Networks," *IEEE Communications Magazine*, vol. 47, no. 4, 2009.

[72] N. Himayat, S. Talwar, A. Rao, and R. Soni, "Interference Management for 4G Cellular Standards [WIMAX/LTE UPDATE]," *IEEE Communications Magazine*, vol. 48, no. 8, 2010.

[73] T. D. Novlan, R. K. Ganti, A. Ghosh, and J. G. Andrews, "Analytical Evaluation of Fractional Frequency Reuse for OFDMA Cellular Networks," *IEEE Transactions on wireless communications*, vol. 10, no. 12, pp. 4294–4305, 2011.

[74] Z. Chen, N. Serafimovski, and H. Haas, "Angle Diversity for an Indoor Cellular Visible Light Communication System," in *Vehicular Technology Conference (VTC Spring), 2014 IEEE 79th*. IEEE, 2014, pp. 1–5.

[75] Z. Zeng, M. D. Soltani, M. Safari, and H. Haas, "Angle Diversity Receiver in LiFi Cellular Networks," in *Proc. IEEE ICC*, Shanghai, China, May. 2019, pp. 1–6.

[76] Z. Zeng, M. D. Soltani, X. Wu, and H. Haas, "Access Point Selection Scheme for LiFi Cellular Networks using Angle Diversity Receivers," in *IEEE Wireless Communications and Networking Conference (WCNC)*, Marrakech, Morocco, April 2019, pp. 1–6.

[77] E. W. Jang, Y. Cho, and J. M. Cioffi, "SPC12-4: Throughput Optimization for Continuous Flat Fading MIMO Channels with Estimation Error," in *Proc. 2006 IEEE Globecom Conf.*, pp. 1–5.

[78] P. Pattanayak and P. Kumar, "SINR Based Limited Feedback Scheduling For MIMO-OFDM Heterogeneous Broadcast Networks," in *Proc. 2016 IEEE Twenty Second National Conf. Commun. (NCC)*, 2016, pp. 1–6.

[79] N. Mokari, F. Alavi, S. Parsaeefard, and T. Le-Ngoc, "Limited-Feedback Resource Allocation in Heterogeneous Cellular Networks," *IEEE Transactions on Vehicular Technology*, vol. 65, no. 4, pp. 2509–2521, 2016.

[80] S. Lloyd, "Least Squares Quantization in PCM," *IEEE Transactions on Information Theory*, vol. 28, no. 2, pp. 129–137, March 1982.

[81] J. Leinonen, J. Hamalainen, and M. Juntti, "Performance Analysis of Downlink OFDMA Frequency Scheduling With Limited Feedback," in *Proc. 2008 IEEE Int. Conf. Commun. (ICC)*, pp. 3318–3322.

[82] X. Liu, E. K. P. Chong, and N. B. Shroff, "Opportunistic Transmission Scheduling With Resource-sharing Constraints in Wireless Networks," *IEEE Journal on Selected Areas in Communications*, vol. 19, no. 10, pp. 2053–2064, 2001.

[83] H. Kim and Y. Han, "An Opportunistic Channel Quality Feedback Scheme For Proportional Fair Scheduling," *IEEE Commun. Lett.*, vol. 11, no. 6, 2007.

[84] Y. Sun and M. Honig, "Asymptotic Capacity of Multicarrier Transmission Over a Fading Channel With Feedback," in *Proc. 2003 IEEE Int. Symp. Inf. Theory*, p. 40.

[85] ——, "Minimum Feedback Rates For Multicarrier Transmission With Correlated Frequency-selective Fading," in *Proc. 2003 IEEE Globecom Conf.*, vol. 3, pp. 1628–1632.

[86] Y. Yao and G. B. Giannakis, "Rate-maximizing power allocation in ofdm based on partial channel knowledge," *IEEE Transactions on Wireless Communications*, vol. 4, no. 3, pp. 1073–1083, 2005.

[87] E. H. Choi, W. Choi, J. G. Andrews, and B. F. Womack, "Power Loading Using Order Mapping in OFDM Systems With Limited Feedback," *IEEE Signal Process. Lett.*, vol. 15, pp. 545–548, 2008.

[88] D. J. Love and R. W. Heath, "OFDM Power Loading Using Limited Feedback," *IEEE Transactions on Vehicular Technology*, vol. 54, no. 5, pp. 1773–1780, 2005.

[89] A. G. Marqués, F. F. Digham, and G. B. Giannakis, "Optimizing Power Efficiency of OFDM Using Quantized Channel State Information," *IEEE Journal on Selected Areas in Communications*, vol. 24, no. 8, pp. 1581–1592, 2006.

[90] Y. Rong, S. A. Vorobyov, and A. B. Gershman, "Adaptive ofdm techniques with one-bit-per-subcarrier channel-state feedback," *IEEE Transactions on Communications*, vol. 54, no. 11, pp. 1993–2003, 2006.

[91] M. Vu and A. Paulraj, "On The Capacity of MIMO Wireless Channels With Dynamic CSIT," *IEEE Journal on Selected Areas in Communications*, vol. 25, no. 7, pp. 1269–1283, 2007.

[92] E. W. Jang, Y. Cho, J.-W. Choi, and J. M. Cioffi, "Scheduling Algorithms For Time-varying Downlink Channels," *IEEE Transactions on Wireless Communications*, vol. 7, no. 6, pp. 2063–2068, 2008.

[93] M. Agarwal, D. Guo, and M. L. Honig, "Channel State and Receiver State Feedback for Frequency-selective Block Fading Channels," in *Inf. Theory, 2008. ISIT 2008. IEEE Int. Symp. on*, 2008, pp. 270–274.

[94] ——, "Multi-carrier Transmission With Limited Feedback: Power Loading Over Sub-channel Groups," in *Proc. 2008 IEEE Int. Conf. Commun. (ICC)*, 2008, pp. 981–985.

[95] P. Svedman, S. K. Wilson, L. J. Cimini, and B. Ottersten, "A Simplified Opportunistic Feedback and Scheduling Scheme for OFDM," in *Proc. 2004 IEEE 59th Veh. Technol. Conf. (VTC)*, vol. 4, pp. 1878–1882.

[96] F. Florén, O. Edfors, and B.-A. Molin, "The Effect of Feedback Quantization on the Throughput of a Multiuser Diversity Scheme," in *Proc. 2003 IEEE Globecom Conf.*, vol. 1, pp. 497–501.

[97] D. Gesbert and M.-S. Alouini, "Selective Multi-user Diversity," in *Proc. 2003 3rd IEEE Int. Symp. Signal Proc. and Inf. Technol. (ISSPIT)*, pp. 162–165.

[98] ——, "How Much Feedback Is Multi-user Diversity Really Worth?" in *Proc. 2004 IEEE Int. Conf. Commun. (ICC)*, vol. 1, pp. 234–238.

[99] S. Sanayei and A. Nosratinia, "Opportunistic Downlink Transmission With Limited Feedback," *IEEE Transactions on Information Theory*, vol. 53, no. 11, pp. 4363–4372, 2007.

[100] J. Chen, R. A. Berry, and M. L. Honig, "Large System Performance of Downlink OFDMA With Limited Feedback," in *Proc. 2006 IEEE Int. Symp. Inf. Theory*, pp. 1399–1403.

[101] V. Hassel, D. Gesbert, M.-S. Alouini, and G. E. Oien, "A Threshold-based Channel State Feedback Algorithm For Modern Cellular Systems," *IEEE Transactions on Wireless Communications*, vol. 6, no. 7, p. 2422, 2007.

[102] A. Jalali, R. Padovani, and R. Pankaj, "Data Throughput of CDMA-HDR a High Efficiency-high Data Rate Personal Communication Wireless System," in *Proc. 2000 IEEE 51th Veh. Technol. Conf. (VTC)*, vol. 3, pp. 1854–1858.

[103] K. Kim, H. Kim, and Y. Han, "A Proportionally Fair Scheduling Algorithm With QoS and Priority in 1xEV-DO," in *Proc. 2002 13th IEEE Int. Symp. on Personal Indoor and Mobile Radio Commun (PIMRC)*, vol. 5, pp. 2239–2243.

[104] S. Dimitrov and H. Haas, "Information Rate of OFDM-Based Optical Wireless Communication Systems With Nonlinear Distortion," *Journal of Lightwave Technology*, vol. 31, no. 6, pp. 918–929, 2013.

[105] B. G. Evans, *Satellite communication systems*. Iet, 1999, vol. 38.

[106] G. Bianchi, "Performance Analysis of the IEEE 802.11 Distributed Coordination Function," *IEEE Journal on Selected Areas in Communications*, vol. 18, no. 3, pp. 535–547, 2000.

[107] S. Sanayei and A. Nosratinia, "Exploiting Multiuser Diversity With Only 1-bit Feedback," in *Proc. 2005 IEEE Wireless Commun. Netw. Conf.*, vol. 2, pp. 978–983.

[108] C. Chen, S. Videv, D. Tsonev, and H. Haas, "Fractional Frequency Reuse in DCO-OFDM-based Optical Attocell Networks," *Journal of Lightwave Technology*, vol. 33, no. 19, pp. 3986–4000, 2015.

[109] X. Lin *et al.*, "Towards Understanding the Fundamentals of Mobility in Cellular Networks," *IEEE Transactions on Wireless Communications*, vol. 12, no. 4, pp. 1686–1698, April 2013.

[110] A. C. Cirik, R. Wang, Y. Hua, and M. Latva-aho, "Weighted Sum-rate Maximization For Full-duplex MIMO Interference Channels," *IEEE Transactions on Communications*, vol. 63, no. 3, pp. 801–815, 2015.

[111] P. Aquilina, A. Cirik, and T. Ratnarajah, "Weighted Sum Rate Maximization in Full-Duplex Multi-User Multi-Cell MIMO Networks," *IEEE Transactions on Communications*, vol. 65, no. 4, pp. 1590–1608, 2017.

[112] "*Physical Layer Procedures*," 3GPP, TS 36.213, 2016.

[113] M. D. Soltani, Z. Zeng, H. Kazemi, C. Chen, H. Haas, and M. Safari, "A Study of Sojourn Time for Indoor LiFi Cellular Networks," in *Submitted to IEEE 30th Annual International Symposium on Personal, Indoor, and Mobile Radio Communications (PIMRC)*, Istanbul, Turkey, September 2019, pp. 1–6.

[114] M. A. Arfaoui, M. D. Soltani, I. Tavakkolnia, A. Ghrayeb, C. Assi, H. Haas, M. Hasna, and M. Safari, "SNR Statistics for Indoor VLC Mobile Users with Random Orientation," in *Proc. IEEE ICC*, Shanghai, China, May. 2019, pp. 1–6.

[115] I. Tavakkolnia, M. D. Soltani, M. A. Arfaoui, , A. Ghrayeb, C. Assi, M. Safari, and H. Haas, "MIMO System with Multi-directional Receiver in Optical Wireless Communications," in *Proc. IEEE ICC*, Shanghai, China, May. 2019, pp. 1–6.

[116] B. Peng and T. Kürner, "Three-Dimensional Angle of Arrival Estimation in Dynamic Indoor Terahertz Channels Using a Forward–Backward Algorithm," *IEEE Transactions on Vehicular Technology*, vol. 66, no. 5, pp. 3798–3811, 2017.

[117] Vieyra Software. Physics toolbox sensor suite. [Online]. Available: https://play.google.com/store/apps/details?id=com.chrystianvieyra.physicstoolboxsuite

[118] F. J. Massey Jr, "The kolmogorov-smirnov test for goodness of fit," *Journal of the American statistical Association*, vol. 46, no. 253, pp. 68–78, 1951.

[119] R. Murray Spiegel, *Theory and Problems of Statistics in SI Units*. McGraw-Hill International Book Company; Singapore, 1972.

[120] S. Kotz, T. Kozubowski, and K. Podgorski, *The Laplace Distribution and Generalizations: a Revisit with Applications to Communications, Economics, Engineering, and Finance*. Springer Science & Business Media, 2012.

[121] P. Vaníček, "Approximate Spectral Analysis by Least-Squares Fit," *Astrophysics and Space Science*, vol. 4, no. 4, pp. 387–391, 1969.

[122] S. Baisch and G. H. Bokelmann, "Spectral Analysis with Incomplete Time Series: An Example from Seismology," *Computers & Geosciences*, vol. 25, no. 7, pp. 739–750, 1999.

[123] N. R. Lomb, "Least-Squares Frequency Analysis of Unequally Spaced Data," *Astrophysics and space science*, vol. 39, no. 2, pp. 447–462, 1976.

[124] J. T. VanderPlas, "Understanding the Lomb-Scargle Periodogram," *The Astrophysical Journal Supplement Series*, vol. 236, no. 1, p. 16, May 2018.

[125] A. A. Purwita, M. D. Soltani, M. Safari, and H. Haas, "Terminal Orientation in OFDM-based LiFi Systems," *IEEE Transactions on Wireless Communications*, 2019.

[126] D. Tse and P. Viswanath, *Fundamentals of wireless communication*. Cambridge university press, 2005.

[127] A. Papoulis and S. U. Pillai, *Random Variables and Stochastic Processes*. McGraw-Hill, New York, 2002.

[128] S. D. Dissanayake and J. Armstrong, "Comparison of ACO-OFDM, DCO-OFDM and ADO-OFDM in IM/DD Systems," *Journal of Lightwave Technology*, vol. 31, no. 7, pp. 1063–1072, 2013.

[129] S. Dimitrov and H. Haas, "Optimum Signal Shaping in OFDM-Based Optical Wireless Communication Systems," in *2012 IEEE Vehicular Technology Conference (VTC Fall)*, Quebec City, QC, Canada, Sept 2012, pp. 1–5.

[130] A. Papoulis and S. U. Pillai, *Probability, Random Variables, and Stochastic Processes and Queueing Theory*. Tata McGraw-Hill Education, 2002.

[131] S. Dimitrov, S. Sinanovic, and H. Haas, "Clipping Noise in OFDM-Based Optical Wireless Communication Systems," *IEEE Transactions on Communications*, vol. 60, no. 4, pp. 1072–1081, April 2012.

[132] R. Mesleh, H. Haas, C. W. Ahn, and S. Yun, "Spatial modulation - a new low complexity spectral efficiency enhancing technique," in *2006 First International Conference on Communications and Networking in China*, Beijing, China, Oct 2006, pp. 1–5.

[133] J. Xiong, Z. Huang, K. Zhuang, and Y. Ji, "A Cooperative Positioning with Kalman Filters and Handover Mechanism for Indoor Microcellular Visible Light Communication Network," *Optical Review*, pp. 1–6, 2016.

[134] D. Wu, Z. Ghassemlooy, W. Zhong, and C. Chen, "Cellular Indoor OWC Systems with an Optimal Lambertian Order and a Handover Algorithm," in *Proc. 7th Int. Symp. Telecommun. (IST)*, Sep. 2014, pp. 777–782.

[135] A. M. Vegni and T. D. Little, "Handover in VLC Systems with Cooperating Mobile Devices," in *Proc. Int. Conf. Comput. Netw. Commun. (ICNC)*, Feb. 2012, pp. 126–130.

[136] E. Dinc, O. Ergul, and O. B. Akan, "Soft Handover in OFDMA Based Visible Light Communication Networks," in *Proc. 2015 IEEE 82th Veh. Technol. Conf. (VTC)*, pp. 1–5.

[137] B. J. Mohler *et al.*, "Visual Flow Influences Gait Transition Speed and Preferred Walking Speed," *Experimental Brain Research*, vol. 181, no. 2, pp. 221–228, Aug. 2007.

[138] L. Bartosch, "Generation of Colored Noise," *International Journal of Modern Physics C*, vol. 12, no. 06, pp. 851–855, 2001.

[139] S. M. Kay, "Efficient Generation of Colored Noise," *Proceedings of the IEEE*, vol. 69, no. 4, pp. 480–481, 1981.

[140] R. F. Fox, I. R. Gatland, R. Roy, and G. Vemuri, "Fast, Accurate Algorithm for Numerical Simulation of Exponentially Correlated Colored Noise," *Physical review A*, vol. 38, no. 11, p. 5938, 1988.

[141] G. N. Tavares and A. Petrolino, "On the Generation of Correlated Gaussian Random Variates by Inverse DTF," *IEEE Transactions on Communications*, vol. 59, no. 1, pp. 45–51, January 2011.

[142] J. M. Geist, "Computer Generation of Correlated Gaussian Random Variables," *Proceedings of the IEEE*, vol. 67, no. 5, pp. 862–863, May 1979.

[143] G. E. Box, G. M. Jenkins, G. C. Reinsel, and G. M. Ljung, *Time series analysis: forecasting and control*. John Wiley & Sons, 2015.

[144] R. Mesleh, H. Elgala, and H. Haas, "Optical Spatial Modulation," *IEEE/OSA Journal of Optical Communications and Networking*, vol. 3, no. 3, pp. 234–244, 2011.

[145] I. Tavakkolnia, C. Chen, R. Bian, and H. Haas, "Energy-efficient adaptive MIMO-VLC technique for indoor LiFi applications," in *Proc. IEEE ICT*, St. Malo, France, Jun. 2018, pp. 331–335.

[146] J. E. Hutton and P. I. Nelson, "Interchanging the Order of Differentiation and Stochastic Integration," *Stochastic processes and their applications*, vol. 18, no. 2, pp. 371–377, 1984.